Institut für Geodäsie und Geoinformation (IGG)

Professur für Geodätische Erdsystemforschung

Climate-driven and intrinsic oceanic excitation of low-frequency polar motion variability

Dissertation
zur Erlangung des akademischen Grades
Doktorin der Ingenieurwissenschaften (Dr.-Ing.)

der Agrar-, Ernährungs- und Ingenieurwissenschaftlichen Fakultät
der Rheinischen Friedrich-Wilhelms-Universität Bonn

von

Lara Börger

aus Simmerath

Bonn 2026

Referent: Dr. techn. Michael Schindelegger

Korreferentin: Univ. Prof. Dr.-Ing. Susanne Glaser

Korreferent: Univ. Prof. Dr. Maik Thomas

Tag der mündlichen Prüfung: 10.03.2026

Angefertigt mit Genehmigung der Agrar-, Ernährungs- und Ingenieurwissenschaftlichen Fakultät der Universität Bonn

Abstract

Earth rotation is fundamental for defining reference systems and applications such as navigation on Earth and in space. In addition to lunisolar torques, internal processes such as mantle deformations or mass redistributions in geophysical fluids affect the rotation of our planet. Along with lunisolar torques, variations in the atmosphere, ocean, terrestrial hydrology, and cryosphere cause small fluctuations, reported as Earth Orientation Parameters and including polar motion and changes in length-of-day (ΔLOD). Since the total angular momentum is conserved, it can only be exchanged between the subsystems of the Earth. The ocean, with its large-scale mass redistributions, induces rotational fluctuations, quantified as excitation functions previously unexplored termed ocean angular momentum (OAM). This thesis aims to shed light on the processes involved in the oceanic excitation of polar motion on interannual time scales. Specifically, the excitation induced by (i) the El Niño–Southern Oscillation (ENSO) and (ii) intrinsic oceanic (i.e., internally generated) variability is quantified. In addition, OAM estimates from three ocean reanalyses are tested for their value in Earth rotation studies, with an eye on potential impacts of the reanalyses' sequential data assimilation (DA) schemes. For periods $<$120 days and after correction of atmospheric effects, the three reanalyses explain 40–50% of equatorial and 30–40% of ΔLOD excitation variance, comparable to a widely used ocean state estimate. Uncertainties remain at longer time scales, reflecting an increased sensitivity to the chosen DA scheme. With the reliability of the OAM series varying across products and time scales, a statistical combination is a good middle ground by suppressing uncertainties. Quantifying ENSO-induced polar motion excitation is the second contribution of this thesis. Previous studies have shown that ENSO modulates ΔLOD through changes in atmospheric winds. Here, the hypothesis is tested whether ENSO excites polar motion through changes in OAM. The ENSO-induced polar motion is derived from four coupled climate models. The mass term is dominant over the motion term (five orders of magnitude) mainly along 90°E with amplitudes of $\pm$4 mas, particularly via a Pacific-Indian basin-wide mass exchange. During three ENSO cycles (1997/98, 2009/10, 2015/16), OAM changes explain 40–50% of the residual observed polar motion excitation variance, but co-occurrence with other broadband signals complicates a clear attribution to ENSO. The final goal is to investigate the excitation signals associated with intrinsic ocean variability, which emerges from non-linear local processes and can attain large (e.g., basin-wide) scales. Ensemble simulations (1995–2015) indicate that intrinsic OAM fluctuations account for $\sim$46% of interannual oceanic excitation, quantified here for the first time. Mass variability is dominated by a single mode of intrinsic bottom pressure fluctuations, which emerges from Drake Passage and exhibits a see-saw pattern between the Atlantic and Southern/Pacific Oceans. Overall, the results in this thesis provide a valuable contribution to understanding ocean-induced low-frequency polar motion variability. Accurate OAM estimates and consideration of model uncertainties due to, e.g., intrinsic variability, are crucial when the goal is to scrutinise rotation data for more subtle effects from other geophysical fluids. Ocean model limitations could be mitigated by assimilating gravity field data or satellite altimetry in future work. In addition, knowledge of the ENSO-induced oceanic excitation signals—as worked out in this thesis—creates an opportunity to improve the accuracy of both OAM estimates and long-term polar motion predictions.

Zusammenfassung

Die Erdrotation ist grundlegend für die Definition von Referenzsystemen und Anwendungen wie die Navigation auf der Erde und im Weltraum. Neben lunisolarer Drehmomente verursachen Massenverlagerungen in Atmosphäre, Hydrosphäre und Kryosphäre Schwankungen in der Polbewegung und der Rotationsrate (ΔLOD). Der Gesamtdrehimpuls bleibt erhalten, Teile davon können jedoch zwischen den Subsystemen ausgetauscht werden. Besonders der Ozean regt durch großskalige Massenumverteilungen Rotationsschwankungen an, welche sich über den ozeanischen Drehimpuls (ocean angular momentum, OAM) quantifizieren lassen. Ziel dieser Arbeit ist die Untersuchung bislang unberücksichtigter Prozesse in der ozeanischen Anregung der niederfrequenten Polbewegung. Konkret werden Anregungssignale im Zusammenhang mit (i) El Niño–Southern Oscillation (ENSO) und (ii) der intrinsischen (d.h., intern generierten) Variabilität des Ozeans betrachtet. Darüber hinaus werden erstmals OAM-Schätzungen aus Ozean-Reanalysen auf ihren Nutzen für Erdrotationsstudien geprüft, insbesondere hinsichtlich möglicher Einflüsse der verwendeten Datenassimilationsschemata. Für $<$120 Tage und nach Reduktion atmosphärischer Beiträge erklären die drei Reanalysen 40–50% der Varianz der äquatorialen und 30–40% der Varianz der ΔLOD-Anregung, vergleichbar mit den Statistiken einer oftmals verwendeten ozeanischen Zustandsschätzung. Auf längeren Zeitskalen lassen sich teils fadenscheinige Fluktuationen in den OAM-Reihen erkennen, wobei eine statistische Kombination der drei Produkte Unsicherheiten reduziert. Im zweiten Kernbeitrag wird anhand des Outputs gekoppelter Klimamodelle untersucht, ob ENSO die Polbewegung durch OAM-Schwankungen anregt. Der Massenterm dominiert das ENSO-Signal in OAM gegenüber dem Bewegungsterm um fünf Größenordnungen mit Amplituden von $\pm$4 mas, insbesondere über einen beckenweiten Massenaustausch zwischen Indik und Pazifik. Für die ENSO-Zyklen in 1997/98, 2009/10 und 2015/16 erklären OAM-Änderungen 40–50% der Varianz der nicht-ozeanischen Polbewegungsanregung, doch überlagernde breitbandige Anregungssignale erschweren eine eindeutige Zuordnung zu ENSO. Schließlich wird die Rolle der intrinsischen Ozeanvariabilität untersucht, welche aus kleinräumigen Instabilitäten hervorgeht, durch Ausgleichsmechanismen im Ozean aber beckenweite Ausdehnung erreichen kann. Ensemble-Simulationen (1995–2015) zeigen, dass die intrinsischen OAM-Schwankungen $\sim$46% der äquatorialen ozeanischen Anregung mit Perioden $>$1 Jahr ausmachen. Die Variabilität des Massenterms ist auf eine einzige Mode an Bodendruckschwankungen zurückzuführen, die vermutlich durch nicht-lineare Dynamik in der Drake-Passage erzeugt wird und ein Dipol-Muster zwischen dem Atlantik und dem Südlichen/-Pazifischen Ozean annimmt. Insgesamt tragen diese Ergebnisse wesentlich zum Verständnis der ozeanischen Anregung der niederfrequenten Polbewegung bei. Genaue OAM-Schätzungen und die Berücksichtigung von Modellunsicherheiten, beispielsweise in Zusammenhang mit intrinsischer Variabilität, sind entscheidend, wenn es darum geht, beobachtete Erdrotationsschwankungen auf kleinere Effekte anderer Fluide hin zu untersuchen. Einschränkungen der Modelle lassen sich in zukünftigen Studien durch die Assimilation von Schwerefeld- oder Satellitenaltimetriedaten verringern. Darüber hinaus bietet das neu gewonnene Wissen um die zu erwartenden OAM-Signale während verschiedener ENSO-Phasen die Möglichkeit, sowohl die Genauigkeit von OAM-Schätzungen als auch Langzeitvorhersagen der Polbewegung zu verbessern.

Acknowledgements

Looking back on the past few years, I can say it has been a challenging yet rewarding journey, filled with valuable lessons. I am proud of what I have achieved and look forward to what the future holds. Above all, I am deeply grateful for the support I have received from many people.

First, I would like to thank my supervisor, Michael Schindelegger, for his invaluable guidance and constant support throughout my doctoral journey. His insightful feedback and enthusiasm for the subject inspired and motivated me, allowing me to grow both scientifically and personally. I am also grateful to Susanne Glaser, who kindly agreed to become a supervisor and offered her valuable support. Moreover, I would like to thank Maik Thomas for his guidance and constructive discussions.

I would like to acknowledge the German Research Foundation (Deutsche Forschungsgemeinschaft, DFG) for supporting the project DISCLOSE (project no. 459392861), which made this research possible.

My warmest thanks go to my colleagues and former colleagues in the GESS, APMG, and GRV groups. I truly appreciated all the inspiring—mostly non-scientific—discussions, help and encouragement they gave me during my time at IGG. You are one of the reasons I always enjoy coming to work. A special thanks goes to my office partner Lana, who has become a close friend and always had an open ear for both scientific and non-scientific discussions. I am also thankful my colleagues at GFZ Potsdam in Section 1.3, especially Henryk Dobslaw, for his support and for always making me feel welcome in Potsdam.

I am deeply grateful to my friends, who have always supported me, listened patiently, and reminded me of what truly matters in life. In particular, I would like to thank Christian, who has been by my side through thick and thin since our student days. My heartfelt thanks also go to Vero, who listened to every detail and always provided great support. Furthermore, I would like to thank Yoshi, Fabi, Andi, and Fynn for always being there—to listen, to laugh, and to help me switch off when needed.

My heartfelt thanks go to my parents, Gaby and Klaus, my stepmother Jenny, my grandparents Ursel and Heinz, and my brother David, for their endless patience, for always having an open door for me, and for believing in me unconditionally. A special thanks goes to my dad, who supported me not only in his role as a father but also with his professional expertise. Without their encouragement and support, this work would not have been possible. Finally, I would like to thank Janik for his unwavering support, for always standing by my side, and for giving me the strength for this journey and to complete this thesis.

Contents

1. Introduction

1.1. Motivation

The rotation of the Earth has fascinated humans for centuries, as it determines our day-night cycle (e.g., Torge, 2003). This period is relevant not only to us, but also for other organisms, since biological rhythms such as plant growth or animal activity are synchronised with day and night (e.g., Kronfeld-Schor et al., 2013). While these biological cycles highlight the influence of Earth rotation on life, its physical characteristics and especially the small deviations from uniform rotation are also relevant to geosciences. For geodesists in particular, Earth rotation is of major importance (e.g., Moritz and Mueller, 1987), as it is one of the three pillars of geodesy[1].

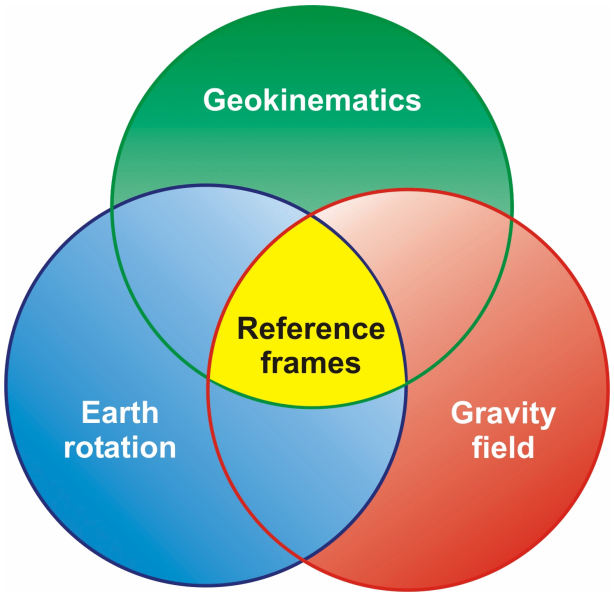

Figure 1.1: The three pillars of geodesy: Geokinematics, gravity field, and Earth rotation, which form the conceptual and observational basis for reference frames. Figure adapted from `https://www.iag-ggos.org/about_ggos/the_three_pillars.php`.

The three pillars—geokinematics, gravity field, and Earth rotation—form the conceptual and observational basis for reference frames (see Figure 1.1). These pillars are, in turn, relevant for observations of the Earth with both terrestrial and space geodetic methods (Torge, 2003;

[1] `https://www.iag-ggos.org/about_ggos/the_three_pillars.php`

Altamimi et al., 2023). In addition to these applications, understanding Earth rotation variations is essential for the navigation and positioning of satellites, precise orbit determination, the realisation of time systems, and Earth system studies.

All of these applications require an accurate understanding of Earth rotation variability (Altamimi et al., 2023). Besides external gravitational forces exerted by the Sun and Moon, which mainly cause long-term variations such as precession and nutation, the Earth is influenced by a variety of internal processes (Gross, 2007). These processes include the deformation of the solid Earth in the crust and mantle, and geophysical processes in components such as the atmosphere, ocean, terrestrial hydrology, and cryosphere. They lead to deformation of the Earth's body, but also to small but measurable changes in Earth rotation, reported as variations in Earth Orientation Parameters (EOPs), including polar motion and changes in length of day (ΔLOD). Owing to the conservation of angular momentum (Munk and MacDonald, 1960; Moritz and Mueller, 1987), the total angular momentum of the Earth system remains constant, but portions of it can be exchanged between the aforementioned subsystems (Gross, 2007).

Among these subsystems, the ocean is particularly important because of its large-scale mass redistributions, its distinct currents and its interactions with the atmosphere (Ponte et al., 1998; Quinn et al., 2019; Harker et al., 2021) as well as the water stored in liquid or frozen form on land (Adhikari and Ivins, 2016). Defining dynamical processes in the ocean include eddies, large-scale circulations, and climate modes such as the El Niño–Southern Oscillation (ENSO). Through mass redistributions and motions associated with these oceanic processes, the angular momentum of the ocean and, in further consequence, that of the solid Earth changes. The angular momentum changes associated with mass motion and redistribution are commonly expressed as *excitation functions*. These functions quantify the contribution of each geophysical fluid to variations in Earth rotation (e.g., Munk and MacDonald, 1960; Barnes et al., 1983; Gross, 2007).

To investigate these processes and their impact on variations of Earth rotation, different types of data are required. Observations provide direct but spatially and temporally limited insights into the real ocean (e.g., Legeais et al., 2016; Tapley et al., 2019). Numerical ocean models, on the other hand, offer complete space-time coverage but are mathematical representations of real world processes and therefore necessarily imperfect (Wunsch and Heimbach, 2013). Models and observations can also be combined through means of data assimilation, but this can introduce kinematic inconsistencies in the ocean's state (Wunsch and Heimbach, 2013). Understanding both the underlying oceanic processes and the quality of their representation in models and observations are therefore crucial for Earth rotation studies.

1.2. State of the art

Changes in Earth rotation are observed by multiple space-geodetic techniques, including Very Long Baseline Interferometry (VLBI), Global Navigation Satellite System (GNSS), Satellite Laser Ranging (SLR), and Doppler Orbitography and Radiopositioning Integrated by Satellite (DORIS, Altamimi et al., 2023). Frequently used data sets are combinations of the four sources, which emphasise the respective strengths of the techniques and ensure high accuracy across all five EOPs (see Chapter 2.2 for a detailed description). Examples are the SPACE2018 series by Ratcliff and Gross (2019) or the International Earth Rotation and Reference Systems Service (IERS) EOP C04 series by Bizouard et al. (2019) (see Chapter 2.3 for further details).

Based on these observational products, the excitations associated with Earth's different geophysical fluids are derived following the excitation formalism originally represented in Munk and MacDonald (1960), which allows for the analysis of the origin of small rotational perturbations (see Chapter 2.4 for further details). The atmospheric excitation, corresponding to changes in atmospheric angular momentum (AAM), is typically drawn from data-constrained reanalyses, such as ERA-Interim (Gross et al., 2003, 2004; Bizouard and Seoane, 2010; Neef and Matthes, 2012; Schindelegger et al., 2013b). To quantify the hydrological component, also referred to as hydrologic angular momentum (HAM), studies have made use both of hydrological models (Dill, 2008; Nastula et al., 2022) and mass changes estimates from satellite gravimetry observations of the Gravity Recovery and Climate Experiment - Follow On (GRACE/-FO) (e.g., Adhikari and Ivins, 2016; Meyrath and van Dam, 2016; Nastula et al., 2019). GRACE/-FO solutions have also featured prominently in the quantifying the cryospheric excitation due mass variability of the Greenland and Antarctic ice sheets (Chen et al., 2013a; Göttl et al., 2021). The oceanic excitation, corresponding to changes in oceanic angular momentum (OAM), is usually drawn from ocean state estimates, such as Estimating the Circulation and Climate of the Ocean (ECCO), or free-running forward models, such as the Max Planck Institute Ocean Model (MPIOM) (Marcus et al., 1998; Ponte et al., 1998; Zhou et al., 2005; Quinn et al., 2019; Harker et al., 2021). When combining the angular momentum estimates for the different sub-systems from diverse sources, one has to pay attention to several issues, including the global mass balance (e.g., Yan and Chao, 2012; Dill and Dobslaw, 2019) and the effects of gravitational attraction and loading (GAL) (e.g., Quinn et al., 2015; Adhikari and Ivins, 2016). The relative importance of the mentioned excitation sources varies strongly across temporal scales, as discussed in the following.

The geophysical fluid excitations are present over a wide range of temporal scales, affecting both polar motion and ΔLOD. For polar motion excitation, large-scale mass movement and redistribution in mid-latitudes are particularly important. At intraseasonal periods, i.e., weeks to several months, the atmospheric component dominates signals of oceanic origin, mainly because of excitations associated with surface pressure (Gross et al., 2003; Nastula and Salstein, 1999). The annual, semi-annual, and ter-annual wobbles are also mostly excited by atmospheric pressure variations according to Gross et al. (2003). At the ter-annual frequency, atmospheric winds, ocean bottom pressure, and oceanic currents contribute with magnitudes comparable to that

of atmospheric pressure (Ponte and Ali, 2002; Gross et al., 2003). For interannual variability, i.e., fluctuations with periods >1 year (yr), oceanic processes mainly excite polar motion along the y-component (longitudes of 90°E), while hydrological processes dominate the x-component (longitudes of 0°)—a phenomenon that can be attributed to the respective spatial geometries (i.e., land-sea distribution, see Chapter 2.5.2 for details, Gross et al., 2003; Chen et al., 2013b).

Conversely, excitations of ΔLOD are governed by mass motions and redistributions concentrated in low latitudes (i.e., around the tropics). At intraseasonal periods, zonal atmospheric winds are the main driver in the excitation of ΔLOD, while the effect of atmospheric pressure and oceanic processes is small (Rosen and Salstein, 1983; Gross et al., 2004). Seasonal ΔLOD variations are also primarily caused by atmospheric winds, particularly between the ground and 10 hPa, with small contributions from atmospheric pressure and oceanic processes (Gross et al., 2004). The dominant mechanism for the excitation of interannual ΔLOD variability are also changes in atmospheric winds, with marginal but non-negligible contributions from atmospheric pressure, oceanic, and hydrological processes (Rosen and Salstein, 1983; Gross et al., 2004; Chen et al., 2000). Furthermore, the strong control of ENSO on zonal AAM and thus ΔLOD at interannual time scales is well-studied (Rosen et al., 1984; Yu et al., 2021).

In summary, seasonal and sub-seasonal polar motion excitation and ΔLOD variations have been subject of comprehensive research and are generally well understood (e.g., Ponte and Rosen, 1994; Chen et al., 2000; Gross et al., 2004; Bizouard and Seoane, 2010; Dill and Dobslaw, 2019; Quinn et al., 2019). However, the excitation budget of polar motion cannot be fully closed when considering only the previously discussed components using the community data set for AAM, OAM, HAM (Gross et al., 2003; Chen et al., 2019). Thus, it is worth investigating how new and hitherto untested angular momentum estimates, such as those from ocean reanalyses, fare in studies of the excitation budget from intra-seasonal to interannual frequencies. Moreover, we have to ask the question whether presently available models represent the spectrum of processes in a credible manner. One aspect that has received no attention so far in the literature is the excitation associated with intrinsic oceanic variability, which is the variability generated by the ocean itself. Additionally, the influence of large-scale climate modes, such as ENSO, on polar motion excitation is currently not or incompletely understood (Marcus et al., 2010).

1.3. Objectives

Despite significant progress in understanding Earth rotation variability, key questions remain concerning the ocean's role in exciting polar motion on interannual time scales. In particular, model imperfections, interactions of the ocean with other Earth system components, and chaotic intrinsic variability continue to challenge our ability to close the excitation budget. Addressing these open issues forms the core motivation of this thesis. The main contribution of the presented work lies in the improved understanding of the processes governing the oceanic excitation of

low-frequency (i.e., interannual) polar motion variability, along with insights into the fidelity of the employed ocean models and data products. The central objective of this thesis is:

Shed light on the processes underlying the oceanic excitation of polar motion on interannual time scales.

To address this objective, the thesis combines geodetic observations with oceanographic modelling through three major tasks, which are interconnected by the unifying concepts of observational consistency, process understanding, and variability assessment. These major tasks are based on my three first-author publications, which are presented here in a logical rather than chronological order:

1. Evaluating the usability of ocean reanalyses for Earth rotation studies, published in:
   Börger, L., Schindelegger, M., Dobslaw, H., & Salstein, D. (2023). Are ocean reanalyses useful for Earth rotation research? *Earth and Space Science*, 10, e2022EA002700.
   `https://doi.org/10.1029/2022EA002700`

2. Analysing the effect of ENSO in polar motion excitation using climate models, published in:
   Börger, L., Lentge, K. M., Schindelegger, M., & Dobslaw, H. (2025). ENSO modulates the oceanic excitation of polar motion. Geophysical Research Letters, 52, e2025GL118576.
   `https://doi.org/10.1029/2025GL118576`

3. Investigating the imprint of oceanic chaos on low-frequency polar motion variability, published in:
   Börger, L., Schindelegger, M., Zhao, M., Ponte, R. M., Löcher, A., Uebbing, B., Molines, J.-M., & Penduff, T. (2025). Chaotic oceanic excitation of low-frequency polar motion variability *Earth System Dynamics*, 10, e2022EA002700.
   `https://doi.org/10.5194/esd-16-75-2025`

Each of these publications highlights one novel aspect in Earth rotation research that has not been examined before by any other study. Together, the three tasks provide a comprehensive, up-to-date assessment of the role of the ocean in exciting polar motion variability on interannual time scales.

1.4. Outline

To emphasise my own contribution to the presented publications, I use active voice in parts of this thesis. The thesis is structured to first introduce the fundamentals and theoretical basis for three published articles, before proceeding to the results. In Chapter 2, I provide an overview of reference systems and frames, observational methods, and the equations of motion. This

includes the definition and realisation of both celestial and terrestrial systems. Moreover, I discuss EOP and the transformation between the celestial and terrestrial systems. This is followed by a description of observational methods, where a distinction is made between local and space-geodetic techniques. Then, I introduce the broad strokes of the theory to study the geophysical excitation of Earth rotation variations. Finally, I connect theory and observations and give an overview of the main geophysical effects on Earth rotation from daily to interannual time scales. This chapter provides the framework for the subsequent analyses.

In Chapter 3, I introduce ocean dynamics by starting with the momentum equations and the fundamental laws of conservation. Then, ocean bottom pressure (p_b), the inverted barometer (IB) effect, non-linear dynamics, and chaotic intrinsic oceanic variability are discussed. Finally, approaches for numerical ocean models and model-data syntheses—such as ocean reanalyses—relevant for Earth rotation studies are presented. Here, I lay the basis for the quantification and understanding of the processes analysed in the subsequent chapters.

Chapter 4 turns to natural climate modes in the Earth system. The focus here is on ENSO, as it is the most prominent climate mode, which has been previously tested for excitation signals, especially those perturbing ΔLOD. The chapter begins with an overview of this particular climate mode, before proceeding to other major climate modes that are known or suspected to be relevant with respect to Earth rotation variations.

I present the first results in Chapter 5, which are based on Börger et al. (2023). This publication focuses on the question as to what extent ocean reanalyses are useful for Earth rotation research. The OAM estimates derived from the reanalyses over the time span 2006–2015 are analysed in the frequency domain, as well as in the temporal domain at subseasonal, seasonal, and interannual scales. Comparisons of the reanalyses-based excitation series are performed with each other, with a joint series from a statistical combination of the three individual OAM series, and with Earth rotation data corrected for other geophysical effects.

In Chapter 6, I investigate possible signals of ENSO in polar motion excitation, as published in Börger et al. (2025b). To that end, four models of the Coupled Model Intercomparison Project Phase 6 (CMIP6) project are used to extract ENSO signatures in p_b and the related OAM based on a regression analysis. The resultant p_b fields from the models are compared with each other and with similar regression results from low-pass filtered GRACE observations. Then, the ENSO-derived OAM (i.e., oceanic excitation) series are evaluated against suitably corrected Earth rotation data to infer how much ENSO might be contributing to polar motion excitation.

Chapter 7 is devoted to exploring, for the first time, the excitation of interannual polar motion through chaotic intrinsic oceanic variability (Börger et al., 2025c). To evaluate the intrinsic variability in OAM, output from the OceaniC Chaos—ImPacts, strUcture, predicTability (OCCIPUT) large ensemble is used. These outputs are analysed in the spectral and temporal domains, complemented by a modal decomposition of the intrinsic p_b fields. Comparisons of the OAM estimates are performed against Earth rotation data corrected for other geophysical fluid effects.

The quantitative analyses are supported by discussions addressing oceanographic, geodetic, and geodynamic aspects.

Finally, the main findings of the thesis are summarised in Chapter 8. Moreover, I provide recommendations for future studies based on these results.

2. Concepts and monitoring of Earth rotation

The Earth is not a rigid body, but it is composed of multiple layers, including the deformable solid Earth (crust and mantle) along with atmosphere, ocean, terrestrial hydrology, and the cryosphere (cf. Figure 2.1). Presence of deformations and relative motion complicates the determination and maintenance of a stable reference frame (Gross, 2007; Petit and Luzum, 2010). This chapter provides an overview of the theoretical concepts and practical realisation of geodetic reference systems and frames, the techniques used to observe Earth rotation variations, the excitation formalism based on the angular momentum approach, and the geophysical processes that induce such variations—particularly oceanic mass redistributions in the low-frequency domain.

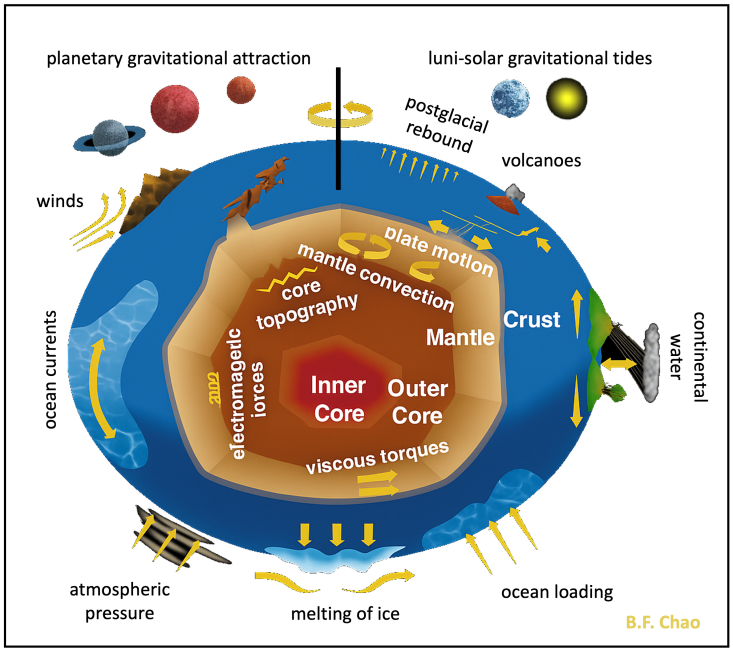

Figure 2.1: Schematic overview of the main Earth system components together with the geophysical processes that act on Earth, along with their interactions. Adapted and customised from `https://connect.agu.org/geodesy/about/about-us`.

2.1. Reference systems and frames

The study of variations of Earth rotation, whether measured from space or on Earth, requires the definition and realisation of a reference system (Torge, 2003). Geodesists distinguish between

a reference system, which is a pure definition or mathematical concept, and a reference frame, corresponding to a physical realisation of the previously defined system. A further distinction is made between a space-fixed and an Earth-fixed reference frame. The Celestial Reference Frame (CRF) is a quasi-inertial system defined by distant extragalactic radio sources whose proper motions can be neglected. In contrast, the Terrestrial Reference Frame (TRF) is a body-fixed, geocentric system defined by precisely determined ground station coordinates and used for positioning on and near the Earth's surface. To convert positions from the TRF to the CRF or vice versa, EOPs are commonly used. Determination of the TRF along with the EOPs is underpinned by conventions, as compiled and published by the IERS (Petit and Luzum, 2010). These conventions ensure that within the reference frame, specific parameters such as origin, scale, orientation, and temporal evolution of these quantities are defined consistently across realisations (Petit and Luzum, 2010).

2.1.1. Celestial Reference Frame

The International Celestial Reference Frame version 3 (ICRF3) is the current realisation of the International Celestial Reference System (ICRS), officially adopted by the International Astronomical Union (IAU) in 2018 (Charlot et al., 2020). The origin of the ICRS is placed in the barycentre of the solar system, i.e., the centre of mass of the sun and planets. The xy-plane is defined in such a way that it is as close as possible to the mean equator and the z-axis (i.e., the pole) is aligned with the direction of the celestial pole. Both definitions refer to the epoch J2000.0, as defined by earlier IAU models of precession and nutation (Charlot et al., 2020).

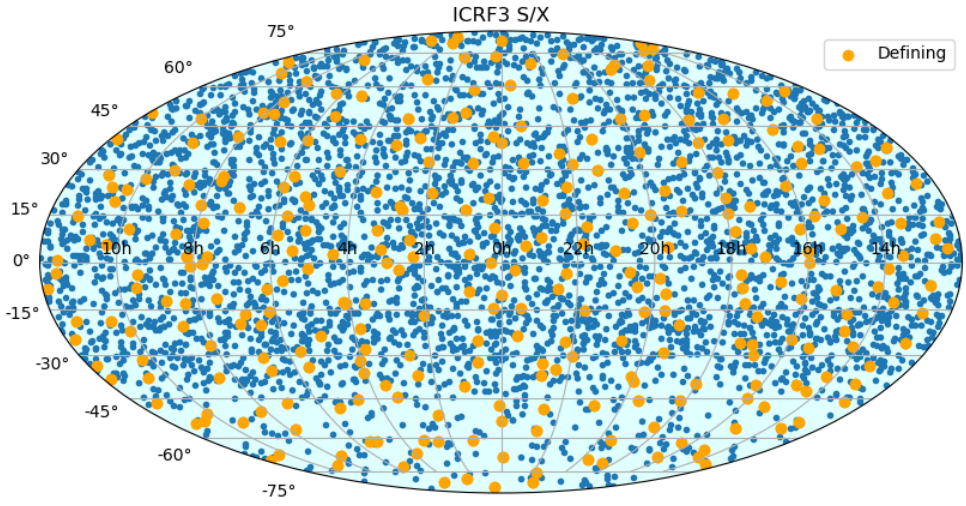

Figure 2.2: Map of the 4,536 radio sources (blue dots) in the S/X band used in the ICRF3 of which 303 defining sources are marked in orange. The defining sources are a subset used to determine the orientation and axes of the ICRF. The non-defining sources are used to densify the frame or improve its overall accuracy, but they do not directly define the frame's orientation (see `https://hpiers.obspm.fr/icrs-pc/icrf/index.php` and Charlot et al., 2020).

The orientation of the ICRS axis is both defined and realised based on the position of extragalactic radiosources, as determined with the technique of VLBI (see Chapter 2.3). The observed objects are primarily quasars, BL-Lacertae objects, and active galactic nuclei, whose apparent position can be considered time-independent (Soffel and Langhans, 2013; Fey et al., 2015; Charlot et al., 2020). Overall, the ICRF3 comprises 4,536 radio sources, including 303 defining sources, in the S/X-band (cf. Figure 2.2), 824 sources in the K-band, and 678 objects in the X/Ka-frequency-bands. This extension leads to an improved global distribution of the sources, increased positional accuracy and better modelling of systematic effects compared to previous realisations. Furthermore, the galactic acceleration of the solar system, which manifests itself as a dipole motion of the source positions, was taken into account for the first time (Charlot et al., 2020). The definition of the geodetic reference system, the determination of EOPs, and the realisation of time systems are among the practical applications of the ICRS and ICRF3 (Petit and Luzum, 2010).

2.1.2. Terrestrial Reference Frame

The TRF is based on concepts of the International Terrestrial Reference System (ITRS), which is a three-dimensional geocentric Cartesian coordinate system that co-rotates with the Earth (Petit and Luzum, 2010). The origin of the ITRS is located in the Earth's centre of mass (including atmosphere and ocean), and the system's scale is consistent with Geocentric Coordinate Time (TCG), ensuring consistency in time measurements. The time dilation at the geocentre is zero, which requires relativistic modelling (Soffel and Frutos, 2016). The orientation of the ITRS is aligned with the reference frame of the Bureau International de l'Heure (BIH), the BIH Terrestrial System 1984 (BTS84), at epoch 1984.0. Within BTS84, the z-axis represents the mean rotation axis between 1900.0 and 1906.0, the x-axis passes through the prime meridian, and the y-axis completes the right-hand system. Each ITRS realisation is required to have no-net-rotation of the geodetic network relative to the previous realisation and thus BTS84, resulting in a constant orientation over time. Furthermore, the changes in the translation and scale parameters with respect to the previous realisation are conventionally set to zero in the combination process of the reference frame and observations (Petit and Luzum, 2010).

The International Terrestrial Reference Frame (ITRF) is the realisation of the ITRS, as materialised through station coordinates and velocities from various space-geodetic observations. Currently involved techniques are VLBI, GNSS, DORIS system, and SLR (cf. Figure 2.3 and Chapter 2.3). The ITRF2020-u2024 is the latest realisation, with the reference epoch set to 2015.0 (Altamimi et al., 2023). This realisation is characterised by improved accuracy and the consideration of the galactic acceleration of the solar system, thereby improving the precision of stationary coordinates to a typical range of 1–2 mm (Altamimi et al., 2023). When determining the velocities of the combined station coordinates and the temporal evolution of the geodetic datum, no-net-rotation conditions are employed in the global adjustment (Petit and Luzum, 2010).

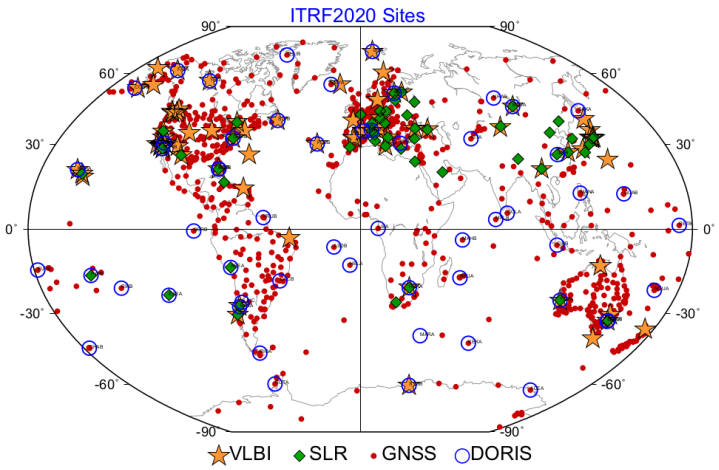

Figure 2.3: Observing sites and techniques contributing to the ITRF2020 (Altamimi et al., 2023). The network includes observations VLBI (orange stars), SLR (green diamonds), GNSS (red dots), and DORIS (blue circles) stations.

2.2. Earth Orientation Parameters

To connect the ICRF and the ITRF, a set of parameters known as EOPs is commonly used. These parameters are essential in both astronomy and geodesy, as they enable precise positioning and time measurements (Torge, 2003; Petit and Luzum, 2010). The set comprises five parameters, including the celestial pole coordinates (X, Y), two angles representing polar motion (x_p, y_p), and an angular quantity that describes the instantaneous rotation phase of the ITRF with respect to the ICRF. A subset of the EOPs are the Earth Rotation Parameters (ERPs), consisting of polar motion and the rotation phase.

The celestial parameters (X, Y) include the phenomena of precession and nutation, which describe the changing orientation of the rotation axis relative to a CRF (Mathews et al., 2002; Capitaine et al., 2003). Both precession and nutation are the responses of the oblate Earth to luni-solar torques and can be predicted almost perfectly. Precession, defined as the axial rotation of the planet around the ecliptic pole, is a long-periodic phenomenon characterised by a 25,800-yr cycle. In contrast, nutation comprises shorter-period oscillations with reduced magnitudes, such as the 18.6-yr oscillation associated with the longitude of the ascending node (Capitaine et al., 2003). Following the IAU resolutions of 2000 and 2006 (Petit and Luzum, 2010, Ch. 5), precession and nutation are accounted for in the ITRF-ICRF transformation by the matrix

$$\mathbf{Q}(t) = \mathbf{R}_3(-E) \cdot \mathbf{R}_2(-d) \cdot \mathbf{R}_3(E + s) \tag{2.1}$$

with the auxiliary variables $E = \arctan(\mathrm{X/Y})$ and $d = \arcsin(\mathrm{Y/E})$ as well as the Celestial Intermediate Origin (CIO) locator s. The quantity s specifies the position of the CIO on the equator of the Celestial Intermediate Pole (CIP) corresponding to the kinematical definition of the non-rotating origin (NRO) in the Geocentric Celestial Reference System (GCRS). The CIP is a conventional reference pole used in the transformation, which refines and replaces

the celestial ephemeris pole used in earlier conventions. Within the IAU2000/2006 framework, the CIP does not coincide with the instantaneous rotation axis of the Earth and has no specific physical meaning. It is merely defined by conventions such that nutation and polar motion are unambiguously separated, while also avoiding short-periodic oscillations in the celestial frame (Petit and Luzum, 2010). The definition of s applies when the CIP is moving with respect to the GCRS, between the reference epoch and the date t, due to precession and nutation (Petit and Luzum, 2010). The matrix $\mathbf{R}_i$ describes the rotation around the respective axis $i = 1, 2, 3$ with the corresponding angle and the parameters (X, Y) indicating the coordinates of the CIP with respect to the ICRS. Note that the nutation matrix $\mathbf{Q}(t)$ can be expressed in different ways depending on the parametrisation choices.

In the classical definition, polar motion refers to the changing position of the rotation axis relative to the body-fixed reference frame, the TRF. In contrast, in newer conventions the pole coordinates (x_p, y_p) refer to the CIP with respect to the ITRS (Petit and Luzum, 2010). Polar motion is influenced by various geophysical effects (see Chapter 2.7 for more details) that reflect dynamic processes in the Earth system rather than external forcing by luni-solar torques. The dominant signals in polar motion are the Chandler Wobble (CW), a free oscillation with a period of $\sim$433 days, and the forced annual oscillation (e.g., Gross, 2007; Kiani Shahvandi et al., 2024). Combined, they give the characteristic beat of 6.3 yrs and peak amplitudes of 9 m, when projected onto the Earth's surface. Polar motion also contains a secular term, i.e., a linear drift of the reference pole that occurs at a rate of 10 cm/yr towards 79°W (Gross, 2007). The main causes for this drift are ongoing mass redistributions in the Earth's mantle in response to how surface loads have changed since the last glacial maximum, an effect known as Glacial Isostatic Adjustment (GIA). Also, there are diurnal and semi-diurnal effects due to gravitational ocean tides, which are regular phenomena that can be predicted very well (Gross et al., 2003; Gross, 2007).

In the transformation, polar motion (x_p, y_p) is accounted for by the matrix $\mathbf{W}(t)$, describing the transformation from the ITRS into an intermediate system, the Terrestrial Intermediate Reference System (TIRS) via

$$\mathbf{W}(t) = \mathbf{R}_3(-s\prime) \cdot \mathbf{R}_2(x_p) \cdot \mathbf{R}_1(y_p). \tag{2.2}$$

Here, $s\prime$ is the Terrestrial Intermediate Origin (TIO) locator, which quantifies the position of the TIO on the equator of the CIP corresponding to the kinematical definition of the NRO in the ITRS. This formulation applies when the CIP is moving with respect to the ICRS due to polar motion (Petit and Luzum, 2010).

The fifth EOP describes variations in the rotation rate, i.e., the angular velocity of the Earth, compared to an atomic frequency standard. There are two common approaches to cast these changes into meaningful parameters: (i) measurement of Universal Time 1 (UT1) and comparison of UT1 to a stable atomic scale, such as the Coordinated Universal Time (UTC), UT1 $-$ UTC $=$ dUT1, and (ii) analysis of perturbations of the nominal rotation rate, that is, ΔLOD. These two

parameters are mathematically related by differentiation in time t as given by

$$\Delta\text{LOD} = -\frac{\text{d}}{\text{d}t}\text{dUT1}. \tag{2.3}$$

Similar to polar motion, ΔLOD is influenced by a range of geophysical effects (see Chapter 2.7). The Earth's core transfers angular momentum to the mantle and thus changes the rotation of the solid Earth on decadal and centennial time scales. Additionally, there are large and persistent harmonic variations, which are associated with solid Earth and ocean tides (Yoder et al., 1981). Subtraction of these tidal signals from the dUT1 or ΔLOD time series reveals many more geophysical effects, e.g., a particular dominant oscillation at the annual frequency with amplitudes up to 2 milliseconds (ms), which is related to seasonal changes in atmospheric winds (Rosen and Salstein, 1983; Gross et al., 2004; Gross, 2007).

The angular parameter is represented in the Earth rotation matrix $\mathbf{R}(t)$, given by

$$\mathbf{R}(t) = \mathbf{R}_3(-ERA). \tag{2.4}$$

This matrix contains the so-called Earth Rotation Angle (ERA), which describes the angle between TIO and CIO measured along the equator of the CIP, and is directly related to UT1. Combined, the transformation from the ITRF to the ICRF, following the IAU resolutions of 2000 and 2006 (Petit and Luzum, 2010, Ch. 5), reads

$$\mathbf{r}_{\text{ICRS}}(t) = \mathbf{Q}(t) \cdot \mathbf{R}(t) \cdot \mathbf{W}(t) \cdot \mathbf{r}_{\text{ITRS}}(t), \tag{2.5}$$

where $\mathbf{r}$ indicates a position vector in the ITRS.

2.3. Observations of Earth rotation

To observe Earth rotation variations, both space-geodetic techniques—such as VLBI, GNSS, SLR, and DORIS—or local measurement methods—like classical gyroscopes, ring laser gyroscopes or the Foucault pendulum—can be used. These techniques differ mainly in the underlying reference system, the measurement principles, and the physical quantities involved (Torge, 2003). The present section gives an overview of both local and space-geodetic techniques, highlighting their advantages and disadvantages.

2.3.1. Local techniques

One of the first experimental proofs of Earth rotation was given by Léon Foucault in 1851 in Paris. He suspended a 2 m long pendulum to observe the rotation of its oscillation plane, which remains fixed in inertial space while the Earth rotates beneath it. In further experiments, he

extended the length of the pendulum to achieve a longer oscillation period and higher accuracy. This experiment is historically significant as it was the first proof of mechanical principles that scientists could observe (Somerville, 1972; Sommeria, 2017). Modern gyroscopes and interferometric devices exploit the principle of inertia in rotating systems, although they are based on different physical mechanisms. This encompasses both conventional gyroscopes and Sagnac interferometers, which implement this principle in different ways. Whereas mechanical gyroscopes are based on the conservation of angular momentum, Sagnac interferometers rely on optical interference effects. A Sagnac interferometer can measure angular rotation relative to an inertial reference frame using the Sagnac effect (Schreiber et al., 2004; Klügel et al., 2005). This effect causes a measurable frequency shift Δf between two laser beams travelling in opposite directions along a closed optical path, given by

$$\Delta f = \frac{4A}{\lambda P}\, \boldsymbol{n} \cdot \boldsymbol{\Omega}, \tag{2.6}$$

where A is the area enclosed by the optical path, λ is the wavelength of the laser light, P is the perimeter (optical path length), $\boldsymbol{n}$ is the unit normal vector to the enclosed area, and $\boldsymbol{\Omega}$ is the angular velocity vector. The scalar product $\boldsymbol{n} \cdot \boldsymbol{\Omega}$ represents the projection of the Earth rotation vector onto the normal vector of the ring laser plane, determining the magnitude of the Sagnac frequency shift. When the normal vector of the ring laser is aligned with the Earth's rotation axis, the Sagnac effect reaches its maximum. In contrast, if the normal vector is orthogonal to the Earth's rotation axis, no effect is observed (Klügel et al., 2005).

Among Sagnac interferometers, a distinction is made between active or passive interferometers. Examples are ring laser gyroscopes and fibre-optic gyroscopes, respectively. While ring laser gyroscopes use a laser source inside the ring, fibre-optical gyroscopes make use of an external laser source (Schreiber and Wells, 2013; Liu et al., 2019). Modern ring laser gyroscopes measure absolute rotation of the Earth in terms of polar motion and ΔLOD. In contrast to space-geodetic techniques, ring laser gyroscopes, such as the G-ring laser in Wettzell (Germany), provide local measurements of Earth's rotation at a fixed location, making them valuable for high-resolution, site-specific observations of rotational variations (Klügel et al., 2005). Thus, ring laser gyroscopes are valuable for complementing global rotation measurements with precise, local observations at fixed locations (Schreiber and Wells, 2013; Schreiber et al., 2023, 2025).

2.3.2. Space-geodetic techniques

With the advent of satellites, radio astronomy, and related technologies, observations of the Earth's rotation using space-geodetic techniques have become possible. Each of the four relevant techniques contributing to the ITRS realisation—that is, VLBI, GNSS, SLR, and DORIS—have their own strengths and weaknesses (Altamimi et al., 2016). In terms of Earth rotation, they have different sensitivities to the EOPs as shown in Table 2.1. Below, the measurement principles of the four techniques, their main error sources, and benefits for EOP determination are presented.

Table 2.1: Comparison of the four space-geodetic techniques with regard to EOP as target parameters. X mark parameters that can be determined, (X) is for reduced determinability and parameters that cannot be determined are indicated by "–".

	VLBI	GNSS	SLR	DORIS	Uncertainty[a]
Precession/nutation	X	(X)	(X)	(X)	–
Polar motion	X	X	X	X	<10 mas
dUT1	X	–	–	–	<2.5 ms
ΔLOD	X	X	X	X	<0.15 ms

[a] Uncertainties are related to the SPACE2019 series by Ratcliff and Gross (2019).

VLBI

In its simplest configuration, a VLBI experiment involves two antennas pointing to the same distant radio source, typically a quasar, and receiving its signal in the same frequency bands (Figure 2.4). The primary observable is the time delay τ, which represents the difference between the two arrival times and is inferred from correlation of the two independent recordings. Knowing τ and the direction to the source allows to resolve the geometry of the experiment, yielding relative coordinates, i.e., the baseline between two antennas, with an accuracy of a few mm (Petit and Luzum, 2010; Schuh and Behrend, 2012). A precisely determined baseline between the antennas is essential, as it enables one to convert the observed τ into accurate information on the Earth's position and rotation (Teke et al., 2012; Schartner et al., 2021).

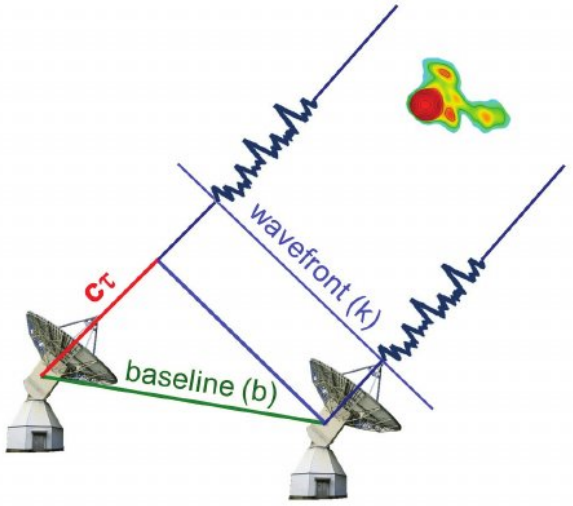

Figure 2.4: The principle of VLBI with the simplest case involving two telescopes according to Teke et al. (2012). The green line is the baseline **b** between the telescopes, dark blue lines are the wavefronts **k** sent from quasar and approaching the telescope, and the red line is the observed time delay τ multiplied with the speed of light c.

As indicated in Table 2.1, VLBI is the only space-geodetic technique that allows for the determination of all five EOPs. In particular, it provides direct access to both celestial pole offsets and UT1, achieving sub-microsecond accuracy. This capability makes VLBI especially valuable for determining components such as nutation, while variations in UT1—more precisely, dUT1—can be used to compute changes in ΔLOD (Schartner et al., 2021).

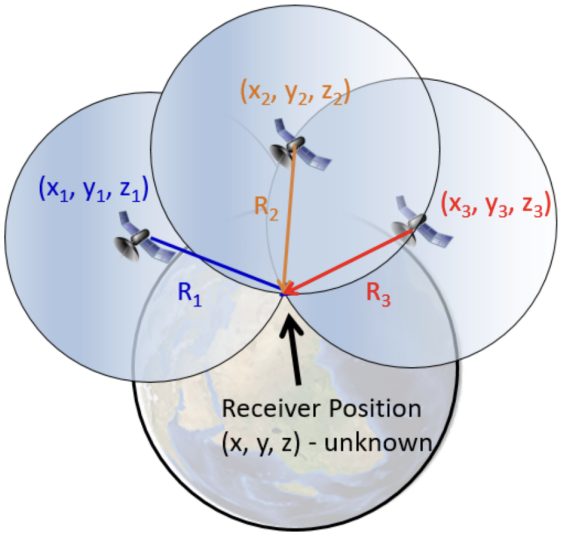

Figure 2.5: Simplified concept for the calculation of the unknown receiver position (black) using three GNSS satellites (blue, orange, red) provided by Peng and Scales (2021). The receiver position is determined by a spherical intersection centred on the positions $(\mathrm{x}_i, \mathrm{y}_i, \mathrm{z}_i)$ of the satellites $i = 1, 2, 3$.

A key advantage of VLBI is the global, albeit inhomogeneous, distribution of its network and the long-term stability provided by over 40 yrs of continuous and precise observations (Altamimi et al., 2023). Despite its advantages, the system is associated with considerable operational costs, related to the installation and maintenance of the large radio telescopes. Additionally, antenna deformations may occur due to thermal and gravitational influences (Nothnagel, 2009). Another limiting factor is the non-hydrostatic component of the tropospheric delay, which is difficult to model (Boehm et al., 2009; Wang et al., 2022). Furthermore, processing and correlating observations in real time is not possible at all sites, because the data volumes are extremely large and regular calibrations are necessary. Mainly, telescopes are only available intermittently, and not all sources are visible at all times for the two participating telescopes. In addition, operation and processing are very expensive and time-consuming (Schuh and Böhm, 2013; Wang et al., 2022).

GNSS

The term GNSS includes various global satellite systems such as the American NAVSTAR GPS (Navigation System with Time And Ranging Global Positioning System, short: GPS), BeiDou of the People's Republic of China, GLONASS (Globalnaja nawigazionnaja sputnikowaja sistema) of Russia, and the European system Galileo. A typical GNSS constellation consists of 24–30 satellites distributed across several orbital planes in Medium Earth Orbit (MEO), ensuring global coverage with at least four satellites visible from any point on the Earth's surface at all times (Hofmann-Wellenhof et al., 2008). The semi-major axis of the satellite orbits is, dependent on the satellite, >25,000 kilometres (km), representing the average distance from the Earth's centre to the satellites in their nearly circular orbits.

To determine the user's position, the receiver simultaneously receives electromagnetic signals from navigation satellites and measures their time of flight, from which the distance to each satellite can be calculated. The frequencies used by GNSS satellites range roughly between 1.2 and 1.6 GHz. For example, GPS transmits on the L1 (1.575 GHz) and L2 (1.228 GHz) frequencies. Typically, multiple frequency bands are used to allow for ionospheric delay corrections of first order, improve positioning accuracy, and increase the robustness of the navigation signals (Hofmann-Wellenhof et al., 2008; Li et al., 2023). Once the distances to the satellites have been determined, the position in the World Geodetic System 1984 (WGS84) is inferred using spherical triangulation, which gives the intersection of three spheres centred on the positions of the satellites (see Figure 2.5). The time difference between the signals from the satellites and the receiver is taken into account to calculate the exact position in space. A fourth satellite is required to calculate the error in the receiver's clock, as the satellites use a high-precision time reference that does not match that of the receiver (Hofmann-Wellenhof et al., 2008).

Uncertainties in the derived position result from effects on satellites, signal propagation, and the ground station (Hofmann-Wellenhof et al., 2008; Teunissen and Montenbruck, 2017; Li et al., 2023). In space, surface forces that are difficult to model perturb the orbit. The satellite clocks are also subject to an error of 10 ns relative to the GPS-time, which causes an error of 3 m in the range between the satellite and the receiver (Hofmann-Wellenhof et al., 2008). Furthermore, the phase centre position varies in time and space, requiring calibration for high-precision applications. On its path between the satellite and the ground station, the signal is affected by ionospheric and tropospheric refraction. In the ionosphere, the propagation delay depends (i) on the electron content along the signal path and (ii) on the frequency used because the ionosphere is a dispersive medium for microwaves. As the ionisation is strongly dependent on location and time, an error of up to 30 m can occur (Coster et al., 2017). Reaching the troposphere, there are delays due to refractivity, which are primarily dependent on altitude and can be determined by air pressure, temperature, and humidity. While the hydrostatic part of the troposphere can be modelled well, the wet part is more difficult to determine. The error in the troposphere is smaller with 2.5 m in zenith, but more difficult to determine than that in the ionosphere (Balidakis et al., 2018; Jones et al., 2020). Finally, the signal may undergo one or more reflections from surfaces such as the ground or water before reaching the receiver, resulting in 'multipath effects' (Larson et al., 2009; Benton and Mitchell, 2011).

An advantage of GNSS is the global coverage of stations and satellites and the possibility of continuous observations, which constrains the orientation changes of the station network and allows for a precise determination of polar motion and ΔLOD. The large number of satellites and observations results in a huge data set, leading to small formal errors in the derived EOPs. However, dUT1 cannot be determined directly, due to its correlation with the orbital inclination, the right ascension of ascending node, and the orbital period (Rothacher et al., 1999; Hellmers et al., 2019).

SLR

SLR employs ultra-short laser pulses to measure the two-way time-of-flight from a ground station to an orbiting target, typically a satellite with corner cube retro-reflectors at an altitude of a few hundred to thousand kilometre (km). An electronic time interval counter is triggered when the pulse arrives back at the ground station (cf. Figure 2.6). From the measured travel time Δt and the speed of light c, the distance d from the satellite to the observing station can be derived according to

$$d = \frac{\Delta t}{2} \cdot c. \tag{2.7}$$

One advantage of the compact nature of the satellites is that it facilitates accurate modelling of non-gravitational forces. In terms of EOP, both ΔLOD and polar motion can be observed (see Table 2.1), but with lower spatial resolution and lower accuracy than VLBI and GNSS, mainly due to the sparse and inhomogeneous distribution of observing sites and the limited accuracy of the inferred station coordinates (Altamimi et al., 2016, 2023). Moreover, the determination of precession and nutation is more challenging, because nutation is strongly correlated with orbital parameters such as inclination and right ascension of ascending node (Rothacher et al., 1999).

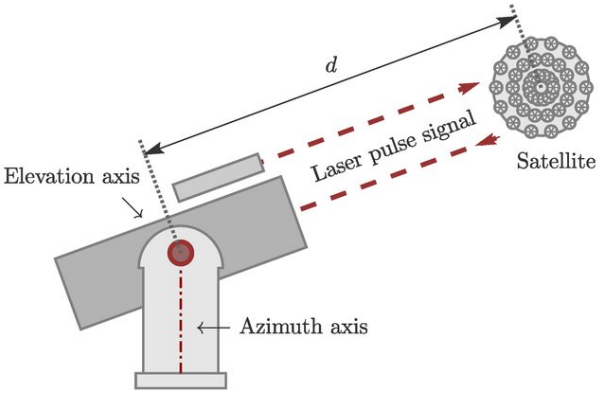

Figure 2.6: Simplified measurement principle of SLR as provided by Lösler et al. (2021). A laser pulse is sent from the observing station to the satellite, where it is reflected. When the pulse arrives back at the ground station, an electronic time interval counter is triggered to measure the time-of-flight.

On its path, the laser beam is only marginally affected by atmospheric refraction, accounted for through standard correction models (cf. Petit and Luzum, 2010, Section 5.1 and 7.1.4). Here, the hydrostatic delay in the troposphere is slightly larger than for microwaves (Drożdżewski and Sośnica, 2024). However, the observations are dependent on the weather, known as the 'Blue Sky effect'. This means observations can only be performed under almost cloudless conditions, which typically occur during high air pressure phases. These conditions cause a depression of the Earth's crust, thus introducing a systematic bias in all SLR-derived observations such as station positions and EOPs, though this effect is well understood and can be modelled in the data processing (Altamimi et al., 2016, 2023).

DORIS

The DORIS system, developed and operated in France, is based on the Doppler principle and is primarily used for determining satellite orbits (Torge, 2003; Hofmann-Wellenhof et al., 2008). Due to the relatively uniform global distribution of its ground stations, known as beacons, DORIS also plays an important role in realising global reference systems and in monitoring Earth rotation variations (cf. Soffel and Langhans, 2013, Chapter 8.2.5).

To track the movement of a satellite relative to the Earth, each beacon transmits signals at two different frequencies, which are received by the satellite (Tavernier et al., 2005). The Doppler count captures how many signal cycles the satellite receives during a given time interval while moving relative to a DORIS station. This count is a direct result of the Doppler effect and gives insight into the relative speed between the satellite and the ground station. By combining many such observations over time, the satellite's orbit can be calculated (Auriol and Tourain, 2010). Although Doppler counts are not as precise as phase measurements, they are robust and accurate enough for many geodetic purposes (Tavernier et al., 2005; Willis et al., 2006).

Besides the balanced network geometry, another strength of DORIS is that many stations are co-located with other space geodetic techniques, forming so-called collocation sites (cf. Figure 2.3). These physical links allow measurements from different techniques to be directly compared and integrated (Altamimi et al., 2023). As for EOPs, DORIS is particularly sensitive to polar motion and ΔLOD, although ΔLOD is not provided by the International DORIS Service (IDS, see Table 2.1). Since its observations are tied to the rotating Earth, DORIS is not sensitive to dUT1, which reflects variations in the Earth's rotation angle in inertial space. Similarly, its sensitivity to precession and nutation is small, as these parameters describe how the Earth's axis moves in the inertial reference frame, something DORIS does not directly observe, because it is operating in an Earth-fixed frame (Tavernier et al., 2005).

In practice, a combination of the four space-geodetic techniques presented above is used to mitigate weaknesses and emphasise strengths, both in terms of reference frame contributions and EOP determinations. An example for a widely used EOP product is the SPACE2018 series by Ratcliff and Gross (2019), derived from a Kalman filter-based combination of multiple space-geodetic techniques. Another possibility is the IERS EOP C04 series by Bizouard et al. (2019), which is generated using a combined adjustment of individual solutions from different analysis centres. The series is computed as a weighted average that accounts for the respective strengths of the methods, resulting in EOPs series of high accuracy and little to no systematic effects.

2.4. Theoretical framework

The theory for describing and modelling Earth rotation variations is based on the equations of gyroscopic motion, which are applied to models of our planet with varying degrees of sophistica-

tion. In the simplest case of a rigid body, Earth's motion in a body-fixed system, such as the TRF, can be described by the Euler equation

$$\boldsymbol{\tau}(t) = \frac{\delta \mathbf{L}(t)}{\delta t} + \boldsymbol{\omega}(t) \times \mathbf{L}(t), \tag{2.8}$$

where $\boldsymbol{\tau}$ describes the external luni-solar torques, t denotes time, and $\boldsymbol{\omega}$ is the angular velocity vector of the rotating system relative to the space-fixed reference system. The angular momentum $\mathbf{L}$ for a rigid body is

$$\mathbf{L}(t) = \mathbf{I}(t)\boldsymbol{\omega}(t), \tag{2.9}$$

where $\mathbf{I}$ is the tensor of inertia. In the rigid-Earth case, $\mathbf{I}(t)$ is invariant, whereas for a deformable Earth, it is time-dependent due to mass redistributions. To transition to a more realistic model of the Earth, deformations and particle movement relative to the body-fixed frame (e.g., due to pressure variations and winds in the atmosphere) are allowed and in that case $\mathbf{L}$ reads

$$\mathbf{L}(t) = \mathbf{I}(t)\boldsymbol{\omega}(t) + \mathbf{h}(t), \tag{2.10}$$

where $\mathbf{h}$ is the relative angular momentum due to deformations and particle motion. Combining equations (2.8) and (2.10) yields the Euler-Liouville equation or just Liouville equation

$$\boldsymbol{\tau}(t) = \frac{\delta}{\delta t}(\mathbf{I}(t)\boldsymbol{\omega}(t) + \mathbf{h}(t)) + \boldsymbol{\omega}(t) \times (\mathbf{I}(t)\boldsymbol{\omega}(t) + \mathbf{h}(t)). \tag{2.11}$$

When introducing perturbations (symbol Δ) by mass displacements and relative angular momentum, the perturbed angular velocity vector $\boldsymbol{\omega}$ reads

$$\boldsymbol{\omega} = \boldsymbol{\omega}_0 + \Delta\boldsymbol{\omega} = \Omega \begin{pmatrix} 0 \\ 0 \\ 1 \end{pmatrix} + \Omega \begin{pmatrix} m_1(t) \\ m_2(t) \\ m_3(t) \end{pmatrix}, \tag{2.12}$$

where Ω is the Earth's mean angular velocity rotating around the z-axis and m_j are the sought-for deviations from uniform rotation. This equation holds in the Tisserand mean-mantle frame, which is a body-fixed reference frame that rotates with the mean angular velocity of the Earth's mantle, excluding relative motions within the deformable mantle but including relative motions within the atmosphere, ocean, and core (Munk and MacDonald, 1960). This is achieved by minimising a global integral of the squared relative angular momentum of the mantle (Wahr, 1982, 1983), thereby defining a reference frame in which the mantle's internal motions do not contribute to the Earth's overall angular momentum. The perturbed tensor of inertia is

$$\mathbf{I} = \mathbf{I}_0 + \Delta\mathbf{I} = \begin{pmatrix} A & 0 & 0 \\ 0 & B & 0 \\ 0 & 0 & C \end{pmatrix} + \begin{pmatrix} \Delta I_{11}(t) & \Delta I_{12}(t) & \Delta I_{13}(t) \\ \Delta I_{21}(t) & \Delta I_{22}(t) & \Delta I_{23}(t) \\ \Delta I_{31}(t) & \Delta I_{32}(t) & \Delta I_{33}(t) \end{pmatrix} \tag{2.13}$$

with the principal moments of inertia A, B, and C given along their respective axes. A and B can be replaced by $A' = (A + B)/2$, since the Earth is almost axisymmetric. The subscript 0 denotes

initial states. Inserting Equations (2.12) and (2.13) into the Liouville equation (Equation 2.11) and assuming that there are no external torques, i.e., $\boldsymbol{\tau} = 0$, leads to

$$m_1(t) + \frac{\mathrm{i}}{\sigma_e}\dot{m}_1(t) = \frac{\Omega^2 \Delta I_{13}(t) + \mathrm{i}\Omega\Delta\dot{I}_{23}(t) + \Omega h_1(t) + \dot{h}_2(t)}{\Omega^2(C - A')} \tag{2.14}$$

$$m_2(t) + \frac{\mathrm{i}}{\sigma_e}\dot{m}_2(t) = \frac{\Omega^2 \Delta I_{23}(t) - \mathrm{i}\Omega\Delta\dot{I}_{13}(t) + \Omega h_2(t) - \dot{h}_1(t)}{\Omega^2(C - A')} \tag{2.15}$$

$$m_3(t) = \frac{-\Omega\Delta I_{33}(t) - h_3(t)}{\Omega C}, \tag{2.16}$$

where the temporal derivative is denoted by a dot ($\dot{}$). The axial component (Equation 2.16) is decoupled from the horizontal components (Equations 2.14–2.15), which determine variations in polar motion. $\sigma_e = \frac{C - A'}{A'}$ is the eigenfrequency of the rotating body, i.e., the Euler frequency for a rigid Earth. The terms on the right-hand side represent geophysical quantities and can be grouped into first-order differential equations, which are referred to as *excitation functions* ψ_i (Munk and MacDonald, 1960). Since the differential equations of the equatorial components are coupled, the excitation functions can be written in complex notation as

$$\hat{\psi}(t) = \frac{\Omega^2 \Delta\hat{I}(t) - \mathrm{i}\Omega\Delta\dot{\hat{I}}(t) + \Omega\hat{h}(t) - \mathrm{i}\dot{\hat{h}}(t)}{\Omega^2(C - A')} \tag{2.17}$$

$$\psi_3(t) = \frac{-\Omega\Delta I_{33}(t) - h_3(t)}{\Omega C} \tag{2.18}$$

with $\hat{\psi} = \psi_1 + \mathrm{i}\psi_2$, $\hat{h} = h_1 + \mathrm{i}h_2$, $\Delta\hat{I} = \Delta I_{13} + \mathrm{i}\Delta I_{23}$, $\hat{L} = L_1 + \mathrm{i}L_2$ and $(\mathrm{i}^2 = -1)$. Combined, Equations (2.14)–(2.16) and Equations (2.17)–(2.18) read

$$\hat{m}(t) + \frac{\mathrm{i}}{\sigma_e}\dot{\hat{m}}(t) = \hat{\psi}(t) \tag{2.19}$$

$$m_3(t) = \psi_3(t). \tag{2.20}$$

2.5. Angular momentum approach

Within the framework of the Euler-Liouville equations, small changes in the Earth's rotation, e.g., due to mass displacements or movements in the atmosphere, oceans or other geophysical fluids, can be analysed in two different ways: In the first approach, the *torque approach*, geophysical fluids are treated as sources of external torques acting on the solid Earth, which are used to compute rotational changes. Conversely, in the second approach, the *angular momentum approach*, the solid Earth and geophysical fluids are treated as one system that conserves its total angular momentum, but exchanges between the subsystems occur. Therefore, analysis of fluid angular momentum changes can be used to infer angular momentum changes of the solid Earth in terms of quantities such as polar motion and ΔLOD (Schindelegger et al., 2013a). The following chapter outlines the angular momentum approach.

2.5.1. Angular momentum functions

If the relative components of the angular momentum h_j and ΔI_{jk} $(j,k = 1,2,3)$ and their temporal deviation are known, for example from models or observations, then Equations (2.14)–(2.16) can be solved for m_j and thus $\boldsymbol{\omega}$. To quantify changes in angular momentum in practice, Equations (2.17)–(2.18) can be expressed as dimensionless *angular momentum functions* $\hat{\chi}$, χ_z through linearisation given by

$$\hat{\psi}(t) = \hat{\chi}(t) - \frac{\mathrm{i}}{\Omega}\dot{\hat{\chi}}(t) \tag{2.21}$$

$$\psi_3(t) = -\chi_3(t). \tag{2.22}$$

Considering the right-hand sides of Equations (2.17)–(2.18), the functions $\hat{\chi}, \chi_3$ can be expressed in terms of $\Delta\mathbf{I}, \mathbf{h}$

$$\hat{\chi}(t) = \frac{1}{\Omega(C-A')}\Omega\Delta\hat{I}(t) + \frac{1}{\Omega(C-A')}\hat{h}(t) = \hat{\chi}^m(t) + \hat{\chi}^v(t) \tag{2.23}$$

$$\chi_3(t) = \frac{1}{\Omega C}\Omega\Delta I_{33}(t) + \frac{1}{\Omega C}h_3(t) = \chi_3^m(t) + \chi_3^v(t) \tag{2.24}$$

(Barnes et al., 1983). The inertia terms are called *mass* or *matter* terms (superscripts m) and the relative angular momenta are called *motion* terms (superscripts v, where v indicates velocity), while the external torques are neglected.

So far, we have assumed a rigid, axisymmetric Earth, subject to small perturbations (Gross, 2007). If we now consider the solid part of the Earth to be elastic, with equilibrium oceans, and core-decoupling, this leads to corrections in $\Delta\mathbf{I}$ and $\mathbf{h}$ due to changes in $\boldsymbol{\omega}$ (i.e., variations in the centrifugal force). Incorporating these effects and applying established numerical values from Table 1 in Gross (2007) throughout this thesis, yields

$$\hat{\chi}(t) = \frac{1.100\Omega\Delta\hat{I}(t) + 1.608\hat{h}(t)}{\Omega(C-A')} \tag{2.25}$$

$$\chi_3(t) = \frac{0.748\Omega\Delta I_{33}(t) + 0.998h_3(t)}{\Omega C}. \tag{2.26}$$

These excitation functions are then also called *effective angular momentum functions*, henceforth *angular momentum functions* or *excitation functions*. With these equations, it becomes feasible to investigate the geophysical excitation of polar motion (Equation 2.25) and changes in the rotation rate (Equation 2.26). The underlying Earth model is then partially elastic and dynamically axisymmetric Earth, including equilibrium oceans and an axially decoupled core (Schindelegger et al., 2013a).

2.5.2. Evaluation of angular momentum functions

To evaluate the geophysical excitation from model output or observations, the angular momentum functions must be cast in a form such that they can be used with the standard output of general circulation models (GCM), e.g., numerical weather or ocean models. Following Munk and MacDonald (1960), the variations $\Delta\mathbf{I}$ and $\mathbf{h}$ are expressed as volume integrals over the relevant fluid domains, yielding integrals over density ρ and horizontal velocities (u, v), i.e., eastward and northward velocities,

$$\begin{aligned}\hat{\chi} &= \frac{-1.100a^4}{C-A'} \iiint \rho \, \sin\phi \, \cos^2\phi \, e^{\mathrm{i}\lambda} \, \mathrm{d}\lambda \, \mathrm{d}\phi \, \mathrm{d}r \\ &\quad + \frac{-1.608a^3}{\Omega(C-A')} \iiint \rho(u \, \sin\phi + \mathrm{i}v) \cos\phi \, e^{\mathrm{i}\lambda} \, \mathrm{d}\lambda \, \mathrm{d}\phi \, \mathrm{d}r \qquad (2.27) \\ &= \hat{\chi}^{\mathrm{m}} + \hat{\chi}^{\mathrm{v}} \\ \chi_3 &= \frac{0.748a^4}{C_{\mathrm{m}}} \iiint \rho \, \cos^3\phi \, \mathrm{d}\lambda \, \mathrm{d}\phi \, \mathrm{d}r \\ &\quad + \frac{0.998a^3}{\Omega C_{\mathrm{m}}} \iiint \rho \, u \, \cos^2\phi \, \mathrm{d}\lambda \, \mathrm{d}\phi \, \mathrm{d}r \qquad (2.28) \\ &= \chi_z^{\mathrm{m}} + \chi_z^{\mathrm{v}},\end{aligned}$$

where a is the mean geocentric radius of the Earth, and (ϕ, λ) represent geographical latitude and longitude. The mass terms $\Delta\hat{I}$ and ΔI_{33} (cf. Equations 2.25 and 2.26) can be expressed in terms of pressure at the lower boundary of the respective fluid (p_{s}) by replacing the vertical integral over density by

$$\frac{1}{g} p_{\mathrm{s}} = \int_0^{p_{\mathrm{s}}} \rho \, \mathrm{d}r, \qquad (2.29)$$

which is the hydrostatic equation based on the assumption that the fluid is in hydrostatic equilibrium, i.e., vertical accelerations are negligible. The mass terms then yield (cf. Barnes et al., 1983; Gross et al., 2003)

$$\Delta\hat{I} = -\frac{a^4}{g} \int_{-\frac{\pi}{2}}^{\frac{\pi}{2}} \int_0^{2\pi} p_{\mathrm{s}} \, \sin\phi \, \cos^2\phi \exp(\mathrm{i}\lambda) \, \mathrm{d}\lambda \, \mathrm{d}\phi \qquad (2.30)$$

$$\Delta I_{33} = -\frac{a^4}{g} \int_{-\frac{\pi}{2}}^{\frac{\pi}{2}} \int_0^{2\pi} p_{\mathrm{s}} \, \cos^3\phi \, \mathrm{d}\lambda \, \mathrm{d}\phi. \qquad (2.31)$$

The constant values in the computations throughout this thesis are specified in Table 2.2.

The equatorial excitation function in Equation (2.30) contains trigonometric terms that determine what regions are most effective in generating fluctuations in $\hat{\chi}$. These trigonometric weights are displayed in Figure 2.7 and span the range $[-1, 1]$. Thus, cancellation effects can occur. In the χ_1 component (panel a), high weights are assigned to the Southern Pacific, Southern

Table 2.2: Constant and geodetic parameters of the Earth adapted from Gross (2007).

a	Ω	A'	C^a	C_m
6371 km	$7.292115{\cdot}10^{-5}$ rad s^{-1}	$8.0102{\cdot}10^{37}$ kg m^2	$8.0365{\cdot}10^{37}$ kg m^2	$7.1236{\cdot}10^{37}$ kg m^2

[a] Value of C includes the core.

Atlantic, and North Atlantic regions. Additionally, parts of Northern Africa, Southern Europe, and the Mediterranean Sea also receive high weighting. In contrast, the χ_2 component (panel b) emphasises the Southern Indian Ocean and portions of the Southern Pacific. In the Northern Hemisphere, χ_2 primarily assigns high weights to land masses, particularly in Central Asia and parts of America.

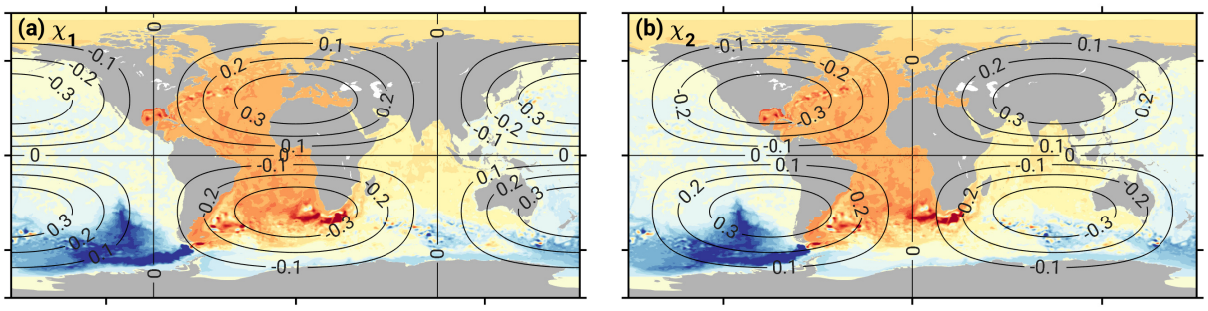

Figure 2.7: Weighting patterns for (a) χ_1 and (b) χ_2, as defined in Equation (2.27). The underlying pattern is the illustration of a basin-wide mode of oceanic variability.

2.6. Connecting theory and observations

Space-geodetic techniques do not observe the movement of the Earth rotation axis directly, but rather the CIP, whose variations are reported as EOP. Use of the above framework with actual rotation data thus requires an analytical connection between the terrestrial motion of the CIP and the instantaneous rotation axis. By considering the properties of rotation matrices, Gross (1992) showed that the sought-for relationship is

$$\hat{m} = \hat{p} - \frac{1}{\Omega}\dot{\hat{p}}, \tag{2.32}$$

where $\hat{p} = x_p + \mathrm{i}y_p$ is the reported polar motion of the CIP in complex notation. Accordingly, $\hat{p}$ and the excitation $\hat{\chi}$ are related through

$$\hat{\chi} = \hat{p} + \frac{1}{\hat{\sigma}_c}\dot{\hat{p}}. \tag{2.33}$$

Here, $\hat{\sigma}_\mathrm{c} = 2\pi(1 + \mathrm{i}/2Q_\mathrm{c})/T_\mathrm{c}$ is the complex-valued Chandler frequency with standard values for $T_\mathrm{c} = 433.0$ days and quality factor $Q_\mathrm{c} = 179$ (Gross et al., 2003). For the axial component, the

relation of the excitation function and ΔLOD or dUT1 reads

$$\chi_3 = \frac{\Delta\mathrm{LOD}}{86,400\,[\mathrm{s}]} = -\frac{\mathrm{d}}{\mathrm{d}t}\mathrm{dUT1}. \tag{2.34}$$

Combined series, such as the SPACE2018 series by Ratcliff and Gross (2019), provide estimates of the motion of the CIP. Analysing these series at the level of excitation requires time differentiation, often referred to as deconvolution. Theoretically, geophysical excitations could also be integrated to yield changes in polar coordinates. However, the excitation functions then include the dominating oscillation of the CW, which is why geodetic observations are usually differentiated or deconvolved (see Chao, 1985, for an in-depth discussion).

2.7. Geophysical effects on Earth rotation

Earth rotation variations can be divided into effects arising from external gravitational torques by other celestial objects and variations associated with geophysical fluid dynamics, e.g., atmosphere, ocean, terrestrial hydrology, or cryosphere (Eubanks, 1993). The material in this chapter pertains to the geophysical fluid motion, where a distinction is made between tidal and non-tidal effects. The former refers to periodic displacements of both solid Earth and fluid masses, whereas non-tidal effects are irregular non-periodic fluctuations that arise from the mass redistribution in the atmosphere, ocean, land hydrology, and the Earth's liquid core. Throughout this work, the excitations of the geophysical fluids are also referred to as AAM, OAM, or HAM.

In addition to the rotational variations caused by fluid dynamics and lunisolar torques, the signatures of the Earth's main free modes, the CW and the Free Core Nutation, show up in rotation data (i.e., polar motion and nutation observations respectively, Gross, 2007). The characteristics of these free modes are set by the Earth's internal structure, principal moments of inertia, and geometry such as the flattening of the Earth's core. The oscillations do not require a continuous external forcing to persist, although they are excited by geophysical processes (Gross et al., 2003; Kiani Shahvandi et al., 2024). The afore-mentioned deconvolution describes the process of removing the signatures of Earth's free modes from the rotation data to arrive at "observed" excitation quantities that can be compared to the modelled geophysical excitation.

To convey an idea of the signal content of the geophysical fluid excitations, Figure 2.8 displays the amplitude spectra of the mass and the motion terms of $\hat{\chi} = \chi_1 + \mathrm{i}\chi_2$. For the spectra of terrestrial hydrology, and the Greenland and Antarctic Ice Sheets, only the mass terms are shown, as studies have demonstrated that the motion term is negligibly small (see Chen et al., 2000; Dobslaw et al., 2010). Overall, all fluids induce pronounced variability for periods $<$1 yr with the atmospheric and oceanic excitation having the highest amplitudes. Furthermore, all fluid components generate excitation signals with seasonal periods. On intraseasonal periods, large-scale surface pressure variations over mid-latitude landmasses are of particular relevance (Nastula and Salstein, 1999; Gross et al., 2003). In the mass term for periods $>$1 year, the atmosphere, ocean and terrestrial

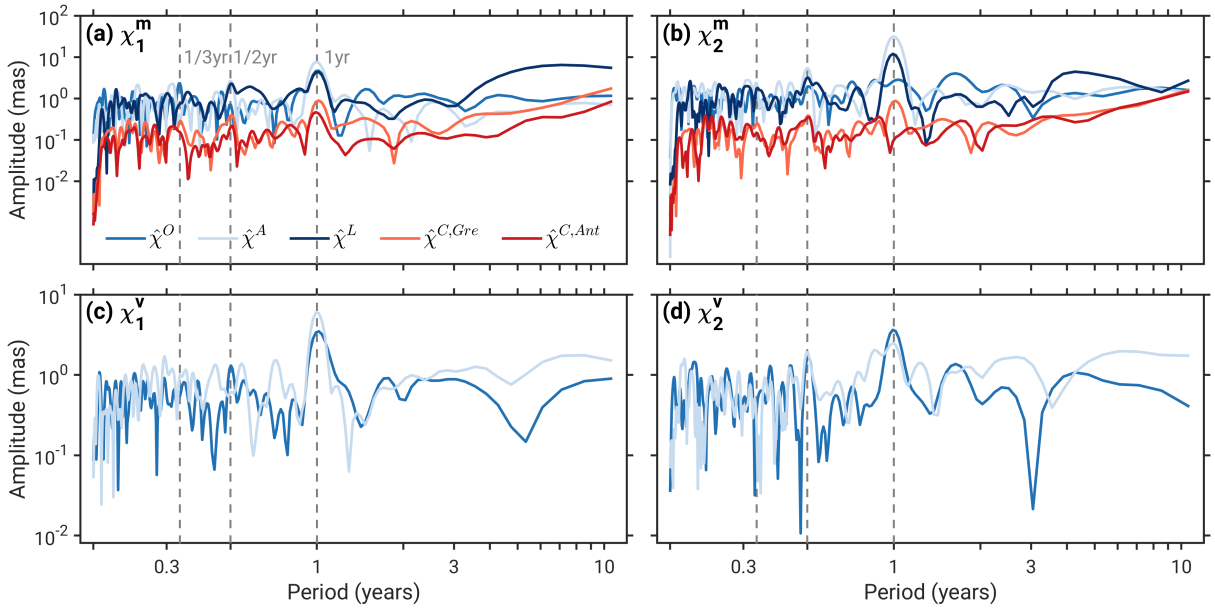

Figure 2.8: Amplitude spectra of polar motion excitation for (a,b) the mass and (c,d) the motion term from different geophysical fluids. Displayed are the spectra for the atmosphere ($\hat{\chi}^A$, light blue), the ocean ($\hat{\chi}^O$, blue), terrestrial hydrology ($\hat{\chi}^L$, dark blue), the Greenland Ice Sheet ($\hat{\chi}^{C,Gre}$, light red), and the Antarctic Ice Sheet ($\hat{\chi}^{C,Ant}$, red). The left panels show the χ_1 components and the right panels depict the χ_2 component. The same data sets as in Börger et al. (2025c) are employed, i.e., ERA-Interim for AAM, OCCIPUT for OAM, and a gravity field reconstruction for HAM and the Antarctic and Greenland Ice Sheet excitations.

hydrology are dominant but from ∼2 yrs on, the amplitude of the excitations from the Greenland Ice Sheet increases in the χ_1 component. In the χ_2 component, both Antarctica and Greenland contribute equally to the polar motion excitation.

When examining the excitation spectra in ΔLOD (see Figure 2.9), all geophysical fluid components exhibit substantial variability at periods $<$1 yr (Gross et al., 2004; Dill and Dobslaw, 2019). Beyond 2 yrs, however, HAM displays the largest amplitudes among the three, primarily due to slow but persistent terrestrial water storage (TWS) changes (Chen et al., 2000). For AAM, the motion term dominates over the mass term, primarily due to changes in zonal winds such as the jet streams in the mid-latitudes of the Northern Hemisphere (Rosen and Salstein, 1983). Conversely, for OAM, the mass term is more prominent than the motion term, which can be attributed to large-scale mass redistributions within the global ocean (Ponte and Rosen, 1994; Gross et al., 2003). Furthermore, large-scale climate modes such as ENSO contribute significantly to ΔLOD variations on interannual time scales, predominantly affecting AAM (Rosen et al., 1984; Yu et al., 2021), while influencing HAM more indirectly via hydrological processes (Chen et al., 2000; Dill and Dobslaw, 2019).

Gravitational attraction and loading

For modelling the excitation budget of polar motion and ΔLOD, it is crucial to ensure mass conservation within the Earth system. A more subtle, non-negligible signal in this context arises

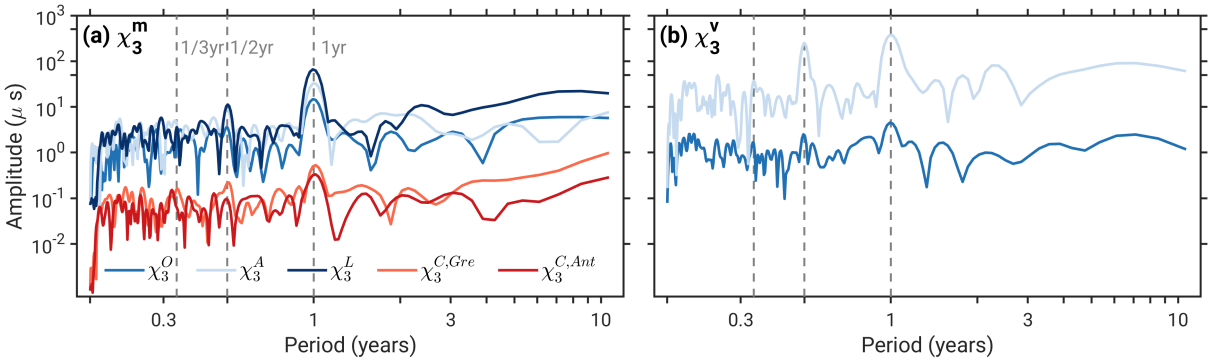

Figure 2.9: Amplitude spectra of ΔLOD, i.e., χ_3, excitations for (a) the mass and (b) the motion term from different geophysical fluids. Displayed are the spectra for the atmosphere ($\hat{\chi}^A$, light blue), the ocean ($\hat{\chi}^O$, blue), terrestrial hydrology ($\hat{\chi}^L$, dark blue), the Greenland Ice Sheet ($\hat{\chi}^{C,Gre}$, light red), and the Antarctic Ice Sheet ($\hat{\chi}^{C,Ant}$, red). Here, the same data sets as for Figure 2.8 are used.

from excitations associated with GAL, which primarily affects polar motion excitation, whereas its contribution to length-of-day variations is comparatively small (e.g., Quinn et al., 2015; Adhikari and Ivins, 2016). These effects describe non-uniform surface loads due to mass redistribution within the Earth system, including variations in atmospheric surface pressure, mass changes over Greenland and Antarctica, and TWS anomalies over the remaining continents. For example, when water moves to the coast due to ice or water displacement, the geoid value rises there due to the gravitational self-attraction of the redistributed mass, thereby maintaining the equipotential condition and restoring the global mass balance (Nakiboglu and Lambeck, 1980). Such surface mass variations induce changes in the gravity field and surface deformation (Farrell and Clark, 1976; Vinogradova et al., 2015) and lead to non-uniform changes of non-steric (i.e., mass-related) sea surface height and associated p_b (Quinn et al., 2015).

Mathematically, the GAL response is obtained by solving the sea level equation globally (Woodward, R. S., 1888; Farrell and Clark, 1976). The sea level equation allows for the calculation of deformations and geoid changes simultaneously to obtain the spatially varying changes in sea level. In the computation, the mass conservation constraint is inherently linked to ensuring that sea level is an equipotential of the Earth's gravity field (Nakiboglu and Lambeck, 1980; Quinn et al., 2015; Adhikari and Ivins, 2016). In addition to load-induced mass exchanges between land and ocean, GAL effects may also arise dynamically from p_b variability driven by atmospheric forcing or intrinsic ocean processes (Vinogradova et al., 2015).

3. Dynamics of the ocean

The ocean is a dynamic system characterised by a variety of physical processes that also affect Earth's rotation through mass redistributions and motions (Gross, 2007). To understand these processes, it is necessary to consider fundamental concepts such as conservation laws and forces acting on a fluid particle (Stewart, 2008). These concepts form the basis for the Navier-Stokes equations, which represent the equations of motion for fluids. Building on these equations, the chapter introduces different established modelling approaches and various types of oceanic variability relevant to the present thesis.

3.1. Momentum equations and dominant forces

To describe the oceanic circulation, the forces acting on a fluid particle are represented in the momentum equations, which are based on Newton's second law (Stewart, 2008; Knauss and Garfield, 2017). The resulting equations are the Navier-Stokes equations, which are commonly used in a simplified form in oceanography in a rotating reference frame. In this context, they are also referred to as governing equations, reading

$$\frac{\partial u}{\partial t} + \text{adv}(u) = -\frac{1}{\rho}\frac{\partial p}{\partial x} + fv + F_x \tag{3.1}$$

$$\frac{\partial v}{\partial t} + \text{adv}(v) = -\frac{1}{\rho}\frac{\partial p}{\partial y} - fu + F_y \tag{3.2}$$

$$\frac{\partial w}{\partial t} + \text{adv}(w) = -\frac{1}{\rho}\frac{\partial p}{\partial z} - g + F_z, \tag{3.3}$$

where the velocities u, v, w are taken along the x, y, and z-direction of a local coordinate system with axes pointing to the East, North, and the vertical (up) component. Moreover, $-\frac{1}{\rho}\frac{\partial p}{\partial i}$ with $i = x, y, z$ is the pressure gradient, f is the Coriolis parameter, acceleration due to gravity is denoted by g, and F_i represents friction, viscosity and external forces per unit mass (e.g., wind stress or tidal forces) (Stewart, 2008). In these equations, the terms on the right-hand side (forces/unit mass) balance the left-hand side (accelerations). The advection terms adv(), which are also known as field acceleration or non-linearities, are defined as

$$\text{adv}(u) = u\frac{\partial u}{\partial x} + v\frac{\partial u}{\partial y} + w\frac{\partial u}{\partial z} \tag{3.4}$$

$$\text{adv}(v) = u\frac{\partial v}{\partial x} + v\frac{\partial v}{\partial y} + w\frac{\partial v}{\partial z} \tag{3.5}$$

$$\text{adv}(w) = u\frac{\partial w}{\partial x} + v\frac{\partial w}{\partial y} + w\frac{\partial w}{\partial z}. \tag{3.6}$$

Table 3.1: Comparison of the magnitudes of the dominant forces, including gravity, the pressure gradient, the Coriolis force, and friction, acting on a fluid particle in units of m s^{-2}. Numbers inferred by the author from Equations (3.1)–(3.3).

	Force [m s^{-2}]			
	gravity[a]	pressure gradient[b]	Coriolis force[b,c]	friction
Magnitude	9.81	$\sim 10^{-6} - 10^{-4}$	$\sim 10^{-4}$	$\sim 10^{-6} - 10^{-5}$

[a] Relevant only in vertical direction (z axis).
[b] In horizontal direction .
[c] For a velocity of 1 m s^{-1} at $\phi = 45°$.

Gravity and pressure gradients coexist, and while gravity continuously pulls water masses downward, the vertical pressure gradient counterbalances this force, as described by the hydrostatic balance (Knauss and Garfield, 2017). This hydrostatic balance is expressed as

$$\frac{\partial p}{\partial z} = -\rho g, \tag{3.7}$$

which shows that pressure increases with depth according to the density distribution (Stewart, 2008). The assumption of hydrostatic balance effectively suppresses instantaneous vertical accelerations. In contrast, in the horizontal direction, only relatively small pressure gradients remain, typically on the order of 10^{-6} to 10^{-4} m s^{-2}, corresponding to about 1 Pa km^{-1} (see Table 3.1), which drive large-scale circulation in combination with the Coriolis force.

Pressure and density structures can further be distinguished as barotropic or baroclinic (Knauss and Garfield, 2017). In the barotropic assumption, the pressure (isobaric) surfaces and density (isopycnic) surfaces are parallel, such that the flow has no vertical shear and the entire water column moves coherently. In simpler terms, the flow is depth-independent. By contrast, for baroclinic phenomena, isobaric and isopycnic surfaces intersect with vertical shear present, which is important for internal waves, instabilities, and mesoscale dynamics. This means that the flow is depth-dependent. Both barotropic and baroclinic dynamics are considered in the literature (Stewart, 2008), depending on the purpose of the study and the involved spatio-temporal scales.

The Coriolis force is a pseudo-force that occurs in a rotating, non-inertial reference frame and becomes important when the particle is in motion (Stewart, 2008). The Coriolis frequency is given by $f = 2\Omega \sin \phi$, where Ω is Earth's angular velocity, and ϕ is the latitude. The Coriolis force always acts at a right angle to the direction of motion and is latitude-dependent, being strongest at the poles and zero at the equator. In the Northern Hemisphere, it deflects moving particle to the right, while in the Southern Hemisphere, it induces a deflection to the left. The magnitude of the Coriolis force is proportional to the velocity of the particle with respect to the Earth, and its effect increases with speed (Knauss and Garfield, 2017). See Table 3.1 for an estimation of the magnitude for 1 m s^{-1} at $\phi = 45°$.

The friction F_i comprises (i) the effects of surface winds that induce waves and currents, (ii) the transfer of kinetic energy between adjacent parcels of water through viscosity, and (iii) boundary layer processes that drain kinetic energy from the ocean and turn it into thermal energy (Stewart,

2008; Knauss and Garfield, 2017). When assuming a wind stress of $\tau_{\text{wind}} \sim 0.1$ N m^{-2} and a depth of 50 m, the friction reaches magnitudes of $\sim 10^{-6}$ m s^{-2}.

3.2. Conservation laws

Conservation laws are fundamental physical principles stating that certain quantities, such as mass, momentum, and energy, remain constant in a closed system, regardless of changes in the system's state. Applied to the global ocean, the conservation laws imply that any imbalance in fluxes of heat, mass, or salinity results in changes in the ocean's average temperature, volume (and thus sea level), or salinity, respectively (Stewart, 2008; Knauss and Garfield, 2017).

Mathematically, mass balance is expressed in the continuity equation for compressible fluids (Knauss and Garfield, 2017). It states that any local increase (decrease) in density must be balanced by a net inflow (outflow) of mass

$$\frac{\partial \rho}{\partial t} + \nabla \cdot (\rho \mathbf{u}) = 0, \tag{3.8}$$

where $\frac{\partial \rho}{\partial t}$ is the change of the density in time, $\mathbf{u} = (u, v)$ is the velocity vector of the considered particle, and $\nabla \cdot (\rho \mathbf{u})$ is the divergence of the mass flux (Stewart, 2008).

In oceanography, the continuity equation is often simplified by assuming incompressibility, leading to a divergence-free velocity field (Stewart, 2008). The Boussinesq approximation is additionally applied, assuming that density variations are small compared to a constant reference density ρ_0 and are only retained when vertical effects such as buoyancy are relevant. This approximation holds well under most oceanic conditions, as density changes caused by temperature and salinity are much greater than those caused by pressure (Stewart, 2008). Under the Boussinesq approximation, the continuity equation simplifies to a statement of no divergence in the flow, i.e.,

$$\nabla \cdot \mathbf{u} = 0. \tag{3.9}$$

The approximation is widely used in global ocean models (Marshall et al., 1997) to efficiently simulate currents, heat transport, salinity distribution, and buoyancy from years to decades. However, when the focus lies on long-term simulations, such as those involving ice melt or mass input by rivers, precipitation, and evaporation, a mass-conserving approach should be used (Stewart, 2008). In the context of excitation of Earth rotation, accurate treatment of mass changes in the ocean is essential (Gross et al., 2003, 2004). Since the Boussinesq approximation conserves volume, a uniform layer with time-dependent thickness can be added to enforce mass conservation (Greatbatch, 1994; Greatbatch et al., 2001).

3.3. Ocean bottom pressure variability and the inverted barometer effect

The pressure at the ocean bottom, denoted as p_b, is an important indicator of ocean mass variations and circulation patterns, relevant for understanding climate variability and sea level fluctuations (e.g., Ponte, 1999; Hughes et al., 2018; Androsov et al., 2020). It reflects changes in the weight of the overlying water column, influenced by freshwater fluxes, ocean currents, and atmospheric pressure variations. Upon integration of the hydrostatic equation over the full water column, p_b can be written as follows (e.g., Ponte, 1999):

$$p_\mathrm{b} = p_\mathrm{a} + \int_{-H}^{0} \rho g \, \mathrm{d}z + \rho_0 g \eta, \tag{3.10}$$

where p_a is the atmospheric surface pressure (or its fluctuation), $\rho = \rho(z)$ is the total density of seawater, ρ_0 represents a constant reference density, and z is the vertical coordinate pointing upwards. The sea level anomaly relative to $z = 0$ is denoted by η. Given the ocean's tendency for an IB response to changes in p_a, one typically writes the sea level anomaly as $\eta = \eta^{\mathrm{IB}} + \eta'$, comprising the IB term $\eta^{\mathrm{IB}} = (\overline{p}_\mathrm{a} - p_\mathrm{a}) / (\rho_o g)$ (Ponte, 1994) and the remaining dynamic component η'. Thus, Equation (3.10) becomes

$$p_\mathrm{b} = \overline{p}_\mathrm{a} + \int_{-H}^{0} \rho g \, \mathrm{d}z + g \rho_0 \eta', \tag{3.11}$$

where $\overline{p}_\mathrm{a}$ is the spatially averaged p_a over the global ocean (Ponte, 1999).

The IB effect represents a static isostatic response to atmospheric surface pressure variations (e.g., Ponte, 1994; Wunsch and Stammer, 1997). Gradients in p_a are balanced by corresponding gradients in η, a rapid adjustment mediated by barotropic waves. As a result, local changes in

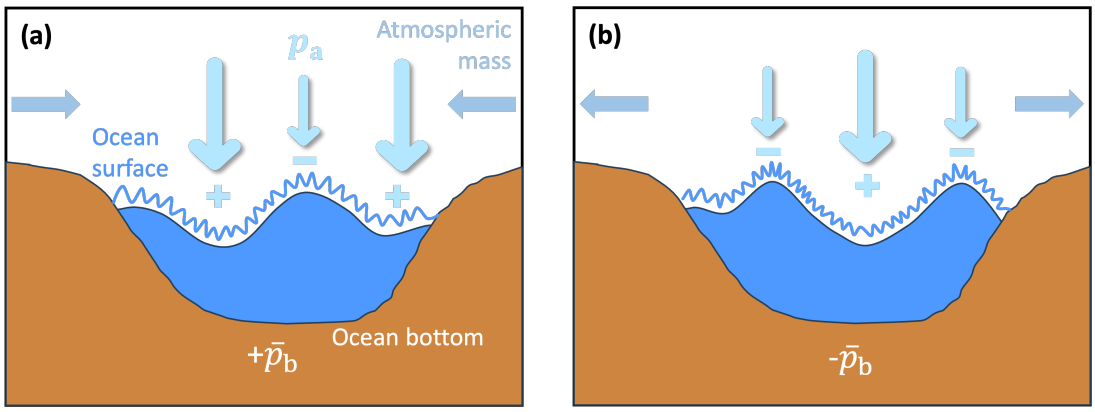

Figure 3.1: Illustration of the IB effect. The land areas are brown, the ocean is blue, and the local atmospheric pressure p_a is represented by the light blue arrow. The mass convergence/divergence in the atmosphere, which changes $\overline{p}_\mathrm{a}$ is shown with the horizontal blue arrows. The barotropic waves that mediate the ocean's IB adjustment are represented by the blue wavy line. Panel (a) depicts the case of high $\overline{p}_\mathrm{a}$ due to mass convergence, causing a positive anomaly in p_b. Panel (b) illustrates that lower $\overline{p}_\mathrm{a}$ results in a negative p_b anomaly.

p_a do not affect p_b. However, changes in $\overline{p}_\mathrm{a}$ cannot be compensated and they thus modulate p_b in a global, uniform manner (cf. Figure 3.1). The IB assumption holds on time scales from several days to seasonal and longer, with only limited deviations at periods of a few days due to barotropic resonances (Wunsch and Stammer, 1997).

In the context of Earth rotation, the separation of p_b into IB and dynamic components is crucial for the correct calculation of OAM. Only the dynamic residual, including the terms $\int_{-H}^{0} \rho g \, \mathrm{d}z + g\rho_0\eta'$ in Equation (3.11), contributes to OAM variability (Ponte, 1997), whereas $\overline{p}_\mathrm{a}$ is commonly considered as part of the AAM functions.

3.4. Non-linear dynamics

So far, we have assumed that oceanic processes are driven by external (e.g., atmospheric, superscript f) forces. These processes include, for example, oceanic currents, atmosphere-ocean interactions and large-scale ocean mass redistributions that affect sea level. Apart from this variability, the ocean itself can generate dynamic fluctuations known as intrinsic or chaotic oceanic variability (superscript i). This variability may originate in non-linear local processes such as baroclinic or barotropic instabilities, arising from vertical density gradients and current shear. Furthermore, intrinsic variability is manifested in mesoscale swirls, i.e., eddies, which are the most visible signature of intrinsic ocean variability, although other mechanisms also contribute (see Figure 3.2 for eddies in the Kuroshio region).

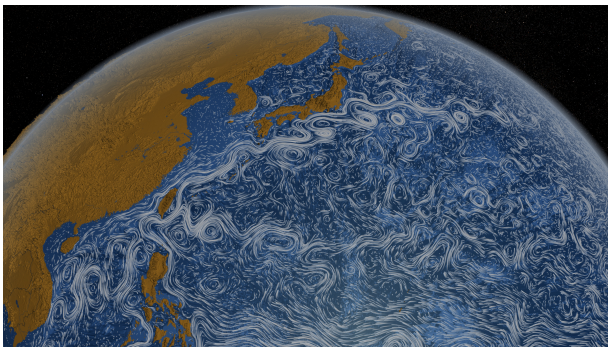

Figure 3.2: Eddies in the Kuroshio region in the period from June 2005 to December 2007 from ECCO2. Figure adapted from NASA Scientific Visualisation Studio (NASA SVS, `https://svs.gsfc.nasa.gov/3827/`).

Mesoscale eddies operate on horizontal scales of 10–100 km and temporal scales of 10–100 days (Rhines, 2019). Figure 3.3 illustrates this variability in the Southern Ocean by comparing a 5-day average snapshot of eddy kinetic energy (EKE) from a single realisation of forced plus intrinsic variability (panel a) and the EKE of the forced variability alone, represented by the ensemble mean of 50 realisations averaged over the period 1980–2015 (panel b). While the 5-day average of forced plus intrinsic variability highlights localised eddies emerging in the lee of topographic features and major current systems, the forced EKE rather emphasises persistent large-scale structures (Hogg et al., 2022). It is, however, also known that the kinetic energy of mesoscale eddies can cascade from smaller to larger spatial and temporal scales, likely as a result of short-lived eddy interactions with large-scale baroclinic instabilities. These interactions lead to upscale energy transfer (e.g., Venaille et al., 2011; Arbic et al., 2014; Sérazin et al., 2018),

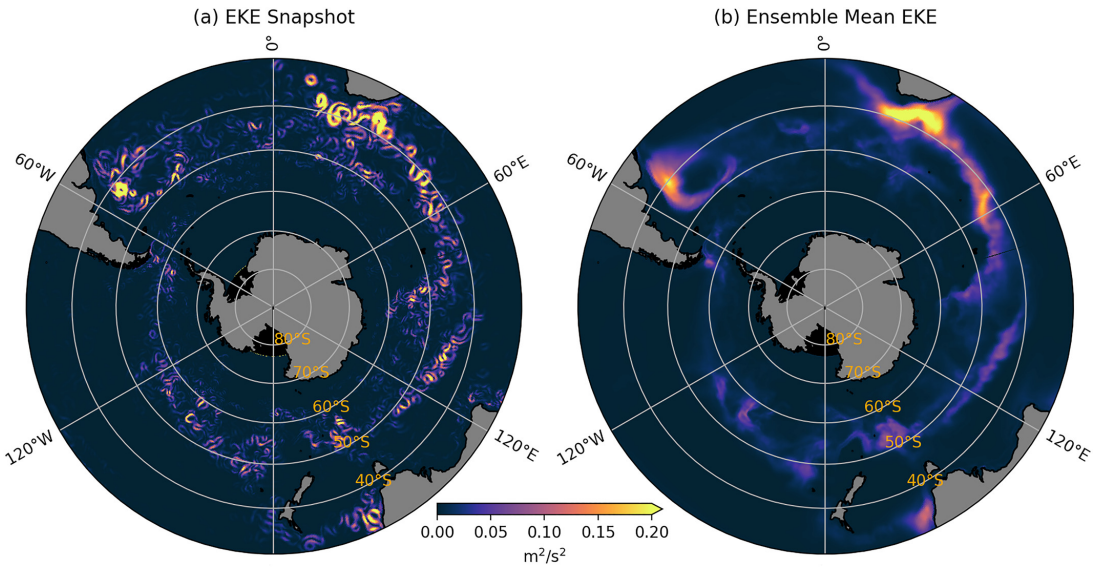

Figure 3.3: 5-day average snapshot of eddy kinetic energy (EKE, in units of $m^2\ s^{-2}$) in the Southern Ocean for (a) of one realisation of forced plus intrinsic variability and (b) the eddy kinetic energy (EKE) of the forced variability alone (i.e., the ensemble mean of a 50-member simulation) averaged over the period 1980–2015. Adapted from Hogg et al. (2022).

a process also referred to as inverse energy cascade. The upscale energy transfer inherent in mesoscale turbulence facilitates coupling between local, small-scale features and basin-scale dynamical adjustments. This scale interaction enables even localised eddy activity to modulate sea level or currents at regional and basin-wide scales at interannual to decadal periods (e.g., Llovel et al., 2018; Leroux et al., 2018; Carret et al., 2021). These multiscale interactions are key to the nature of non-linear ocean dynamics and underscore the need for eddy-resolving or eddy-consistent models to realistically simulate variability at regional to global scales, and to assess the limits of ocean predictability (Penduff et al., 2014; Hogg et al., 2022).

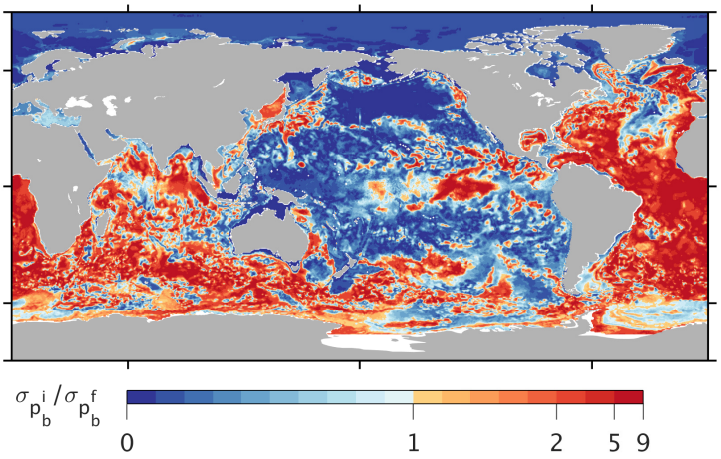

Figure 3.4: Ratio of the standard deviation of the intrinsic ocean bottom pressure $\sigma^i_{p_b}$ and the standard deviation of the forced oceanic component of $\sigma^f_{p_b}$ derived from the OCCIPUT (OceaniC Chaos–ImPacts, strUcture, predicTability) large ensemble (Penduff et al., 2014). Time series at each grid cell are low-pass filtered to periods ≥20 days.

Recent studies that use eddy-permitting simulations with grid spacings $\leq 1/4^\circ$ further suggest that non-linear dynamics generate imprints of chaotic intrinsic variability in local p_b across most of the ocean (Zhao et al., 2021). In addition, evidence has been given for the existence of random fluctuations in p_b between entire basins (Zhao et al., 2023). Overall, the intrinsic component of p_b may be as large or even larger than the forced component in eddy-rich regions (cf. Figure 3.4). These regions include, for example, large parts of the Atlantic and Southern

Oceans, and the Japanese Trench. These findings naturally raise the question as to whether the large-scale, chaotic variability in the oceanic mass field also imprints onto integrated quantities such as OAM.

3.5. Ocean modelling

One approach to studying ocean dynamics is to interpret observations, including remote sensing data, such as from GRACE/-FO (Tapley et al., 2019) and satellite altimeters (e.g., Le Traon et al., 2025), and in-situ observations, such as from ARGO (e.g., Legeais et al., 2016). Observations provide direct insight into the real ocean, but they are often limited in their spatial and temporal coverage. Satellite data may have high spatial resolution but for the ocean, they are typically constrained to surface properties, while in-situ measurements offer depth profiles, albeit sparse and irregularly distributed. To complement these limitations, numerical ocean general circulation models are essential tools for understanding and simulating ocean currents, interactions, and variability (e.g., Wunsch and Heimbach, 2013; Stammer et al., 2016). In the following chapters, the structural and conceptual aspects of modelling will be discussed.

3.5.1. Data-constrained ocean models

Physical oceanography has seen the growth of several types of ocean modelling approaches, which differ in their methodology and application. In the field of Earth rotation, several studies (e.g., Quinn et al., 2019; Harker et al., 2021) have advocated for the use of ocean state estimates such as ECCO. State estimates provide a physically consistent reconstruction of the ocean by finding model parameters and initial conditions that best reproduce observations through the model's governing equations (cf. Equations 3.1–3.3, Forget et al., 2015; ECCO Consortium et al., 2017). In this context, the conservation laws (cf. Chapter 3.2) are strictly enforced, and the models also typically adopt the Boussinesq approximation (cf. Equation 3.9 in Chapter 3.2). This ensures that the resulting ocean state is dynamically consistent and suitable for applications such as Earth rotation studies (Wunsch and Heimbach, 2013; Ponte et al., 2001). State estimates are commonly realised using adjoint methods, which is a transformation of the forward model. In this procedure, the derivative, i.e., the gradient, of the objective function (e.g., a cost function representing deviations between the model and observations and their counterparts) is calculated with reference to the input parameters of the forward model (Wunsch and Heimbach, 2013). In ECCO, the adjoint method is employed to compute the sensitivity of the ocean model to different parameters, e.g., how temperature and salinity (output) change due to changes in wind (input). However, due to repeated forward and backward integrations of the global ocean model over long periods, this procedure is computationally expensive (Wunsch and Heimbach, 2013; Stammer et al., 2016).

Ocean reanalyses, on the other hand, also reconstruct the ocean's state by combining oceanic observations with a general circulation model driven by historical estimates of surface winds, heat, and freshwater using a data assimilation (DA) algorithm. DA approaches typically include three-dimensional variational assimilation (3D-Var), four-dimensional variational assimilation (4D-Var, which also broadly applies to ECCO), and ensemble methods, where the state of the ocean is estimated sequentially at discrete times (Wunsch and Heimbach, 2013). Here, available observations are incorporated into the model via updates to forecast or background states, and information from past observations is kept through multiple assimilation cycles. Figure 3.5 illustrates this step, where the model background $X_{background}$ is updated by an increment $X_{increment}$ and thereby initialised with $X_{analysis}$ (Pilo et al., 2018). Although these approaches are resource-intensive, they are less computationally expensive than adjoint-based state estimates and therefore can be applied in operational reanalyses (Stammer et al., 2016). However, they can introduce dynamical inconsistencies or unphysical changes in the ocean state, as they do not strictly follow conservation laws when the model state is abruptly adjusted toward observations to align model output with data within specified uncertainties (Wunsch and Heimbach, 2013; Pilo et al., 2018; Storto et al., 2019). However, the impact of DA schemes on OAM, and the resulting kinematic inconsistencies, remains untested (Harker et al., 2021).

Uncertainties are usually not provided by either ocean reanalyses and ocean state estimates, although the error covariance matrix is required in the DA framework of ocean reanalyes or for state estimates in the optimisation process. Generally, uncertainties can be derived from ensemble simulations of reanalyses or estimated from the optimisation procedure used in state estimates (Stammer et al., 2016). Table 3.2 provides a summary of the key differences between ocean state estimates and ocean reanalyses.

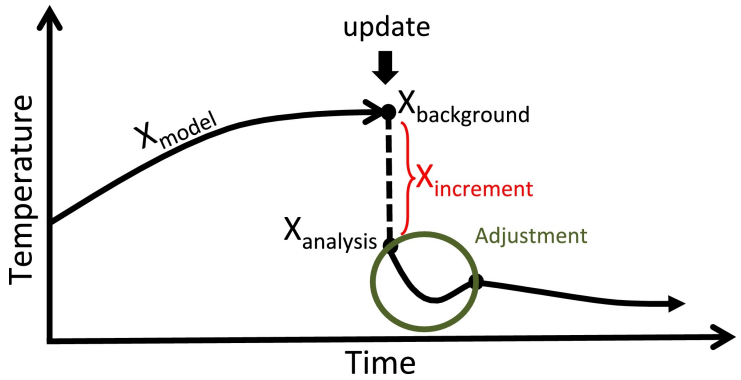

Figure 3.5: Scheme of data assimilation showing the evolving ocean state X vector over time. In the update step, the model background $X_{background}$ is updated by $X_{increment}$, thereby initialising the model for forward integration during the next analysis window with $X_{analysis}$. Figure adapted from Pilo et al. (2018).

Table 3.2: Comparison of ocean state estimates and ocean reanalyses.

	State Estimate	Ocean Reanalysis
Objective	Reconstruction of the ocean state	Reconstruction of the ocean state
Method	Adjoint for a dynamically consistent ocean state	Sequential data assimilation may introduce dynamical inconsistencies
Model parameters	Iteratively updated model to best fit observations	Fixed model throughout all assimilation windows
Application	Earth system studies and geophysical applications (e.g., mass budgets, Earth rotation)	Climate studies, variability and trend analysis, operational monitoring
Uncertainties	Used in the optimisation process, but typically not provided to users	Used in the DA framework, but typically not provided directly to users
Examples	ECCO	GLORYS2v4, ORAS5, FOAM-GloaSea5

3.5.2. Ensemble methods and OCCIPUT

Apart from the single simulations presented above, ensemble methods are a useful tool for quantifying uncertainties, for forecasting purposes, or to analyse non-linear dynamics (see Chapter 3.4). One specific example is the OCCIPUT large ensemble, which has been designed to explore the intrinsic oceanic variability on interannual-to-decadal time scales of ocean/sea-ice hindcasts (see e.g., Penduff et al., 2014; Sérazin et al., 2015; Zhao et al., 2023). More specifically, OCCIPUT has been used to study the intrinsic variability in regional sea level (Llovel et al., 2018; Carret et al., 2021), large-scale volume transports (Leroux et al., 2018; Cravatte et al., 2021), or in p_b (Zhao et al., 2021, 2023). However, global high-resolution ensemble simulations such as OCCIPUT are computationally expensive and thus limited in number and availability (Bessières et al., 2017; Chassignet and Xu, 2021).

OCCIPUT consists of 50 ensemble members with simulations based on the Nucleus for European Models of the Ocean (NEMO) model covering the period 1960–2015. The particular NEMO setup employs a tri-polar grid with a horizontal resolution of $1/4\,^\circ$ (Penduff et al., 2014). Initially, a common 21-yr spin-up with one ensemble member is performed to ensure a dynamically consistent state. Subsequently, the ensemble members are generated by applying small stochastic perturbations to the density equation during 1960 on each realisation (see Figure 3.6, Brankart et al., 2015). Following Bessières et al. (2017), the perturbations are implemented through the stochastic parametrisation scheme embedded in NEMO 3.5. This technique ensures that each ensemble member diverges from the unperturbed member due to random fluctuations in the buoyancy term, while preserving a dynamically consistent ocean state (Penduff et al., 2014; Bessières et al., 2017). The small perturbations on the density equation can then affect mesoscale eddies leading to slightly different realisations (Penduff et al., 2014; Brankart et al., 2015). Finally, each ensemble member is integrated forward in time, driven by the same atmospheric forcing. Here, the DRAKKAR forcing set DFS 5.2 (Dussin et al., 2016) is used, which is based on

ERA-Interim and is provided at a 6-hourly temporal resolution.

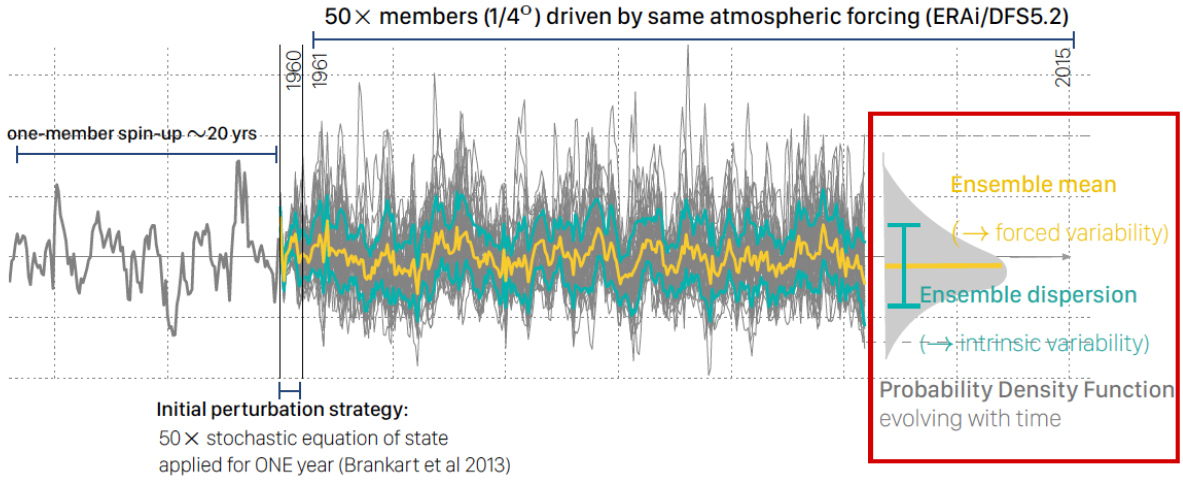

Figure 3.6: The OCCIPUT ensemble is generated from a common spin-up (leftmost part of the figure). This is followed by a stochastic perturbation of each ensemble member in 1960 and afterwards each state is integrated forward in time driven by the same atmospheric forcing. Figure adapted from `https://meom-group.github.io/projects/occiput/`.

The spread of the ensemble members in Figure 3.6 quantifies the effect of the intrinsic oceanic variability, while the ensemble mean represents the forced signal, mainly driven by atmospheric winds (Penduff et al., 2014). The ensembles derived from this probabilistic framework can reproduce key statistical properties of ocean variability at eddying resolution. In particular, the ensemble spread is largest in regions of strong mesoscale activity, such as the Southern Ocean or the Gulf Stream, where intrinsic variability dominates over the forced signal. Furthermore, the ensemble spread was shown to cascade from mesoscale to longer time scales, pointing to a realistic evolution over space and time. These results confirm that the stochastic perturbation approach effectively samples the intrinsic oceanic variability (Bessières et al., 2017).

3.5.3. Relevant model output for Earth rotation studies

To compute the oceanic excitation of polar motion, Equations (2.27) or (2.30) are evaluated. To that end, ocean model output is required, that is, density ρ or ocean bottom pressure p_b and horizontal velocities (u, v). Models commonly provide velocities as part of their diagnostic output, but not ρ. Instead, ρ must be computed from model fields of potential temperature and practical salinity. Potential temperature is the temperature that a sea water parcel would have if subjected adiabatically (i.e., without heat exchange) to a reference pressure. Practical salinity is a salinity variable that accounts for reference pressure conditions (Stewart, 2008). These variables are usually named *thetao* (potential temperature) and *so* (practical salinity). These fields are four-dimensional with [latitude, longitude, depth, time]. To derive ρ from potential temperature and practical salinity, I use the MATLAB® routines from the Gibbs SeaWater (GSW)

Oceanographic Toolbox, which consider the thermodynamic properties of sea water (McDougall and Barker, 2011):

1. Compute pressure P from depth z and latitude ϕ:

```
P = gsw_p_from_z(z, phi)
```

2. Compute conservative temperature CT from potential temperature *thetao* and practical salinity *so*:

```
T = gsw_CT_from_pt(so, thetao)
```

3. Compute absolute salinity SA from practical salinity *so*, pressure P, and coordinates (λ, ϕ):

```
SA = gsw_SA_from_SP(so, P, lambda, phi)
```

4. Finally, compute density ρ from the previously derived values of SA, CT, and P:

```
rho = gsw_rho_t_exact(SA, CT, P)
```

In the calculation of p_b (Equation 3.11), both surface height and bottom topography must be considered (Adcroft et al., 1997). On the one hand, the local sea surface height above geoid, denoted as *zos*, is added to the top ocean cell during the vertical integration of Equation (2.27) to represent the actual sea surface height. Moreover, the model output is given without considering the partial cells used in the numerical model itself, resulting in an idealised, step-wise representation of the ocean bottom (see Figure 3.8, panel a). Therefore, bathymetry data (e.g., the ETOPO1 data set of Amante and Eakins, 2009, see Figure 3.7) are used to better approximate the geometry of the seafloor.

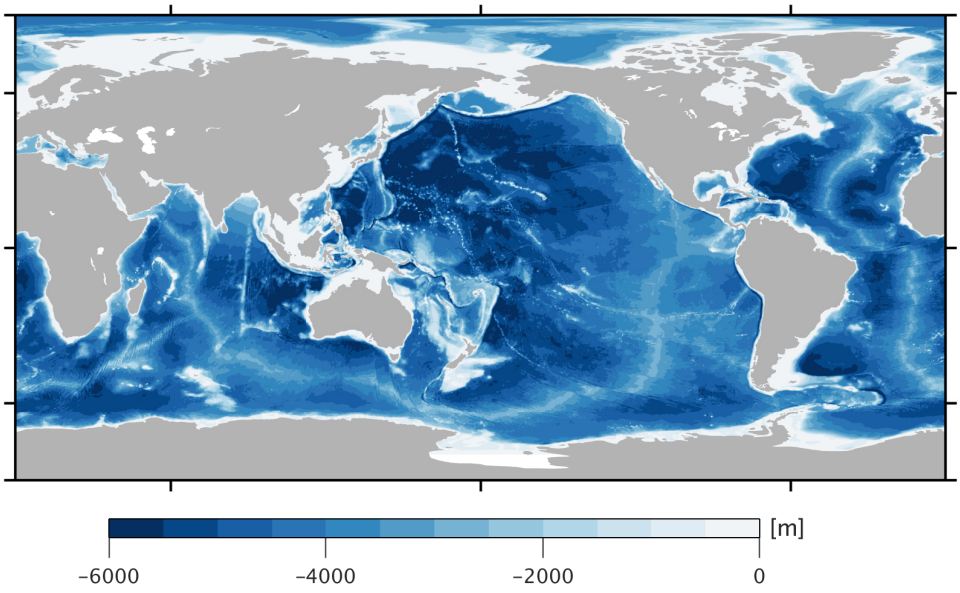

Figure 3.7: Ocean bathymetry (in units of m) of the ETOPO1 data set (Amante and Eakins, 2009).

In detail, the cells at the ocean bottom are scaled by a factor HFAC to consider mixed or partial cells after the fact (see Figure 3.8b and Adcroft et al., 1997). HFAC is defined as

$$\text{HFAC}(\phi, \lambda, h) = \frac{d(\phi, \lambda) - z(\phi, \lambda, h)}{\Delta z(h)}, \tag{3.12}$$

where $d(\phi, \lambda)$ is the bathymetry at (ϕ, λ), $z(\phi, \lambda, h)$ is the depth at the same position but at layer h, and $\Delta z(h)$ is the thickness of the layer h. HFAC takes values in the range $[0, 1]$ and is applied as a multiplier to the bottom-most layer of the vertical integration in Equation (3.11) (Adcroft et al., 1997).

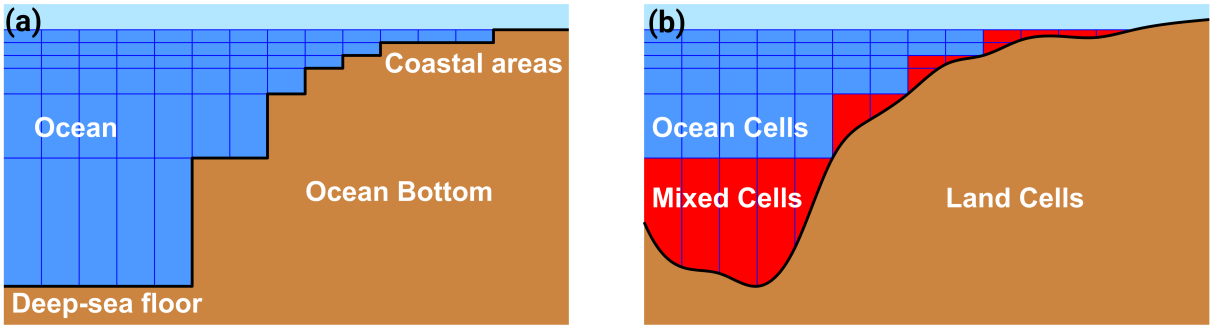

Figure 3.8: Sketch of the lower ocean model cells: (a) model configuration with a uniform ocean surface and an idealised ocean bottom, and (b) the actual bathymetry, where the bottom cells are partial (mixed) cells. Figures adapted from Lentge (2024).

4. Climate modes in the Earth system

The physical principles described in Chapter 3 provide a detailed understanding of the motions and interactions in the ocean. Building on this, the following chapter is dedicated to large-scale climatic phenomena that arise from the coupling between ocean and atmosphere.

4.1. Introduction to climate modes

The Earth's climate system is characterised by various forms of internal variability that arise from complex interactions between the ocean, atmosphere, and other components. One manifestation of such interactions are climate modes, which act on characteristic spatial and temporal scales (cf. Figure 4.1). Climate modes typically exhibit quasi-oscillatory behaviour with their phases described by proxies or index series (McPhaden, 2015). Climate modes can influence important environmental variables such as temperature and precipitation in distant regions, and they thus have a global impact (Wang and Schimel, 2003). While their global impact is generally smaller than that of externally forced changes, it is nonetheless non-negligible. Additionally, by redistributing mass on a global scale, climate modes can even affect the Earth's rotation, but that remains an underresearched question (see Chapter 1).

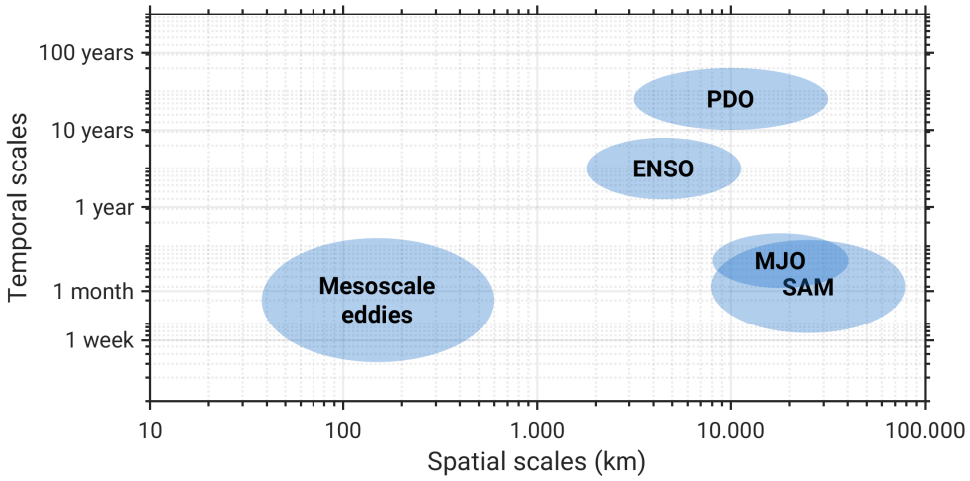

Figure 4.1: Spatial (in units of km) and temporal scales of eddies and the four climate modes ENSO, Pacific Decadal Oscillation (PDO), Madden-Julian Oscillation (MJO), and Southern Annular Mode (SAM).

4.2. El Niño–Southern Oscillation

One of the most prominent examples of climate modes is ENSO, which arises from interactions of the atmosphere with the ocean and was first described by Bjerknes (1966). This phenomenon is characterised by anomalous changes in sea surface temperature (SST) in the tropical Pacific (Bjerknes, J., 1969). ENSO influences temperatures and precipitation in that region, also affecting global weather and extreme events through atmospheric teleconnections (McPhaden et al., 2006; McPhaden, 2015). Usually, ENSO occurs every 2–7 years and lasts 9–12 months.

4.2.1. Dynamics and development

ENSO is associated with three phases: The normal (or neutral) phase, El Niño, and La Niña (see Figure 4.2, McPhaden et al., 2006; McPhaden, 2015). During the normal phase (left panel), the trade winds blow from east to west, pushing the warm surface water to the western Pacific, i.e., towards Indonesia and Papua New Guinea. This causes cold deep water to rise in the eastern Pacific, off the west coast of South America, a process called upwelling. The thermocline, the transition between water layers of different temperatures, therefore rises in the eastern Pacific and sinks towards the western Pacific. The absorption of heat and moisture by the trade winds results in a decrease in their density and induces an upward movement of the air masses in the western Pacific region. This phenomenon is known as convection. Subsequently, clouds form, resulting in increased precipitation. Thereafter, the air masses move eastward, descending into the eastern Pacific over the cold water. This circulation is known as the Walker circulation (McPhaden, 2015).

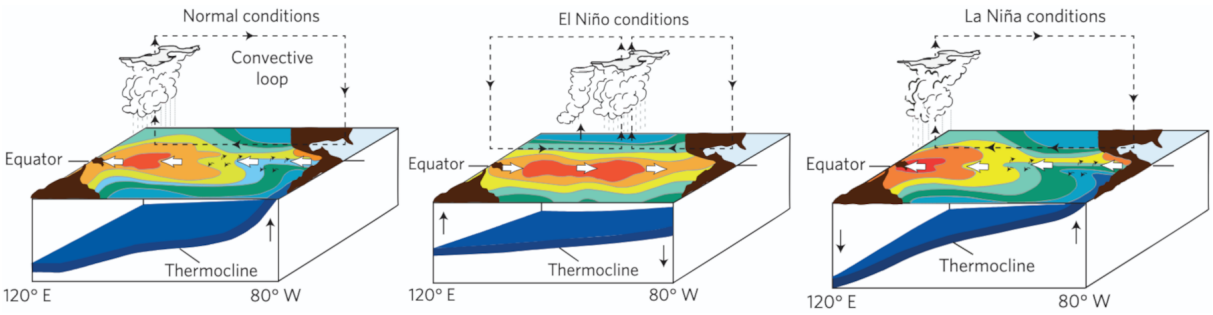

Figure 4.2: Illustration of winds, ocean currents, thermocline (blue area), and atmospheric circulation in the tropical Pacific during the three ENSO phases: Normal (left panel), El Niño (middle panel), La Niña (right panel), adapted from McPhaden (2015).

During El Niño (middle panel of Figure 4.2), the nominal trade winds weaken in a spatially non-uniform manner, accompanied by episodic westerly wind bursts, leading to an anomalous west-to-east flow (McPhaden, 2015). Therefore, the warm surface water is prevented from being carried towards the western Pacific, and upwelling does not occur. This means there is less warm surface water in the western Pacific and the region where warm air masses ascend shifts towards the central Pacific. Consequently, the thermocline ascends in the western Pacific, while it

descends in the eastern Pacific. This leads to high precipitation in the eastern Pacific, whereas it is dry in the western tropical Pacific.

Finally, La Niña is the counterpart to El Niño (right panel of Figure 4.2) and describes an intensification of the normal phase. The trade winds strengthen, enhancing upwelling along the eastern Pacific coast. As a result, the SST becomes exceptionally cold, and the thermocline steepens significantly. Convection shifts further westward, and the cooling in the eastern Pacific exceeds that observed during neutral conditions (McPhaden, 2015).

4.2.2. Global effects

Through large-scale teleconnections, ENSO affects the global climate, manifesting in phenomena such as droughts and floods. The consequences of this phenomenon can be far-reaching, impacting various aspects of society, including agriculture, public health, infrastructure, transportation, water safety, along with impacts on ecosystems and biodiversity (McPhaden et al., 2006). Specifically, El Niño leads to drier and warmer conditions in regions such as Australia, Indonesia, and neighbouring countries (cf. Figure 4.3 a), whereas parts of South America's west coast experience increased rainfall (McPhaden et al., 2006). In South and East Africa, El Niño can lead to dry conditions in the rainy season and wet conditions during the dry season (Wang and Schimel, 2003). Although not shown on Figure 4.3 (a), ENSO influences atmospheric pressure and consequently winds in the Amundsen Sea Sector and Bellingshausen Basin via wave trains, which is reflected in a p_b response there (e.g., Boening et al., 2011; Qin et al., 2022). Furthermore, Chambers (2011) detects p_b variability in the north-western Pacific, which is potentially due to ENSO.

In contrast to El Niño, wetter and colder conditions prevail in Australia, Indonesia, or neighbouring countries during La Niña (cf. Figure 4.3 b). Both positive and negative phases of ENSO are associated with changes in the atmospheric and oceanic circulation at relatively large scales. Such circulations can lead to mass redistribution within the atmosphere-ocean system, for example through changes in precipitation patterns, and may therefore contribute to interannual variations of Earth rotation. A well-known example is the weakening of the trade winds during El Niño, inducing an increase in ΔLOD.

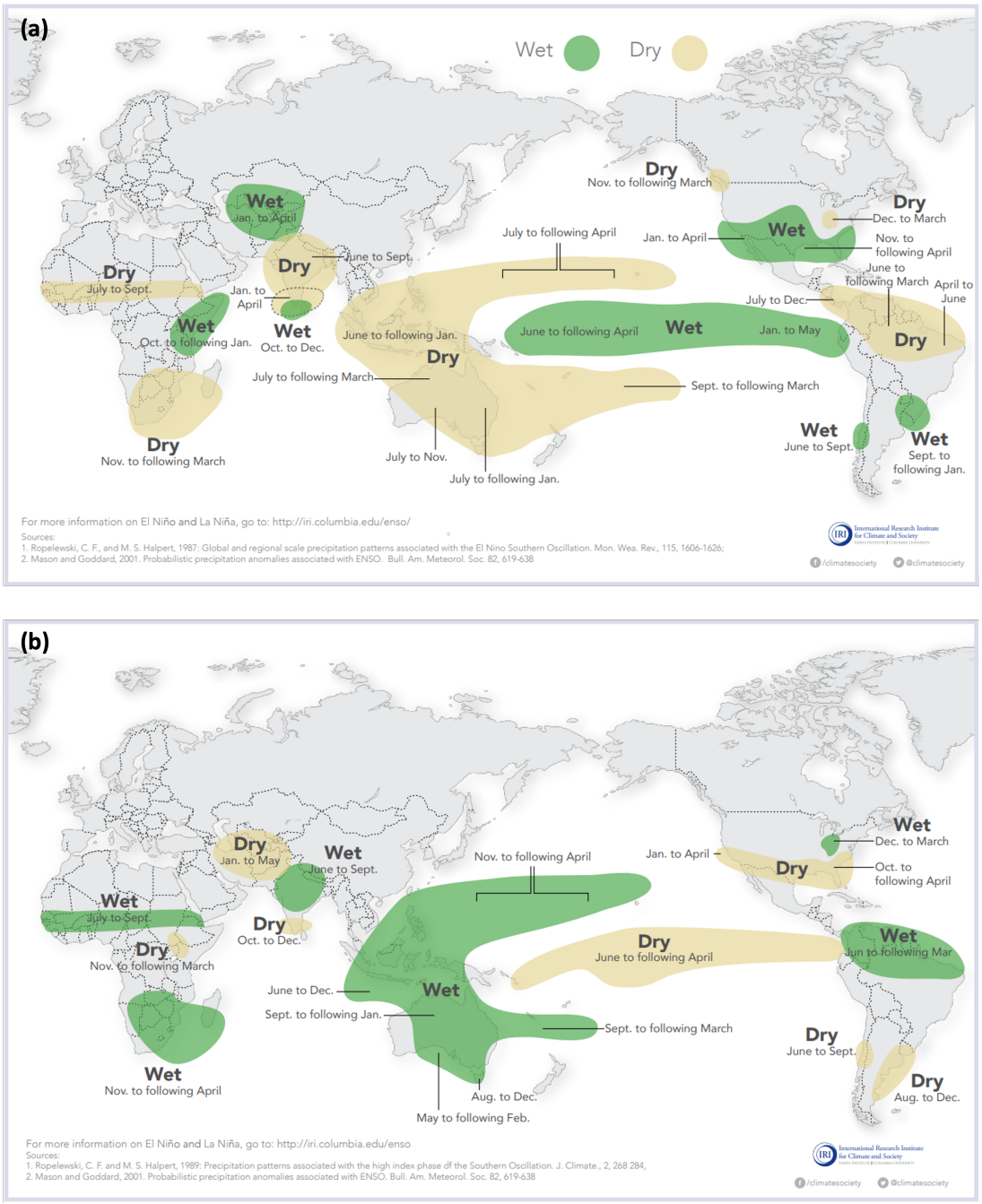

Figure 4.3: Rainfall and dry regions around the world and their seasons associated with (a) El Niño and (b) La Niña. Adapted from `https://www.weather.gov/fwd/teleconnections`.

4.2.3. Monitoring, Modelling and Forecasting of ENSO

To understand and predict the behaviour of ENSO, various indicators or methods such as index series, predefined monitoring regions, or climate models are available (McPhaden et al., 2006). The ENSO regions are geographical areas for observing SST changes. Currently, four regions are defined for operational monitoring, as displayed in Figure 4.4. The Niño 1 and Niño 2 regions are combined into Niño 1+2 (green), which is used as an early indicator for El Niño. The

Niño 3 region (purple) is defined in the eastern tropical Pacific and is particularly relevant for describing the anomalous atmospheric circulation, while the Niño 4 region (orange) is defined in the western tropical Pacific. The Niño 3.4 region (red), a transitional zone between Niño 3 and 4, exhibits high variability on El Niño time scales.

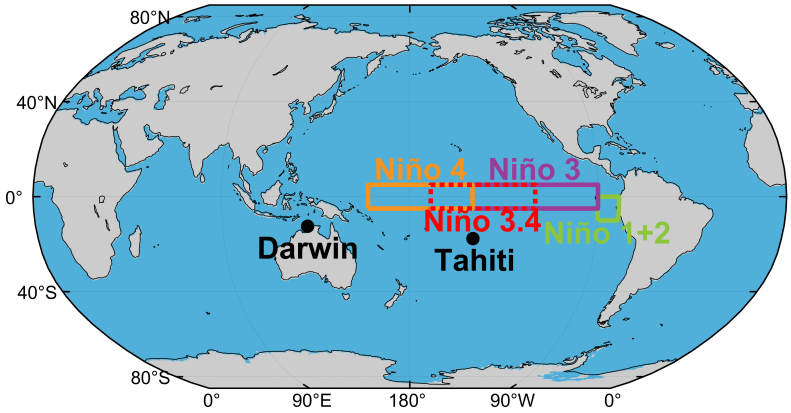

Figure 4.4: Locations of different predefined regions for the ENSO indices. The black dots show the two air pressure measuring stations for the definition of the Southern Oscillation Index (SOI) and the green box shows the Niño 1+2 region, the purple box is the Niño 3 region, the orange box the Niño 4 region and the red box displays the Niño 3.4 region. Taken from Lentge (2024).

Index series

Index series are defined from key atmospheric and oceanic variables, primarily SST anomalies associated with ENSO (see Chapter 4.2.1), allowing for the quantification of ENSO phases. The best-known examples are the Southern Oscillation Index (SOI), Oceanic Niño Index (ONI), and the Multivariate ENSO Index (MEI). Each index reflects a different aspect of the coupled ocean-atmosphere system. SOI, which reflects the atmospheric component of ENSO, has been in use for the longest time and was first formulated by Walker and Bliss (1932). It is based on the difference in air pressure between Tahiti and Darwin, Australia (see Figure 4.4), and records the large-scale pressure fluctuations between the western and eastern tropical Pacific.

MEI, on the other hand, represents both the atmospheric and oceanic components, including sea level pressure, SST, zonal and meridional surface winds, and outgoing longwave radiation, which are combined using an empirical orthogonal function (EOF) analysis (Wolter and Timlin, 1993, 1998). This multidimensional approach makes the MEI a particularly valuable tool in ENSO research and in the prediction of global climatic impacts.

The most widely used and standardised index today is ONI (Bamston et al., 1997). It is based on deviations of SST in the Niño 3.4 region (see Figure 4.4) from the average of a 30-year base period, calculated as a 3-month running mean of SST anomalies. For ONI and MEI, positive values typically indicate El Niño conditions and negative values La Niña, with a $\pm 0.5°$C threshold

for ONI. In contrast, a positive SOI indicates La Niña and negative values El Niño.

Climate models

Climate models or coupled atmosphere-ocean GCMs have been previously used to describe and explore the characteristics and evolution of ENSO (e.g., Bellenger et al., 2014; Brown et al., 2020; Wang et al., 2023). Climate models are mathematical representations of the Earth's complex climate system, capable of simulating most physical processes in the atmosphere, ocean, terrestrial hydrology, the cryosphere, and the biosphere. The anthroposphere is also a relevant component, but not necessarily included in all climate models (McPhaden et al., 2006). By linking different subsystems and taking their interactions into account, climate models can help to improve our understanding of the climate system and predict future climate changes. A major challenge in climate modelling is the structural model uncertainty due to imperfect parametrisations of sub-grid scale physical processes, coarse spatial resolution, or other approximations to achieve feasible runtimes. The processes of interest in turn determine the model's temporal, horizontal, and vertical resolution (Eyring et al., 2016; Stocker, 2016).

The current state-of-the-art in climate modelling is encapsulated by the CMIP6 project, an international initiative designed to evaluate, compare, and improve climate models through coordinated experiments (Eyring et al., 2016). For this, climate researchers perform standardised experiments to better understand the capabilities and limitations of climate models and to be able to predict future climate developments more precisely. CMIP6 includes the components Diagnostic, Evaluation and Characterization of Klima (DECK), the Model Intercomparison Projects (MIPs), and historical simulations. While DECK includes basic experiments that are performed continuously to characterise the models and check their performance across different simulations, the MIPs extend these standard experiments by focusing on specific scientific questions, such as the study of aerosols, ocean variability, or land-use change. The historical simulations of CMIP6 reproduce past climate conditions and variability in a statistical sense, covering the period from 1850 to 2014. These simulations are driven with observed and reconstructed forcings, including natural influences (e.g., volcanic aerosols and solar radiation variability) and anthropogenic influences (e.g., greenhouse gas concentrations such as CO_2, CH_4, N_2O, aerosols, and land use changes). Historical simulations also provide a foundation for future climate projections and help identify and correct systematic model biases (Eyring et al., 2016).

Forecasting

As mentioned above, forecasts or predictions of ENSO are based either on index extrapolation or on climate model simulations (Barnston et al., 2012; Wang et al., 2020). ENSO forecasts are important for society (e.g., agriculture, fisheries, flood risk, McPhaden et al., 2006; Wang et al., 2017), but predictability is limited by the so-called spring barrier in March–June, whose causes

are not fully understood (World Meteorological Organization, 2025). Chaotic, short-term weather anomalies and stochastic influences, e.g., wind anomalies, limit the predictability (Wang et al., 2020). Decadal fluctuations like the PDO and differences between El Niño types, for example, Eastern Pacific vs. Central Pacific types, also complicate precise forecasts. Despite progress, forecast quality has tended to decline since the 2000s (Hu et al., 2020). Extreme events like the aborted El Niño in 2014 or the unexpected Coastal El Niño in 2017 demonstrate that reliable ENSO forecasts are often only feasible within a lead time of a few months (Ramírez and Briones, 2017).

4.2.4. Signatures in Earth rotation

ENSO is known to have a strong impact on zonal AAM (see Figure 4.5 and e.g., Salstein and Rosen, 1986; Ponte and Rosen, 1999; Marcus et al., 2010). The increase in zonal AAM associated with stronger subtropical jet streams leads to a slowdown in the rotational speed of the solid Earth and thus to an increase in ΔLOD, shown first by Rosen et al. (1984). Ponte and Rosen (1999) analysed mountain and friction torques to explain the development of these AAM anomalies over time and to explain different flavours of El Niño events. In contrast to the zonal component, any equatorial AAM response to ENSO is cancelled out by area-weighted regional contributions to the mass term (i.e., the ellipsoidal torque, see Marcus et al., 2010, for a discussion). Figure 4.6 illustrates the covariance of atmospheric surface pressure with the SOI, whose contributions largely cancel globally due to the ellipsoidal torque pattern (Marcus et al., 2010). Thus, when considering AAM alone, there are no apparent ENSO signals in polar motion excitation.

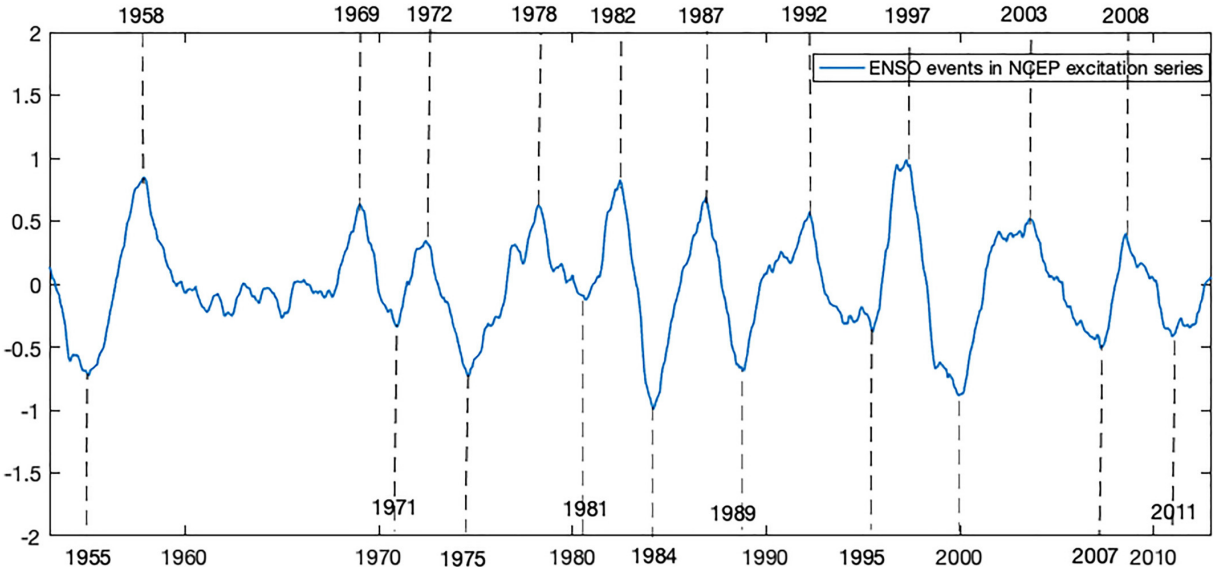

Figure 4.5: ENSO events in interannual AAM series in units of ms from the NCEP (National Centers for Environmental Prediction) atmospheric reanalysis in the period from 1953–2013. Adapted from Yu et al. (2021).

On the time scales on which ENSO operates, oceanic and hydrological mass redistributions play a key role in inducing Earth rotation variations. Several studies have highlighted ENSO-

related TWS changes in specific regions (e.g., Stuck et al., 2006; Phillips et al., 2012; Liu et al., 2020), suggesting a potential ENSO signature in HAM, and thus it is conceivable to suggest that ENSO might also leave its imprint on HAM. However, preliminary analyses in this regard yield ambiguous results (Lone Stumpe, personal communication, 2025). On the other hand, ocean mass redistributions, particularly through coupled teleconnections or basin-wide adjustments to wind stress forcing, are likely involved in the response of geophysical fluids to ENSO. Identifying the imprint of ENSO in the excitation of polar motion through oceanic excitation is a central goal of this thesis.

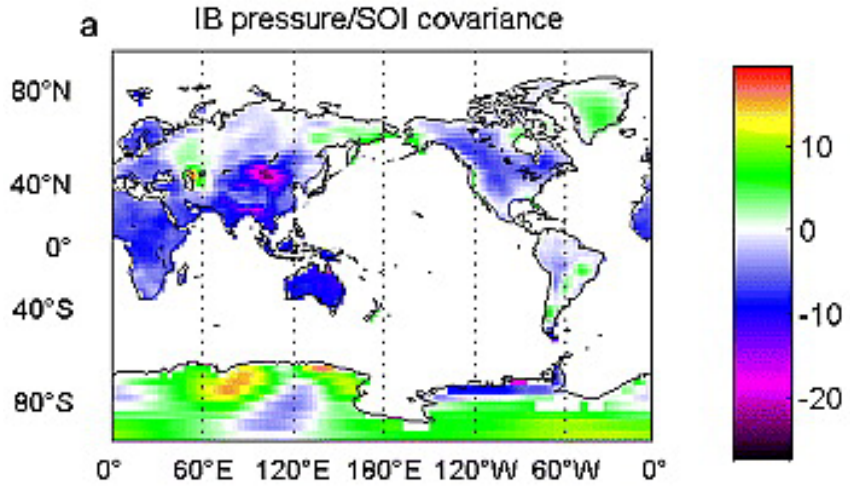

Figure 4.6: Covariance of the atmospheric surface pressure with the SOI (delayed by 3 months), in units of hPa. Figure adapted from Marcus et al. (2010).

4.3. Considerations beyond ENSO

In addition to ENSO, several other large-scale climate modes influence the dynamics of Earth's atmosphere and ocean, and may thus induce AAM and OAM changes that leave an imprint on polar motion or ΔLOD. Previous works have alluded to PDO, the SAM, and the MJO. These modes are not the central focus of this thesis, but a brief overview is warranted to convey a sense of the spectrum of climate-related excitation mechanisms of Earth rotation.

PDO is a climate mode in the Pacific Ocean characterised by SST variability, similar to ENSO, over several decades (Mantua et al., 1997; Deser et al., 2004; Wang et al., 2017). It typically lasts 20–30 yrs and mainly affects the Northern Pacific and North America, which makes the oscillation a potential driver for Earth rotation variations (Lambert, 2019). Like ENSO, PDO is associated with warm (conventionally referred to as the negative phase) and cool (positive) phases (cf. Figure 4.7, Mantua et al., 1997). Furthermore, it has an impact on the location of the jet streams and the large-scale wind field (Mantua et al., 1997; Mantua and Hare, 2002). Moreover, it should be noted that PDO can modulate ENSO, as PDO influences background conditions in the tropical and northern Pacific (see e.g., Verdon and Franks, 2006; Ma et al., 2022).

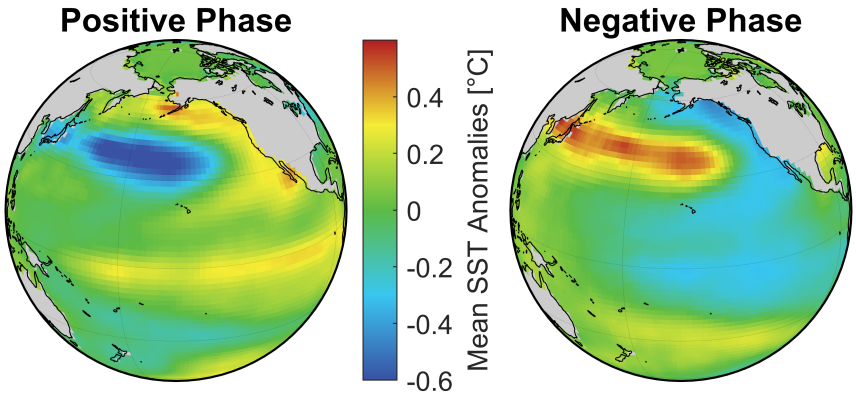

Figure 4.7: Characteristics of SST during positive (left) and negative (right) PDO phases. Figure provided by Lentge (2024).

In contrast, SAM is a climate pattern in the Southern Hemisphere and is sometimes referred to as Antarctic Oscillation (Aoki, 2002) or Southern Mode (Stepanov and Hughes, 2006). It is essentially a ring of variability in atmospheric pressure and wind patterns, extending from the South Pole to mid-latitudes like New Zealand and southern Australia. During the positive phase (cf. left panel of Figure 4.8), winds contract poleward, leading to higher pressure in mid-latitudes. In contrast, in its negative phase (cf. right panel of Figure 4.8), winds expand equatorward, resulting in more storms in southern mid-latitudes (Figure 4.8). Due to its large-scale character, especially in the mid-latitudes (Stepanov and Hughes, 2006), this mode possibly affects polar motion. Correlations with CW have been reported (Lambert, 2019; Naghibi et al., 2023) and SAM may also contribute to ΔLOD variations through atmospheric teleconnections that extend into tropical regions.

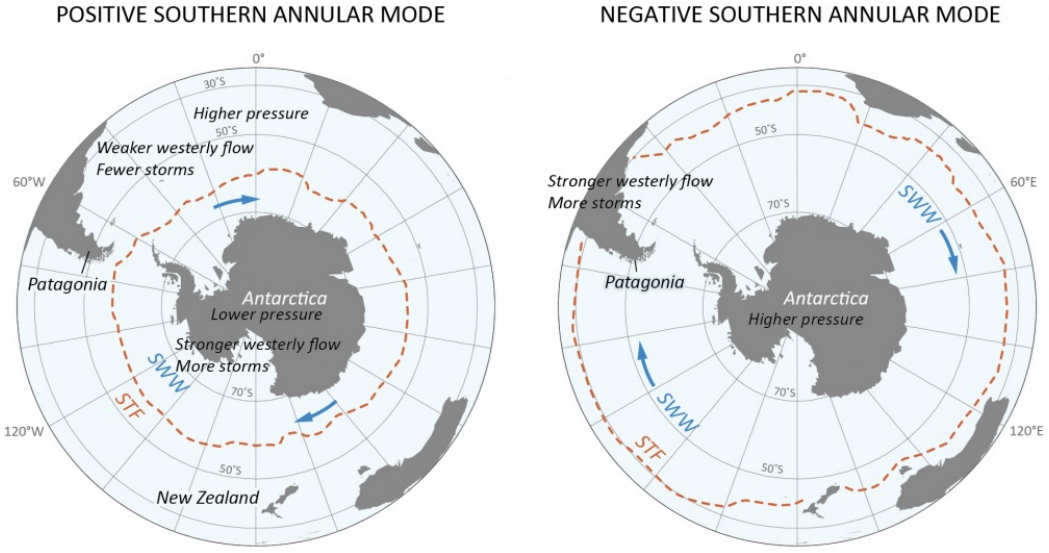

Figure 4.8: Positive (left) and negative (right) phases of SAM. During a positive phase, Southern Westerly Winds (SWW) (blue arrows) and the subtropical front (STF) (orange dotted line) contract toward Antarctica, resulting in higher pressure in the mid-latitudes and lower pressure near the pole. In contrast, during the negative phase, the SWW and STF shift equatorward, leading to lower pressure over the mid-latitudes and higher pressure near the pole. Figure from `https://www.antarcticglaciers.org/glaciers-and-climate/southern-annular-mode/`.

Another prominent climate mode is MJO, which is a large-scale, eastward-moving pattern of enhanced and suppressed tropical rainfall, winds, and pressure changes around the Maritime Continent (including Indonesia, the Philippines, Borneo, New Guinea, the Malay Peninsula, and the surrounding seas), acting on weekly to monthly (i.e., intraseasonal) time scales (Madden and Julian, 1972). Typically, an MJO event starts over the Indian Ocean, with a zone of enhanced rainfall and thunderstorm activity, and then progresses eastward towards the Pacific Ocean (see Figure 4.9). MJO influences the strength and location of tropical cyclones and can affect weather patterns in various regions around the world, particularly in the mid-latitudes (Madden and Julian, 1972). However, MJO also co-occurs with ENSO despite the different time scales due to couplings in the atmosphere-ocean system (e.g., Marcus et al., 2001).

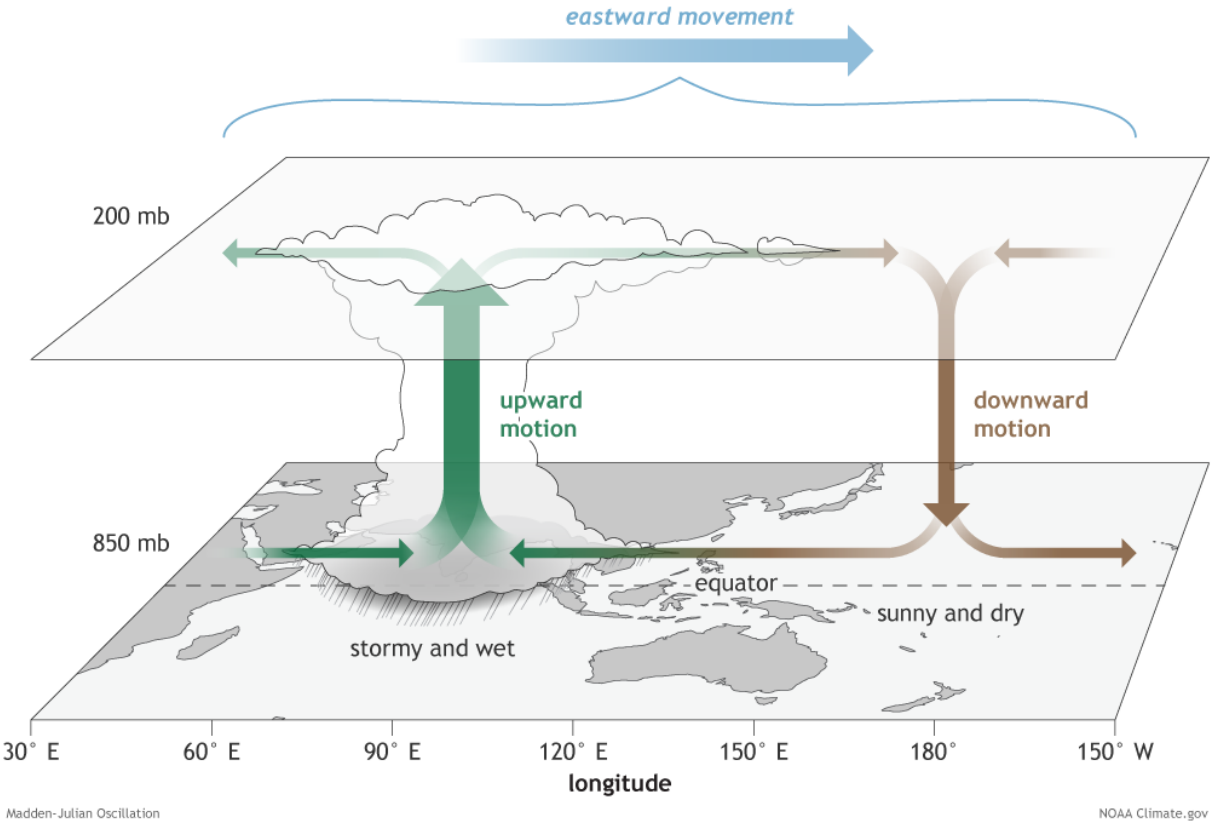

Figure 4.9: Illustration of the state of the surface and the atmosphere during an MJO event. Shown are an enhanced rainfall phase over the Indian Ocean and the suppressed rainfall over the western central Pacific. Horizontal arrows indicate wind anomalies. Over time, the system propagates eastward around the globe and returns to its initial location. Figure from `https://www.climate.gov/news-features/blogs/enso/what-mjo-and-why-do-we-care`.

Beyond its regional climate impacts, MJO also has an imprint on Earth rotation through mass redistribution. Afroosa et al. (2021) demonstrated that MJO affects polar motion by modulating atmospheric surface winds that induce a see-saw in p_b, or equivalently ocean mass, in the Indo-Pacific basin on intraseasonal time scales. Figure 4.10 demonstrates the wobbling of the Earth caused by a see-saw in p_b during an enhanced rainfall phase of MJO. The wind stress northwest of Australia (white arrows) force several types of waves. Among them are westward-propagating planetary Rossby waves that facilitate a basin-wide adjustment of the Indian Ocean to initial winds near Australia, leading to a spatially uniform barotropic p_b oscillation (pinkish patch).

This further triggers an anticlockwise circulation around the Australian continent (black/yellow arrows). The mass surplus in the Indian Ocean is compensated by a mass deficit in the Pacific (and vice versa), which is an adjustment that is mediated by fluxes through the Indonesian Straits (see e.g., Rohith et al., 2019; Afroosa et al., 2021). Such a large-scale mass fluctuation in the Indo-Pacific has a very favourable geometry for exciting polar motion variability (Afroosa et al., 2021).

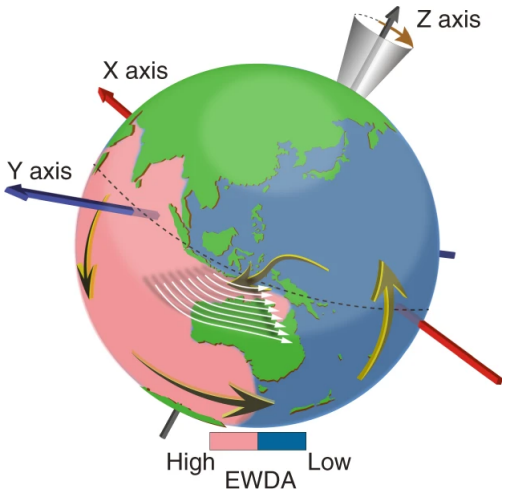

Figure 4.10: Simplified representation of a see-saw in p_b during an enhanced rainfall phase of MJO cycle. The green colour represents land areas, the red area indicates a high intraseasonal equivalent water depth anomaly (EWDA) and the blue area a low one. The wobble of the z-axis is indicated by the brown arrow and the equator is represented by the black dotted line. The white arrows are the boreal winds caused by MJO, whose magnitude increases in a southerly direction. These winds induce a barotropic circulation (yellow arrows) around Australia, which in turn leads to the see-saw in p_b and thus ocean mass between Indian and Pacific oceans. Figure adapted from Afroosa et al. (2021).

5. Are ocean reanalyses useful for Earth rotation research?

This chapter addresses open questions related to the synthesis of ocean models with oceanographic data, particularly concerning DA schemes. It is structured as follows: First, publication-related information is provided, including the abstract, paper reference, data availability statement, acknowledgements, copyright statement, and author contributions. This is followed by the published article. Finally, Chapter 5.6 provides a summary of the problem, methodology, data, and results.

Chapter abstract

Oceanic circulation and mass-field variability play important roles in exciting Earth's wobbles and length-of-day changes (ΔLOD), on time scales from days to several years. Modern descriptions of these effects employ oceanic angular momentum (OAM) series from numerical forward models or ocean state estimates, but nothing is known about how ocean reanalyses with sequential data assimilation (DA) would fare in that context. Here, we compute daily OAM series from three $^1/_4\,^\circ$ global ocean reanalyses that are based on the same hydrodynamic core and input data (e.g., altimetry, Argo) but different DA schemes. Comparisons are carried out (i) among the reanalyses, (ii) with an established ocean state estimate, and (iii) with Earth rotation data, all focusing on the period 2006–2015. The reanalyses generally provide credible OAM estimates across a range of frequencies, although differences in amplitude spectra portend a sensitivity to the adopted DA scheme. For periods less than 120 days, the reanalysis-based OAM series explain $\sim$40–50% and $\sim$30–40% of the atmosphere-corrected equatorial and axial geodetic excitation, similar to what is achieved with the state estimate. We find mixed performance of the reanalyses in seasonal excitation budgets, with some questionable mean ocean mass changes affecting the annual cycle in ΔLOD. Modelled excitations at interannual frequencies are more uncertain compared to OAM series from the state estimate and show hints of DA artefacts in one case. If users are to choose any of the tested reanalyses for rotation research, our study points to the Ocean Reanalysis System 5 as the most sensible choice[1].

[1]The article follows in a modified form (submitted version), where the nomenclature has been harmonised with the previous chapters. However, the content of the original published article is not modified.

Published manuscript

Börger, L., Schindelegger, M., Dobslaw, H., & Salstein, D. (2023). Are ocean reanalyses useful for Earth rotation research? *Earth and Space Science*, 10, e2022EA002700. https://doi.org/10.1029/2022EA002700

Data availability statement

The data sets used in this study are available from the following links: Ocean reanalyses (https://resources.marine.copernicus.eu/product-detail/GLOBAL_REANALYSIS_PHY_001_031/INFORMATION), OAM from ECCOv4r3 (https://isdc.gfz-potsdam.de/ggfc-oceans/oam/), ETOPO1 (https://www.ncei.noaa.gov/access/metadata/landing-page/bin/iso?id=gov.noaa.ngdc.mgg.dem:316), GRACE JPL Release 06 mascons (https://podaac-tools.jpl.nasa.gov/drive/files/GeodeticsGravity/tellus/L3/mascon/RL06/JPL/v02/CRI/netcdf), and SPACE2018 rotation data (https://keof.jpl.nasa.gov/combinations/). All angular momentum estimates analysed in this study (except those from ECCOv4r3) are provided in Börger and Schindelegger (2022).

Acknowledgements

We are grateful for comments and suggestions provided by two anonymous reviewers. This work was supported by the German Research Foundation (DFG, Project no. 459392861).

Copyright

Author contributions

The results presented in this thesis are the original work of the author, with contributions from the co-authors in the areas of conceptualisation, planning, drafting and revising the initial article draft.

Lara Börger: Data curation, Formal analysis, Investigation, Methodology, Software, Validation, Visualisation, Writing - original draft, Writing - review & editing. **Michael Schindelegger**: Conceptualisation, Funding acquisition, Methodology, Supervision, Writing - original draft, Writing - review & editing. **Henryk Dobslaw**: Funding acquisition, Writing - review & editing. **David Salstein**: Writing - review & editing.

5.1. Introduction

Mass motion and redistribution in geophysical fluids excite Earth's wobbles and length-of-day changes with varying efficacy on different time scales. While atmospheric contributions to these rotational fluctuations are relatively well determined through reanalysis data sets (Gross et al., 2003, 2004; Bizouard and Seoane, 2010; Neef and Matthes, 2012; Schindelegger et al., 2013b), uncertainties increase as one invokes—apart from the somewhat elusive core processes (Pais and Hulot, 2000; Mound, 2005; Kuang et al., 2019)—oceanic (Marcus et al., 1998; Ponte et al., 1998; Zhou et al., 2005; Quinn et al., 2019; Harker et al., 2021), hydrological (Adhikari and Ivins, 2016; Meyrath and van Dam, 2016; Nastula et al., 2019), and cryospheric (Chen et al., 2013a; Göttl et al., 2021) effects in the planet's angular momentum budget. Here we are primarily concerned with modelling the non-tidal oceanic component in polar motion and length-of-day excitations, on time scales from a few days out to several years. Different to all previous studies on the subject (see Quinn et al., 2019; Harker et al., 2021, for recent works), we draw estimates of OAM from novel ocean reanalyses, rather than free-running numerical forward models or ocean state estimates. These ocean reanalyses are conceptually equivalent to atmospheric reanalyses, which emerged more than 20 years ago, but they have remained untested for Earth rotation applications.

Ocean reanalyses are based on an ocean general circulation model, which is fitted to in situ and satellite observations by means of DA (Wunsch and Heimbach, 2013; Storto et al., 2019). During the applied DA, reanalyses often use filter approaches, which vary depending on the exact purposes of the reanalysis. In oceanography, common approaches are for example, some variant of Kalman Filter or three dimensional variational assimilation (3D-Var), where the state of the ocean is estimated sequentially at discrete times. Here, available observations are connected with model states, which can be both forecasts and backgrounds and where, due to several assimilation cycles, information from past observations are included. However, ocean reanalyses can be impacted by unphysical or abrupt changes in state variables, when the forward-propagating model state is allowed to jump towards observations to enforce consistency between model and data within given uncertainties (Wunsch and Heimbach, 2013; Pilo et al., 2018; Storto et al., 2019). This may be potentially critical for Earth rotation research, since violation of conservation laws and kinematic inconsistencies are likely to project on global budgets (Wunsch and Heimbach, 2013) and globally integrated quantities such as OAM. On the other hand, if the physical inconsistencies are small, ocean reanalyses will usefully complement OAM estimates from other sources, which

have their own limitations (e.g., high latency or coarse model resolution).

To test ocean reanalyses for their OAM signals and shed light on the impact of sequential DA on these global kinematic quantities, we use members of an ensemble of eddy-permitting ocean reanalyses, each produced by a different weather prediction and ocean monitoring service. The ensemble members are based on the same numerical ocean model and the same volumes of oceanographic data, but they use different DA schemes. This special product was created with the intent to quantify uncertainties of the deduced ocean state, whereas here we are interested in the credibility and uncertainties of the associated OAM changes. A secondary objective in our work is to combine the reanalysis-based OAM values with excitation estimates for other geophysical fluids and assess how well the total modelled excitation agrees with observed rotation fluctuations on sub-seasonal, seasonal, and interannual time scales. Furthermore, we use a statistical combination of the OAM series from single reanalyses to infer a higher-quality excitation series with reduced levels of noise and systematic error. In the following, we introduce the excitation formalism and mathematical description to combine the OAM functions (Section 5.2), describe the ocean reanalyses and ancillary data sets (Section 5.3), discuss the results (Section 5.4), before drawing conclusions and making suggestions for future improvements.

5.2. Mathematical background

5.2.1. Combination of OAM functions

In this article, we probe excitation functions from three individual ocean reanalyses, along with a combined series aimed at reducing the noise level (i.e., shortcomings in single-model excitation functions). In generic notation, let $\mathbf{x}(t)$ be a combination of different, uncorrelated time series $\mathbf{x}^i(t)$

$$\mathbf{x}(t) = \sum_{i=1}^{N} \omega_i \mathbf{x}^i(t), \tag{5.1}$$

where $i = 1, ..., N$ and the quality of each series is represented by weights

$$\omega_i = \frac{(\mathrm{Var}(\epsilon_i))^{-1}}{\sum_{j=1}^{N}(\mathrm{Var}(\epsilon_j))^{-1}}, \tag{5.2}$$

which are normalised such that $\sum_i \omega_i = 1$. $\mathrm{Var}(\epsilon)$ denotes the variance of the noise, which may be estimated using the three-cornered hat method (Koot et al., 2006). The three-cornered hat method assumes a stochastic process $\boldsymbol{x}^i$ with $i = 1, ..., N$ and M samples to consist of signal S and noise ϵ^i components

$$\mathbf{x}^i = S + \epsilon^i. \tag{5.3}$$

The signal is the same for every time series, but the noise differs. One could take differences between time series to approximate ϵ^i under the assumption that the noises are uncorrelated. In our case, such an approach is problematic, as the reanalyses are identically configured and rely on the same oceanographic observations (see Section 5.3.1). Tavella and Premoli (1994) proposed a generalisation of the three-cornered hat method for correlated noise components. In this method, the time series $\mathbf{x}^i$ are stored in a matrix $\mathbf{X}$ with dimensions $M \times N$, where each column contains one time series. The expected values, which are determined by

$$\overline{\mathrm{x}}^i = \frac{1}{M}(\mathrm{x}_1^i + \mathrm{x}_2^i + ... + \mathrm{x}_M^i), \tag{5.4}$$

are similarly stored in a matrix $\overline{\mathbf{X}}$, where the columns again represent time series. In addition, a matrix $\mathbf{R}$ is then defined by

$$\mathbf{R} = \frac{1}{M-1}[\mathbf{X} - \overline{\mathbf{X}}]^T[\mathbf{X} - \overline{\mathbf{X}}] \tag{5.5}$$

representing the covariance of the individual noises, i.e., $\mathbf{R}^{ij} = \mathrm{Cov}(\epsilon^i, \epsilon^j)$. Different to Tavella and Premoli (1994) and Koot et al. (2006), who pursued numerical approaches, we compute the covariance matrix $\mathbf{R}$ by applying Eq. (5.5) directly. Working backwards to Eq. (5.1), we deduce combined excitation series for each coordinate direction, and for mass and motion terms separately. The underlying weights, listed in Table 5.1, are time-invariant and assume different numerical values across the three reanalyses. In particular, the weights of the motion terms ($\chi^{\mathrm{v}}_{1,2,3}$) and the axial mass term χ^{m}_3 deviate considerably from $1/3$, meaning that the combined series is not a simple average of the three individual series. As an example, the combined equatorial and axial motion terms are comparatively more influenced by one reanalysis (GLORYS, cf. Section 5.3.1, $\omega_i \approx 0.4$) than by the other two reanalyses ($\omega_i \approx 0.3$). Supplemental checks of the behaviour of weights in different spectral bands showed that the ω_i cover a wider range of values on interannual time scales ($\sim$0.2–0.5 for both mass and motion terms) than in the sub-seasonal band ($\sim$0.3–0.4). However, for simplicity, we consider all frequency bands at once when combining the reanalyses. The resulting time series are referred to as “Combination" hereinafter.

Table 5.1: Weights per OAM function component for the determination of the combined series.

	GLORYS	ORAS	FOAM
χ^{m}_1	0.340	0.335	0.325
χ^{m}_2	0.334	0.320	0.345
χ^{m}_3	0.294	0.519	0.187
χ^{v}_1	0.406	0.360	0.234
χ^{v}_2	0.415	0.310	0.275
χ^{v}_3	0.447	0.270	0.283

5.3. Data sets

5.3.1. Ocean reanalyses

We derive OAM functions from three out of four members of the eddy-permitting ocean reanalysis ensemble provided by CMEMS (Copernicus Marine Environment Monitoring Service, Desportes et al., 2019). All reanalyses cover the period 1993–2019 and are based on the ocean model NEMO3 (Nucleus for European Models of the Ocean version 3). Sea surface temperature observations, daily sea level anomalies, sea ice concentration as well as temperature and salinity profiles are used to constrain the three-dimensional ocean state as NEMO3 is integrated forward in time. The model itself is configured on a $^1/_4\,^\circ$ horizontal tri-polar grid with each 75 vertical layers. The thickness of these layers increases from 1 m at the surface, to 10 m at 100 m depth and to 200 m at the bottom. Six-hourly buoyancy and momentum fluxes from ERA-Interim are used as common forcing data (Dee et al., 2011).

Our analysis period is from 2006 to 2015, which allows us to examine oceanic excitations and Earth rotation fluctuations with sub-seasonal, seasonal and (to some extent) interannual frequencies. The choice of this 10-year period is dictated by computational constraints, but also by the availability of complementary AAM series and other auxiliary data sets (e.g., satellite gravimetry). From the CMEMS product, we use the Global Ocean Reanalysis and Simulation 2 version 4 (GLORYS2v4, for short: GLORYS), the Ocean Reanalysis System 5 (ORAS5, for short: ORAS) and the Forecast Ocean Assimilation Model - Global Seasonal forecast system version 5 (FOAM-GloSea5, for short: FOAM). These ensemble members were selected mainly because GLORYS and ORAS use different DA schemes, whereas ORAS and FOAM use a similar DA scheme but different assimilation windows, which may or may not impact the reconstructed state and thus OAM quantities. GLORYS employs the SAM2 (Système d'Assimilation Mercator version 2) method based on a singular evolutive extended Kalman filter (SEEK) formulation and a 7-day assimilation window. Future and past observations relative to the window mid-point are used to perform the analysis in 7-day intervals (Lellouche et al., 2013; Garric and Parent, 2017). The DA software for ORAS and FOAM is NEMOVAR, an incremental three-dimensional variational assimilation approach (Blockley et al., 2014; Zuo et al., 2017). One difference between these two reanalyses consists in the assimilation window, which is 5 days for ORAS and 1 day for FOAM (cf. Table 5.2). In addition, ORAS accounts for representation errors in observation and structure, as well as analysis errors in surface forcing. These uncertainty estimates were derived by perturbing initial conditions, observations, and forcing, and performing the ocean state reconstruction for a total of five times (Zuo et al., 2019).

All three reanalyses use climatological, seasonally varying river discharge, and GLORYS additionally considers seasonal ice shelf discharge. Combined with evaporation minus precipitation over the ocean, the continental freshwater input leads to global ocean mass fluctuations, which are relevant for excitations of ΔLOD. In this context, the surface nudging scheme of the reanalyses

Table 5.2: Selected components of the ocean reanalyses used in this study. Table adapted from Desportes et al. (2019).

Reanalysis	GLORYS2V4	ORAS5	FOAM-GloSea5v13
Processing centre	Mercator Ocean	ECMWF	UK Met Office
Ocean model	NEMO3.1	NEMO3.4.1	NEMO3.4
Surface nudging	No, but flux correction on precipitation	Yes	Yes
DA scheme	SAM2 (SEEK) 7-day assimilation window	NEMOVAR (3D-Var) 5-day assimilation window	NEMOVAR (3D-Var) 1-day assimilation window
Uncertainties	Observation and background error variances from statistical methods (Lellouche et al., 2013)	Representation errors in observation and structure and analysis errors (Zuo et al., 2017)	Observation and background error variances from statistical methods (Blockley et al., 2014)

becomes interesting (Table 5.2). Surface nudging is not applied in GLORYS in favour of a flux correction on precipitation. The correction corresponds to an addition or removal of a thin, spatially uniform layer of mass at each analysis step—a reasonably accurate approach given the strong tendency towards an equilibrium response to loading by variable freshwater fluxes (Ponte, 2006).

From the selected reanalyses, we use daily fields of potential temperature and salinity to compute density ρ, eastward and northward velocities and the sea surface height η for calculating the angular momentum functions (Equations 2.27–2.28). The data are available at CMEMS (Copernicus Marine Service, 2019). Consistent with the model bathymetry adopted in the three reanalyses, we use a $1/4\,^{\circ}$-averaged version of the 60-arcminute ETOPO1 data set (Amante and Eakins, 2009; NOAA National Geophysical Data Center, 2009) as lower bound in the vertical integration of dynamical fields (Equations 2.27–2.28). Because the reanalyses treat ice-shelf cavities as land, the water bodies underneath ice shelves do not contribute to the global OAM integrals.

5.3.2. ECCOv4

OAM mass and motion terms from the ECCOv4r3 state estimate (ECCOv4 for short) are used as a point of comparison in this study. The ECCOv4 state estimates are iterative fits of the Massachusetts Institute of Technology general circulation model (MITgcm, Marshall et al. (1997)) to most oceanic in-situ and satellite data, including in situ hydrographic profiles, Argo float observations, sea surface height estimates from satellite altimetry, and bottom pressure anomalies from the GRACE mission. The adjustment is accomplished via the adjoint method, which propagates model-data misfits—distributed in space and time—to variations of uncertain model inputs, such as initial conditions, forcing fields, and coefficients of subgrid scale parameterisations. A forward integration of the MITgcm under the adjusted inputs yields new model-data misfits, and the procedure is repeated until an acceptable fit is found. Being an exact solution to a general circulation model, the ECCOv4 state estimates preserve dynamic and kinematic consistency, such that there are no spurious sources or sinks of tracers, volume, momentum, and derived global quantities (e.g., OAM). The MITgcm setup underlying ECCOv4 is Boussinesq volume-conserving,

has a nominal horizontal resolution of 1°, and contains 50 layers in the vertical, ranging from 10 m thickness at the surface to 460 m at the bottom (Forget et al., 2015; ECCO Consortium et al., 2017). Newer releases, which contain forcing by barometric pressure, are not considered in this study, given that pressure loading is also absent in the ocean reanalyses. From the ECCOv4 OAM series made available by the IERS SBO (International Earth Rotation and Reference Systems Service, Special Bureau for the Oceans, `https://isdc.gfz-potsdam.de/ggfc-oceans/`, Last access: 14.04.2022), we choose the version that includes net effects of freshwater flux from continental and atmospheric reservoirs into the ocean.

5.3.3. Ancillary data sets

A possible means of inferring fluctuations in the mass term associated with terrestrial hydrology and ice bodies is to use satellite gravimetry data of the GRACE mission. From 2002 to 2017, GRACE monitored surface mass changes in the Earth system, available as unconstrained global gravity field solutions (or derived quantities) with a nominal sampling period of 1 month (Tapley et al., 2019). Here, we use Release-06 GRACE mascon gravity fields provided by the Jet Propulsion Laboratory (JPL), which are solutions in terms of mass concentration blocks instead of spherical harmonics (Watkins et al., 2015). The surface mass changes are computed for each equal-area $3° \times 3°$ spherical cap mascon and are then eventually sampled to a $0.5°$ latitude-longitude grid. A process-based Coastline Resolution Improvement filter is employed to separate mass signals near the land-ocean boundary by source region. As is standard, the JPL processing includes a replacement of the zonal degree-2 coefficient with a more accurate estimate from Satellite Laser Ranging (SLR). We subset the monthly mascon solutions to total water storage anomalies (TWSA) over land and ice sheets by clipping oceanic areas, using a land-ocean mask provided with the data set. Over the 10 years considered, the GRACE data contains 13 gaps of 30 or 60 day duration, but none between 2006 and 2010. We fill these gaps with seasonal sinusoids, estimated from available epochs at each location, plus a residual derived from a principal component analysis of globally gridded non-seasonal fluctuations. The resulting gridded TWSA are readily converted into angular momentum functions, which we abbreviate as “hydrology/ice" in figures, tables, and some of the text below.

For consistency with the atmospheric forcing in the ocean reanalyses, AAM series are based on ERA-Interim data (see Schindelegger et al., 2013b, for details). We use mass term estimates corrected for the IB effect and time-average 6-hourly to daily values centred at midnight.

The Earth rotation data in our excitation budget considerations are the SPACE2018 series by Ratcliff and Gross (2019), deduced from a Kalman filter-based combination of various space geodetic measurements (Very Long Baseline Interferometry, Global Positioning System, SLR). Here, we take daily polar motion and ΔLOD estimates sampled at midnight. From the ΔLOD values, we remove tidal contributions at 80 spectral lines using the model by Ray and Erofeeva (2014). Similarly, long-period tidal effects in polar motion are accounted through the conventional

model (Petit and Luzum, 2010), with the fortnightly component replaced by the Mf solution of Ray and Egbert (2012).

5.4. Results

5.4.1. Signal content

To illustrate characteristics of the OAM functions across a range of frequencies, we show the amplitude spectra for equatorial mass and motion terms in Figure 5.1. Since the axial terms are small in magnitude and discussed as time series to some extent below, they are omitted. Estimates of power P were first computed with a 512-point Fast Fourier Transform, using the method of Welch, P. (1967), and then converted into amplitudes $A = \sqrt{2P}$.

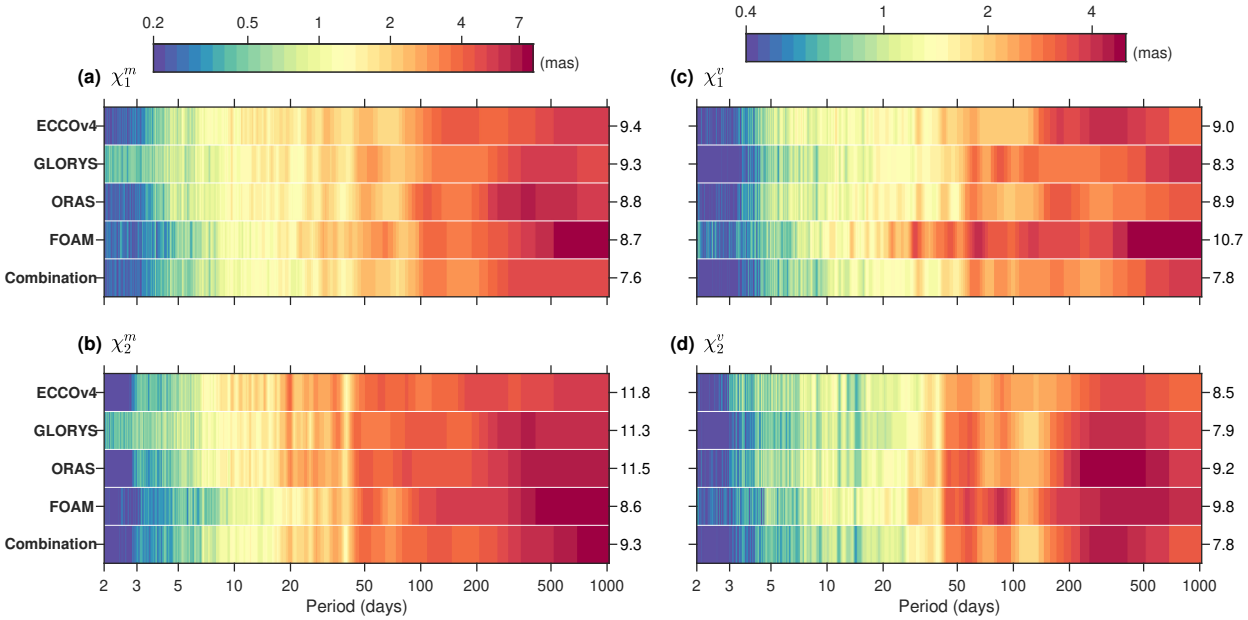

Figure 5.1: Amplitude spectra (in mas) for the equatorial mass terms $\chi^{\mathrm{m}}_{1,2}$ (a,b) and motion terms $\chi^{\mathrm{v}}_{1,2}$ (c,d) for ECCOv4, the three reanalyses, and the combined series, which is dubbed "Combination". The RMS of each time series (in mas) is specified on the right side of the panels.

Both mass terms (Figure 5.1, panels a and b) follow a red spectrum, but the χ^{m}_2 component is more energetic than χ^{m}_1 for periods longer than 20 days; cf. Gross et al. (2003) and Harker et al. (2021). The ECCOv4 and ORAS mass terms bear a close resemblance to each other in all bands, except near the annual frequency in χ^{m}_1, where ORAS amplitudes exceed those of ECCOv4 by $\sim$2 mas (milliarcseconds). GLORYS exhibits 2-day to 5-day oscillations not seen in other reanalyses, while FOAM has enhanced variability on interannual time scales. Neither feature is carried through to the Combination, as it suppresses fluctuations in OAM when covariance among the reanalyses is lacking. In χ^{m}_1 (Figure 5.1a), the spectra of all reanalyses are similar,

except for the mentioned variability of GLORYS. Evident in all estimates of χ_2^{m} (Figure 5.1b) is a suite of oscillations with periods between 20 and 50 days, interrupted by a pronounced trough of energy around 40 days. These spectral patterns are likely related to strong barotropic variability in the Bellingshausen Basin (see Fukumori et al., 1998; Fu, 2002; Weijer, 2015) and Australian-Antarctic Basin (Weijer, 2010; Harker et al., 2021), both leading to a clear signal in the χ_2 component.

Turning to the motion term χ_1^{v} (Figure 5.1c), FOAM stands out with enhanced power across all frequencies but particularly at periods between 20 and 100 days. By contrast, the spectra of GLORYS and ORAS are less steep at intraseasonal periods and only moderately pick up power beyond the annual frequency. The Combination contains weighted information of all reanalyses with FOAM being less weighted than the other two reanalyses, resulting in spectral characteristics comparable to those of GLORYS and ORAS. Variability in the χ_2^{v} component (Figure 5.1d) is distributed over frequency in a similar fashion across all models (including ECCOv4), with noticeable cusps of energy near 50-day and 90-day periods. Other features, including a broad and comparatively energetic peak in ORAS around the annual frequency, remain specific to only one reanalysis.

In summary, the OAM series from the three reanalyses are far from identical, despite their origin in a common numerical model, constrained by the same oceanographic data. The differences seen in Figure 5.1 thus reflect the impact of the DA scheme (Table 5.2) or global parameter choices (e.g., drag coefficients, to which we have no access to). It is very unlikely that the freshwater flux schemes (Table 5.2) cause some of the $\hat{\chi}$ differences, since the contribution of these mass fluxes to the OAM variance in the equatorial direction does not exceed 1.5% (value estimated from comparing two ECCOv4 OAM solutions with and without freshwater loads, Quinn et al., 2019). Moreover, currents involved in the response to freshwater fluxes are restricted to time scales of a few days (Durand et al., 2019), implying that differences among reanalyses in the motion terms must be explained by other processes. In fact, the χ_1^{v} and χ_2^{v} spectra provide strong indications that each DA method introduces its own, somewhat arbitrary perturbations to the dynamical model state, as speculated in Section 5.1. Below we assess whether these perturbations to OAM quantities are relevant in comparisons to Earth rotation data.

5.4.2. Sub-seasonal band

For the sub-seasonal band, we consider periods below the small ter-annual wobble and thus high-pass filter time series at a cutoff frequency of $1/120$ days^{-1}, as in Harker et al. (2021). The agreement between geodetic and geophysical excitation is quantified in terms of the Root-Mean-Square (RMS) of their difference and the Percentage of Variance Explained, as presented in Table 5.3. To compute the PVE of the oceanic excitation, IB-corrected atmospheric effects are removed from the geodetic excitation and the residual is then compared with the OAM functions. During 2006–2015, the atmosphere accounts for 56.2% of the deconvolved polar motion variance and

Table 5.3: Excitation budget for sub-seasonal oscillations 2006–2015[a]

	χ_1	χ_2	$\hat{\chi}$	χ_3
RMS Observation	21.1	32.9	39.1	140.1
PVE by atmosphere				
ERA-Interim (IB)	53.7 (14.3)	57.3 (21.3)	56.2 (25.7)	93.7 (34.7)
PVE by ocean in atmosphere-corrected geodetic excitation				
ECCOv4	35.6 (11.5)	45.0 (15.9)	42.1 (19.6)	30.9 (29.0)
GLORYS	27.5 (12.2)	50.3 (15.2)	43.3 (19.5)	28.8 (32.7)
ORAS	40.4 (11.1)	51.9 (14.9)	48.4 (18.6)	29.9 (27.8)
FOAM	−1.1 (14.5)	33.6 (17.6)	22.9 (22.7)	−15.8 (37.8)
Combination	42.0 (11.0)	56.2 (14.3)	51.8 (18.0)	40.1 (27.2)
PVE by sum of atmosphere and ocean				
ERA-Interim + ECCOv4	70.2	76.5	74.7	95.7
+ GLORYS	66.4	78.8	75.2	95.8
+ ORAS	72.4	79.5	77.4	95.5
+ FOAM	53.2	71.6	66.2	92.7
+ Combination	73.1	81.3	78.9	96.2
PVE by secondary terms in residual series				
Hydrology/Ice	−0.5	−1.7	−1.2	0.4

[a] Values are PVE, except for the first line, and the corresponding RMS of residuals is in parentheses. Units are [mas] for equatorial terms and [μs] for the axial term.

93.7% of sub-seasonal ΔLOD signals (cf. Gross et al., 2003, 2004; Harker et al., 2021), such that the RMS of the residuals is 25.7 milliarcseconds (mas) for $\hat{\chi}$ and 34.7 μs in the χ_3 component.

Looking in detail at the statistics of the OAM solutions in Table 5.3, we see that the variance reduction in the equatorial components is greater than in the axial component, as is well known (Gross et al., 2003, 2004). For most models, the RMS of residuals drops to ∼19 mas in $\hat{\chi}$ and ∼29 μs in χ_3. FOAM forms an exception and produces negative PVE values in the χ_1 and χ_3 components, meaning that the variance increases when removing FOAM from the atmosphere-corrected geodetic excitation. One interpretation of this result could be that the frequent (daily) adjustments of the FOAM forward model towards the data increase the amount of unphysical signals in the reanalysed state and thus the noise in the OAM series. As for the other OAM data sets, ECCOv4 has a slightly lower PVE in $\hat{\chi}$ compared to GLORYS and ORAS, while in the axial component the PVE for all three data sets hovers around 30%. Hence, some of the reanalyses, despite their possible shortcomings, match or improve upon a dynamically consistent state estimate in excitation budgets. This result is an indication for the benefits of high horizontal model resolution ($^1/_4\,^\circ$ in the reanalyses vs. 1° in ECCOv4) consistent with findings in Harker et al. (2021). More to the point, by conflating the three reanalysis series in a statistical meaningful way (Section 5.2.1), we achieve highest variance reduction with the Combination, amounting to 51.8% ($\hat{\chi}$) and 40.1% (χ_3). Accordingly, when comparing the sum of atmosphere and ocean with the geodetic excitation, the Combination also has the highest PVE, cf. Table 5.3. In detail, we find variance reductions of up to 78.9% and 96.2% for $\hat{\chi}$ and χ_3, suggesting that atmospheric and oceanic excitations explain a large fraction, but not all of the observed variability on sub-seasonal time scales.

When adding hydrological and cryospheric contributions to these considerations, the PVE in

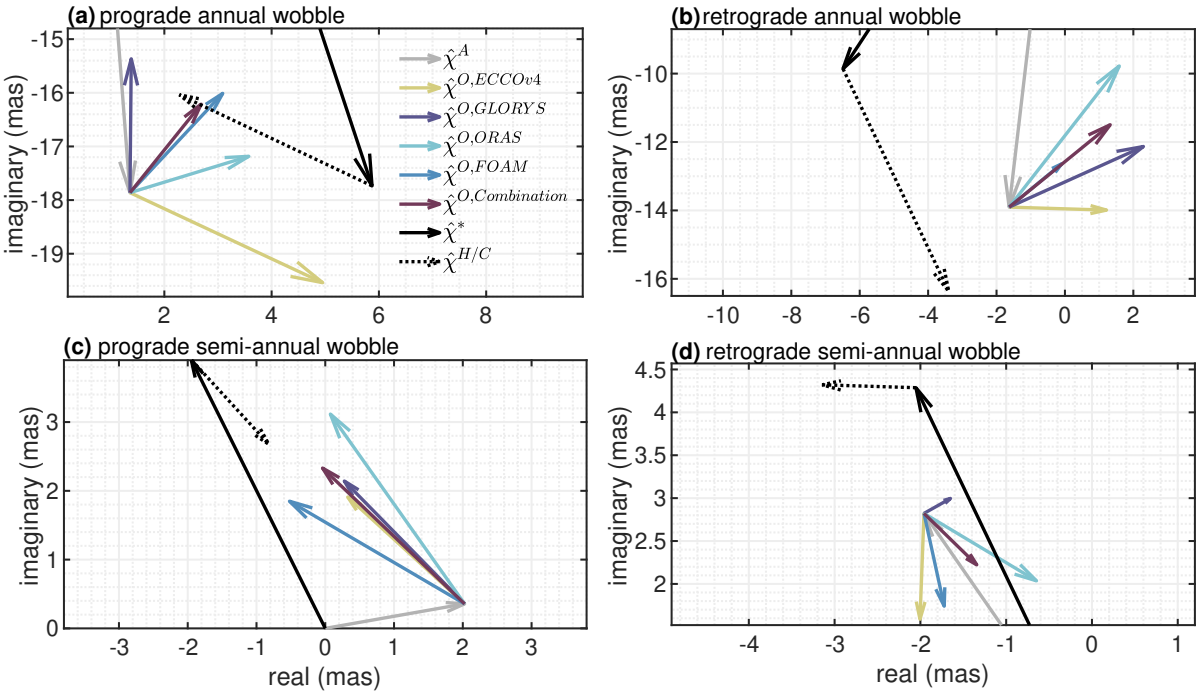

Figure 5.2: Phasor plots for the annual (a,b) and semi-annual (c,d) polar motion excitation during 2006–2015, split up in prograde (left column) and retrograde oscillations (right column). Geodetic excitation ($\hat{\chi}^{*}$) minus hydrology/ice ($\hat{\chi}^{H/C}$, black phasors) should be compared with the sum of atmospheric excitation ($\hat{\chi}^{A}$, grey) and oceanic excitation ($\hat{\chi}^{O}$) from any of five sources (ECCOv4, GLORYS, ORAS, FOAM, Combination). Reference date for phase is 1 January 2006, 12 UTC.

residual series of geodetic, atmospheric and oceanic excitation are very small. Values are negative in the equatorial component and they do not exceed 0.4% in the axial direction. Thus, secondary excitation processes in other Earth system components—as represented by the coarse-resolution GRACE fields—fail to account for the residual geodetic excitation. The remaining gaps in Earth's sub-seasonal rotation budget may be rather due to missing effects of barometric pressure loading in the ocean models, over- or underestimation of tropospheric winds (Schindelegger et al., 2013b), imperfect representation of (i) atmospheric planetary waves, (ii) mass exchange across ocean basins (Afroosa et al., 2021) or (iii) topographically constrained oceanic excitations (Harker et al., 2021), or simply high-frequency noise in the rotation data (Dill et al., 2020).

5.4.3. Seasonal oscillations

Figure 5.2 shows phasor plots for annual and semi-annual oscillations in polar motion excitation, as deduced from a least-squares harmonic analysis. Here, we compare the geodetic excitation, corrected for hydrology/ice effects, with the combined atmosphere-ocean excitation signals for the different OAM solutions. In the prograde annual component (Figure 5.2a), imposing the Combination or any of the reanalyses onto the atmospheric excitation gives a phasor sum that is very close to the observation, to within 0.3–1.5 mas. In comparison, the ECCOv4 estimate has the wrong phase and is too large in magnitude ($\sim$4 mas), similar to previous ECCO state

estimates (Gross et al., 2003). In the retrograde annual wobble excitation (Figure 5.2b), all OAM solutions, including ECCOv4, form a cluster with phases between -2° to 52°, meaning that they point away from the corrected geodetic excitation when added to the ERA-Interim phasor. Owing to enhanced power in the mass term, GLORYS and ORAS have the largest amplitudes in the retrograde annual band, more than twice as large as the amplitude of FOAM. Complementary to these illustrations, we list amplitude and phase estimates for annual harmonics of polar motion excitation from individual fluids, various sums of them, and rotation data in Table 5.6. Compared with earlier such decompositions (e.g., Gross et al. (2003) for the period 1980–2000, see also Dobslaw et al. (2010)), the annual wobble is more energetic over the time span analysed here. Our results indicate that this is due to an enhanced atmospheric contribution in the prograde part. The $\sim$12 mas amplitude in the retrograde part probably arises from several excitation processes or simply a favourable phase constellation, but the imperfect budget closure in that component prohibits more solid conclusions.

Looking at the bottom panels in Figure 5.2, polar motion excitation signals at the semi-annual frequency are generally a factor of 3–4 smaller than at the annual frequency. However, oceanic effects remain at 2–3 mas in magnitude (see Table 5.6), turning them into the single most effective excitation process for the prograde semi-annual wobble over the 10-year period considered. All reanalyses and ECCOv4 yield very similar phasors in the prograde band, which—when added to the atmospheric contribution—agree with the corrected geodetic excitation to within 1.5 mas. By contrast, adding the oceanic estimates for retrograde semi-annual oscillations to that of the atmosphere (Figure 5.2d) draws the modelled excitation farther away from the observation. The magnitude of the disparity (2.1 mas) is about 40% of the observed excitation amplitude, suggesting that there are still considerable errors in presently available angular momentum data sets. Nonetheless, and of interest in the context of this study, the seasonal polar motion excitation signals deduced from ocean reanalyses are broadly consistent with the adopted reference solution (ECCOv4) except for the prograde annual term.

Results from least-squares adjustment of seasonal sinusoids in the χ_3 component are depicted in Figure 5.3. In the annual component (Figure 5.3a), the length-of-day observation ΔLOD, corrected for hydrology/ice effects, is largely consistent with the sum of ERA-Interim and all OAM solutions, although discrepancies remain. The χ_3 signal is dominated by the mass term (χ_3^{m}), which we list in Table 5.4, along with the counteracting contribution from hydrological and (small) cryospheric effects (Dill and Dobslaw, 2019). All OAM data sets suggest a χ_3^{m} peak in October (phase $\sim$280°), but amplitudes vary from 69 µs in ECCOv4 to about 105 µs in GLORYS and FOAM. This difference is potentially revealing shortcomings in the two reanalyses, as ECCOv4 incorporates monthly GRACE solutions of ocean bottom pressure (OBP) and should therefore provide the most credible estimate of χ_3^{m}. Before exploring the matter somewhat further, we take a brief look at the semi-annual χ_3 oscillation in Figure 5.3b. Atmospheric effects account for nearly all of the observed length-of-day change, leaving a residual of merely $\sim$15 µs, similar to what we see at the annual frequency. However, the hydrological excitation signal at the semi-annual period is weak (and also uncertain, 8.0 $\pm$ 2.7 µs), implying that only a very small oceanic contribution is required to close the excitation budget. In this light, the spread of oceanic

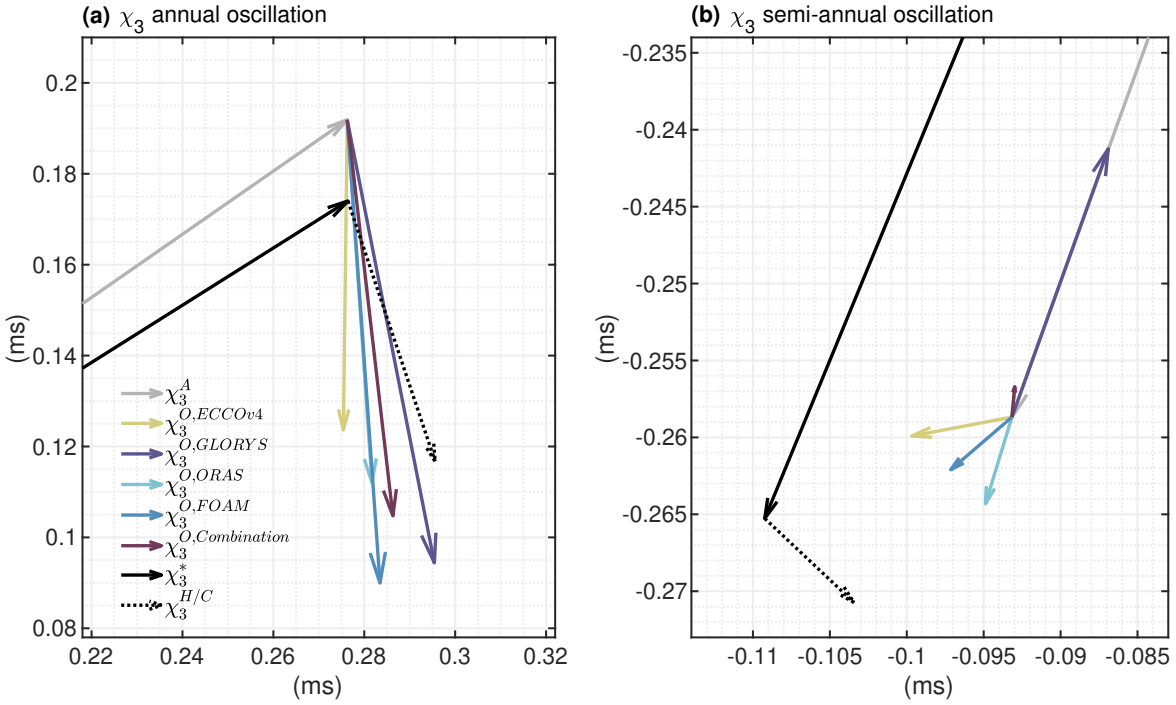

Figure 5.3: Phasor plots for the annual (a) and semi-annual (b) ΔLOD excitation during 2006–2015. Geodetic excitation ($\hat{\chi}^*$) minus hydrology/ice ($\hat{\chi}^{H/C}$, black phasors) should be compared with the sum of atmospheric excitation ($\hat{\chi}^A$, grey) and oceanic excitation ($\hat{\chi}^O$) from any of five sources (ECCOv4, GLORYS, ORAS, FOAM, Combination). Reference date for phase is 1 January 2006, 12 UTC.

Table 5.4: Phase and Amplitude for the annual and semi-annual χ_3^{m} component.

	Annual		Semi-annual	
	Amplitude [μs]	Phase [°]	Amplitude [μs]	Phase [°]
ECCOv4	68.88 ± 0.68	277.23 ± 0.56	5.42 ± 0.68	188.15 ± 7.14
GLORYS	102.49 ± 0.95	284.65 ± 0.53	21.98 ± 0.94	62.53 ± 2.46
ORAS	75.02 ± 0.82	280.53 ± 0.62	2.90 ± 0.82	330.16 ± 16.09
FOAM	105.42 ± 1.77	278.37 ± 0.96	1.10 ± 1.76	348.16 ± 92.09
Combination	88.69 ± 0.80	281.45 ± 0.52	6.68 ± 0.80	47.75 ± 6.89
Hydrology/Ice	60.40 ± 2.65	108.51 ± 2.53	7.96 ± 2.66	136.74 ± 19.14

χ_3 estimates in Figure 5.3b is not too surprising. ECCOv4, ORAS, and FOAM phasors generally point toward the hydrology-corrected ΔLOD estimate, although the magnitude appears to be too small and the separation into mass and motion term contributions remains unclear (cf. the diverging χ_3^{m} estimates in Table 5.4). Most anomalous in the semi-annual band is the GLORYS phasor, which is governed by a very large signal in the mass term (20 μs) that inevitably carries through to the Combination.

Shifting the focus again to the annual oscillation, we illustrate time series of χ_3^{m} from the three reanalyses and ECCOv4 in Figure 5.4a, where a second-order peaking filter (Orfanidis, 1996) was applied to all excitation functions to extract the time-variable annual signal. In keeping with Table 5.4, the χ_3^{m} series from ECCOv4 and ORAS agree very well with each other (save a 1-year period in 2011–2012), while FOAM and GLORYS have excess amplitudes of a few tens of μs

and more variable phases throughout. To examine the anomalous behaviour in more detail, we include in Figure 5.4a a plot of the daily-sampled FOAM excitation function before applying the peaking filter. The series has several spikes (both positive and negative) and abrupt transitions, e.g., in early 2007, late 2009 and 2011, or throughout the year 2013, which clearly contribute to the large annual amplitude of χ_3^{m} from FOAM in Table 5.4. Erratic features of this kind also occur in the GLORYS OAM function, although the intraseasonal noise is smaller than in FOAM (not shown).

Given that χ_3^{m} is sensitive to changes of the global ocean mass (see, e.g., Yan and Chao, 2012), one hypothesis to test is whether erroneous freshwater fluxes received from the atmosphere account for the large annual oscillation in FOAM and GLORYS. This is a physically plausible thread to follow, because the local mass gained or lost via atmospheric freshwater fluxes is spread evenly over the global ocean surface in a matter of days (Durand et al., 2019). Hence, we computed changes in the global ocean mass in FOAM and quantified—using a vertically integrated form of Equation (2.28)—how much it contributes to χ_3^{m} in Figure 5.4a. The resulting time series, illustrated in Figure 5.4b (blue curve), is of appreciable variance and shares many features with the actual χ_3^{m} function from FOAM, but fails to echo a number of spikes (e.g., in spring 2007, 2011, and 2013). Thus, deficiencies in the axial OAM mass term in some of the reanalyses can only be partially associated with erroneous freshwater fluxes. Further suspects are a too energetic response to atmospheric wind stress torques (cf. Ponte et al., 2001) or spurious dynamics incurred during DA, which is not an unreasonable assumption given the results with FOAM in other parts of our analysis.

5.4.4. Interannual variability

Figure 5.5 shows the interannual signals of oceanic excitation computed from ECCOv4, the three reanalyses and the Combination in comparison to geodetic observations corrected for atmospheric, hydrological and cryospheric effects. Both AAM and TWS changes are important excitation processes on interannual time scales, which is why we use them for the computation of the residuals. To isolate the interannual signal, we have applied a high-pass filter with a cutoff frequency of $1/365$ days^{-1} after removing the mean, trend and the seasonal oscillations estimated in a least-squares adjustment. The interannual signal was then obtained by subtracting the high-pass-filtered series from the seasonally corrected excitation function. For all solutions and all components, the mass term dominates over the motion term, typically by factors of 1.3 in χ_1, 4 in χ_2, and 10 in χ_3. With regard to the GRACE-based mass terms used to correct the geodetic excitation, it should be kept in mind that these contain both hydrological and cryospheric effects, but additional tests by us have shown that the contribution from ice has a much smaller impact on interannual time scales than land hydrology.

From Figure 5.5 we see that both in χ_1 and χ_2, ECCOv4 agrees reasonably well with the reduced observations. Likewise, the Combination—providing a middle ground to the three reanalyses—

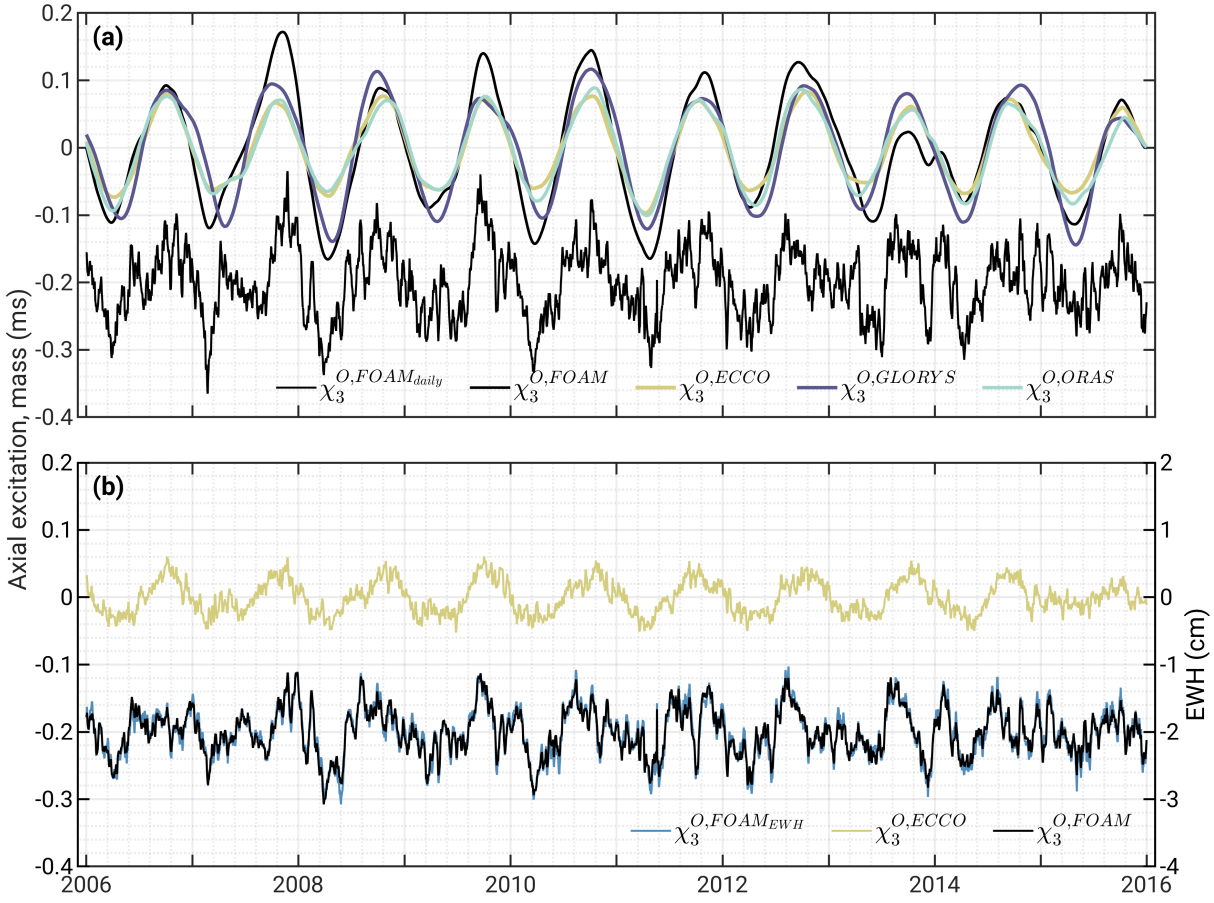

Figure 5.4: (a) Annual excitation signals in χ_3^{m} for 2006–2015 derived from $\left(\chi_3^{O,ECCO}\right)$, GLORYS $\left(\chi_3^{O,GLORYS}\right)$, ORAS $\left(\chi_3^{O,ORAS}\right)$ and FOAM $\left(\chi_3^{O,FOAM}\right)$, and the daily OAM series of FOAM $\left(\chi_3^{O,FOAM_{daily}}\right)$, arbitrary offset applied). In panel (b), we show mass term excitation functions computed from global ocean mass fluctuations in FOAM $\left(\chi_3^{O,FOAM}, \text{black curve}\right)$ and ECCOv4 $\left(\chi_3^{O,ECCO}, \text{olive curve}\right)$ with daily sampling. The underlying FOAM ocean mass series $\left(\chi_3^{O,FOAM_{EWH}}\right)$ is also plotted, with scale and units (cm of equivalent water height, EWH) indicated by the y-axis on the right. Signal content with periods longer than 12 months has been removed from all time series.

captures most of the peaks and troughs in the reduced observations, especially before 2013. FOAM has the largest fluctuations in time, which is consistent with the amplitude spectra shown in Figure 5.1. However, the pronounced positive excitation signals in FOAM around 2010 in χ_1 (∼10 mas) and around 2012 in both χ_2 (∼15 mas) and χ_3 (∼100 µs) have no correspondence in the observations, suggesting that they are spurious and possibly DA artefacts.

From early to late 2009, a sharp decline of χ_2 is evident in all solutions. We interpret this feature as the manifestation of a positive OBP anomaly in the ocean, projecting onto a negative OAM anomaly due to the longitude of its likely source region. In fact, Boening et al. (2011) found a record increase in GRACE-based Southern Ocean OBP in the Bellingshausen Basin, caused by an anomalous anti-cyclonic flow potentially related to El Niño in 2009/2010. Another clear and

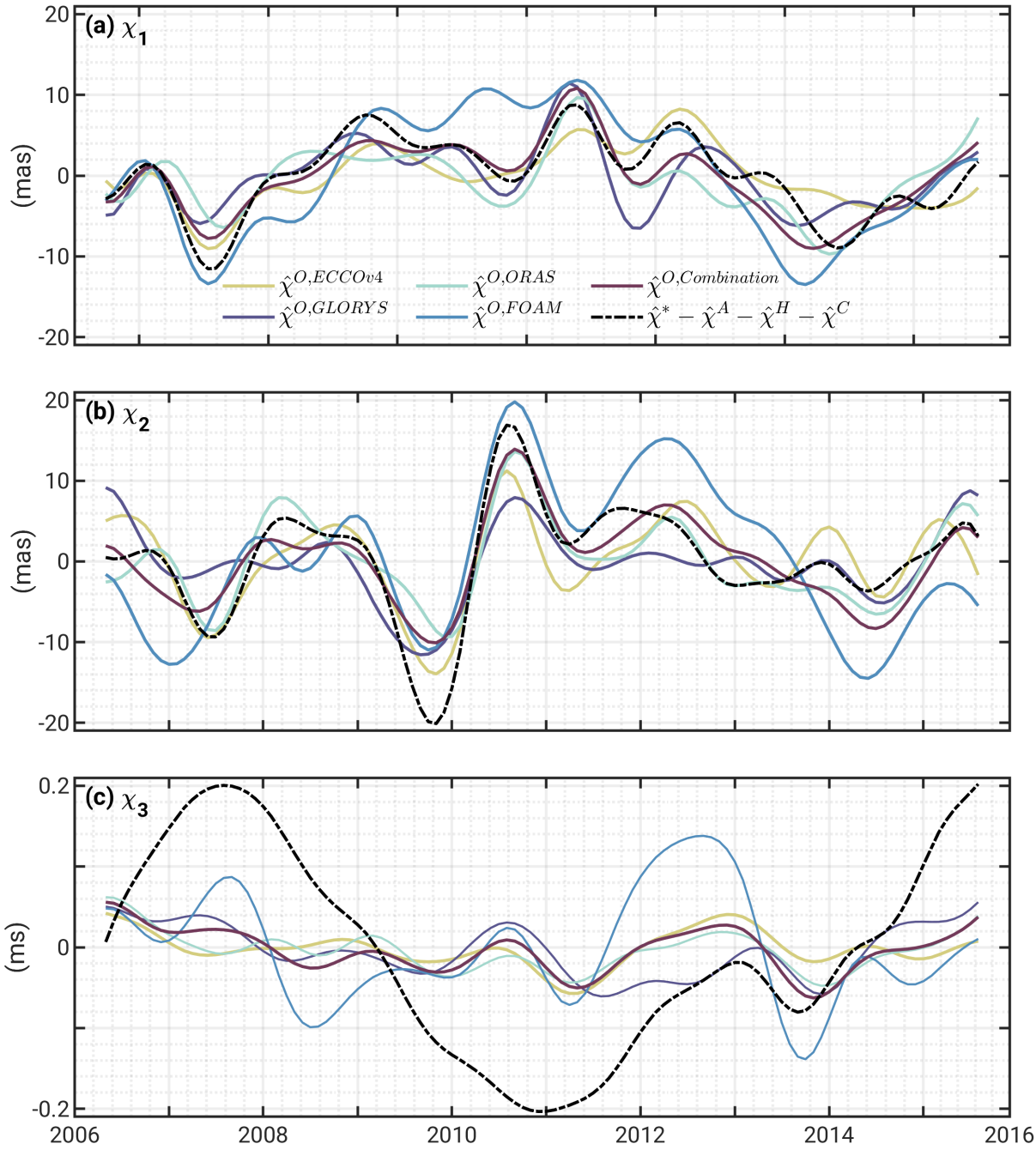

Figure 5.5: Interannual excitation signals $\chi_{1,2,3}$ as deduced from ECCOv4, GLORYS, ORAS, FOAM, the Combination $\left(\hat{\chi}^{O}\right)$ and GRACE-based hydrology/ice in comparison with the geodetic excitation–AAM–HAM $\left(\hat{\chi}^{*} - \hat{\chi}^{A} - \hat{\chi}^{H} - \hat{\chi}^{C}\right)$ from 2006 through 2015. Four months were clipped both at the beginning and at the end of the time series to avoid filter artefacts.

physically motivated excitation signal is a large ($\pm$200 µs) oscillation with a period of 5 to 6 years in the reduced length-of-day observations (χ_3 component). The causative mechanism is the exchange of angular momentum between the mantle and the core, mostly governed by the gravitational coupling between the two interior components (Chen et al., 2019).

Continuing the budget considerations of the preceding Sections, Table 5.5 shows the PVE and the correlation coefficients for excitations on interannual time scales (2006 to 2015). As before,

Table 5.5: Modelled versus observed excitations on interannual time scales, 2006–2015[a].

	χ_1	χ_2	$\hat{\chi}$	χ_3
PVE by atmosphere				
ERA-Interim (IB)	28.4 (0.53)	−43.9 (−0.19)	−19.5 (0.06)	21.1 (0.50)
PVE by ocean in atmosphere-corrected geodetic excitation				
ECCOv4	72.7 (0.86)	72.4 (0.85)	72.5 (0.85)	10.0 (0.38)
GLORYS	54.3 (0.63)	57.1 (0.38)	56.2 (0.44)	22.5 (0.51)
ORAS	54.8 (0.57)	71.8 (0.72)	66.1 (0.66)	17.7 (0.51)
FOAM	16.6 (0.66)	0.5 (0.83)	5.9 (0.76)	−15.6 (0.09)
Combination	76.8 (0.70)	74.0 (0.81)	74.9 (0.75)	17.2 (0.45)
PVE by sum of atmosphere and ocean				
ERA-Int. + ECCOv4	78.8 (0.89)	70.1 (0.85)	73.6 (0.86)	29.9 (0.57)
ERA-Int. + Combination	81.9 (0.79)	71.8 (0.59)	75.9 (0.66)	35.4 (0.59)
PVE by sum of atmosphere, ocean and hydrology/ice				
ERA-Int. + ECCOv4 + Hyd./Ice	85.2 (0.92)	84.7 (0.92)	84.9 (0.92)	19.1 (0.49)
ERA-Int. + Combination + Hyd./Ice	87.4 (0.93)	85.6 (0.93)	86.2 (0.93)	25.5 (0.53)

[a] Values are PVE and the corresponding correlation coefficient is in parentheses.

the PVE is computed by comparing residual series with the oceanic excitation, while for the computation of the correlation coefficients, we use Pearson's R. The PVE results reflect what can be seen in Figure 5.5. ECCOv4 explains the atmosphere-corrected polar motion excitation by more than 72%, whereas the three reanalyses have smaller explained variances. Yet again, our combined OAM function mitigates noise and systematics of individual reanalysis series, such that in the χ_1 component, the PVE of the Combination (77%) is higher than that of the reanalyses (17–55%) and also ECCOv4. In χ_2, the skill of ORAS is only slightly worse than that of the Combination, and similar margins are seen in the complex-valued component $\hat{\chi}$. Residual ΔLOD signals are explained to some extent by ECCOv4, GLORYS and ORAS (10–23%), while the PVE of FOAM is negative. In fact, FOAM performs worst in all three components, with the discrepancies being caused by the large, and arguably unphysical long-period fluctuation apparent in Figure 5.1 (panels a,b) and in Figure 5.5.

For completeness, Table 5.5, also includes statistics for the direct comparison of observed excitation with the sum of modelled excitations from different geophysical fluids. Joint consideration of atmospheric and oceanic effects yields PVE values of ∼74% and ∼76% in $\hat{\chi}$, and ∼30% and ∼35% in χ_3, dependent on whether ECCOv4 or the Combination is used as OAM source. Addition of hydrology and ice contributions reduces the total ΔLOD PVE to 19% and 26%, respectively, but these numbers should be interpreted with caution, given that we have not removed (or modelled) the ∼5-year oscillation due to core processes. By contrast, incorporating the GRACE-based mass term in the polar motion excitation budget improves the PVE to ∼85% (ECCOv4) and ∼86% (Combination), with the correlation coefficient being as high as 0.93 in the latter case. We conjecture that the residual in the comparison of geodetic and geophysical excitation of Earth's wobbles in Table 5.5 is due to errors in 3D wind fields and atmospheric forcing data over the ocean, representation errors in ocean models (e.g., bathymetry and the omission of circulation underneath ice shelves) or uncertainties of long wavelength features in the GRACE-based mass terms.

5.5. Summary and outlook

We have evaluated whether or not angular momentum estimates from ocean reanalyses are useful for Earth rotation research. By and large, one can answer in the affirmative, although the quality of the OAM series varies with time scale and the specifics of sequential DA applied. At sub-seasonal periods from 2 to 120 days, the reanalyses offer similar skill in explaining atmosphere-corrected geodetic excitation as an established ocean state estimate ($\sim$43–52% in $\hat{\chi}$ and $\sim$29–40% in χ_3), a result partially attributed to the benefits of high horizontal and vertical model resolution. As evident from the (low) PVE values for FOAM in Table 5.3, reanalyses are not free from error at short periods, but a statistical combination can successfully suppress noise and DA artefacts inherent to such single-reanalysis OAM series. While for annual frequencies, all tested OAM estimates blend in well with atmospheric and hydrological excitations to produce reasonably well-closed rotation budgets, larger discrepancies occur for semi-annual frequencies. Analysis of interannual variability is somewhat limited by the relatively short (10-year) time window, but from results in Section 5.4.4 it is clear that here, the reanalyses may not always compete with ECCOv4. The spread among reanalyses is appreciable and the large anomaly in FOAM-based OAM series after 2012 (particularly in χ_3) is a dubious feature as highlighted by our excitation budget considerations. If users are to choose any of the tested reanalyses, we recommend to use ORAS by European Centre for Medium-Range Weather Forecasts (ECMWF). Interestingly, DA products by ECMWF are also a well established source for computing AAM series, and they have been shown to fulfil global kinematic constraints across a range of time scales (Schindelegger et al., 2013b).

The encouraging results notwithstanding, there is obvious room for improvement of ocean reanalyses in the context of Earth rotation research. We especially propose to consider the dynamic ocean response to atmospheric pressure loading, which plays an important role in forcing rapid (sub-weekly) rotation signals (Ponte and Ali, 2002). To some extent, it also acts on monthly to interannual time scales, at odds with a perfect IB behaviour (Piecuch et al., 2022). Following the example of ECCOv4, it should be relatively straightforward for ocean reanalyses to assimilate monthly GRACE gravity field solutions as bottom pressure observations. Such development could help better constrain the equatorial and axial OAM mass terms, as well as global ocean mass (and thus ΔLOD) fluctuations caused by freshwater fluxes. In this context, a mass balance constraint could be incorporated in each assimilation step to ensure that there are no spurious fluctuations in the total ocean mass due to sequential DA. Only as much mass should be drawn from, or added to the ocean as the net effect of freshwater fluxes from the atmosphere, continental hydrology, and cryospheric components implies. Given that evaporation and precipitation fields from atmospheric models are still afflicted with errors, it would also be desirable to find ways for correcting these fluxes during the DA and bring them into consistency with the reconstructed ocean state (Quinn et al., 2019).

Appendix A: Seasonal prograde and retrograde oscillations in $\hat{\chi}$

Table 5.6 shows the annual and semi-annual amplitudes and phases for prograde and retrograde oscillations in $\hat{\chi}$ estimated in a least-squares adjustment.

Table 5.6: Annual and semi-annual amplitude and phase[a] estimates for prograde and retrograde oscillations in $\hat{\chi}$.

	Prograde		Retrograde	
	Amplitude [mas]	Phase [°]	Amplitude [mas]	Phase [°]
		Annual oscillation		
Observed	18.68 ± 0.23	-71.68 ± 0.70	11.80 ± 0.40	-123.35 ± 1.92
Atmosphere				
ERA-Interim (IB)	17.91 ± 0.04	-85.65 ± 0.13	14.00 ± 0.06	-96.69 ± 0.25
Ocean				
ECCOv4	3.97 ± 0.36	-25.03 ± 5.20	2.85 ± 0.40	-1.75 ± 7.98
GLORYS	2.50 ± 0.00	89.46 ± 0.08	4.31 ± 0.33	24.29 ± 4.43
ORAS	2.32 ± 0.37	17.01 ± 9.26	5.23 ± 0.24	52.04 ± 2.64
FOAM	2.53 ± 0.27	46.95 ± 6.03	1.99 ± 0.30	39.50 ± 8.68
Combination	2.12 ± 0.21	51.18 ± 5.66	3.81 ± 0.26	39.18 ± 3.88
Atmosphere + Ocean				
ERA-Int. + ECCOv4	20.16 ± 0.16	-75.78 ± 0.47	14.04 ± 0.06	-85.03 ± 0.24
ERA-Int. + Combination	16.43 ± 0.10	-80.59 ± 0.36	11.57 ± 0.07	-83.43 ± 0.36
Atmosphere + Ocean + Hydrology/Ice				
ERA-Int. + ECCOv4 + Hyd./Ice	23.22 ± 1.04	-55.38 ± 2.58	8.82 ± 1.11	-127.11 ± 7.20
ERA-Int. + Combination + Hyd./Ice	19.35 ± 0.95	-58.38 ± 2.81	6.49 ± 1.27	-134.63 ± 11.23
		Semi-annual oscillation		
Observed	4.37 ± 0.36	116.52 ± 4.69	4.75 ± 0.35	115.58 ± 4.17
Atmosphere				
ERA-Interim (IB)	2.06 ± 0.63	9.98 ± 17.51	3.43 ± 0.36	124.75 ± 6.07
Ocean				
ECCOv4	2.30 ± 0.30	137.57 ± 7.40	1.23 ± 0.02	-92.16 ± 0.70
GLORYS	2.50 ± 0.26	134.41 ± 5.97	0.35 ± 0.32	29.40 ± 52.41
ORAS	3.38 ± 0.23	125.28 ± 3.90	1.53 ± 0.34	-30.94 ± 12.79
FOAM	2.95 ± 0.34	149.63 ± 6.54	1.11 ± 0.08	-77.70 ± 4.31
Combination	2.86 ± 0.24	136.30 ± 4.89	0.86 ± 0.24	-44.27 ± 16.12
Atmosphere + Ocean				
ERA-Int. + ECCOv4	1.94 ± 0.13	80.29 ± 3.89	2.56 ± 0.61	141.61 ± 13.71
ERA-Int. + Combination	2.33 ± 0.01	90.98 ± 0.30	2.60 ± 0.37	121.14 ± 8.09
Atmosphere + Ocean + Hydrology/Ice				
ERA-Int. + ECCOv4 + Hyd./Ice	3.38 ± 1.75	127.06 ± 29.69	2.25 ± 0.22	85.65 ± 5.61
ERA-Int. + Combination + Hyd./Ice	3.87 ± 1.67	130.44 ± 24.73	2.63 ± 1.07	65.34 ± 23.36

[a] IB is inverted barometer; reference date for phase is 1 January 2006, 12 UTC.

5.6. Chapter summary and context

Before addressing the main objective of this thesis—the analysis of unknown oceanic signals in polar motion—questions regarding the use and performance of contemporary ocean models in Earth rotation studies are clarified in Chapter 5. The particular emphasis is on ocean reanalyses as a form of model-data synthesis that have been unused to deduce oceanic excitation signals in polar motion and ΔLOD. Pure forward models aside (e.g., Dobslaw and Dill, 2018; Harker et al., 2021), the established data set in Earth rotation studies to derive OAM estimates is the ocean state estimate ECCO, which has a nominal horizontal resolution of 1°. In contrast, emerging ocean reanalyses, run at a horizontal resolution of $1/4^\circ$, are based on forward models that are combined with observations in a sequential DA framework to reconstruct the ocean's state. However, its processing, particularly the impact of the DA scheme and kinematic inconsistencies arising from the assimilation process (cf. Chapter 3.5.1), is still insufficiently understood in Earth rotation studies.

To address these questions, this study compares OAM daily estimates of three ocean reanalyses—namely Global Ocean Reanalysis and Simulation 2 version 4 (GLORYS2v4, for short: GLORYS), the Ocean Reanalysis System 5 (ORAS5, for short: ORAS) and the Forecast Ocean Assimilation Model - Global Seasonal forecast system version 5 (FOAM-GloSea5, for short: FOAM)—provided by CMEMS (Copernicus Marine Environment Monitoring Service, Desportes et al., 2019). All reanalyses cover the period 1993–2019, are based on the same ocean model and ingest the same input data. However, the reanalyses employ different DA schemes: GLORYS uses the SAM2 (SEEK) algorithm with a 7-day assimilation window, whereas ORAS and FOAM assimilate observations with the three-dimensional approach NEMOVAR. However, the two reanalyses differ in their assimilation windows, which are 5 days for ORAS and 1 day for FOAM. Table 5.2 lists the main differences and similarities of the reanalyses with regard to DA. As opposed to the reanalyses, ECCO Version 4 Release 3 (ECCOv4r3, in short: ECCOv4) iteratively fits the Massachusetts Institute of Technology general circulation model (MITgcm, Marshall et al., 1997) to satellite observations and in-situ data using the adjoint method. Thereby, ECCOv4 ensures both dynamic and kinematic consistency (Fukumori et al., 1998; ECCO Consortium et al., 2017), which may be violated in sequential DA methods (cf. Chapter 3.5.1).

The analysis period is 2006–2015, for which the OAM estimates of each reanalysis are compared with (i) each other, (ii) against a statistical combination of all three oceanic excitation solutions, (iii) ECCO, and (iv) to Earth rotation data. To derive OAM from Equation (2.27), temperature and salinity fields are used to compute the density with the GSW routines (see Section 3.5.3). From this, the mass term is then computed, and the motion term is derived from horizontal velocities. The combined series is calculated using the generalised cornered hat method, which assigns weights to each component based on its variance (see Section 5.2.1 for details). To compare the OAM as excitation estimates against Earth rotation data (SPACE2018 series by Ratcliff and Gross, 2019), these observed excitations must be corrected for atmospheric contributions from ERA-Interim (Schindelegger et al., 2013b) and hydrological and cryospheric contributions derived

from Release-06 GRACE mascon gravity fields provided by the Jet Propulsion Laboratory (JPL, Tapley et al., 2019). The analysis itself comprises comparisons of the signal content in both the frequency and time domains across sub-seasonal, seasonal, and interannual time scales based on analysis of the excitation budget, the PVE, computation of phase and amplitude, and visualisations.

A first comparison is presented for the amplitude spectra of the χ_1 and χ_2 mass and motion term components. Overall, the reanalyses show different amplitude spectra, despite the similarities in their processing choices. The amplitude spectra reveal that the χ_2 mass term is generally more energetic than χ_1 for periods longer than 20 days, with both components following a red spectrum. ECCOv4 and ORAS agree well across frequencies, except for a stronger annual signal in χ_1^{m} in ORAS. FOAM exhibits enhanced variability at interannual scales and higher amplitudes in χ_1^{v}, particularly between 20–100 days, while GLORYS shows oscillations at 2–5 days. All reanalyses have a common minimum near 40 days in the mass term and energy increases at $\sim$50 and $\sim$90 days in χ_2^{v}, with only ORAS showing a pronounced annual peak. The deviations of the models in terms of their amplitude spectra may be the result of differences in the applied DA schemes (Table 5.2) or potentially also differences in global parameter choices, which are unpublished and thus hard to verify.

The subsequent analyses are performed in the temporal domain, including the sub-seasonal band, seasonal oscillations and the interannual band. In the sub-seasonal band, i.e., periods $<$120 days, the reanalyses show comparable performance to ECCOv4 ($\sim$43–52% in $\hat{\chi}$ and $\sim$29–40% in χ_3) in the atmosphere-corrected geodetic excitation. This is likely attributed to their higher horizontal and vertical model resolution, which allows for better representation of regional oceanic circulations controlled by bottom topography (Harker et al., 2021). The PVE values (cf. Table 5.3), especially the ones for FOAM, indicate that the reanalyses are not error-free at those periods, but the combined series has better skill as it suppresses noise and DA artefacts. Remaining residuals suggest that other processes, such as pressure loading effects or high-frequency noise in Earth rotation data are present at these time scales.

At the annual prograde polar motion, the atmospheric plus oceanic excitation from the reanalyses reproduces the geodetic excitation corrected for hydrological and cryospheric effects, while ECCOv4 stands out due to a large phase offset and overestimated amplitude. In the retrograde component, phase shifts are evident in all OAM estimates, with GLORYS and ORAS showing the highest amplitudes due to their larger mass terms. The oceanic signals in the semi-annual prograde polar motion are dominant (2–3 mas) with a good agreement of the atmospheric plus oceanic excitation of all models. In contrast, the performance of all oceanic solutions is low in the retrograde component. The annual variability in the χ_3 component is largely explained by atmosphere-ocean excitation, with the mass term being the dominant contributor, but the amplitudes of the reanalyses vary. In the semi-annual component of χ_3, the atmospheric effects dominate with small oceanic contributions, although GLORYS features an anomalously large mass term.

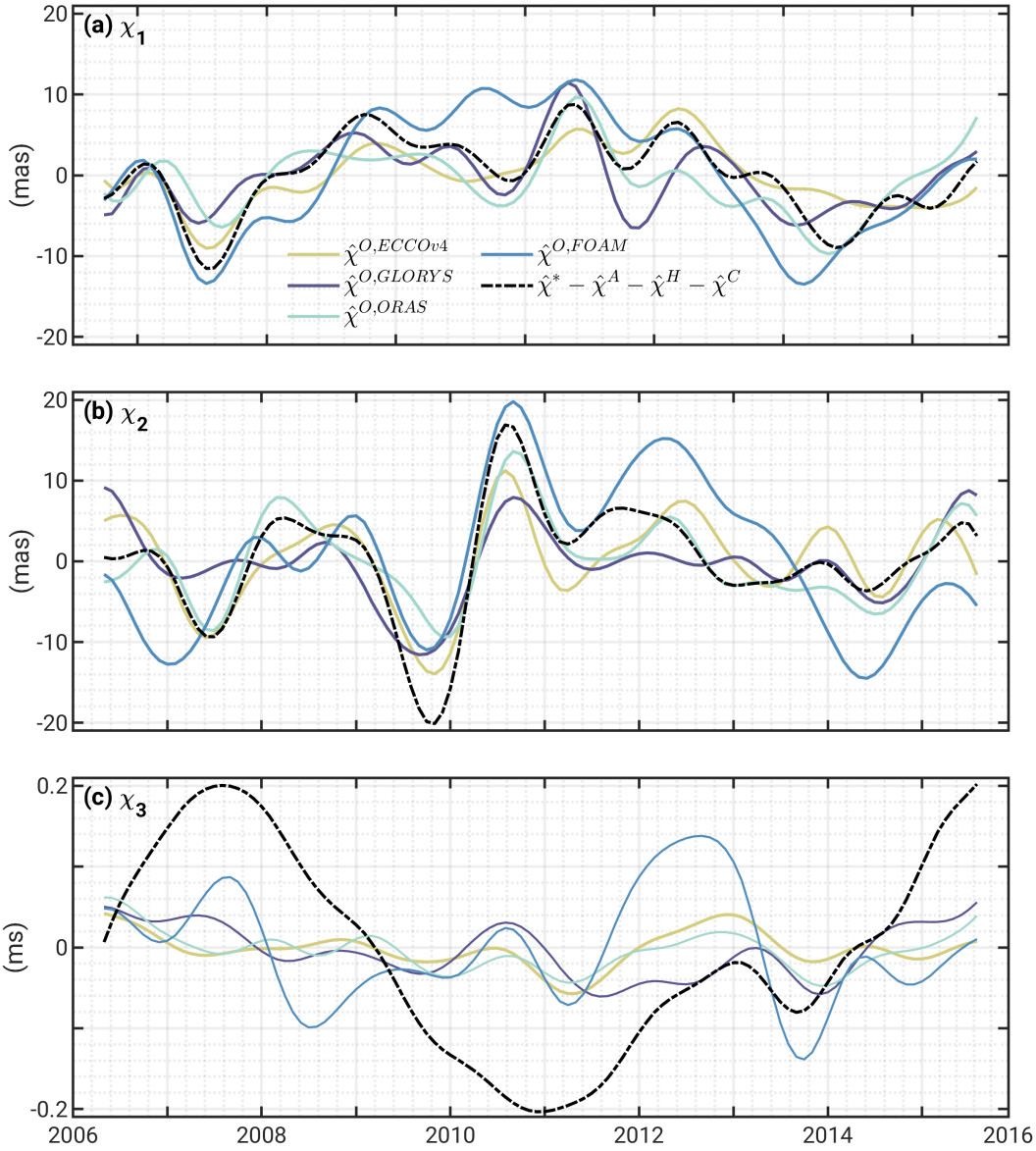

Figure 5.6: Interannual excitation signals $\chi_{1,2,3}$ as deduced from ECCOv4, GLORYS, ORAS, FOAM and GRACE-based hydrology/ice in comparison with the geodetic excitation–AAM–HAM from 2006 through 2015. Four months were clipped both at the beginning and at the end of the time series to avoid filter artefacts.

When looking at interannual variability (Figure 5.6), which is limited by the relatively short time span, the reanalyses cannot compete with ECCOv4. FOAM, in particular, exhibits spurious long-period signals in the χ_3 component after 2012, likely due to assimilation artefacts. Among the reanalyses, ORAS performs best and is thus recommended for OAM applications. The Combination further improves agreement with observations by mitigating model-specific biases, especially in χ_1 and $\hat{\chi}$. Overall, ECCOv4 explains over 72% of the atmosphere-corrected polar motion excitation (cf. Figure 5.7), and the Combination even reaches 77% in χ_1. Across all data sets, the mass term clearly dominates interannual variability. The pronounced χ_2 anomaly in 2009, seen across all models, is linked to an increase in Southern Ocean p_b attributed to the

2009/10 El Niño (see Boening et al., 2011, and Chapter 6). Meanwhile, a 5–6 year oscillation in χ_3, likely caused by core-mantle coupling, remains unmodelled. Including GRACE-based hydrological/cryospheric mass terms significantly improves the excitation budget, while remaining residuals likely stem from errors in wind forcing, ocean model limitations, or uncertainties attributed to the GRACE-based mass term.

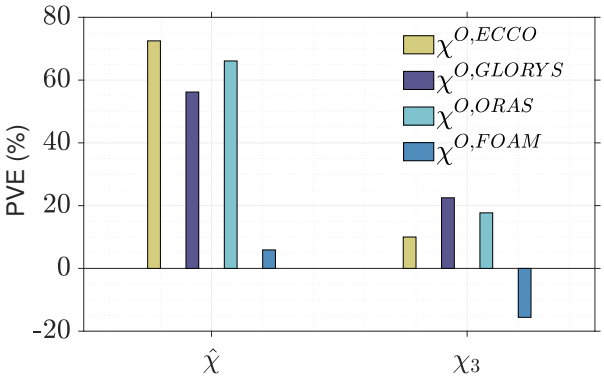

Figure 5.7: PVE of ECCOv4, GLORYS, ORAS, and FOAM in equatorial ($\hat{\chi}$) and axial (χ_3) components on interannual time scales of the atmosphere-corrected geodetic excitation.

This chapter provides valuable context and knowledge regarding the use of data-constrained ocean models for Earth rotation studies. Apart from horizontal and vertical model resolution (Harker et al., 2021), the choice of the DA scheme in ocean reanalyses leads to differences in the OAM estimates from various sources, especially the longer the time scale. These sensitivities should be borne in mind when modelling oceanic contributions Earth rotation variations, e.g., when subtracting a single (and necessarily imperfect) model-based solution for $\hat{\chi}^O$ and χ_3^O from the geodetic excitation to reveal more subtle effects from other geophysical fluids.

6. ENSO modulates the oceanic excitation of polar motion

This chapter presents a first-time investigation of the influence of ENSO on the oceanic excitation of polar motion. ENSO is a phenomenon that is well-known for its strong impact on zonal atmospheric angular momentum and thus ΔLOD, but a similar effect in polar motion excitation remains unclear so far. The chapter is structured as follows: First, publication-related information is presented, including the abstract, paper reference, data availability statement, acknowledgements, copyright statement, and author contributions. The published article follows. Finally, Chapter 6.5 provides a summary of the problem, methodology, data, and key findings.

Chapter abstract

The El Niño–Southern Oscillation (ENSO) exerts a strong control on interannual length-of-day variations, but its imprint on polar motion excitation remains to be identified. We explore the hypothesis that part of this imprint is embedded in oceanic angular momentum (OAM) changes, particularly that component driven by ocean bottom pressure (p_b) variations. Analysis of coupled climate model output suggests that the main ENSO signatures in p_b are intensified fluctuations in the Bellingshausen Basin and a large-scale see-saw between Pacific and Indian oceans. These patterns are also present in satellite gravimetry data and primarily excite polar motion along 90°E. Inferred OAM changes account for ∼40–50% of the variance in observed polar motion excitation during El Niño/La Niña cycles, upon removal of known geophysical fluid effects. However, given the co-occurrence of ENSO and other (oceanic) excitation signals, polar motion data may only provide limited insights into variability of this climate mode.

Plain language summary

The El Niño–Southern Oscillation (ENSO) is a climate mode that impacts weather around the world and slows down the rotation of the Earth every two to seven years. However, it is still unclear whether ENSO also influences polar motion, that is, the horizontal movement of the pole of rotation. In this study, we show that ENSO does indeed influence polar motion by changing the spatial distribution of ocean mass. Specifically, during an El Niño event, water moves away from

the Indian Ocean and the coast of Australia to spread across the Pacific Ocean. As a result, the axis and thus the pole of rotation slightly shift toward the Pacific. We describe this phenomenon with the help of climate models, but demonstrate that the characteristic changes in ocean mass and polar motion are also partly seen in global ocean and Earth observations. However, as other climate and mass fluctuations are happening at the same time, it is hard to say how ENSO behaves exactly just by looking at polar motion observations.

Published manuscript

Börger, L., Lentge, K. M., Schindelegger, M., & Dobslaw, H. (2025). ENSO modulates the oceanic excitation of polar motion. Geophysical Research Letters, 52, e2025GL118576. https://doi.org/10.1029/2025GL118576

Data availability statement

Monthly p_b anomalies over 1850–2014 and lagged regression fields for all four CMIP6 models have been placed at https://zenodo.org/records/15065185 (Börger et al., 2025a). For the OAM estimates from MPIOM and DEBOT, see https://rz-vm480.gfz.de/repository/entry/show?entryid=73d23da5-4728-4b91-852d-2a630957b307 (Dobslaw and Dill, 2018) and https://zenodo.org/records/13322321 (Börger et al., 2024a). The atmospheric, cryospheric, and hydrological angular momentum time series used in this work are available at https://zenodo.org/records/12664036 (1995–2015, Börger et al., 2024b).

Acknowledgements

Lara Börger, Konstantin M. Lentge, Michael Schindelegger, and Henryk Dobslaw were supported by the German Research Foundation (DFG, Project no. 459392861). We thank two anonymous reviewers for their helpful comments.

Copyright

Author contributions

The results presented in this thesis are the original work of the author, with contributions from the co-authors in the areas of conceptualisation, planning, drafting, and revising the initial manuscript. Konstantin Lentge analysed ENSO in p_b of various models, including those used in this study, as part of his Master's thesis (Lentge, 2024). These analyses were adapted and repeated by me for the purposes of this study.

Lara Börger: Data curation, Formal analysis, Investigation, Methodology, Software, Validation, Visualisation, Writing - original draft, Writing - review & editing. **Konstantin M. Lentge**: Data curation, Formal analysis, Investigation, Methodology, Software, Validation, Visualisation, Writing - review & editing. **Michael Schindelegger**: Conceptualisation, Funding acquisition, Methodology, Supervision, Validation, Writing - review & editing. **Henryk Dobslaw**: Funding acquisition, Writing - review & editing.

6.1. Introduction

ENSO, originating in the tropical Pacific, is Earth's strongest natural climate signal at interannual time scales. It oscillates between warm (El Niño), cold (La Niña), and neutral phases, driving temperature, precipitation, and ocean circulation (McPhaden, 2015). Through its teleconnections, ENSO modulates climate variability worldwide (McPhaden et al., 2006; Liu and Alexander, 2007), affecting ecosystems and human societies (McPhaden et al., 2006). Apart from sea level and surface temperature, one possible variable for studying oceanographic effects of climate modes is ocean bottom pressure (p_b) (Ponte, 1999). p_b provides information about mass redistribution in the ocean, which is closely linked to circulation patterns and therefore likely also to ENSO (Boening et al., 2011; Chambers, 2011; Qin et al., 2022).

Changes in ocean currents and the distribution of ocean mass, or equivalently p_b, lead to fluctuations in OAM, parts of which are transferred to the solid Earth. The results are measurable variations in Earth's rotation, including changes in angular velocity and the horizontal movement of a conventional reference pole relative to the Earth's crust. This motion is commonly referred to as wobble or polar motion (Gross, 1992). While ENSO is known to affect changes in length-of-day through anomalous zonal low-latitude winds (Rosen et al., 1984; Zheng et al., 2003; Lambert et al., 2017; Yu et al., 2021), similar atmospheric effects on polar motion are absent (Marcus et al., 2010). Here, we explore whether ENSO modulates equatorial OAM and the resultant oceanic excitation of polar motion.

Given that the available satellite gravimetry record only samples a few ENSO events (Pfeffer et al., 2022), we mainly use output from long coupled atmosphere-ocean model simulations under the Coupled Model Intercomparison Project phase 6 (CMIP6, Eyring et al., 2016). Specifically, we

extract ENSO-induced p_b and horizontal velocity variations from four CMIP6 models, validate the p_b results against satellite gravimetry observations, synthesise the expected ENSO signal in OAM, and quantify the contributions of that signal to polar motion excitation.

6.2. Materials and methods

6.2.1. CMIP6 models

We use coupled climate model output from simulations of the CMIP6 historical period 1850–2014 at monthly sampling (Eyring et al., 2016). The four selected models—CMCC-ESM2 (Lovato et al., 2021, in short: CMCC), EC-Earth3 (EC-Earth Consortium, 2019, EC-Earth), MIROC6 (Tatebe and Watanabe, 2018, MIROC), and MRI-ESM2 (Yukimoto et al., 2019, MRI)—are based on different ocean models, each with a nominal resolution of 100 km. Other CMIP6 models with realistic p_b signal content (Figures S1–S2 in Supporting Information S1) were also tested, confirming the results from the four selected models. While CMCC and EC-Earth use NEMO, the model underlying MIROC is COCO4.9, whereas MRI-ESM2 employs MRI.COM4.4. Furthermore, the climate models differ in their choice of the atmospheric component (see Table S1 in Supporting Information S1) and physics parameterisations, leading to somewhat diverging outcomes. With the selected models, we thus sample both structural and parametric uncertainty. To derive monthly p_b, we use temperature, salinity, and surface elevation fields (cf. Ponte, 1999) and incorporate the ETOPO1 bathymetry (Amante and Eakins, 2009) to consider fraction cells at the ocean bottom (Börger et al., 2023). After vertical integration, a monthly-varying spatial mean is subtracted to reduce the full bottom pressure to dynamic p_b anomalies. Additionally, we determine monthly barotropic velocity fields from modelled meridional and zonal velocities.

As ENSO is characterised by index series, we first compare the ONI provided by the National Oceanic and Atmospheric Administration (NOAA, Climate Prediction Center, 2017) with similar index series computed from the four CMIP6 models (Figure 6.1). The index is based on sea surface temperature anomalies, see Text S1 in Supporting Information S1. While the NOAA reference series is shown from 1925 to the present, the CMIP6 series are given for the period 1915–2014, thus also spanning 100 yrs. These two types of ONI series cannot be expected to agree in magnitude, duration, and frequency of ENSO, because (i) models are necessarily imperfect, and (ii) climate modes in CMIP6 have random phases. In Figure 6.1, CMCC and MIROC display higher amplitudes and occasionally longer event durations than those evident in the NOAA reference. In contrast, the MRI and EC-Earth models more closely match the magnitudes and duration of observed ENSO events, although the peaks occur too frequently in MRI. These differences among the models suggest a notable spread in the representation of ENSO, meaning that our conclusions are drawn from a relatively broad solution space. Below, the ONI series specific to each model are applied to calculate lagged p_b regression fields.

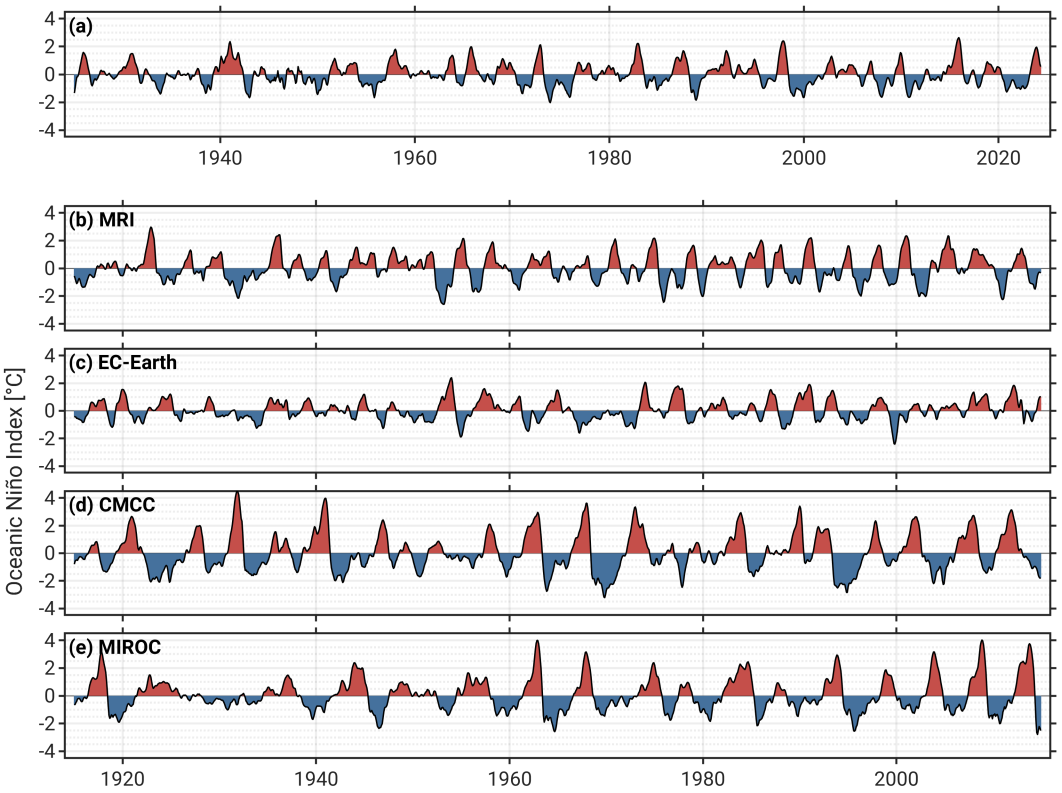

Figure 6.1: ONI series from the (a) NOAA reference and (b–e) sea surface temperature deviations of the four CMIP6 models (MRI, EC-Earth, CMCC, and MIROC) over a period of 100 years. The respective time periods are 1925–2024 (NOAA) and 1915–2014 (CMIP6 models). The common threshold used to indicate El Niño and La Niña is ± 0.5°C.

6.2.2. Analysis of p_b fields

Lagged regression is frequently used in climate studies to analyse dependencies between time-shifted variables (Trenberth et al., 2002; McPhaden et al., 2006; Mayer et al., 2016). Here we apply the method to analyse the relationship between ONI and p_b anomalies or barotropic velocities from the CMIP6 models. The calculations are based on a linear equation

$$Y(t \pm \tau) = \alpha_\tau + \beta_\tau X(t) + \epsilon_\tau \tag{6.1}$$

in which the dependent variable Y (e.g., the p_b anomalies) is shifted by τ time steps against the independent variable X (e.g., ONI) at time t. The coefficient α_τ describes the y-intercept, whereas β_τ represents the slope of the regression line. Through Equation (6.1), τ becomes the temporal coordinate and any connection to absolute time is dropped. This way, model results can be compared to observations around particular ENSO events even if those events do not appear in the original model record (Figure 6.1). To estimate the regression coefficients, we use a least-squares adjustment, which minimises the error term, denoted as ϵ_τ. In the subsequent analysis of p_b, we focus on the regression slopes.

We apply the regression analysis to the CMIP6 models and, for validation purposes, to p_b estimates from the GRACE satellites and its Follow-On (GRACE-FO) mission (Tapley et al., 2019).

Specifically, we use monthly Release-06 GRACE mascon p_b fields, provided by the Goddard Space Flight Center from 2002/04 to 2023/12 on a 0.5° latitude-longitude grid (Loomis et al., 2019). Over the 22 years considered, the GRACE data contain occasional gaps of 30 or 60 days, and one extended period of missing data in 2017–2018, marking the transition period between GRACE and GRACE-FO. Following an adjustment for local jumps in p_b due to intense earthquakes (Text S2 in Supporting Information S1), the spatial mean is reduced, and a low-pass filter with a cut-off frequency of 0.5 years^{-1} is applied. In the following, this data set is referred to as "GRACE".

6.2.3. Polar motion excitation

We denote the geodetic or observed excitation as $\hat{\chi}^*$ and separately consider excitations due to mass redistributions and particle motion in geophysical fluids (e.g., Wahr, 1982), particularly those due to atmosphere ($\hat{\chi}^\mathrm{A}$), ocean ($\hat{\chi}^\mathrm{O}$), terrestrial hydrology ($\hat{\chi}^\mathrm{H}$), and Greenland/Antarctic ice sheets ($\hat{\chi}^\mathrm{C}$), cf., e.g., Börger et al. (2025c). We primarily compare the oceanic excitation with the observed excitation reduced for atmospheric, hydrological, and cryospheric effects, i.e.,

$$\hat{\chi}^* - \hat{\chi}^\mathrm{A} - \hat{\chi}^\mathrm{H} - \hat{\chi}^\mathrm{C} \quad = \quad \hat{\chi}^\mathrm{O}. \tag{6.2}$$

For the excitation by non-oceanic sources (i.e., $\hat{\chi}^\mathrm{A}$, $\hat{\chi}^\mathrm{H}$, $\hat{\chi}^\mathrm{C}$), we use the same data sets as in Börger et al. (2025c), who found relatively good agreement between observed and modelled polar motion excitation over 1995–2015 on interannual time scales without invoking core effects. Here, we extend all excitation series to the period 1995–2019. For cross-checks on the oceanic excitation, we use an OAM series of the Max-Planck-Institute for Meteorology Ocean Model (MPIOM, Jungclaus et al., 2013) from 1995–2023 provided by GFZ (Dobslaw and Dill, 2018). Additionally, we use the OAM motion term from a global barotropic model (DEBOT, Einšpigel and Martinec, 2017), as employed in Harker et al. (2021) and Kiani Shahvandi et al. (2024).

6.3. Results

6.3.1. ENSO in p_b

Figure 6.2 illustrates the lagged regression fields for three selected lags at −10, 0, and 10 months from the four CMIP6 models and GRACE (cf. Section 6.2.2). The lags reflect the temporal evolution of the ENSO imprint on p_b, which can represent either El Niño or La Niña, depending on the sign of the ONI applied in a subsequent analysis step. The regression coefficient represents the slope of the regression line at each cell, which depends entirely on the magnitudes and similarities of the two variables being compared. In physical terms, the regression coefficients

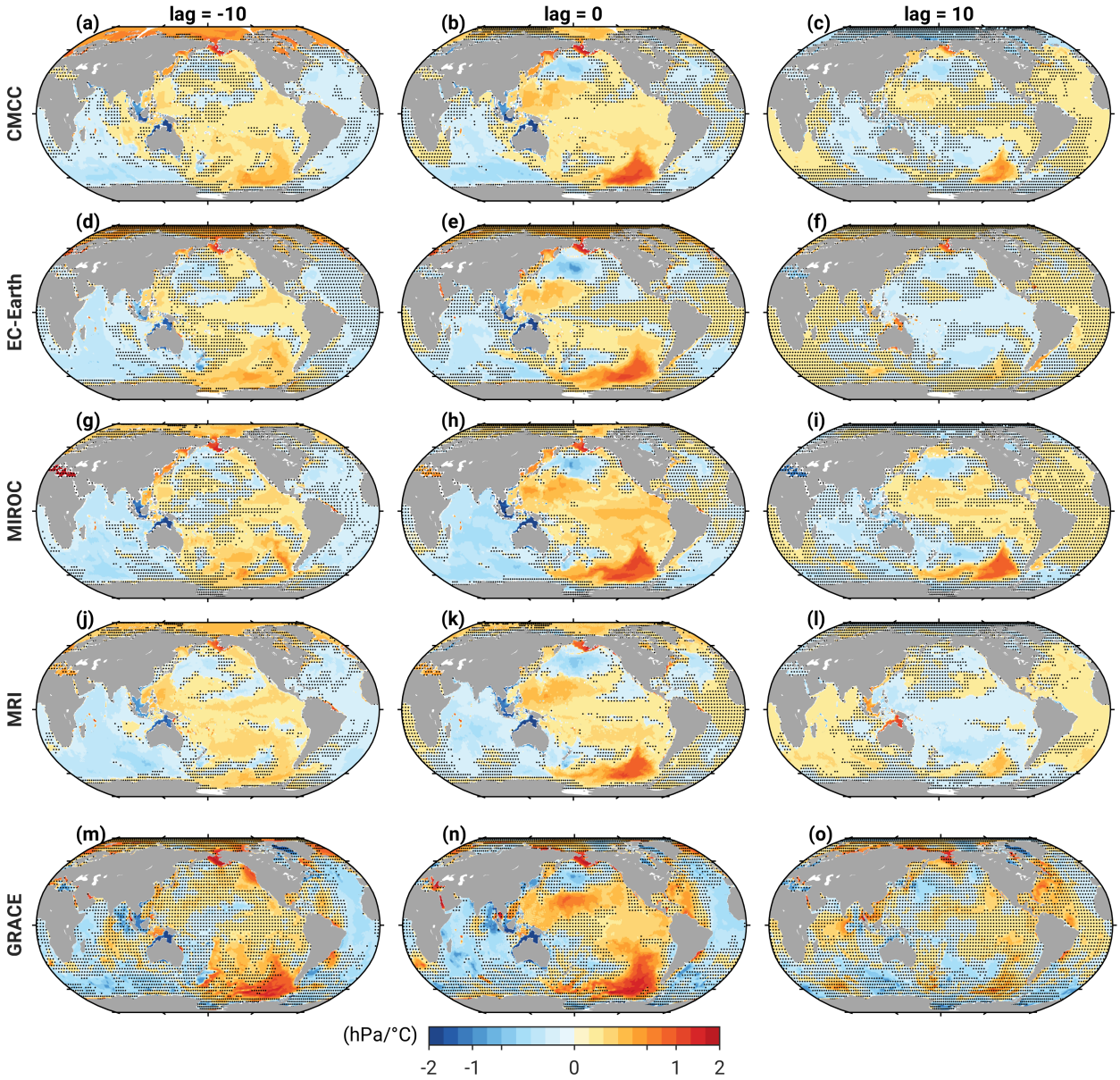

Figure 6.2: Results of the lagged regression of monthly p_b fields onto ONI from (a–c) CMCC, (d–f) EC-Earth, (g–i) MIROC, and (j–l) MRI and for comparison (m–o) the GRACE GSFC mascons. We show three selected lags -10 (left column), 0 (middle column), and 10 (right column). The black points mark statistically insignificant values at 90% confidence.

indicate the change in p_b at any given point for a one-fold change in ONI, independent of absolute time.

We generally observe consistent regression patterns across the models and GRACE in the Pacific, Indian Ocean, and Arctic regions. A certain bipolarity between basins exists at all selected lags, but for -10 and 0 months, widespread positive regression coefficients are apparent in the Pacific and Arctic, while negative coefficients are present in the Indian and Atlantic Oceans. At lag $=$ 10 months, the models and GRACE are less consistent, which suggests that the intensity and phase with which ENSO decays (or reverses) are captured differently in the models and GRACE. MRI and EC-Earth demonstrate negative regression coefficients in the Pacific and positive coefficients

in the Indian Ocean, while CMCC and MIROC exhibit delayed reactions, and suggest negative anomalies in the Pacific. Furthermore, the Arctic is also affected by p_b changes and co-oscillates with other basins. The presence of a see-saw (i.e., bipolar) pattern even in the absence of a strong Bellingshausen Basin mode (see below) suggests that this large-scale oscillation possibly originates from Australia, particularly its continental shelf. The processes at work could be similar to those described by Rohith et al. (2019) and Afroosa et al. (2021), that is, local winds north and northwest of Australia generate boundary waves that lead to a basin-wide adjustments with opposite polarity between Pacific and Indian oceans (see Figure S6 in Supporting Information S1).

At lag $= -10$ months, all CMIP6 models and GRACE show high negative regression coefficients (up to -2 hPa/°C) on the Australasian Shelf. In the Bellingshausen Basin, models peak near 0.5 hPa/°C, while GRACE reaches 2 hPa/°C (Qin et al., 2022). Due to the considerably shorter time span of the GRACE data (∼22 years vs. 165 years), extreme events, such as the one in 2015 (ONI $= 2.6$°C), exert a strong impact on the calculated coefficients. During the El Niño event (lag $= 0$ months), the model-based ENSO signal in p_b is most prominent in the centre of the Bellingshausen Basin, with ≥ 1 hPa/°C. These p_b fluctuations are predominantly influenced by ENSO-driven atmospheric pressure and wind stress changes over the Amundsen Sea (Sasgen et al., 2010; Ponte and Piecuch, 2014; Scott Yiu and Maycock, 2019). At lag $= 10$ months, the models are not in accordance; GRACE suggests < 0.75 hPa/°C in the Bellingshausen Basin and MIROC reaches coefficients around 1 hPa/°C. Since p_b gradients are primarily maintained by wind stress variations, correlations may reduce quickly after an event when other mechanisms start to dominate the large-scale winds.

As a validation, we consult the PVE (defined in Text 4 in Supporting Information S1) for three El Niño events (2009/10, 2015/16, 2023/24). We consider the PVE by ENSO-induced p_b patterns in low-pass filtered (period ≥ 2 years) GRACE fields (Figure 6.3). The lagged regression is performed for 21 months spanning from ± 10 months around the ENSO event for the models CMCC, EC-Earth, and MIROC only, since the results of MIROC and MRI are similar. For completeness, the PVE results for MRI and also for selected La Niña events are illustrated in Figures S7–S8 in Supporting Information S1. To compare the lagged regression results with the p_b changes of GRACE, we scale the model fields from Figure 6.2 and other lags with the observed ONI of the respective event. White patches indicate regression coefficients with a value < 0.15 hPa/°C, while negative PVE values are colored blue.

Overall, MIROC shows fewer white patches than the other two models, likely because the nominal p_b changes during El Niño are largest for MIROC. Across all events and models, the PVE results are fairly consistent in structure in the western, northern, and south-eastern Pacific, in parts of the Indian Ocean and the Arctic, i.e., regions where regression coefficients are largest (cf. Figure 6.2). The most substantial discrepancies are observed in and around the Bellingshausen Basin. While CMCC and EC-Earth exhibit positive PVE values (∼30%) within the basin centre, all models demonstrate higher PVE values exceeding 70% at basin margins. During the 2015/16 El Niño event (right column of Figure 6.3), with ONI $= 2.6$°C, all models tend to exhibit

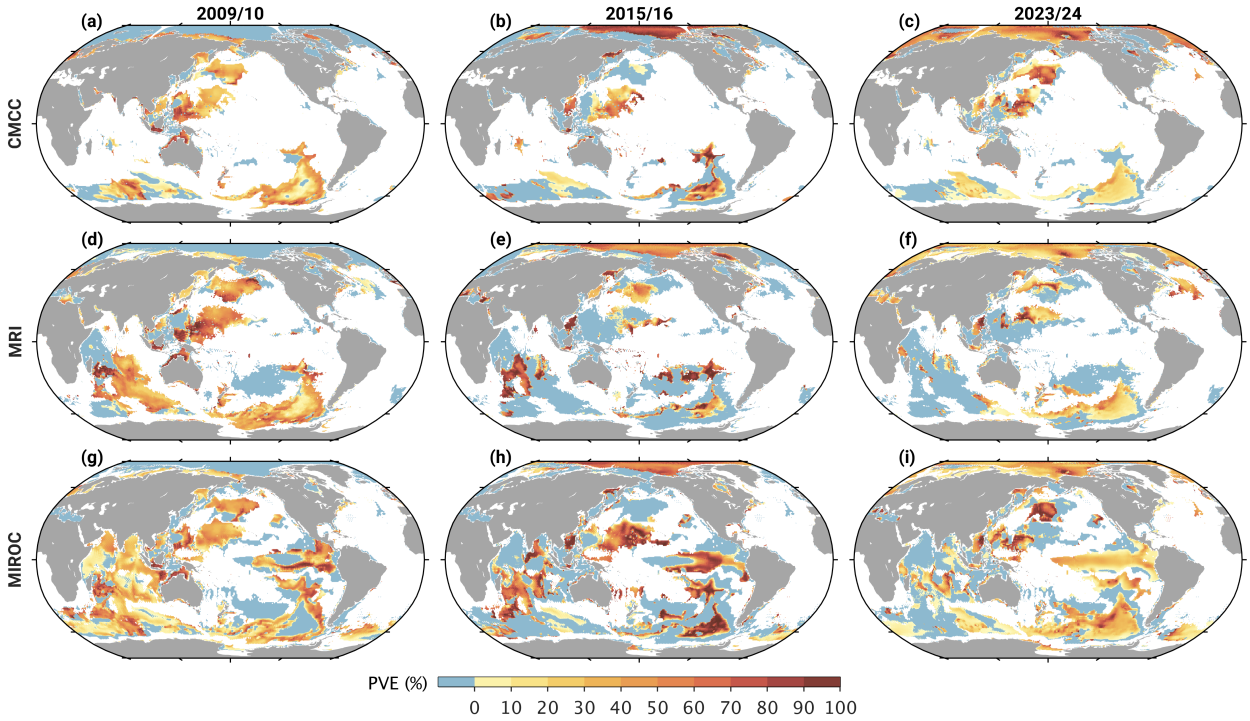

Figure 6.3: Percentage of Variance Explained in the interannually filtered GRACE-based p_b fields by ENSO signals, as deduced from three selected CMIP6 models (a–c) CMCC, (d–f) MRI, (g–i) and MIROC. The analysed El Niño events are 2009/10 (ONI $= 1.6°$C, left column), 2015/16 (ONI $= 2.6°$C, middle column), and 2023/24 (ONI $= 2.0°$C, right column). For each event, we use 21 lags ($\pm$10 months). White areas indicate grid points with regression coefficients smaller than 0.15 hPa/°C.

negative or strongly positive values. ENSO is merely one of several phenomena that contribute to GRACE-derived p_b changes. Other climate modes (e.g., Pacific Decadal Oscillation), wind-forced variability, or basin modes emerging from internal non-linear dynamics also influence p_b at these time scales (Ponte and Piecuch, 2014; Delforge et al., 2022; Pfeffer et al., 2022; Niu et al., 2022; Zhao et al., 2023; Börger et al., 2025c). Consequently, ENSO cannot always be reflected in the PVE. Overall, Figure 6.3 indicates that ENSO does not play a dominant role globally, although it can be regionally important and vary in prominence from event to event.

6.3.2. ENSO in polar motion excitation

We now examine the role of ENSO in the low-frequency equatorial excitation budget for three selected El Niño and subsequent La Niña events in 1997/98, 2009/10, and 2015/16. To this end, a high-pass filter with a cut-off frequency of 2 years^{-1} is applied to each detrended excitation series, except the CMIP6 series, and the residual geodetic excitation $\hat{\chi}^* - \hat{\chi}^\mathrm{A} - \hat{\chi}^\mathrm{H} - \hat{\chi}^\mathrm{C}$ is compared against an estimate for the ENSO signal in $\hat{\chi}^\mathrm{O}$. Each event spans 47 months, represented by lags from -10 to 36 months. This covers a full ENSO cycle, including potential transitions into La Niña. To compute the oceanic excitation of ENSO from the CMIP6 models, we first multiply the respective regression fields by the corresponding ONI of the event and then apply

monthly-varying spatial masks based on significance tests to suppress regions unrelated to ENSO (see Text S3 and Figures S9–S11 in Supporting Information S1). The suppressed regions have been found to exert a minor influence on the excitation (cf. Figure S14 in Supporting Information S1).

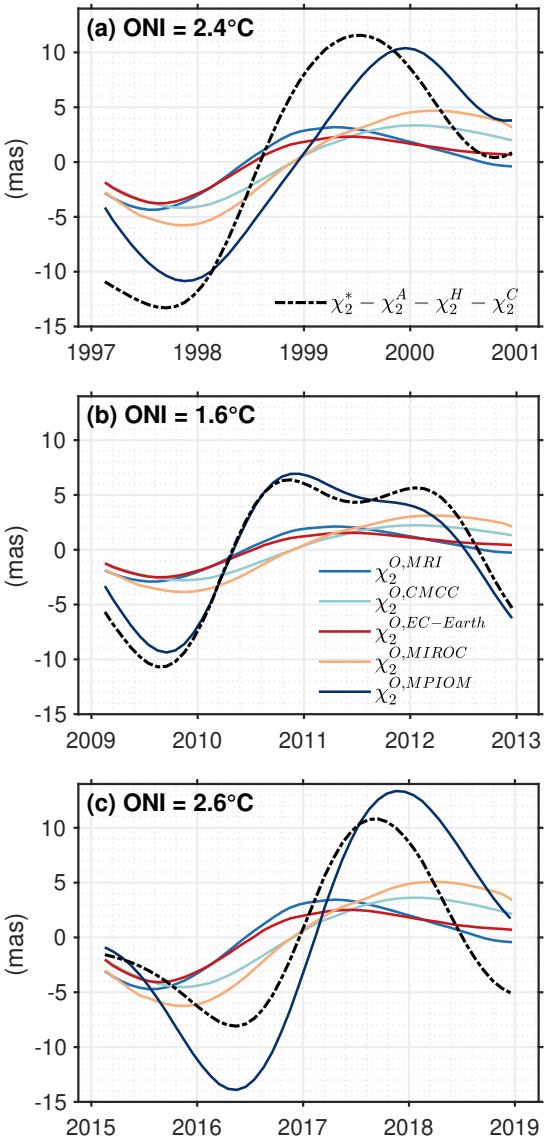

Figure 6.4: ENSO-induced oceanic excitation in the χ_2^{O} mass term derived from CMCC ($\chi_2^{\mathrm{O,CMCC}}$), EC-Earth ($\chi_2^{\mathrm{O,EC\text{-}Earth}}$), MRI ($\chi_2^{\mathrm{O,MRI}}$) and MIROC ($\chi_2^{\mathrm{O,MIROC}}$) compared to the interannually filtered geodetic excitation minus atmospheric, hydrological, and cryospheric contributions ($\chi_2^* - \chi_2^{\mathrm{A}} - \chi_2^{\mathrm{H}} - \chi_2^{\mathrm{C}}$) for the El Niño events in (a) 1997/98, (b) 2009/10 and (c) 2015/16. The full oceanic excitation from MPIOM ($\chi_2^{\mathrm{O,\,MPIOM}}$, mass + motion) is also shown.

Given the bipolar p_{b} pattern observed in the Pacific and Indian oceans (Figure 6.2), the ENSO signal is particularly strong for the χ_2 component, reaching 5 mas in magnitude (see Figure 6.4). In contrast, the χ_1 component is only marginally affected (± 1 mas, see Figure S13 in Supporting Information S1), cf. Afroosa et al. (2021) for a similar phenomenon on intra-seasonal time scales. We thus focus on the χ_2 component for the remainder of the text. Furthermore, the mass term is dominant over the motion term by a factor of 10^5 (Figure S12 in Supporting Information S1) due to equatorially confined barotropic velocities (Figures S3–S4 in Supporting Information S1). Masking experiments confirm that the ENSO signal in χ_2 is mainly driven by the large-scale see-saw in p_{b}, and not the signals in the Bellingshausen Basin or North Pacific (see Figure S15 in Supporting Information S1).

The CMIP6-derived excitations in Figure 6.4 reveal a common signal through of -3 to -6 mas during El Niño, reversing to positive χ_2^{O} values during La Niña conditions. This behaviour is evident in all models and all events, pointing to a characteristic ENSO imprint in the χ_2 component (cf. Figure 6.4). EC-Earth and MRI exhibit similar behaviour, and CMCC and MIROC show comparable characteristics too, consistent with the synthesised p_{b} fields (Figure 6.2). However, a phase shift is observed in the χ_2 series of EC-Earth and MRI relative to CMCC and MIROC, as the former show steeper slopes and earlier La Niña peaks. Comparing the models to the residual geodetic excitation, we find a good degree of similarity, as the observations also indicate a negative (positive) excitation anomaly during El Niño (La Niña). The discrepancy in the amplitudes is typically a factor of $\sim$3. In contrast, MPIOM agrees better in magnitude with the reduced observation. This can be attributed to the fact that

the MPIOM series are derived from the full p_b and velocity fields, which include atmosphere-driven broadband variations at periods ≥ 2 years. If the MPIOM p_b record is restricted to ENSO signals in the same way as the climate models (see Figure S5 in Supporting Information S1), its oceanic excitation would be very close the CMIP6 curves in Figure 6.4.

Table 6.1: Observed vs. modelled χ_2 excitation for three selected ENSO events[a]

	1997/98	2009/10	2015/16
RMS of χ_2^*	4.1	5.4	9.3
PVE by χ_2^O in residual series $\chi_2^* - \chi_2^A - \chi_2^H - \chi_2^C$			
CMCC	45.3 (6.7)	35.5 (4.9)	50.1 (4.4)
EC-Earth	40.9 (6.9)	38.0 (4.8)	35.4 (5.0)
MIROC	55.7 (6.0)	42.6 (4.6)	50.1 (4.4)
MRI	47.7 (6.5)	46.2 (4.4)	37.8 (4.9)
MPIOM	77.1 (4.3)	95.2 (1.4)	39.8 (4.8)
PVE by χ_2^O in residual series $\chi_2^* - \chi_2^A - \chi_2^H - \chi_2^C - \chi_2^{v,MPIOM}$			
CMCC	43.9 (5.4)	57.0 (2.7)	−49.6 (3.9)
EC-Earth	47.5 (5.2)	53.5 (2.8)	−2.5 (3.2)
MIROC	49.7 (5.1)	66.2 (2.5)	−139.3 (4.9)
MRI	57.8 (4.7)	60.5 (2.6)	2.4 (3.2)
PVE by χ_2^O in residual series $\chi_2^* - \chi_2^A - \chi_2^H - \chi_2^C - \chi_2^{v,DEBOT}$			
CMCC	46.3 (6.8)	34.9 (4.9)	50.3 (4.0)
EC-Earth	39.7 (7.3)	37.7 (4.8)	42.9 (4.3)
MIROC	57.9 (6.1)	41.8 (4.6)	46.6 (4.2)
MRI	45.4 (6.9)	46.0 (4.5)	48.6 (4.1)

[a]Values are Percentage of Variance Explained (PVE) and the corresponding RMS of residuals (milliarcseconds) in parentheses, except for the first line. All time series have been detrended and filtered to periods ≥ 2 years. Statistics are computed for temporal arcs from −10 to 36 months around the respective El Niño peak in December. The CMIP6 χ_2^O estimates are for the mass term only.

When quantifying the effect of model-based ENSO oceanic excitation on observed polar motion, the CMIP6 models account for 35–56% of the residual geodetic excitation, while MPIOM explains 40–95% (cf. Table 6.1). For all selected ENSO events, CMCC and MIROC explain more of the residual excitation than EC-Earth and MRI. The differences in PVE likely stem from the slight phase shifts also identified in the model-based ONI calculations (cf. Figure 6.1). MPIOM shows the highest PVE values during the comparatively weak 2009/10 event (cf. Figure 6.4b).

To assess the correspondence between the ENSO-derived excitation and a residual observed excitation without oceanic motion term signals, we subtract χ_2^v of either MPIOM or DEBOT from the left side of Equation (6.2). Since no motion term is error-free, we test two models to obtain an approximate idea of the uncertainties involved. For the ENSO events in 1997/98 and 2009/10, we observe consistent results with both MPIOM and DEBOT χ_2^v; all models account for more variance in the residual geodetic excitation when a motion term estimate is subtracted (e.g., 53–66% with MPIOM and 35–46% with DEBOT in 2009/10). Except for MRI, the CMIP6 models demonstrate negative PVE values for the 2015/16 event when χ_2^v from MPIOM is reduced. This

may be attributed to imperfectly modelled circulations in the Southern Ocean in MPIOM, which will inevitably manifest in polar motion (Harker et al., 2021).

6.4. Summary and conclusions

Using CMIP6 models, we have delineated the ENSO fingerprints in both p_b and polar motion excitation. Our results show that ENSO is indeed present in equatorial Earth rotation variations at periods ≥ 2 years through oceanic mass redistribution. In the regression analysis, we observe largely consistent p_b patterns across all models and all three lags (-10, 0, 10), notably in the Pacific, Indian Ocean, and Arctic regions, with a distinct anti-correlation across the basins. This pattern, projecting onto the χ_2 component, may stem from local winds or mass convergence/divergence on the Australian continental shelf, driving boundary waves and large-scale adjustments (Rohith et al., 2019; Afroosa et al., 2021). Our analysis reveals that while the CMIP6 models and GRACE generally agree on the key features of ENSO-related p_b variations (Figure 6.2), these signatures are overprinted by other mass redistribution effects, such as broadband wind-forced variability, over most of the ocean (Figure 6.3).

The change in the oceanic mass term excitation during a typical transition from El Niño (~ -4 mas) to La Niña ($\sim$4 mas) dominates by far any motion term contribution and is partly reflected in the observed excitation after appropriate processing (Figure 6.4). In numbers, the implied χ_2^O signal, as synthesized from the four climate models, accounts for $\sim$40–50% of the variance in $\chi_2^* - \chi_2^\mathrm{A} - \chi_2^\mathrm{H} - \chi_2^\mathrm{C}$ across the analyzed events (Table 6.1). These statistics suggest a prominent, but not necessarily leading role for ENSO in driving ocean-induced interannual polar motion variability. Thus, even for Earth's dominant climate mode, polar motion appears to be less of a proxy for large-scale atmosphere–ocean circulation changes than length-of-day variations (Salstein and Rosen, 1986; Scaife et al., 2022). Nevertheless, the canonical response of the oceanic excitation to ENSO, as inferred here from climate model simulations, might be considered in long-term polar motion predictions (Kur et al., 2024), despite current limitations in accurate predictions of El Niño events (Hu et al., 2024).

6.5. Chapter summary and context

Chapter 6 presents a systematic exploration of the imprint of ENSO on the excitation of low-frequency polar motion variability. While ENSO is known to strongly influence ΔLOD via AAM changes, no clear effect on polar motion has been identified so far (see Chapter 4.3). The lead followed here is that of a few previous works (Boening et al., 2011; Chambers, 2011; Qin et al., 2022) that have reported ENSO signals in p_b in several regions of the world ocean, primarily in the Pacific. Thus, this chapter tests the hypothesis that ENSO excites polar motion primarily through oceanic rather than atmospheric processes.

To address this question, a lagged regression is applied on p_b of four CMIP6 models onto ONI: CMCC-ESM2 (Lovato et al., 2021, in short: CMCC), EC-Earth3 (EC-Earth Consortium, 2019, EC-Earth), MIROC6 (Tatebe and Watanabe, 2018, MIROC), and MRI-ESM2 (Yukimoto et al., 2019, MRI). The selection suffices the purpose of the study, since analyses including additional CMIP6 models with realistic p_b variability produce consistent results and yield no further insights. The lagged regression fields are (i) evaluated against GRACE p_b observations filtered to periods $\geq$ 2 yrs and (ii) used to derive the ENSO-driven signals in equatorial OAM. The OAM series are then compared against suitably corrected geodetic excitation and to oceanic excitation derived from MPIOM. Corrections include atmospheric, hydrological, and cryospheric excitation for three well-observed ENSO events (1997/98, 2009/10, 2015/16). These three events were selected due to their differing strengths, i.e., index values, and the availability of validation data. In this work, ONI is used as index series.

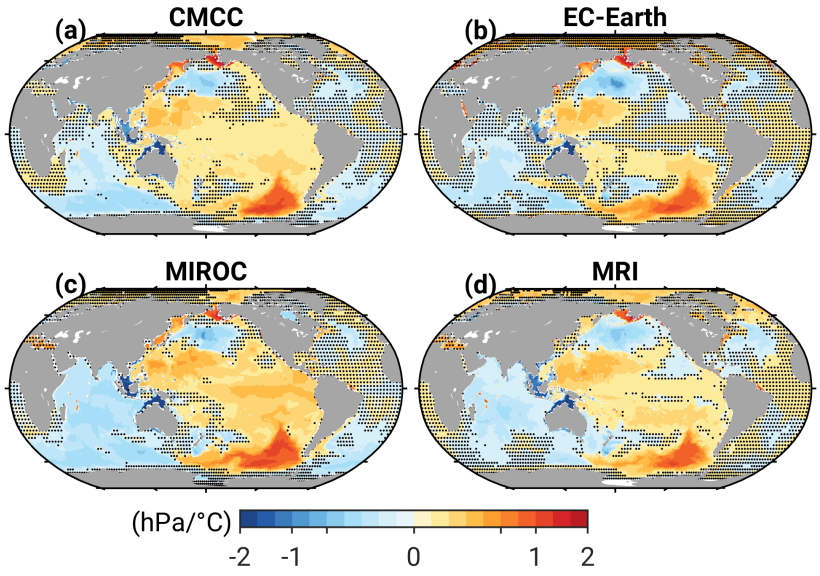

Figure 6.5: Lagged regression fields of monthly p_b fields onto ONI at lag = 0 months from (a) CMCC, (b) EC-Earth, (c) MIROC, and (d) MRI. The black points mark statistically insignificant values at 90% confidence.

The inferred lagged regression fields suggest largely consistent p_b patterns across all four CMIP6

models and all three lags (−10, 0, 10) exist, particularly in the Pacific, Indian Ocean, and Arctic regions. Moreover, a pronounced anti-correlation between ocean basins, most notably between the Pacific and Indian Ocean, emerges. Figure 6.5 shows the synthesised p_{b} fields at lag = 0 months, highlighting the good agreement of the four models and the asymmetric behaviour of the Pacific and Indian Ocean. This see-saw is likely driven by local winds or mass convergence/divergence near or on the Australian continental shelf, driving boundary waves and large-scale adjustments (Rohith et al., 2019; Afroosa et al., 2021). GRACE and the CMIP6 models generally show consistent p_{b} signatures (Figure 6.2), though they are affected by other oceanic processes, such as broadband wind-forced variability, over most of the ocean (Figure 6.3).

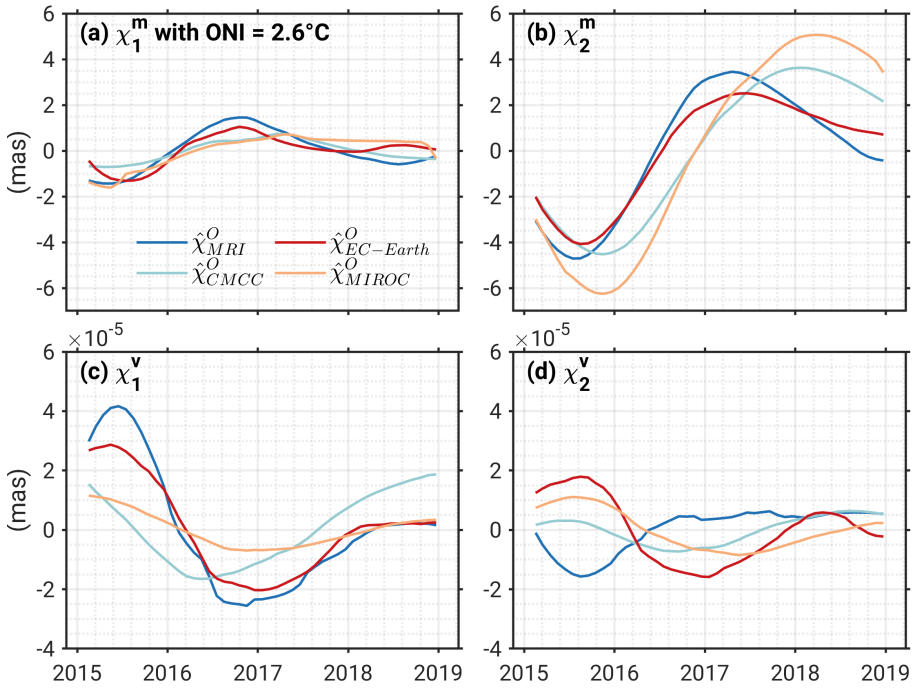

Figure 6.6: ENSO-induced OAM in χ_1 (left column) and χ_2 (right column) for the event in 2015/16 with an ONI of 2.6°C from the four CMIP6 models CMCC ($\hat{\chi}^O_{CMCC}$), EC-Earth ($\hat{\chi}^O_{EC-Earth}$), MIROC ($\hat{\chi}^O_{MIROC}$), and MRI ($\hat{\chi}^O_{MRI}$) for the (a, b) mass and (c, d) motion term.

Equation (2.27) is then evaluated to derive OAM estimates from the lagged regression fields with lags spanning −10 to +36 months around an ENSO event to cover a full ENSO cycle. The observed excitation and the contributions from atmospheric, terrestrial hydrology, and cryospheric components is low-pass filtered to periods ≥2 yrs. Figure 6.6 shows the excitations in χ_1 (left panels) and χ_2 (right panels) for the mass (upper panels) and the motion term (lower panels) for the ENSO event in 2015/16 with an ONI of 2.6°C. Note that, for the two other events in 1997/98 and 2009/10, the curves are similar but with a lower magnitude dependent on the applied ONI (2.4°C in 1997/98 and 1.6°C in 2009/10). From Figure 6.6 is evident that ENSO is most prominent in the χ_2 component, which is largely due to the see-saw pattern observed in the regression analysis (cf. weighting patterns in Figure 2.7). During El Niño the ENSO-induced OAM changes are in the range of −3 to −6 mas in χ_2 and during La Niña between 2–5 mas (cf. Figure 6.6 b). Moreover, the mass term dominates over the motion term by five orders of

magnitude (see Figure 6.6 upper panels vs. lower panels), since the only notable signals in horizontal velocities are concentrated near the equator.

When comparing the ENSO-induced OAM changes to the corrected geodetic (observed) excitation, the model-based series account for ∼40–50% of the observed variance across the analysed events (see Figure 6.7), whereas OAM deduced from MPIOM explains 40–95% (Table 6.1). The better agreement of MPIOM with the residual geodetic excitation can be attributed to the fact that OAM from MPIOM is derived from the full p_b and velocity fields, including atmosphere-driven broadband variations at periods ≥2 years. Moreover, the OAM estimates of the synthesised p_b fields are compared to the geodetic excitation that is corrected for a motion term derived either from MPIOM or from David Einšpigel's Barotropic Ocean Tide model (DEBOT, Einšpigel and Martinec, 2017; see Kiani Shahvandi et al., 2024, for the application of this model to OAM problems). This analysis gives insight into the agreement of the motion term-free residual geodetic excitation and the ENSO-induced OAM changes pertaining to the mass term. Two models are tested because motion term estimates are generally not free of error. The results are consistent for the events in 1997/98 and 2009/10, showing PVE values of 44–58% with MPIOM and 40–58% with DEBOT in 1997/98 and 53–66% with MPIOM and 35–46% with DEBOT in 2009/10. In 2015/16, three of the four CMIP6 models have negative PVE values that appear with MPIOM. These discrepancies are likely due to imperfectly modelled circulations in the Southern Ocean in MPIOM, which will inevitably manifest in polar motion excitation (Harker et al., 2021). In comparison, all four CMIP6 models account for 43–50% of the variance in the motion term-free residual geodetic excitation with DEBOT.

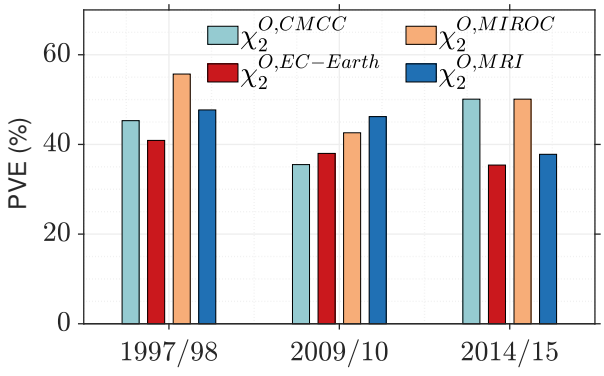

Figure 6.7: PVE of the four CMIP6 models CMCC, EC-Earth, MIROC, and MRI for the three ENSO events in 1997/98, 2009/10, and 2014/15 in the χ_2 component of the geodetic excitation corrected for contributions from the atmosphere, terrestrial hydrology and the cryosphere.

Delineating the signatures of ENSO in p_b and OAM is a first key contribution to the thesis' overarching goal, i.e., exploring unknown signals in low-frequency polar motion variability. Although the climate models indicate a notable role of ENSO in the oceanic excitation (modulations of ±4 mas), it is not the dominant driver. Therefore, polar motion appears to be less suited as a proxy for large-scale atmosphere-ocean circulation changes than is the case for the axial component (Salstein and Rosen, 1986; Scaife et al., 2022). One window of opportunity, though, arises from current efforts in improving predictions of El Niño events (Hu et al., 2024). Taking the excitation signals described in this chapter as the canonical response of OAM to ENSO, it may be possible to increase the fidelity of OAM and thus long-term polar motion predictions.

7. Chaotic oceanic excitation of low-frequency polar motion variability

This chapter investigates the role of oceanic intrinsic variability in the excitation of low-frequency polar motion. In contrast to the previous chapter, which is devoted a specific signal arising from atmosphere-ocean interactions, this chapter considers signals that originate from the ocean itself. The chapter is organized as follows: First, publication-related information is presented, including the abstract, paper reference, data availability statement, acknowledgments, copyright statement, and author contributions. Then, the published article follows. Finally, Chapter 7.5 summarises the main problem, methodology, data, and key results.

Chapter abstract

Studies of Earth rotation variations generally assume that changes in non-tidal oceanic angular momentum (OAM) manifest the ocean's direct response to atmospheric forces. However, fluctuations in OAM may also arise from chaotic intrinsic ocean processes that originate in local non-linear (e.g., mesoscale) dynamics and can map into motions and mass variations at basin scales. To examine whether such random mass redistributions effectively excite polar motion, we compute monthly OAM anomalies from a 50-member ensemble of eddy-permitting global ocean/sea-ice simulations that sample intrinsic variability through a perturbation approach on model initial conditions. The resulting OAM (i.e., excitation) functions, $\hat{\chi}^{\mathrm{O}}$, are examined for their spread, spectral content, and role in the polar motion excitation budget from 1995 to 2015. We find that intrinsic $\hat{\chi}^{\mathrm{O}}$ signals are comparable in magnitude to the forced component at all resolved periods except the seasonal band, amounting to $\sim$46% of the total oceanic excitation (in terms of standard deviation) on interannual time scales. More than half of the variance in the intrinsic mass term contribution to $\hat{\chi}^{\mathrm{O}}$ is associated with a single, global mode of random bottom pressure variability, likely generated by non-linear dynamics in the Drake Passage. Comparisons of observed interannual polar motion excitation against the sum of known surficial mass redistribution effects are sensitive to the representation of intrinsic $\hat{\chi}^{\mathrm{O}}$ signals: Reductions in the observed excitation variance can be as high as 68%, or as low as 50% depending on the choice of the ensemble member. Chaotic oceanic excitation thus emerges as a new factor to consider when interpreting low-frequency polar motion changes in terms of core-mantle interactions or

employing forward-modelled OAM estimates for Earth rotation predictions[1].

Published manuscript

Börger, L., Schindelegger, M., Zhao, M., Ponte, R. M., Löcher, A., Uebbing, B., Molines, J.-M., & Penduff, T. (2025). Chaotic oceanic excitation of low-frequency polar motion variability *Earth System Dynamics*, 10, e2022EA002700. https://doi.org/10.5194/esd-16-75-2025

Data availability statement

All geophysical angular momentum estimates analysed in this study have been placed at https://doi.org/10.5281/zenodo.12664036 (Börger et al., 2024b).

Acknowledgements

Lara Börger and Michael Schindelegger were supported by the German Research Foundation (DFG, Project no. 459392861). Work at AER (Rui M. Ponte and Mengnan Zhao) was supported by NASA through GRACE Follow-On Science Team grants 80NSSC20K0728 and 80NSSC24K1154. The work from Bernd Uebbing has been funded by KI-FOR Algorithmic Data Analytics for Geodesy (AlgoForGe) by DFG, project number 459420781. The results of this research have been achieved using the PRACE Research Infrastructure resource CURIE based in France at TGCC. This work is a contribution to the OCCIPUT and IMHOTEP projects. OCCIPUT has been funded by ANR through contract ANR-13-BS06-0007-01. IMHOTEP is being funded by CNES through the Ocean Surface Topography Science Team (OSTST).

Copyright

[1]The article follows in a modified form (submitted version), where the nomenclature has been harmonised with the previous chapters. However, the content of the original published article is not modified.

Author contributions

The results presented in this thesis are the original work of the author, with contributions from the co-authors in the areas of conceptualization, planning, drafting, and revising the initial manuscript. Mengnan Zhao processed the OAM mass term using code originally written by me (Lara Börger) to reduce data transfer. Jean-Marc Molines provided barotropic velocity fields, and Anno Löcher supplied reconstructed gravity field coefficients, which I post-processed and provided to Bernd Uebbing for the computation of the fingerprints. I then used these fingerprints to compute the angular momentum associated with GAL.

Lara Börger: Data curation, Formal analysis, Investigation, Methodology, Software, Validation, Visualisation, Writing - original draft, Writing - review & editing. **Michael Schindelegger**: Conceptualisation, Formal analysis, Funding acquisition, Methodology, Supervision, Validation, Writing - original draft, Writing - review & editing. **Mengnan Zhao**: Data curation, Formal analysis, Writing - review & editing. **Rui M. Ponte**: Conceptualisation, Funding acquisition, Writing - review & editing. **Anno Löcher**: Formal analysis, Writing - review & editing. **Bernd Uebbing**: Formal analysis, Writing - review & editing. **Jean-Marc Molines**: Data curation, Writing - review & editing. **Thierry Penduff**: Funding acquisition, Writing - review & editing.

7.1. Introduction

Changes in ocean currents and the global distribution of ocean mass imply variability in OAM. Transfer of portions of this momentum to the solid Earth causes measurable fluctuations in the latter's rotation, comprising both changes in angular velocity and the movement of a conventional pole relative to Earth's crust–commonly referred to as wobble, or polar motion (Gross, 1992). Past studies (e.g., Ponte et al., 1998; Gross et al., 2003; Bizouard and Seoane, 2010; Harker et al., 2021; Afroosa et al., 2021; Börger et al., 2023) have shown that variability in non-tidal OAM is indeed a prominent source for wobble excitation on time scales from days to several years, modulating or even exceeding the rotational contributions of other geophysical fluids. An assumption in all of these works is that the path to accurate OAM estimates is to encode known physics in a numerical ocean model and integrate that very model in time under the necessary external (mostly atmospheric) forcings, either with or without data constraints. However, such an approach overlooks the possibility of a significant random component in the evolving ocean state, emerging internally within the fluid irrespective of atmospheric fluctuations. Evidently, any such intrinsic, chaotic variability would be inaccessible—or at least challenging to capture—with usual means of forward or inverse modelling.

A well-known example of the ocean's intrinsic variability is the non-linear, turbulent flow as manifested in mesoscale eddies. While these eddies operate at typical scales of O(10–100) km and O(10–100) days (Rhines, 2019), their kinetic energy is known to cascade toward much

larger spatial and longer temporal scales (e.g., Venaille et al., 2011; Arbic et al., 2014; Sérazin et al., 2018). In detail, ocean simulations performed in the eddying regime (at grid spacings $\leq 1/4\,^\circ$) have demonstrated that interactions between relatively short-lived mesoscale eddies and large-scale baroclinic instability can generate chaotic interannual to secular variability in regional sea level (e.g., Llovel et al., 2018; Carret et al., 2021), large-scale volume transports (Leroux et al., 2018; Cravatte et al., 2021), or the eddy field itself (Hogg et al., 2022). Moreover, the same simulations suggest that nonlinear dynamics feed random fluctuations in ocean mass between entire basins (Zhao et al., 2023). Given this large-scale chaotic imprint on dynamical variables, intriguing questions arise as to whether oceanic intrinsic variability also affects OAM and what such random variability potentially means for the interpretation of polar motion observations.

We address these open questions using output from a $1/4\,^\circ$ large-ensemble ocean hindcast experiment, as analysed in numerous previous studies of oceanic chaos and its inverse cascades (e.g., Leroux et al., 2018; Sérazin et al., 2018; Cravatte et al., 2021; Hogg et al., 2022). Similar to ensemble methods in climate science (e.g., Maher et al., 2021), the member simulations are generated from a single model under identical external forcing but perturbed initial conditions, allowing one to disentangle intrinsic from forced (i.e., atmosphere-driven) variability. Focus is lain on the period from 1995 to 2015 and particularly the interannual band, where oceanic effects are a leading cause for wobble excitation, along with continental hydrology (Gross et al., 2003; Wińska, 2022; Börger et al., 2023). We separate the ensemble OAM estimates into forced and intrinsic components and assess their contributions to the observed wobble excitation in the presence of mass change and motion elsewhere in the Earth system. This, in turn, calls for a consideration of all known climatic excitations of polar motion, as described below.

7.2. Methods

7.2.1. Basic framework and data

The “geodetic" (or observed) excitation of polar motion is labelled as $\hat{\chi}^*$ throughout this work. We specifically use rotation data from the daily-sampled SPACE2018 series (Ratcliff and Gross, 2019) that employs a Kalman filter to adjust measurements from the primary space-geodetic techniques. We remove long-period tidal effects in polar motion using the conventional model of Petit and Luzum (2010), deconvolve $\hat{p}$, and finally average the daily $\hat{\chi}^*$ values to monthly estimates.

In comparisons with $\hat{\chi}^*$, we consider excitations from four main climate system components, comprising the atmosphere (denoted to as $\hat{\chi}^{\mathrm{A}}$), the ocean ($\hat{\chi}^{\mathrm{O}}$), the continental hydrosphere ($\hat{\chi}^{\mathrm{H}}$), and the cryosphere as represented by the Greenland and Antarctica ice sheets ($\hat{\chi}^{\mathrm{C}}$). The satellite data underlying $\hat{\chi}^{\mathrm{H}}$ and $\hat{\chi}^{\mathrm{C}}$, along with the ensemble approach to oceanic excitation (Chapter 7.2.2) constrain us to have monthly sampling. For consistency with the ocean model

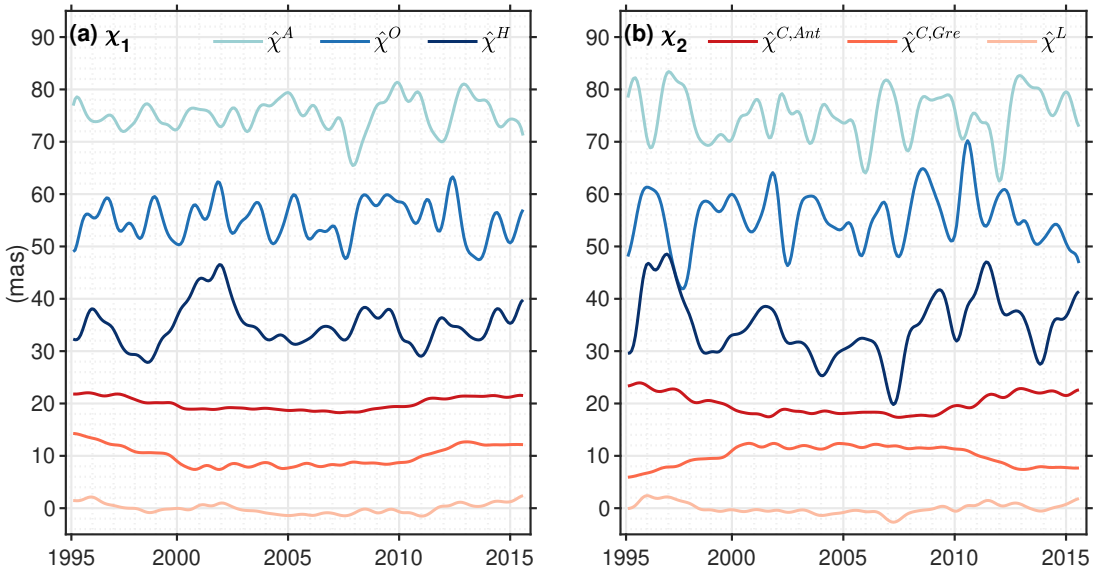

Figure 7.1: Modeled excitation $\hat{\chi} = \chi_1 + \mathrm{i}\chi_2$ of interannual polar motion (in milliarceseconds), from 1995 through 2015, separated into contributions from atmosphere ($\hat{\chi}^{\mathrm{A}}$, light blue), ocean ($\hat{\chi}^{\mathrm{O}}$, blue), terrestrial hydrology ($\hat{\chi}^{\mathrm{H}}$, dark blue), the Antarctic Ice Sheet ($\hat{\chi}^{\mathrm{C,Ant}}$, red), the Greenland Ice Sheet ($\hat{\chi}^{\mathrm{C,Gre}}$, orange), and gravitational attraction and loading ($\hat{\chi}^{\mathrm{L}}$, creme). Interannual signals were obtained by removing each time series' trend and seasonality and low-pass filtering the residual series with a cutoff period of 14 months. Four months were clipped both at the beginning and at the end of the time series to avoid filter artefacts. The $\hat{\chi}^{\mathrm{O}}$ estimate is from an arbitrary OCCIPUT ensemble member. For traceability, we compare our estimates of $\hat{\chi}^{\mathrm{H}}$, both unfiltered and low-pass filtered, with GRACE-only $\hat{\chi}^{\mathrm{H}}$ time series in the Supplement (Figs. S1 and S2).

output analysed here, we use atmospheric angular momentum time series from the ERA-Interim reanalysis of the European Centre for Medium-Range Weather Forecasts (Dee et al., 2011). The $\hat{\chi}^{\mathrm{A}}$ series is an extension of a previous calculation by us (Schindelegger et al., 2013b) and accounts for excitation signals associated with the ocean's inverted barometer (IB) response to atmospheric pressure loading. Figure 7.1 shows that on interannual time scales (here periods $\geq$ 14 months[2]), the atmosphere is somewhat less effective than the ocean in exciting Earth's wobbles, particularly through χ_1 (cf. Gross et al., 2003). Peak-to-peak amplitudes in χ_2^{A} occasionally attain 15 mas and are largely governed by mass redistribution over Northern hemisphere landmasses (Nastula and Salstein, 1999).

Contributions to $\hat{\chi}^{\mathrm{m}}$ from continental hydrology—or equivalently, TWS—and the cryosphere are deduced from time-variable gravity fields, as practiced in previous works (e.g., Chen et al., 2013a; Adhikari and Ivins, 2016; Nastula et al., 2019; Göttl et al., 2021). To cover the same 21-year period (1995–2015) as for our oceanic excitation series, we use a long-term reconstruction of monthly gravity fields based on satellite tracking data (Löcher and Kusche, 2021, updated version). The approach pursued for this reconstruction is to expand surface mass changes from the GRACE/-FO (Tapley et al., 2019) mission into EOFs and use the leading EOFs as basis

[2]This cutoff period was chosen to effectively suppress the seasonal components in the excitation time series. For studying the excitation of the Chandler wobble at $T_{\mathrm{c}} = 433.0$ days, which is not attempted here, a different approach to analysis would be required (see Gross, 2000).

functions for gravity field modelling in the processing of the tracking observations. The solution has no temporal gaps and preserves the spatial resolution of GRACE/-FO gravity fields (i.e., wavelengths of ∼300 km) also for times prior to GRACE. We synthesise the monthly varying Stokes coefficients as equivalent water heights across Earth's surface, mask out the ocean, and partition the mass anomalies into changes over the Greenland Ice Sheet, the Antarctic Ice Sheet, and land. Spatial leakage effects near continental boundaries and ice sheet margins are mitigated using an iterative forward modelling algorithm (Chen et al., 2015); see Appendix 7.4 for details. Figure 7.1 illustrates that hydrological mass changes drive large (∼10–15 mas) interannual to intradecadal variations in polar motion excitation (Adhikari and Ivins, 2016; Meyrath and van Dam, 2016). De-trended time series for cryospheric sources ($\hat{\chi}^{\mathrm{C}}$) reveal residual long-term drifts that bear on the accelerated melting of polar ice sheets (Chen et al., 2013a; Deng et al., 2021).

In addition to $\hat{\chi}^{\mathrm{A,O,H,C}}$, we account for non-uniform mass changes in the ocean due to gravitational attraction and loading (GAL), defining the excitation function $\hat{\chi}^{\mathrm{L}}$. Processes described by GAL are the continent-ocean net mass transfer, the gravitational attraction of water toward mass anomalies anywhere in the Earth system, the crustal deformation under these loads, and the ensuing changes in Earth's gravitational field (e.g., Clarke et al., 2005). The surface mass variations arising from these effects are long-wavelength in nature, leading to small but non-negligible angular momentum changes (Quinn et al., 2015; Adhikari and Ivins, 2016, Fig. 7.1). We calculate the GAL effects on ocean mass and distribution by solving the sea level equation (Farrell and Clark, 1976), assuming elastic (i.e., instantaneous) deformation of a rotating Earth and a purely static adjustment in the ocean. The considered loads are gridded monthly anomalies of TWS, cryospheric mass, and IB-corrected atmospheric pressure, taken from the same sources as those adopted for our $\hat{\chi}^{\mathrm{A,H,C}}$ estimates; see Appendix 7.4.

7.2.2. Oceanic excitation

We study the externally forced and chaotic intrinsic components of oceanic excitation based on a 50-member ensemble of eddy-permitting ocean/sea ice simulations from the OCCIPUT project (Penduff et al., 2014). The OCCIPUT large ensemble was generated using a global $^1/_4\,^\circ$ tri-polar grid setup of the NEMO engine for Boussinesq ocean dynamics and thermodynamics. The full ensemble hindcast spans 56 years (1960–2015). Following a common 21-year spin-up simulation, a small stochastic perturbation was applied in the density equation of each member throughout the year 1960 (Brankart et al., 2015), triggering the dispersion of the individual simulations and subsequent saturation of the ensemble spread (which occurs more quickly in turbulent, eddy-rich areas, Penduff et al., 2014; Bessières et al., 2017). These 50 realisations of the time-evolving ocean state were then integrated forward from their respective, slightly perturbed initial conditions and driven by the same 6-hourly atmospheric data from the DRAKKAR forcing set DFS 5.2 (Dussin et al., 2016), which itself is based on ERA-Interim. As the ensemble members are identical in terms of the numerical model, boundary conditions, and atmospheric forcing, their spread can be solely attributed to non-linear ocean dynamics. Note also that the existence, origin,

and spatio-temporal scales of this intrinsic variability is consistent across eddy-permitting and eddy-resolving ocean models (e.g., Sérazin et al., 2015).

To keep the involved data volumes manageable, we analyse the OCCIPUT ensemble output from 1995 to 2015 (cf. Zhao et al., 2021) and focus on monthly mean values. Specifically, we evaluate the mass and motion terms of $\hat{\chi}^{\mathrm{O}}$ (see Chapter 2.5.2 or Appendix A of the original published paper) from monthly averages of ocean bottom pressure, $p_{\mathrm{b}} = p_{\mathrm{b}}(\mathbf{x}, t)$, and vertically-averaged northward and eastward currents, $\overline{u}(\mathbf{x}, t)$ and $\overline{v}(\mathbf{x}, t)$, where $\mathbf{x}$ represents horizontal space. Each of the three variables $\xi(\mathbf{x}, t) \in (p_{\mathrm{b}}, \overline{u}, \overline{v})$ consists of externally forced and intrinsic signals, i.e.,

$$\xi(\mathbf{x}, t, \mu) = \xi^{\mathrm{f}}(\mathbf{x}, t) + \xi^{\mathrm{i}}(\mathbf{x}, t, \mu), \tag{7.1}$$

where μ is a running index over the 50 ensemble members, superscript f indicates the forced variability common to all members, and i identifies the intrinsic signal. As in previous studies (see in particular Hogg et al., 2022), we estimate the forced component at a given month and location by the ensemble mean $\xi^{\mathrm{f}}(\mathbf{x}, t) = \langle \xi(\mathbf{x}, t, \mu) \rangle$, adopting $\langle \cdot \rangle$ as the ensemble-mean operator. Upon separating signals as per Eq. (7.1), we compute angular momentum time series (Chapter 2.5.2, Appendix A in the original published paper) for forced and intrinsic contributions to $(p_{\mathrm{b}}, \overline{u}, \overline{v})$, as well as for their sum. Hence, intrinsic variability in oceanic excitation (abbreviated as $\hat{\chi}^{\mathrm{O,i}}$) is distinguished from forced variability ($\hat{\chi}^{\mathrm{O,f}}$) at the level of spatially distributed dynamical variables, and not based on excitation time series.

Throughout this work, p_{b} denotes ocean bottom pressure anomalies, obtained by removing for each ensemble member a common time-mean reference pressure field and a spatial mean p_{b} value per month and ensemble member. The latter correction prevents small biases or drifts in $\hat{\chi}^{\mathrm{O}}$ caused by spurious global ocean mass changes in OCCIPUT under the Boussinesq approximation. Legitimate contributions to the globally averaged p_{b}, which would be removed by the correction, pertain to the freshwater flux into the ocean from atmospheric and continental sources. However, this term is accounted for through the framework of GAL, and thus in $\hat{\chi}^{\mathrm{L}}$. Note that the OCCIPUT simulations do not consider static effects, such as long-period tides or the pole tide, and thus these phenomena are absent from $\hat{\chi}^{\mathrm{O,f}}$.

7.3. Results and discussion

7.3.1. Overview in spectral domain

A natural first step is to assess the magnitude and importance of the intrinsic oceanic excitation in relation to the externally forced component across a range of frequencies. In Figs. 7.2 and 7.3, we

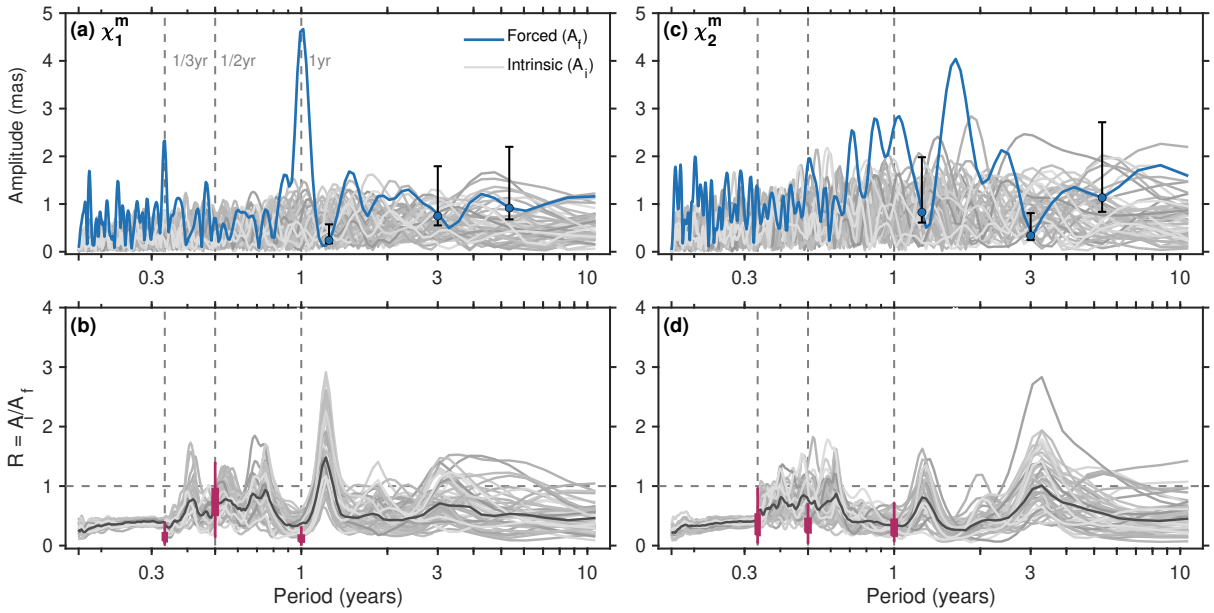

Figure 7.2: Spectral representation of the OCCIPUT-based estimates of intrinsic and forced oceanic excitation of polar motion, 1995–2015. Shown are amplitudes A_i and A_f (in milliarcseconds) of the intrinsic and forced oceanic mass term, $\hat{\chi}^\mathrm{m}$, in (a) χ_1 and (c) χ_2, deduced from a 512-point Fast Fourier Transform using Welch's method (Welch, P., 1967). Black vertical bars indicate 68% confidence limits for selected frequencies. Panels (b, d) illustrate spectrally smoothed versions of the chaotic amplitude fraction $R = A_\mathrm{i}/A_\mathrm{f}$ (dimensionless), estimated from the excitation time series with seasonal terms removed. Black solid lines mark the respective median across the 50 realisations of R. Statistics for the annual, semiannual, and terannual terms—computed separately based on seasonal cycle fits to $\hat{\chi}^{\mathrm{O,i}}$ and $\hat{\chi}^{\mathrm{O,f}}$—are summarized by the purple whiskers; box edges indicate the 25th and 75th percentiles and vertical bars extend to the minimum/maximum values of seasonal R.

show amplitude spectra (symbol A) for $\hat{\chi}^{\mathrm{O,i}}$ (50 realizations) and $\hat{\chi}^{\mathrm{O,f}}$ (1 realization), separated into mass and motion terms and the two coordinate directions. For comparison purposes, we form chaotic amplitude fractions, $R = A_\mathrm{i}/A_\mathrm{f}$, representing the ratio of intrinsic over forced amplitude per frequency (not to be mixed up with time-invariant fractions of variance considered in previous OCCIPUT analyses, e.g., Carret et al., 2021; Hogg et al., 2022). Values of R are computed separately for (a) annual, semiannual, and terannual harmonics extracted from $\hat{\chi}^{\mathrm{O,i}}$ and $\hat{\chi}^{\mathrm{O,f}}$, and (b) the deseasonalized excitation functions. We smooth the estimated fractions under (b) using a moving window, with window sizes decreasing (essentially linearly) from 21 frequency bins at the high end of the spectrum to 1 bin at the longest period.

As apparent from Figs. 7.2 and 7.3 (panels a/c), the intrinsic oceanic excitation is embedded in a relatively flat spectrum, bounded by amplitudes of ∼1.5–2.0 mas in the mass term and ∼0.7–1.0 mas in the motion term. This spectral characteristic renders the chaotic excitation comparable in magnitude to the forced variability at most, but not all frequencies. Notable exceptions occur in χ_2^v and wherever $\hat{\chi}^{\mathrm{O,f}}$ features peaks in seasonality. Values of R are close to 0.15 for the dominant (∼3.5 mas) annual harmonic in both χ_1^v and χ_2^v, along with similarly small fractions at periods of 1 and 1/3 yr in χ_1^m. We can tentatively interpret the results for χ_1^m in terms of intrinsic-vs-forced ratios of p_b signals from previous OCCIPUT analyses (Zhao et al., 2021). In particular, Fig. 3

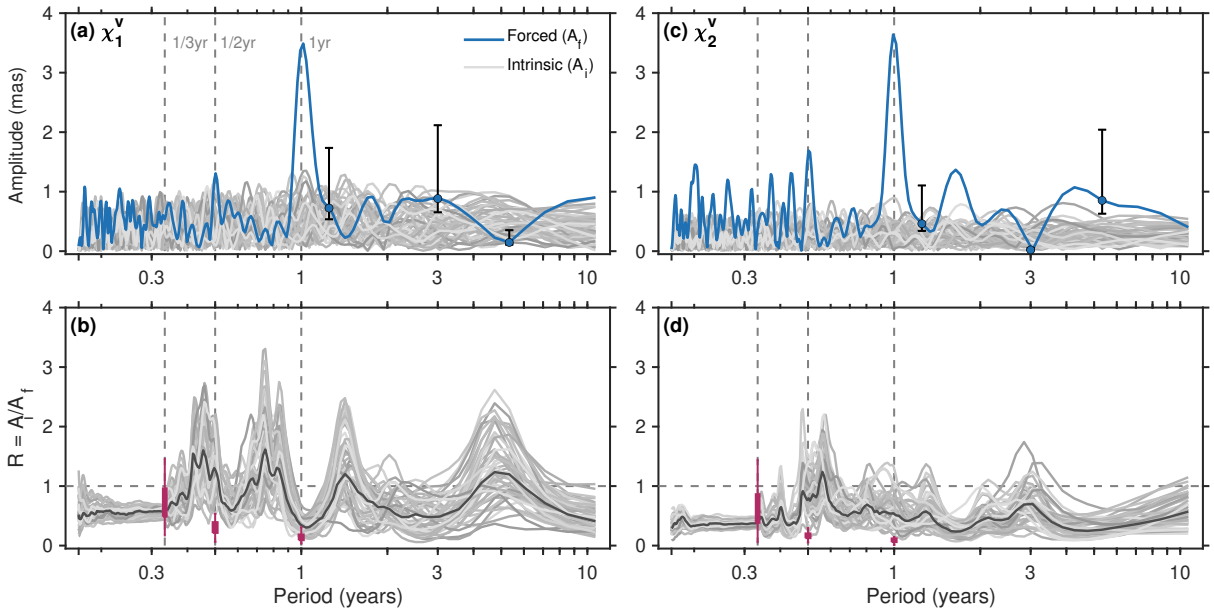

Figure 7.3: As in Fig. 7.2 but for the two components of the motion term $\hat{\chi}^{\mathrm{v}}$.

of Zhao et al. (2021) places large intrinsic contributions to the seasonal p_{b} cycle over western boundary currents and the eddying Southern Ocean, with little sign of long-wavelength effects that would drive strong variability in $\hat{\chi}^{\mathrm{O,i}}$.

Switching from seasonal harmonics to the broadband spectral behaviour in Figs. 7.2 and 7.3, we observe a gradual increase in the chaotic amplitude fraction from ∼0.3 to ∼0.6 as periods lengthen from 60 to 120 days. This is followed at intraannual frequencies by somewhat of a plateau of the median R near 0.9 in the mass term, along with a broadening of the ensemble spread to $R \approx 0.3$–2.0 in all OAM components. The prominence of $\hat{\chi}^{\mathrm{O,i}}$ at these periods (roughly 120 to 300 days) coincides with the dominant time scale for emergence of mesoscale eddies (Chelton et al., 2011) and the ensuing nonlinear inverse cascades (e.g., Arbic et al., 2014; O'Rourke et al., 2018; Sérazin et al., 2018). Concurrently, the forced oceanic excitation is relatively weak at intraannual periods (especially in χ_1^{O}, Figs. 7.2a and 7.3a), making this specific band another attractive (future) target for exploring the polar motion imprint of oceanic chaos. We note, though, that the intraannual wobble excitation is largely dominated by atmospheric mass redistribution effects (Gross et al., 2003).

For the interannual signals central to this work, the spectral representations in Figs. 7.2 and 7.3 indicate appreciable power in $\hat{\chi}^{\mathrm{O,i}}$ relative to $\hat{\chi}^{\mathrm{O,f}}$, even at sub-decadal periods and particularly in χ_1^{O}. Some low-frequency, intrinsic oceanic process must thus be at work at scales large enough to perturb the globally integrated OAM quantities (see Chapter 7.3.2). More specific to Figs. 7.2 and 7.3, we observe a number troughs in the forced amplitude A_{f} that in turn afford peaks in the chaotic amplitude fractions. Such maxima in R are seen, for example, for periods $T \approx 1.2$–1.3 years in all four $\hat{\chi}^{\mathrm{O}}$ components or near 3 years in the two mass terms (spectral uncertainty is generally large, though). By contrast, the forced component exceeds the intrinsic amplitude by a factor of about two at $T \approx 1.6$ years in both mass and motion terms of χ_2^{O}. One can therefore expect any time series of interannual χ_2^{O} signals to feature stronger deterministic variability than

χ_1^{O}.

For a condensed view of Figs. 7.2 and 7.3, we have additionally formed ratios between intrinsic and forced standard deviations, i.e., $\sigma_{\mathrm{i}}/\sigma_{\mathrm{f}}$, calculated from $\hat{\chi}^{\mathrm{O,i}}$ and $\hat{\chi}^{\mathrm{O,f}}$ time series. Summing up mass and motion terms, and filtering the participating time series to periods $\geq$ 14 months, we obtain $\sigma_{\mathrm{i}}/\sigma_{\mathrm{f}}$ values of 0.50–0.83 (median 0.69) for χ_1^{O} and 0.28–0.50 (median 0.36) for χ_2^{O}. Similar calculations for the complex-valued quantity $\hat{\chi}^{\mathrm{O}}$ yield $\sigma_{\mathrm{i}}/\sigma_{\mathrm{f}}$ ratios in the range of 0.38–0.60 and a median at 0.47. When taking σ_{i} relative to the variability of the total oceanic excitation, the median is 0.46 in the case of $\hat{\chi}^{\mathrm{O}}$ (range 0.43–0.50). These numbers emphasise the importance of chaotic contributions to equatorial OAM changes on time scales much longer than typically associated with the life cycles of mesoscale eddies.

7.3.2. Modal decomposition

Analysis of the space-time variability in modelled intrinsic p_{b} fields—denoted as $p_{\mathrm{b}}^{\mathrm{i}}$—can reveal more about the provenance of the chaotic OAM signals apparent in Figs. 7.2 and 7.3. Following Zhao et al. (2023), we have decomposed each of the 50 realisations of $p_{\mathrm{b}}^{\mathrm{i}}$ into real-valued EOFs patterns and the associated principal components. We find a common leading EOF (mode 1 hereafter), accounting for 16% to 22% of the global $p_{\mathrm{b}}^{\mathrm{i}}$ variance. This particular mode, displayed exemplarily for one ensemble member in Fig. 7.4a, exhibits a distinct global structure, characterised by covariability across the Atlantic, the Arctic, and partly the Indian Ocean, while much of the Southern Ocean oscillates with opposite sign. The suggested origin for this mode lies in Drake Passage (Zhao et al., 2023). Here, strong eddies and random current fluctuations, possibly involving interaction with topography (Provost et al., 2011), are thought to induce sharp bottom pressure gradients, evident in Fig. 7.4a between Cape Horn and the South Shetland Islands. The basin-wide $p_{\mathrm{b}}^{\mathrm{i}}$ anomalies seen elsewhere in the ocean would then be the result of fast barotropic adjustment to these local gradients along H/f contours (Zhao et al., 2023, where H is the local water depth, and f is the Coriolis parameter).

The described processes, while of different nature than the nonlinear inverse energy cascades noted in Chapter 7.1, are unique in that they produce a global pattern of mass redistribution with opposite polarity between ocean basins. Such large-scale see-saws of mass have been previously shown to be an effective source of polar motion excitation; cf., e.g., Afroosa et al. (2021). We have thus synthesised monthly $p_{\mathrm{b}}^{\mathrm{i}}$ grids from mode 1 alone and deduced the corresponding oceanic excitation (that is, the oceanic mass term, Chapter 2.5.2, Appendix A in the original published paper). The so-derived estimates of $\hat{\chi}^{\mathrm{O,i}}$ are compared in Table 7.1 against the full $\hat{\chi}^{\mathrm{O,i}}$ functions from OCCIPUT in terms of the PVE. This simple evaluation demonstrates that mode 1 is indeed the leading driver for the mass component of intrinsic oceanic excitation, across time scales and for both χ_1 and χ_2. Specifically, at the interannual periods of interest in this work, the OAM changes associated with $p_{\mathrm{b}}^{\mathrm{i}}$ mode 1 explain 39% to 97% of the variance in the $\hat{\chi}^{\mathrm{O,i}}$ mass term, with a median PVE of 63% across the 50 ensemble members. These numbers encapsulate

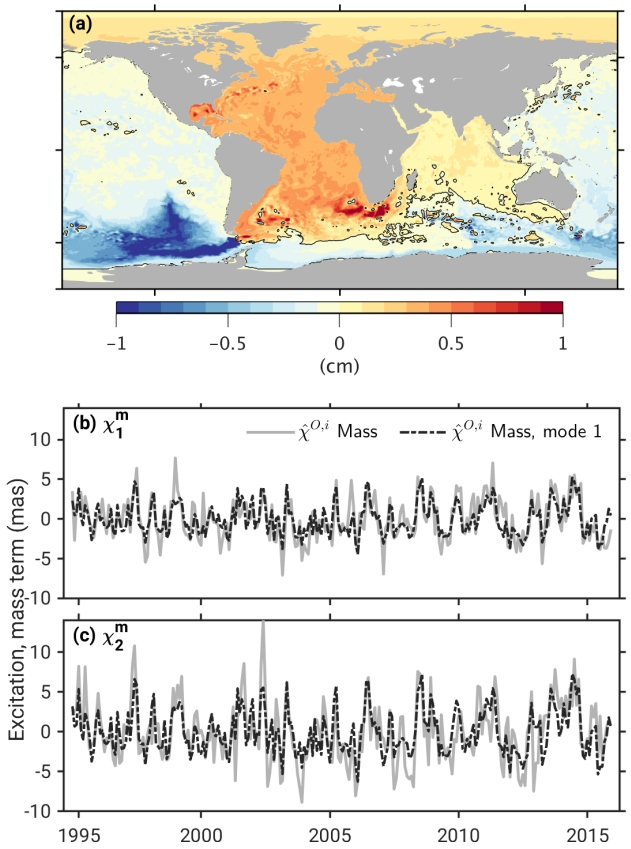

Figure 7.4: Attribution of the mass term of $\hat{\chi}^{\mathrm{O,i}}$ to global-scale intrinsic bottom pressure variability, $p_{\mathrm{b}}^{\mathrm{i}}$. Shown is (a) the leading EOF mode of $p_{\mathrm{b}}^{\mathrm{i}}$ variability (in centimetre) for ensemble member 47, and (b, c) the corresponding equatorial oceanic excitation signal (dashed black curve), obtained from synthesising mode 1 in time and space and computing the associated OAM time series. The full intrinsic oceanic excitation, derived from $p_{\mathrm{b}}^{\mathrm{i}}$ without modal partitioning, is plotted in grey. We selected member 47 for this comparison as its statistics in Table 7.1 are close to the median percentage of variance explained by mode 1 in $\hat{\chi}^{\mathrm{O,i}}$. Note that other ensemble members suggest a mode 1 structure very similar to the one shown in panel (a); see also Zhao et al. (2023).

the idea that localised mesoscale processes somewhere in the world ocean govern variability in a truly global and geophysically relevant quantity.

7.3.3. Interannual variability

We now examine the role of oceanic chaos in the low-frequency equatorial excitation budget over 1995–2015. To that end, Fig. 7.5 shows the residual geodetic excitation, obtained by subtracting from $\hat{\chi}^{*}$ modelled contributions from the atmosphere, terrestrial hydrology, the two ice sheets, and GAL; cf. the respective time series in Fig. 7.1. Together, these non-oceanic sources account for 29.7% of the variance in the full equatorial geodetic excitation (Table 7.2), governed in large parts by the PVE in χ_1 (51.6%). The residual is to be compared with 51 variants of oceanic excitation from OCCIPUT, comprising both the forced component ($\hat{\chi}^{\mathrm{O,f}}$) and 50 realizations of $\hat{\chi}^{\mathrm{O}}$ (i.e., $\hat{\chi}^{\mathrm{O,f}} + \hat{\chi}^{\mathrm{O,i}}$). Intrinsic processes clearly add extra variability to estimates of $\hat{\chi}^{\mathrm{O}}$ relative to $\hat{\chi}^{\mathrm{O,f}}$, as conveyed by an ensemble spread of nearly ± 5 mas throughout the analysis period. This

Table 7.1: Contribution of mode 1 $p_{\mathrm{b}}^{\mathrm{i}}$ variability to the intrinsic component of the oceanic mass term, 1995–2015[a]

	χ_1	χ_2	$\hat{\chi} = \chi_1 + \mathrm{i}\chi_2$
PVE in $\chi_j^{\mathrm{O,i}}$ by EOF mode 1			
min	38.4	35.0	40.4
median	56.6	49.6	52.3
max	97.4	97.9	97.7
PVE in low-frequency $\chi_j^{\mathrm{O,i}}$ by EOF mode 1[b]			
min	35.6	28.3	39.0
median	67.8	63.9	63.3
max	96.7	97.1	96.8

[a]Values are Percentage of Variance Explained (PVE) by a monthly-varying $\hat{\chi}^{\mathrm{O,i}}$ mass term computed from mode 1 vs. the full intrinsic mass term. Subscript j is used to discriminate between χ_1, χ_2, and $\hat{\chi}$.
[b]Participating time series filtered to periods ≥ 14 months.

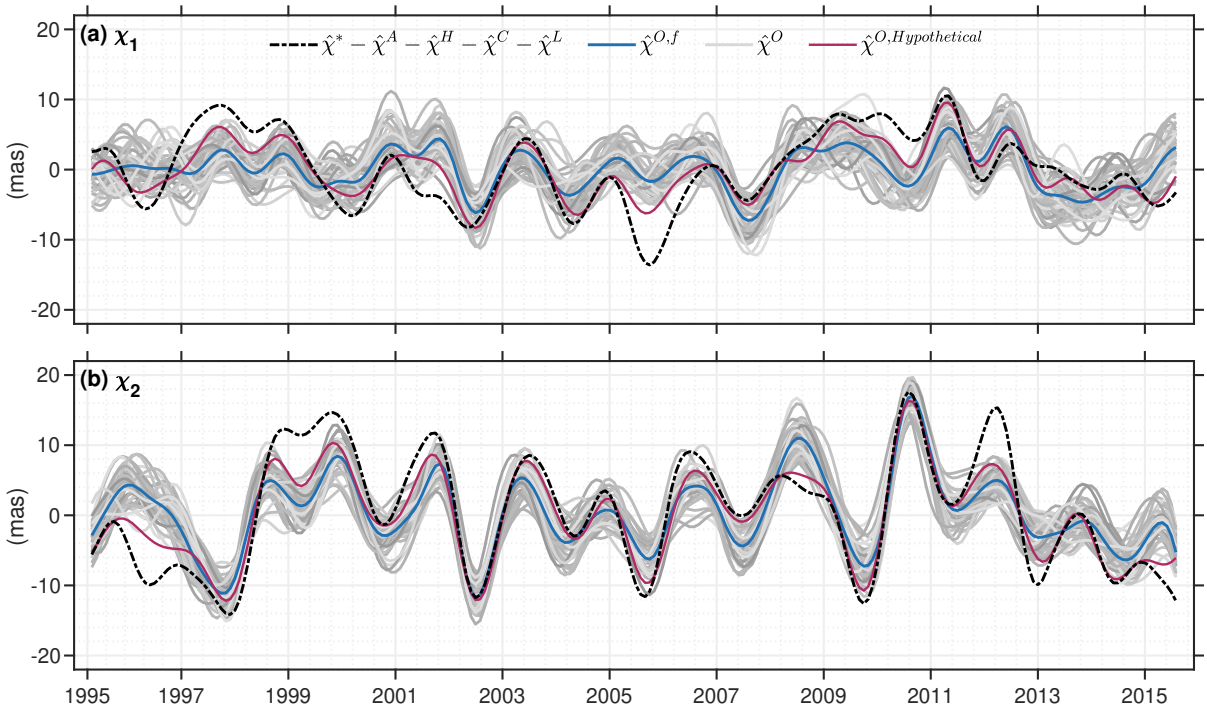

Figure 7.5: The low-frequency polar motion excitation budget from 1995 to 2015 in the presence of oceanic chaos. Shown are (as dashed black lines) the (a) χ_1 and (b) χ_2 components of geodetic excitation ($\hat{\chi}^*$)—corrected for contributions from the atmosphere ($\hat{\chi}^{\mathrm{A}}$), terrestrial hydrology ($\hat{\chi}^{\mathrm{H}}$), ice sheets ($\hat{\chi}^{\mathrm{C}}$), and GAL ($\hat{\chi}^{\mathrm{L}}$)—compared with 50 estimates of oceanic excitation from OCCIPUT ($\hat{\chi}^{\mathrm{O}}$, gray curves), the OCCIPUT ensemble mean ($\hat{\chi}^{\mathrm{O,f}}$, blue curve), and a hypothetical ensemble member (purple curve) producing the best match with the corrected geodetic excitation. All time series have been detrended, filtered to periods $T \geq 14$ months, and cut back by 4 months at the two endpoints.

is an important result that implies some leeway in how to evaluate and interpret the observed excitation of Earth's wobbles on interannual time scales.

Table 7.2: Observed vs. modelled excitation of interannual polar motion, 1995–2015[a,b]

	χ_1	χ_2	$\hat{\chi} = \chi_1 + \mathrm{i}\chi_2$
RMS of χ_j^*	7.5	8.6	11.4
PVE in χ_j^* by non-oceanic sources			
$\chi_j^{\mathrm{A}} + \chi_j^{\mathrm{H}} + \chi_j^{\mathrm{C}} + \chi_j^{\mathrm{L}}$	51.6 (5.2)	13.3 (8.0)	29.7 (9.6)
PVE in χ_j^* by OCCIPUT, χ_j^{O}			
Forced	18.5 (6.8)	35.4 (6.9)	28.2 (9.7)
Ensemble members	[−17.5–27.4] ([6.4–8.1])	[10.2–44.7] ([6.4–8.2])	[5.3–34.2] ([9.3–11.1])
PVE by OCCIPUT χ_j^{O} in residual series $\chi_j^* - \chi_j^{\mathrm{A}} - \chi_j^{\mathrm{H}} - \chi_j^{\mathrm{C}} - \chi_j^{\mathrm{L}}$			
Forced	23.9 (4.5)	62.1 (5.0)	50.8 (6.7)
Ensemble members	[−24.4–35.1] ([4.2–5.8])	[44.8–64.6] ([4.8–6.0])	[29.1–53.7] ([6.5–8.1])
Hypothetical member[c]	77.4 (2.5)	87.4 (2.9)	84.0 (3.8)
PVE in χ_j^* by sum of excitation processes $\chi_j^{\mathrm{A}} + \chi_j^{\mathrm{O}} + \chi_j^{\mathrm{H}} + \chi_j^{\mathrm{C}} + \chi_j^{\mathrm{L}}$			
Forced	63.1	67.1	65.4
Ensemble members	[39.8–68.6]	[52.1–69.3]	[50.2–67.5]
Hypothetical member[c]	89.0	89.1	89.0

[a]Values are Percentage of Variance Explained (PVE) and the corresponding RMS of residuals (milliarcseconds) in parentheses, except for the first line. Entries for ensemble members apply to the sum of the forced and intrinsic signals. All time series have been detrended and filtered to periods $T \geq 14$ months. Subscript j in the intermediate headers is used to discriminate between χ_1, χ_2, and $\hat{\chi}$.

[b]Replacing the SPACE2018 series in the analysis by other, more recent Earth rotation determinations changes the tabulated PVE values by 0.2% at most.

[c]Hypothetical member drawn from the $\hat{\chi}^{\mathrm{O}}$ ensemble based on a constraint of minimum distance to the residual observed excitation, see the main text.

Adopting the forced component from OCCIPUT as a middle ground for an estimate of $\hat{\chi}^{\mathrm{O}}$ reduces the RMS of the residual equatorial geodetic excitation from 9.6 mas to 6.7 mas ($\mathrm{PVE} = 50.8\%$). Similarly, we can select from any of the 50 ensemble members as valid representations of the time-evolving ocean state and thus $\hat{\chi}^{\mathrm{O}}$. This approach to evaluation leads to a considerable spread in the statistics in Table 7.2, involving a few ensemble members that exhibit slightly better skill than the forced component (minimum $\hat{\chi}$ RMS of 6.5 mas, $\mathrm{PVE} = 53.7\%$), but also a number of cases that reduce little variance (only 1.5 mas in RMS) of the residual geodetic excitation. A total of 15 members even yield negative PVE values in χ_1. However, these statistics are not to be taken to define absolute bounds on the efficacy of OAM in exciting low-frequency polar motion, as the intrinsic variability in any of the ensemble members is merely a random realisation of the potential intrinsic variability in the real world. In fact, oceanic chaos may act to produce yet other time series of $\hat{\chi}^{\mathrm{O}}$ that are also consistently close to the residual geodetic excitation, while still lying within the ensemble spread in Fig. 7.5.

We have constructed such a hypothetical—but still legitimate—equatorial OAM function by identifying, month per month and in the complex plane, the particular OCCIPUT $\hat{\chi}^{\mathrm{O}}$ sample closest to the reduced observation (i.e., $\hat{\chi}^*$ minus non-oceanic sources). As one switches from one low-pass filtered member to the other, small jumps are incurred, requiring an additional round of smoothing to periods ≥ 14 months. As per design, the resulting time series follow the residual geodetic excitation more tightly than $\hat{\chi}^{\mathrm{O,f}}$ or any of the ensemble members (Fig. 7.5). The improved correspondence is also reflected in the PVE by the hypothetical $\hat{\chi}^{\mathrm{O}}$ (84.0% of the

reduced geodetic excitation), leaving only 3.8 mas of interannual RMS variability unexplained. Likewise, using the hypothetical member instead of the ensemble mean in evaluating the sum of all geophysical fluid excitations against $\hat{\chi}^*$ increases the PVE from 65.4% to 89.0%. For comparison, selecting from the original OCCIPUT members to form the total surface layer excitation yields PVE values from 50.2% to 67.5%. Overall, these statistics illustrate the sensitivity of such budget analysis to the representation of chaotic OAM signals.

As evident from Fig. 7.5, the 3.8 mas RMS signal unaccounted for in the observations is mostly made up by discrepancies between geodetic and geophysical excitations before early 2002 (i.e., the launch of GRACE), large differences throughout the year 2005 in χ_1 (to a lesser extent also 2009/2010), and a $\sim$7 mas cusp around the turn of 2011/2012 in χ_2. It is possible that part of the discrepancies arise from errors in OCCIPUT, related to, e.g., imperfectly modelled energetic circulations in the Southern Ocean (Ponte and Piecuch, 2014; Harker et al., 2021). A more likely source, though, are residual errors in the adopted gravity fields that project onto the interannual excitation budget, particularly through TWS changes and the associated fluctuations in $\hat{\chi}^{\mathrm{H}}$. Comparing our hydrological time series in Fig. 7.1 with GRACE-only estimates of $\hat{\chi}^{\mathrm{H}}$ in Fig. S2 in the Supplement does indeed point to differences over some of the afore-mentioned periods (2009/2010 in χ_1, 2011/2012 in χ_2). It therefore appears that the specifics of the gravity field reconstruction—including the limited spectral sensitivity of the involved satellites and the temporal parameterisation in terms of GRACE/-FO EOFs (Löcher and Kusche, 2021)—occasionally compromise the accuracy of the derived hydrological angular momentum changes. More detailed exploration of these factors is left for future studies.

Although the geophysical models and data used in this study are necessarily imperfect, it is worth inspecting the excitation budget from yet another angle. In Fig. 7.6 we show amplitude spectra for the two components of $\hat{\chi}^*$ minus all climate system-related excitations, including for present purposes also the forced oceanic component ($\hat{\chi}^{\mathrm{O,f}}$). Spectral power in these residuals—while not well resolved within our 21-year analysis window—may be due the said errors in the adopted angular momentum series. Alternatively, residual power may point to secondary excitation processes left out of the considerations and coming from, e.g., the Earth's core (Chen et al., 2019; Ding et al., 2019; Kuang et al., 2019). Inferences along the latter lines are however complicated by the difficulty in accounting for the intrinsic component of oceanic excitation, $\hat{\chi}^{\mathrm{O,i}}$, as expressed by the gray background spectra in Fig. 7.6. In detail, the OCCIPUT ensemble suggests a likelihood for $\hat{\chi}^{\mathrm{O,i}}$ to attain amplitudes between 0 and 1.5 mas across all interannual and sub-decadal frequencies; cf. also Figs. 7.2 and 7.3. Selecting always the most energetic ensemble member at each frequency (blue lines in Fig. 7.6) raises the upper bound for intrinsic effects even further, to about 2 mas.

A 1.0–1.5 mas uncertainty in modelled wobble excitation due to oceanic chaos is generally comparable in size to the residual geodetic excitation across most frequencies (black dashed curves in Fig. 7.6). This prompts the question as to what extent it is possible to conclusively link such residuals to the dynamics of Earth's deep interior. For instance, Chen et al. (2019) suggested that a $\sim$2 mas oscillation with a period of $T = 5.9$ yrs—left after correcting the observed excitation

over 1962–2018 for modeled atmospheric, oceanic, and hydrological effects—may be caused by the exchange of equatorial angular momentum between the outer core and the mantle via the electromagnetic torque (Kuang et al., 2019). However, analyses of satellite-derived degree-2 Stokes coefficients (Rosat et al., 2021) fail to support this idea, while our Fig. 7.6 illustrates that a considerable portion of any interannual $\hat{\chi}^*$ residual may simply be due to mis-modelled oceanic effects. Furthermore, the possibility of intrinsic OAM signals exciting polar motion at the level of 1.0–1.5 mas even at sub-decadal periods ($T = 5$–10 years) adds uncertainty to attempts of detecting the inner core wobble (ICW, Rochester and Crossley, 2009) from rotation data. Recent studies (e.g., Ding et al., 2019) have made the case for a 8.7-year prograde harmonic in residual polar motion to be the signature of the ICW, at an amplitude of just 2.67 ± 0.04 mas. However, the OAM product used by Ding et al. (2019) to remove oceanic contributions from the observations did not account for intrinsic variability, implying that the error bars on the inferred ICW amplitude are likely too optimistic. Substantiating the evidence for core effects in polar motion data on sub-decadal time scales will most certainly require further improvements in modelling surface layer processes, comprising in particular oceanic and hydrological angular momentum changes (Rosat et al., 2021; Rekier et al., 2022).

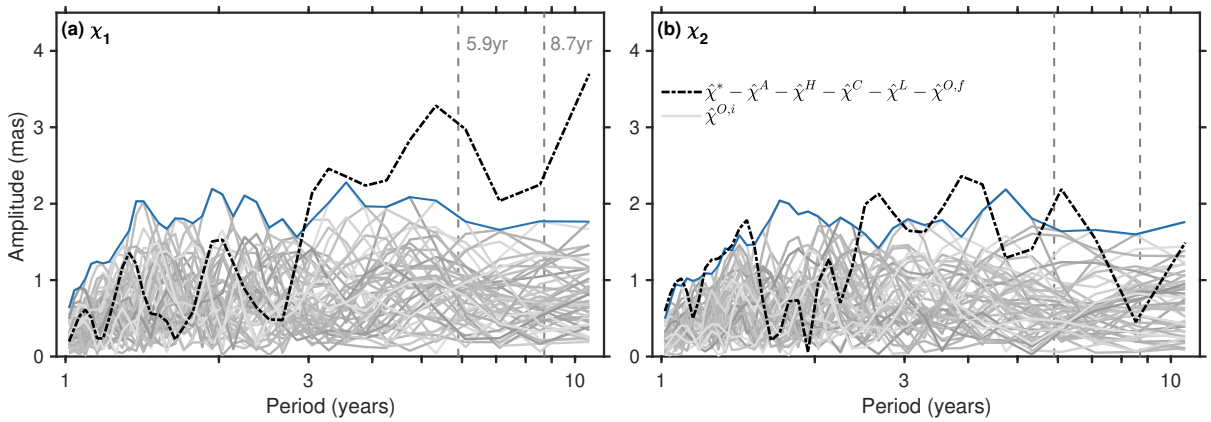

Figure 7.6: Amplitude spectra (in milliarcseconds) of $\hat{\chi} = \chi_1 + \mathrm{i}\chi_2$ over 1995–2015 for the intrinsic oceanic excitation (50 realizations of $\hat{\chi}^{\mathrm{O,i}}$, gray lines), in comparison to the residual geodetic excitation (black-dotted line), obtained by subtracting from $\hat{\chi}^*$ estimated contributions from atmosphere, terrestrial hydrology, ice sheets, GAL, and the forced oceanic excitation ($\hat{\chi}^{\mathrm{O,f}}$); cf. the expression in the legend. The upper envelope of the intrinsic terms is represented by the blue line.

7.4. Summary and conclusions

The 50-member OCCIPUT ensemble investigated in this study advocates for a prominent role of oceanic intrinsic variability in equatorial OAM changes from intraseasonal to interannual time scales. This marks the arrival of a new player on the scene of Earth rotation variations, with implications for tests of closure in the polar motion excitation budget and yet unmodelled geophysical processes (Table 7.2 and Fig. 7.6). In terms of attribution, we have been able to relate most of the mass-driven signals in $\hat{\chi}^{\mathrm{O,i}}$ (median PVE $= 63\%$ at periods ≥ 14 months) to

one particular mode of intrinsic p_b variations that likely manifests the free barotropic adjustment of the main ocean basins to nonlinearly-induced p_b anomalies near Drake Passage (cf. Fig. 7.4 and Zhao et al., 2023). As in many other parts of the Southern Ocean, low-frequency changes in eddy activity around Drake Passage are strongly random in character (Hogg et al., 2022), thus providing a plausible explanation as to why variability in $\hat{\chi}^{O,i}$ is a considerable fraction (43–50%, see Chapter 7.3.1) of the total oceanic excitation of polar motion even on interannual time scales. A caveat to be acknowledged, though, is that all of these inferences are based on simulations. The credibility of OCCIPUT-based OAM series is however clear from Table 7.2, and comparisons with monthly GRACE/-FO fields have shown that the leading p_b^i mode inherent to the ensemble could be present in satellite observations (Zhao et al., 2023). In addition, the Southern Ocean eddy field in the $1/4^\circ$ OCCIPUT runs is slightly less intense than in altimetry data (Carret et al., 2021; Hogg et al., 2022), suggesting that our estimates for the chaotic contribution to wobble excitation are rather of conservative nature.

Our results underscore the challenge of accurately representing oceanic effects for polar motion studies. In general, high horizontal model resolution ($\leq 1/4^\circ$) is preferred in accounting for wind-driven OAM changes (Harker et al., 2021). However, a single, high-resolution baroclinic model run would also produce one specific realization of the intrinsic component that is unlikely to match the phase of the observed one. Conversely, pursuing a probabilistic approach with a large eddy-permitting ensemble such as OCCIPUT may be computationally impracticable, especially on an operational basis and at the (sub-)daily resolution now common for rotation studies (Dobslaw and Dill, 2018). Better constraining the chaotic component of $\hat{\chi}^{O,i}$ will most certainly require an eddying ocean model assimilating, amongst other observations, altimetric sea level anomalies and GRACE/-FO estimates of p_b (i.e., extensions of the ocean reanalyses analysed in Börger et al., 2023). In the absence of such frameworks, the ensemble spreads and statistics presented in the present work provide indications of the errors incurred by methods that neglect intrinsic OAM variations. We expect these error quantifications to be useful for prediction purposes (e.g., Dobslaw and Dill, 2018; Kiani Shahvandi et al., 2022) and the geophysical interpretation of the residual geodetic excitation of polar motion from intraseasonal to sub-decadal time scales.

Appendix B: Terrestrial hydrology and cryosphere

The monthly gravity fields used for the determination of $\hat{\chi}^{\mathrm{H}}$ and $\hat{\chi}^{\mathrm{C}}$ over the 1995–2015 period are computed from tracking observations to up to 16 satellites from both satellite laser ranging (SLR) and the Doppler Orbitography and Radiopositioning Integrated by Satellites (DORIS) system. The problem is treated in terms of variational equations and cast as an iterative fit of forward-modelled satellite orbits to the observations. In representing the gravity field, low-degree spherical harmonics are combined with EOFs derived by principal component analysis of GRACE/-FO gravity fields. This hybrid representation, developed in Löcher and Kusche (2021), allows for the same effective wavelengths as the GRACE/-FO solutions while reducing the number of parameters to an amount appropriate for techniques less sensitive to gravity field details. As the approach leaves some scope for the choice of the base functions, the monthly fields in this study are computed as weighted means of 15 solutions employing various numbers of EOFs (up to 14) and spherical harmonics (from degree 2 to 5).

The coordinates of the SLR and DORIS stations entering the solution are part of the International Reference Frame 2014 (ITRF2014, Altamimi et al., 2016), corrected for tidal and non-tidal loading as appropriate. The force modelling for all satellites accounts for pole tides as per conventions (Petit and Luzum, 2010) and ocean pole tides following Desai (2002). Short-term mass variations in atmosphere and ocean are removed via the GRACE dealiasing product AOD1B RL06 (the GAC coefficients, Dobslaw et al., 2017) except for degree-1 terms. Furthermore, the force model includes the gravitational effect of glacial isostatic adjustment (GIA) based on the model of A et al. (2013); choice of another GIA estimate has negligible effects on our polar motion results. For consistency, we also remove the A et al. (2013) model from the GRACE/-FO solutions prior to expanding them into EOFs. Neither GIA nor the AOD1B product is restored to the final gravity fields. Co- and post-seismic deformation signals are left uncorrected.

In a subsequent step, we also deduce degree-1 coefficients (i.e., geocentre displacements), by keeping the gravity field invariant and estimating station coordinates for all SLR sites using a no-net-rotation condition. The common mode of translation across the so-derived stations reveals the time-variable offset of the geocentre relative to the ITRF2014. Over the GRACE/-FO time span, our degree-1 time series is very similar to, but somewhat noisier than the widely used estimate of Swenson et al. (2008). Prior to assigning this geocentre model to the monthly solutions, we subtract degree-1 contributions from the atmosphere (based on ERA-Interim with IB) and the ocean (based on forced OCCIPUT p_{b}). This correction avoids double-counting of long-wavelength mass variations in our analysis, associated in particular with atmospheric pressure changes over land.

The recovered gravity fields inherit the directional error structures (stripes) from the GRACE/-FO EOFs and thus require filtering in post-processing. We use a standard decorrelation and anisotropic smoothing kernel (DDK2, Kusche et al., 2009) to that end. Each monthly set of Stokes coefficients (including degree-1 terms) is then mapped to gridded ($1^\circ \times 1^\circ$) surface mass

anomalies and iteratively corrected for signal leakage across continental boundaries into the ocean. Our approach closely follows Chen et al. (2015). In short, the algorithm (a) takes a first guess of the true, gridded mass distribution, (b) derives a “predicted" mass field from (a) by expanding and re-synthesizing it using spherical harmonics up to degree 60, and (c) successively corrects the prediction—and thus the current guess for the true mass distribution—to yield closer agreement with the particular month’s observed mass anomalies. The latter also defines the first guess but with values over the ocean replaced by their spatial mean. This delineation leads to a sharp transition between the ocean and land (or ice sheets, respectively) that is kept for all guesses in the iteration. We separately iterate land, Greenland, and Antarctica, always permitting adjustments to local mass values within 600 km from the coast and correcting the spatial mean over the ocean accordingly to conserve total mass. Acceptable convergence is typically achieved after five iterations per modelled region. The resulting mass change fields, used as inputs for Eq. (2.30), are illustrated in terms of their standard deviation in Figs. 7.7a–7.7c.

Appendix C: Gravitational attraction and loading

To quantify the effect of surface mass loads on polar motion excitation, we combine mass load estimates from different sources, generally separated by Earth system compartment. For a precise net excitation estimate, allowance should be made for transports of water between continents and the ocean, leading to the residual excitation $\hat{\chi}^{\mathrm{L}}$. We require our estimate of $\hat{\chi}^{\mathrm{L}}$ to be consistent with the physics of GAL, such that the total load mass is conserved and the modelled sea level is an equipotential of Earth’s gravity field (Nakiboglu and Lambeck, 1980; Quinn et al., 2015; Adhikari and Ivins, 2016). Under the assumption that these mass fluxes and gravitational effects cause no relevant dynamic variations in the ocean (e.g., Kuhlmann et al., 2011), the resultant non-uniform water mass displacements may be estimated by solving the sea level equation (Woodward, R. S., 1888; Farrell and Clark, 1976). Here, sea level is taken relative to the deformed crust, equivalent to a change in p_{b} in the absence of atmospheric pressure variations. We solve the sea level equation in the spectral domain based on a global fingerprint inversion framework (Rietbroek et al., 2016; Uebbing et al., 2019) that accounts for solid Earth deformation, perturbations in the gravitational potential, sea level changes due to rotational feedback from the GAL-induced mass variations, and global mass conservation. The Earth’s deformation is assumed to be elastic, as is customary for sub-decadal phenomena.

We apply four different loads, comprising (a) atmospheric surface pressure variations, mass changes over (b) Greenland and (c) Antarctica, and (d) TWS anomalies over the remaining continents. The atmospheric loads are monthly mean pressures from ERA-Interim, with values over the ocean replaced by their time-varying spatial mean; cf. Quinn et al. (2015). For terms (b)–(d), we use the satellite-based and leakage-corrected surface mass estimates described in Appendix B. In adopting these loads in the sea level equation, we assume that all continental mass changes are related to variations in water (or ice) mass and consequently added to or removed

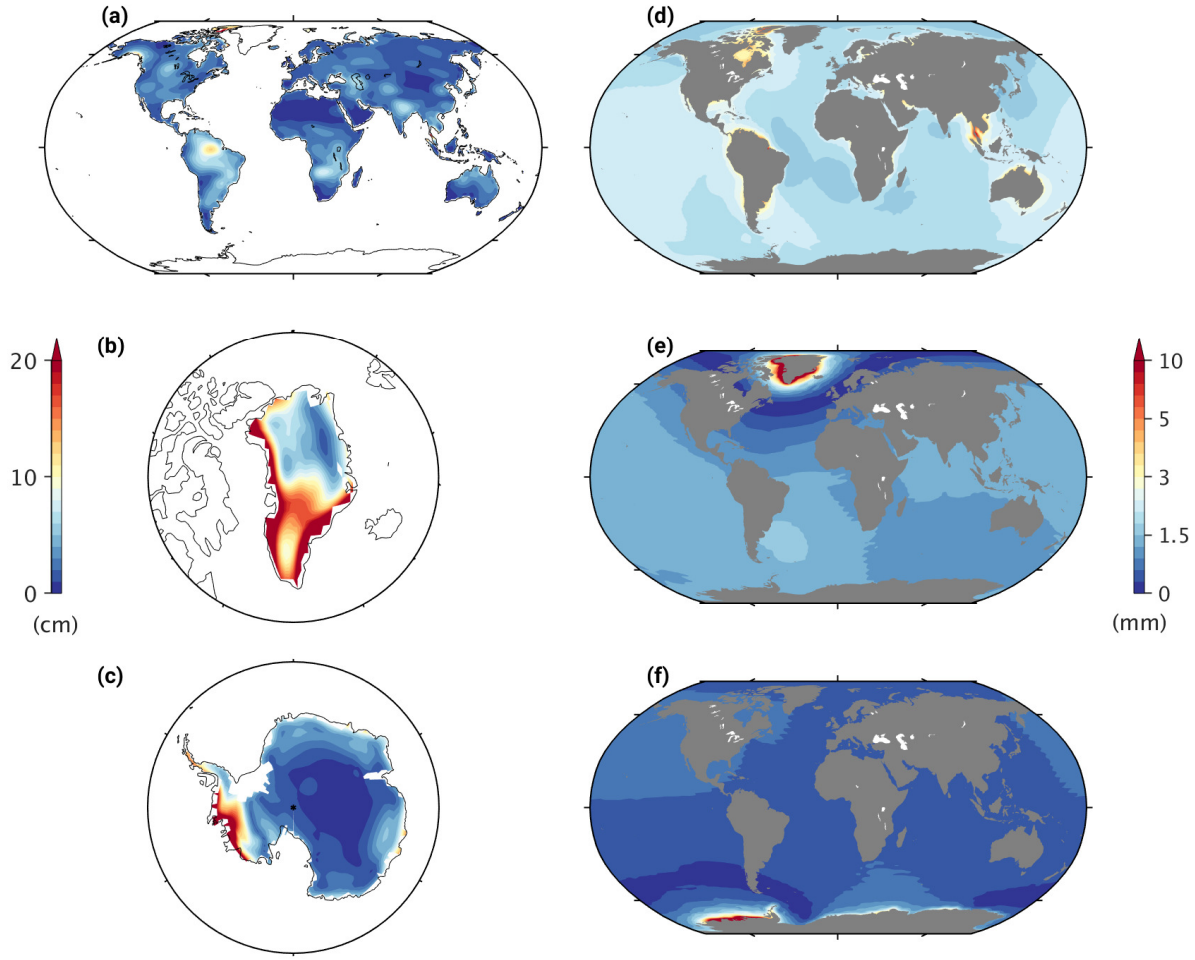

Figure 7.7: Standard deviation of (a–c) interannual surface mass changes over continents, as deduced from long-term gravity field solutions, and (d–f) associated GAL-induced mass redistribution in the ocean, from 1995 to 2015. Mass and GAL signals are depicted separately for (a,d) land hydrology, (b,e) Greenland, and (c,f) Antarctica. Units are centimeter of equivalent water height. Trends, seasonal oscillations, and sub-annual signals have been removed from each grid point's time series and therefore do not contribute to the picture. Note that the large (∼20 cm) localized mass anomaly on the northern Malay Peninsula in panel (a) is a tectonic, rather than a hydrological signal; the corresponding GAL field in the area (panel b) should therefore be treated with caution.

from the ocean. Fig. 7.7 illustrates the so-derived GAL fluctuations in space (bar the atmospheric contribution), while the total excitation signal ($\hat{\chi}^{\mathrm{L}}$) is shown in Fig. 7.1. On the interannual time scales considered here, the atmospheric contribution to $\hat{\chi}^{\mathrm{L}}$ is very small, featuring a standard deviation of less than 0.20 mas.

A final, more subtle issue is that GAL effects may also arise from dynamic p_{b} variability, as driven by atmospheric forcing or intrinsic ocean processes, and not by land-ocean mass transfer (Vinogradova et al., 2015). These gravitational effects were omitted in the OCCIPUT simulations, so we account for them after the fact, in keeping with the ocean's tendency for an equilibrium response to body forces at periods longer than a few months. Restricting the loads to dynamic ocean mass changes simplifies the GAL algorithm to a convolution of p_{b} anomalies with the

proper Green's function (Vinogradova et al., 2015). We have applied a spherical harmonic version of this convolution (Schindelegger et al., 2018) to a few OCCIPUT ensemble members and the p_b ensemble mean. The derived excitation series were found to differ in detail but agree in terms of their interannual peaks ($\sim$1 mas in χ_1, $\sim$1.5 mas in χ_2). Thus, for the purpose of this study, we represent the ocean-dynamics GAL signal using the p_b ensemble mean only and impose the implied mass redistribution on each of the 50 ensemble members. The GAL effects due to ocean dynamics are therefore contained in $\hat{\chi}^\mathrm{O}$, and not in $\hat{\chi}^\mathrm{L}$.

7.5. Chapter summary and context

Chapter 7 addresses the chaotic oceanic variability as introduced in Chapter 3.4 in the context of Earth rotation variations. Ocean modelling efforts for rotation studies have hitherto assumed that changes in the ocean are mainly driven by external forces, e.g., atmospheric winds and barometric pressure variations. However, as is now well documented, the ocean itself can generate substantial variability in the absence of external forces—a phenomenon also known as oceanic intrinsic variability or oceanic chaos (e.g., Penduff et al., 2014; Zhao et al., 2021, 2023). This intrinsic variability likely originates in non-linear local processes such as mesoscale eddies, but it can also manifest in large-scale (i.e., basin-wide) adjustments in ocean mass (Zhao et al., 2023). These large-scale adjustments are potentially relevant for Earth rotation studies, particularly those concerned with polar motion excitation. Since next to terrestrial hydrology, oceanic effects are a primary driver for low-frequency polar motion variability, the focus of this analysis is the interannual frequency band.

Ensemble methods are a proven means to disentangle intrinsic from forced oceanic variability, which is challenging or impossible with single forward runs or inverse modelling. The OCCIPUT large ensemble includes 50 simulations based on the NEMO ocean model from 1960–2015. The model is set up on a $^1/_4\,^\circ$ tri-polar grid and formulated under the Boussinesq assumption (Penduff et al., 2014). The realisations are generated from a common 21-year spin-up. Afterwards, small perturbations on the density equation are applied throughout the year 1960, and the so-derived ensemble members are then integrated forward using the exact same atmospheric forcing (DRAKKAR DFS 5.2, Dussin et al., 2016). Under this concept and approach, the spread of the ensemble members can be attributed to the intrinsic variability. The analysis period in this study is 1995–2015 (cf. Zhao et al., 2021) for which monthly means of p_b and barotropic velocities $(\overline{u}, \overline{v})$ are used to derive OAM using the formalism in Equation (2.30) for the mass term and Equation (2.27) for the motion term. Each ensemble member consists of a forced and an intrinsic part. To distinguish between the two components, an ensemble mean is calculated from the ensemble members, representing the forced component (cf. Equation 7.1). Analyses are then performed (i) in the spectral domain of the OAM estimates, (ii) with a modal decomposition of the intrinsic p_b fields (p_b^i), and (iii) in the temporal domain at interannual frequencies. The latter is realised by a comparison with a residual geodetic excitation corrected for contributions from the atmosphere, hydrology, cryosphere, and GAL.

The oceanic chaotic variability is first analysed in the spectral domain, separated into forced and intrinsic components, and further into χ_1 and χ_2 for the mass (Figure 7.2) and motion (Figure 7.3) terms. Additionally, the amplitude fraction (R) of the intrinsic (superscript i) oceanic excitation and the externally forced (superscript f) variability ($R = {}^{A_i}/_{A_f}$) is shown. At the annual frequency in χ_1^m, χ_1^v, and χ_2^v and the terannual component of χ_1^m, the ratios are ~ 0.15 highlighting the dominance of forced over intrinsic excitation series. In contrast, between 120 and 300 days, median values of R approach 0.9 in the mass terms, and the ratio ranges between 0.3–2.0 across all components. At interannual scales, elevated amplitude fractions are found

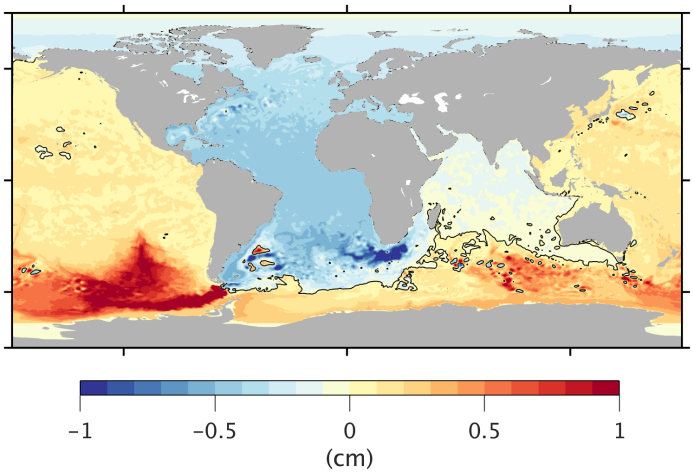

Figure 7.8: The leading mode in p_b of Ensemble member 19 of an EOF analysis. The mode exhibits a bipolar structure between the Atlantic and the Southern as well as the Pacific Oceans.

near 1.2–1.3 yrs in all $\hat{\chi}^O$ components and around 3 yrs in the mass terms, while a minimum appears near 1.6 yrs in mass and motion terms of χ_2, where the forced component dominates and R drops to about 0.5.

Switching to the temporal domain, an EOF analysis is first performed to assess the spatial pattern that govern variability of the modelled intrinsic p_b fields. This analysis reveals that most of the intrinsic signal can be attributed to the leading mode (mode 1), which explains between 16–22% of the global p_b^i variance. This mode likely reflects barotropic adjustments of the major ocean basins to non-linear p_b anomalies near Drake Passage (cf. Figure 7.8; Zhao et al., 2023). Converting the mode-1 spatial patterns and temporal variability to OAM changes shows that this mode accounts for 35–97% of the intrinsic oceanic excitation in both χ_1 and χ_2. The higher PVE values at the level of excitation compared to p_b^i can be attributed to the trigonometric weighting patterns in the OAM integrals (see Figure 2.7), which emphasise p_b signals of large (e.g., basin-wide) extent, rather than strong localised anomalies.

Looking at the interannual time series in both components in Figure 7.9, a spread of the ensemble members (intrinsic + forced) of ± 4 mas around the forced oceanic excitation is evident. In numbers, the ensemble members account for -24–35% of the variance in χ_1 and 45–65% of the variance in χ_2 of the corrected geodetic excitation, whereas the forced component explains 24% in χ_1 and 62% in χ_2 (cf. Figure 7.10). The higher PVE values in the χ_2 component can be explained by the geometry of the p_b and velocity fields (cf. weighting patterns in Figure 2.7). The results demonstrate that the intrinsic variability plays a prominent role in inducing equatorial OAM changes at interannual periods.

These results suggest that the intrinsic oceanic variability is a non-negligible contributor to the polar motion excitation budget, particularly at interannual frequencies. Thus, this study forms the second key contribution to the central aim of the thesis. Accounting for oceanic chaos is also relevant when the goal is to detect more subtle excitation signals due to other geophysical

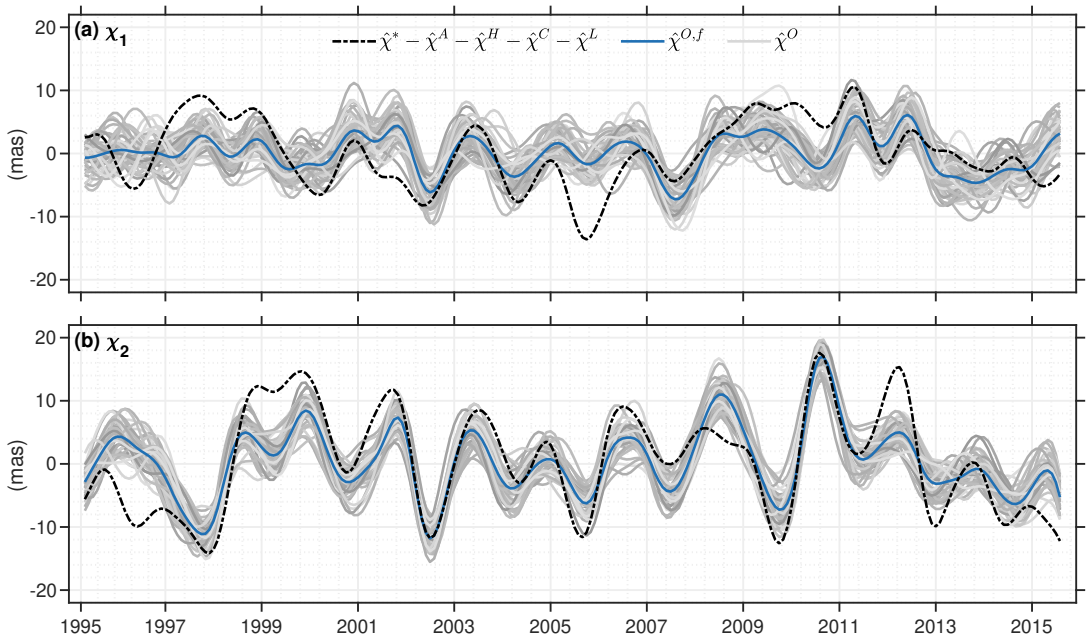

Figure 7.9: The low-frequency polar motion excitation budget from 1995 to 2015 in the presence of oceanic chaos. Shown are (as dashed black lines) the (a) χ_1 and (b) χ_2 components of geodetic excitation ($\hat{\chi}^*$)—corrected for contributions from the atmosphere ($\hat{\chi}^{\mathrm{A}}$), terrestrial hydrology ($\hat{\chi}^{\mathrm{H}}$), ice sheets ($\hat{\chi}^{\mathrm{C}}$), and GAL ($\hat{\chi}^{\mathrm{L}}$)—compared with 50 estimates of oceanic excitation from OCCIPUT ($\hat{\chi}^{\mathrm{O}}$, gray curves), and the OCCIPUT ensemble mean ($\hat{\chi}^{\mathrm{O,f}}$, blue curve). All time series have been detrended, filtered to periods $T \geq 14$ months, and cut back by 4 months at the two endpoints.

fluids (e.g., the core) from actual rotation data. Moreover, intrinsic oceanic variability introduces additional uncertainty in polar motion prediction studies, emphasising the need for a detailed understanding and knowledge of the processes in the ocean. The intrinsic variability is one of these processes, which has so far remained untested in Earth rotation studies. Incorporating intrinsic variability in OAM estimates therefore represents an important step toward further closure of the excitation budget and increasing the physical realism of the underlying models.

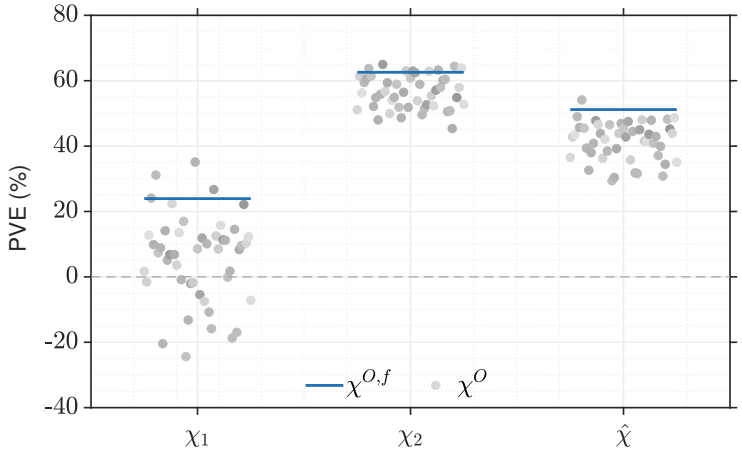

Figure 7.10: PVE of the forced component and the ensemble members in interannual equatorial (χ_1 and χ_2) and axial (χ_3) components of the geodetic excitation corrected for contributions from the atmosphere, terrestrial hydrology, Antarctic/Greenland Ice Sheets, and GAL.

8. Summary, conclusion, and outlook

The main objective of this thesis is to shed light on previously unknown processes underlying the oceanic excitation of low-frequency polar motion variability. In line with this goal, the work presented introduces two new players: (i) ENSO-induced OAM changes and (ii) the excitation associated with intrinsic oceanic variability. In unravelling these phenomena, I make use of both observations and models, particularly the output of climate models and large ensemble ocean simulations. In this regard, a further advance and new aspect in Earth rotation research is the evaluation of the skill of data-constrained ocean reanalyses in the excitation budget.

8.1. Summary and conclusion

First, OAM series from the ocean reanalyses GLORYS, ORAS5, and FOAM are tested for their signal content and value in evaluations of the polar motion and ΔLOD excitation budgets. The new OAM excitations are generally useful for Earth rotation studies, but show differences across time scales that may reflect a dependence on the applied DA scheme. At sub-seasonal and annual periods, the reanalysis skill is comparable to ECCOv4 (PVE of $\sim$43–52% in residual geodetic excitation of $\hat{\chi}$ and $\sim$29–40% in χ_3), while larger discrepancies arise at semi-annual and interannual scales (PVE of 72% of ECCOv4 in atmosphere-corrected geodetic excitation vs. 0.5–71% PVE of the reanalyses). FOAM, in particular, shows spurious signals in the interannual χ_3 component, which is attributed to the applied DA scheme that presumably leads to jumps in state variables and thus to kinematic inconsistencies. The analyses point to the use of ORAS5, if users have to choose a specific reanalyses for Earth rotation problems.

Second, ENSO is analysed as a potential mechanism to excite polar motion via oceanic mass-field-variability. This investigation represents a first key contribution to the central goal of this thesis. While the effect of ENSO on ΔLOD changes is well known, no similar effect on polar motion excitation has been detected so far. The analysis using CMIP6 model output and GRACE data shows that ENSO explains about 40–50% of an atmosphere-hydrology-cryosphere-corrected geodetic excitation of the χ_2 component during the selected El Niño events of 1997/98, 2009/10, and 2015/16 with amplitudes of $\pm$4 mas. The excitation is dominated by the OAM mass term, since ENSO-related currents are concentrated near the equator. Although the impact of ENSO on polar motion excitation is much more subtle than its influence on ΔLOD, knowledge of the nominal ENSO signature in OAM could be beneficial for improving long-term polar motion

predictions. This could be achieved by incorporating forecasts of the state of ENSO (Hu et al., 2024).

Finally, the role of intrinsic oceanic variability in polar motion excitation is investigated for the first time. This study is another essential contribution to the main objective of the thesis. Ensemble simulations from OCCIPUT indicate that local non-linear processes, most likely near Drake Passage, generate large-scale intrinsic (i.e., random) mass redistributions that contribute to polar motion excitation. In OCCIPUT and on interannual time scales, the intrinsic component of OAM accounts for 43–50% of the variance of the equatorial oceanic excitation and, making it a relevant factor for efforts that aim to close the excitation budget. Moreover, the consideration of the intrinsic oceanic variability is important when exploring hidden (i.e., secondary) excitation signals due to other geophysical fluids. For applications in the realm of polar motion prediction, the intrinsic variability introduces additional uncertainty. These implications emphasise the need for a detailed understanding and knowledge of the forced and internal processes in the ocean. Chaotic processes, in particular, are difficult to capture with single deterministic runs because such runs represent only one realisation of intrinsic variability, if they resolve the necessary scales and scale-interactions at all. Thus, ensemble approaches are required.

In summary, this thesis demonstrates that previously unconsidered oceanic phenomena—both ENSO and chaotic intrinsic variability—play an important role in the excitation of low-frequency polar motion variability. The studies presented directly contribute to the objective of this thesis by exploring processes underlying the oceanic excitation of polar motion on interannual time scales, while also providing insights into the value of ocean reanalyses for Earth rotation studies. However, all conclusions should be interpreted in light of remaining uncertainties related to model errors and the limited spatial and temporal coverage of the utilised observations and simulations.

8.2. Outlook

The findings of this thesis open further avenues of research to advance our understanding of oceanic contributions to the excitation of polar motion and ΔLOD. Building on the hypothesis of this thesis, future work could extend the analysis presented in Chapter 4.3 to additional climate modes, such as PDO and SAM. Likewise, mechanisms behind the intrinsic oceanic variability could be further investigated.

Earth rotation variability

As introduced in Chapter 4, climate modes affect global atmospheric variability through teleconnections, which are also imparted on the ocean. Particularly, the roles of PDO and SAM in exciting

polar motion remain unclear compared to ENSO or MJO. Nevertheless, correlations between PDO and SAM phases and CW excitation have been reported (e.g., Lambert, 2019; Naghibi et al., 2023). Similar to ENSO and MJO, geometry is important here, as both PDO and SAM primarily affect circulation in the mid-latitudes. Future work should specifically address the decadal imprint of the PDO on polar motion excitation and ΔLOD variations, and the role of the Southern Ocean in the SAM-related excitation. Such studies might again draw on a regression analysis to extract the dominant patterns in the mass fields and barotropic currents. Investigations of this kind will contribute to improving our understanding of the interannual oceanic excitation, potentially yielding also a step towards closure of the excitation budget.

The imprint of intrinsic oceanic variability on Earth rotation variability, warrants closer exploration, particularly with regard to the excitation of the CW. Initial tests with the OCCIPUT ensemble output and OAM series strongly suggest that intrinsic variability also figures in the excitation of the CW. Figure 8.1 shows the power spectral density (PSD, panel a) and excitation power (panel b) for an 11-year moving window. The power ranges from 2.15–12.40 mas^2 for the sum of atmospheric and OCCIPUT ensemble (i.e., oceanic) excitation compared to 7.33 mas^2 for the observed geodetic excitation. If we consider only the forced oceanic excitation, it is evident that it has less power compared to the atmospheric excitation. However, when considering full ensemble members (forced plus intrinsic), one obtains a broad spread of PSD values that can exceed the atmospheric power and encompass also the observed excitation.

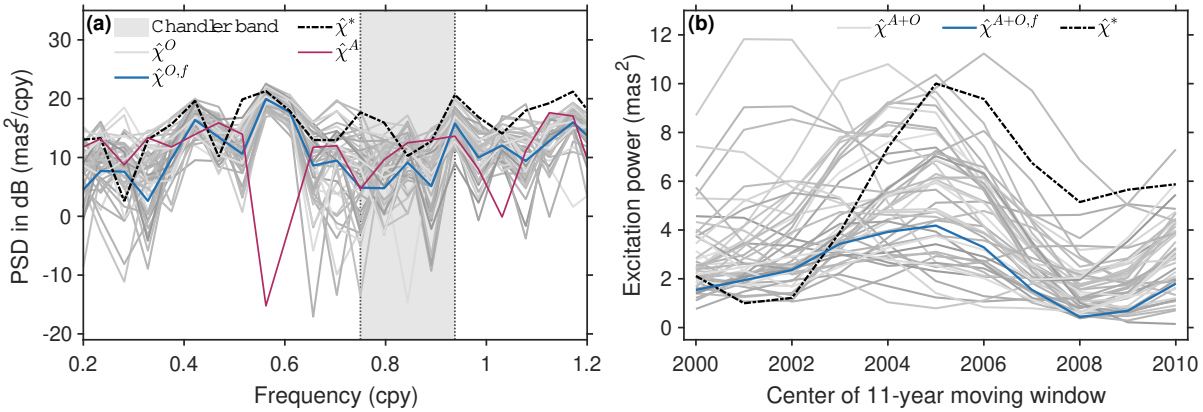

Figure 8.1: Panel (a) shows the power spectral density (PSD) estimates around the CW frequency in units of decibel (db) from observed excitation (black dotted), ensemble members (grey), forced oceanic (blue), and atmosphere (purple) from 1995–2015. Panel (b) illustrates the temporal evolution of the Chandler band excitation power for moving 11-year windows over 1995–2015 for the geodetic excitation (black dotted), the sum of atmosphere and the ensemble members (grey), atmosphere and the forced oceanic (red), and the atmosphere and ECCO (purple).

Going beyond this spectral view, an 11-year moving window analysis (Figure 8.1b) shows a broad peak in the observed CW excitation around 2005 ($\sim$10 mas^2), along with a trough in 2001 ($\sim$1 mas^2). Adding atmospheric contributions to the forced oceanic excitation from OCCIPUT produces a similar temporal variability but with slightly lower power and a trough around 2008. Adding the atmospheric excitation to each of the 50 ensemble members (forced plus

intrinsic variability) gives individual peaks of $\sim$10 mas^2, though these are usually not aligned with observations. The mismatch reflects the fact that any ensemble member contains merely a random realisation of the true intrinsic variability, so phases will not align. However, the overall spread of the ensemble member solutions in Figure 8.1b suggests that intrinsic oceanic variability can provide excitation power that is comparable to that of the atmosphere, underscoring its potential role in driving temporal variations of the CW excitation. To analyse this relationship in more detail and draw robust conclusions, the time series need to be extended.

Ocean modelling

Aside from identifying geophysical drivers, further progress also depends on advances in ocean modelling and DA. With regard to intrinsic variability, the generation mechanisms and characteristics in ocean models remain incompletely understood. To that end, ocean models that allow for flexible meshes, such as the Finite-Element/volumE Sea ice-Ocean Model version 2 (FESOM2, Koldunov et al., 2019), are an attractive choice. Using such modelling approaches, regional refinements in dynamically active regions, are possible by retaining the global domain and keeping computational costs manageable. With such tools it may be possible to track down the exact origin of the basin-wide mode of p_b variability that governs the intrinsic signal in equatorial OAM and is suspected near Drake Passage.

Furthermore, specially designed ocean model or reanalysis for Earth rotation applications would be beneficial for the community. The creation of these products should consider the findings and conclusions of earlier studies and the material presented in this thesis. Specifically, the models or reanalyses should be kinematically consistent and contain no spurious OAM signals (e.g., due to sequential DA methods), while also being run at sufficiently high resolution to faithfully represent variability controlled by ocean bottom topography. Reanalyses may further benefit from considering the dynamic ocean response to atmospheric pressure loading and by assimilating GRACE/-FO p_b data along with other oceanographic observations. Moreover, OAM fluctuations due to intrinsic variability could be accounted for through measures of uncertainty or model spread (preferably, deduced from continuously updated ensemble simulations).

Based on these considerations, the suggestions are summarised in the following four points:

1. Investigating the imprint of PDO and SAM on polar motion excitation and ΔLOD variations.

2. Assessing the role of oceanic chaos in CW excitation.

3. Performing detailed studies of intrinsic ocean variability using ensemble simulations with emphasis on variables that control OAM changes (p_b, barotropic currents).

4. Developing a dedicated ocean model or reanalysis for Earth rotation studies, that is kinemat-

ically consistent, assimilates GRACE/-FO p_b data, and accounts for the effects of intrinsic variability.

Together, these efforts are expected to improve the fidelity of OAM estimates, which will be useful for prediction purposes, for further closing the ΔLOD and polar motion excitation budgets, and for studying more subtle excitation signals yet to be uncovered in the observational record.

Bibliography

A, G., Wahr, J., and Zhong, S. (2013). Computations of the Viscoelastic Response of a 3-D Compressible Earth to Surface Loading: An Application to Glacial Isostatic Adjustment in Antarctica and Canada. *Geophysical Journal International*, 192(2):557–572.

Adcroft, A., Hill, C., and Marshall, J. (1997). Representation of Topography by Shaved Cells in a Height Coordinate Ocean Model. *Monthly Weather Review*, 125(9):2293 – 2315.

Adhikari, S. and Ivins, E. R. (2016). Climate-Driven Polar Motion: 2003–2015. *Science Advances*, 2(4):e1501693.

Afroosa, M., Rohith, B., Paul, A., Durand, F., Bourdallé-Badie, R., Sreedevi, P. V., de Viron, O., Ballu, V., and Shenoi, S. S. C. (2021). Madden-Julian Oscillation Winds Excite an Intraseasonal See-Saw of Ocean Mass That Affects Earth's Polar Motion. *Communications Earth & Environment*, 2(1):139.

Altamimi, Z., Rebischung, P., Collilieux, X., Métivier, L., and Chanard, K. (2023). ITRF2020: An Augmented Reference Frame Refining the Modeling of Nonlinear Station Motions. *Journal of Geodesy*, 97(5):47.

Altamimi, Z., Rebischung, P., Métivier, L., and Collilieux, X. (2016). ITRF2014: A new release of the International Terrestrial Reference Frame modeling nonlinear station motions. *Journal of Geophysical Research: Solid Earth*, 121(8):6109–6131.

Amante, C. and Eakins, B. (2009). ETOPO1 1 Arc-Minute Global Relief Model: Procedures, Data Sources and Analysis. NOAA Technical Memorandum NESDIS NGDC-24. Last access: 6 January 2023.

Androsov, A., Boebel, O., Schröter, J., Danilov, S., Macrander, A., and Ivanciu, I. (2020). Ocean Bottom Pressure Variability: Can It Be Reliably Modeled? *Journal of Geophysical Research: Oceans*, 125(3):e2019JC015469.

Aoki, S. (2002). Coherent Sea Level Response to the Antarctic Oscillation. *Geophysical Research Letters*, 29(20).

Arbic, B. K., Müller, M., Richman, J. G., Shriver, J. F., Morten, A. J., Scott, R. B., Sérazin, G., and Penduff, T. (2014). Geostrophic Turbulence in the Frequency–Wavenumber Domain: Eddy-Driven Low-Frequency Variability. *Journal of Physical Oceanography*, 44(8):2050–2069.

Auriol, A. and Tourain, C. (2010). DORIS System: The New Age. *Advances in Space Research*, 46(12):1484–1496.

Balidakis, K., Nilsson, T., Zus, F., Glaser, S., Heinkelmann, R., Deng, Z., and Schuh, H. (2018). Estimating Integrated Water Vapor Trends From VLBI, GPS, and Numerical Weather Models: Sensitivity to Tropospheric Parameterization. *Journal of Geophysical Research: Atmospheres*, 123(12):6356–6372.

Bamston, A. G., Chelliah, M., and Goldenberg, S. B. (1997). Documentation of a Highly ENSO-related Sst Region in the Equatorial Pacific: Research Note. *Atmosphere-Ocean*, 35(3):367–383.

Barnes, R., Hide, R., White, A., and Wilson, C. (1983). Atmospheric Angular Momentum Fluctuations, Length-of-Day Changes and Polar Motion. *Proceedings of the Royal Society of London. Series A*, 387(1792):31–73.

Barnston, A. G., Tippett, M. K., L'Heureux, M. L., Li, S., and DeWitt, D. G. (2012). Skill of Real-Time Seasonal ENSO Model Predictions during 2002–11: Is Our Capability Increasing? *Bulletin of the American Meteorological Society*, 93(5):631–651.

Bellenger, H., Guilyardi, E., Leloup, J., Lengaigne, M., and Vialard, J. (2014). ENSO Representation in Climate Models: From CMIP3 to CMIP5. *Climate Dynamics*, 42(7-8):1999–2018.

Benton, C. J. and Mitchell, C. N. (2011). Isolating the Multipath Component in GNSS Signal-to-noise Data and Locating Reflecting Objects. *Radio Science*, 46(6):2011RS004767.

Bessières, L., Leroux, S., Brankart, J.-M., Molines, J.-M., Moine, M.-P., Bouttier, P.-A., Penduff, T., Terray, L., Barnier, B., and Sérazin, G. (2017). Development of a Probabilistic Ocean Modelling System Based on NEMO 3.5: Application at Eddying Resolution. *Geoscientific Model Development*, 10(3):1091–1106.

Bizouard, C., Lambert, S., Gattano, C., Becker, O., and Richard, J.-Y. (2019). The IERS EOP 14C04 solution for Earth Orientation Parameters Consistent with ITRF 2014. *Journal of Geodesy*, 93(5):621–633.

Bizouard, C. and Seoane, L. (2010). Atmospheric and Oceanic Forcing of the Rapid Polar Motion. *Journal of Geodesy*, 84(1):19–30.

Bjerknes, J. (1966). A Possible Response of the Atmospheric Hadley Circulation to Equatorial Anomalies of Ocean Temperature. *Tellus A: Dynamic Meteorology and Oceanography*, 18(4):820.

Bjerknes, J. (1969). Atmospheric Teleconnections From The Equatorial Pacific. 97(3):163–172.

Blockley, E. W., Martin, M. J., McLaren, A. J., Ryan, A. G., Waters, J., Lea, D. J., Mirouze, I., Peterson, K. A., Sellar, A., and Storkey, D. (2014). Recent Development of the Met Office Operational Ocean Forecasting System: An Overview and Assessment of the New Global FOAM Forecasts. *Geoscientific Model Development*, 7(6):2613–2638.

Boehm, J., Heinkelmann, R., Mendes Cerveira, P. J., Pany, A., and Schuh, H. (2009). Atmospheric Loading Corrections at the Observation Level in VLBI Analysis. *Journal of Geodesy*, 83(11):1107–1113.

Boening, C., Lee, T., and Zlotnicki, V. (2011). A Record-High Ocean Bottom Pressure in the South Pacific Observed by GRACE. *Geophysical Research Letters*, 38(4).

Boergens, E., Dobslaw, H., and Dill, R. (2020). COST-G GravIS RL01 Continental Water Storage Anomalies. V. 0005. GFZ Data Services.

Börger, L., Lentge, K. M., and Schindelegger, M. (2025a). Monthly Ocean Bottom Pressure Anomalies from CMIP6 Climate Models [Dataset].

Börger, L., Lentge, K. M., Schindelegger, M., and Dobslaw, H. (2025b). ENSO Modulates the Oceanic Excitation of Polar Motion. *Geophysical Research Letters*, 52(18):e2025GL118576.

Börger, L. and Schindelegger, M. (2022). Angular Momentum Estimates for Geophysical Fluids, 2006–2015 [Dataset].

Börger, L., Schindelegger, M., Dobslaw, H., and Salstein, D. (2023). Are Ocean Reanalyses Useful for Earth Rotation Research? *Earth and Space Science*, 10(3):e2022EA002700.

Börger, L., Schindelegger, M., and Kiani Shahvandi, M. (2024a). Consistent Set of Atmospheric and Oceanic Angular Momentum 1994–2022 [Dataset].

Börger, L., Schindelegger, M., Zhao, M., Ponte, R. M., Löcher, A., Uebbing, B., Molines, J.-M., and Penduff, T. (2025c). Chaotic Oceanic Excitation of Low-Frequency Polar Motion Variability. *Earth System Dynamics*, 16(1):75–90.

Börger, L., Schindelegger, M., Zhao, M., Ponte, R. M., Löcher, A., Uebbing, B., Molines, J.-M., and Penduff, T. (2024b). Angular Momentum Estimates for Global Geophysical Fluids, 1995–2015 [Dataset].

Brankart, J.-M., Candille, G., Garnier, F., Calone, C., Melet, A., Bouttier, P.-A., Brasseur, P., and Verron, J. (2015). A Generic Approach to Explicit Simulation of Uncertainty in the NEMO Ocean Model. *Geoscientific Model Development*, 8(5):1285–1297.

Brown, J. R., Brierley, C. M., An, S.-I., Guarino, M.-V., Stevenson, S., Williams, C. J. R., Zhang, Q., Zhao, A., Abe-Ouchi, A., Braconnot, P., Brady, E. C., Chandan, D., D'Agostino, R., Guo, C., LeGrande, A. N., Lohmann, G., Morozova, P. A., Ohgaito, R., O'ishi, R., Otto-Bliesner, B. L., Peltier, W. R., Shi, X., Sime, L., Volodin, E. M., Zhang, Z., and Zheng, W. (2020). Comparison of Past and Future Simulations of ENSO in CMIP5/PMIP3 and CMIP6/PMIP4 Models. *Climate of the Past*, 16(5):1777–1805.

Capitaine, N., Wallace, P. T., and Chapront, J. (2003). Expressions for IAU 2000 Precession Quantities. *Astronomy & Astrophysics*, 412(2):567–586.

Carret, A., Llovel, W., Penduff, T., and Molines, J.-M. (2021). Atmospherically Forced and Chaotic Interannual Variability of Regional Sea Level and Its Components Over 1993–2015. *Journal of Geophysical Research: Oceans*, 126(4):e2020JC017123.

Chambers, D. P. (2011). ENSO-Correlated Fluctuations in Ocean Bottom Pressure and Wind-Stress Curl in the North Pacific. *Ocean Science*, 7(5):685–692.

Chao, B. F. (1985). On the Excitation of the Earth' Polar Motion. *Geophysical Research Letters*, 12(8):526–529.

Charlot, P., Jacobs, C. S., Gordon, D., Lambert, S., De Witt, A., Böhm, J., Fey, A. L., Heinkelmann, R., Skurikhina, E., Titov, O., Arias, E. F., Bolotin, S., Bourda, G., Ma, C., Malkin, Z., Nothnagel, A., Mayer, D., MacMillan, D. S., Nilsson, T., and Gaume, R. (2020). The Third Realization of the International Celestial Reference Frame by Very Long Baseline Interferometry. *Astronomy & Astrophysics*, 644:A159.

Chassignet, E. P. and Xu, X. (2021). On the Importance of High-Resolution in Large-Scale Ocean Models. *Advances in Atmospheric Sciences*, 38(10):1621–1634.

Chelton, D. B., Schlax, M. G., and Samelson, R. M. (2011). Global Observations of Nonlinear Mesoscale Eddies. *Progress in Oceanography*, 91(2):167–216.

Chen, J., Wilson, C. R., Kuang, W., and Chao, B. F. (2019). Interannual Oscillations in Earth Rotation. *Journal of Geophysical Research: Solid Earth*, 124(12):13404–13414.

Chen, J. L., Wilson, C. R., Chao, B. F., Shum, C. K., and Tapley, B. D. (2000). Hydrological and Oceanic Excitations to Polar Motion And Length-of-Day Variation. *Geophysical Journal International*, 141(1):149–156.

Chen, J. L., Wilson, C. R., Li, J., and Zhang, Z. (2015). Reducing Leakage Error in GRACE-observed Long-Term Ice Mass Change: A Case Study in West Antarctica. *Journal of Geodesy*, 89(9):925–940.

Chen, J. L., Wilson, C. R., Ries, J. C., and Tapley, B. D. (2013a). Rapid Ice Melting Drives Earth's Pole to the East. *Geophysical Research Letters*, 40(11):2625–2630.

Chen, W., Ray, J., Li, J., Huang, C., and Shen, W. (2013b). Polar Motion Excitations for an Earth Model with Frequency-Dependent Responses: 1. A Refined Theory with Insight into the Earth's Rheology and Core-Mantle Coupling. *Journal of Geophysical Research: Solid Earth*, 118(9):4975–4994.

Clarke, P. J., Lavallée, D. A., Blewitt, G., van Dam, T. M., and Wahr, J. M. (2005). Effect of Gravitational Consistency and Mass Conservation on Seasonal Surface Mass Loading Models. *Geophysical Research Letters*, 32:L08306.

Climate Prediction Center (2017). Description of Changes to Oceanic Niño Index (ONI). https://origin.cpc.ncep.noaa.gov/products/analysis_monitoring/ensostuff/ONI_change.shtml.

Copernicus Marine Service (2019). Global Ocean Ensemble Physics Reanalysis. https://resources.marine.copernicus.eu/product-detail/GLOBAL_REANALYSIS_PHY_001_031/INFORMATION, Last access: 19 August 2022.

Coster, A. J., Goncharenko, L., Zhang, S.-R., Erickson, P. J., Rideout, W., and Vierinen, J. (2017). GNSS Observations of Ionospheric Variations During the 21 August 2017 Solar Eclipse. *Geophysical Research Letters*, 44(24).

Cravatte, S., Sérazin, G., Penduff, T., and Menkes, C. (2021). Imprint of Chaotic Ocean Variability on Transports in the Southwestern Pacific at Interannual Timescales. *Ocean Sciences*, 17(2):487–507.

Dee, D. P., Uppala, S. M., Simmons, A. J., Berrisford, P., Poli, P., et al. (2011). The ERA-Interim Reanalysis: Configuration and Performance of the Data Assimilation System. *Quarterly Journal of the Royal Meteorological Society*, 137(656):553–597.

Delforge, D., de Viron, O., Durand, F., and Dehant, V. (2022). The Global Patterns of Interannual and Intraseasonal Mass Variations in the Oceans from GRACE and GRACE Follow-On Records. *Remote Sensing*, 14:1861.

Deng, S., Liu, S., Mo, X., Jiang, L., and Bauer-Gottwein, P. (2021). Polar Drift in the 1990s Explained by Terrestrial Water Storage Changes. *Geophysical Research Letters*, 48(7):e2020GL092114.

Desai, S. D. (2002). Observing the Pole Tide with Satellite Altimetry. *Journal of Geophysical Research: Oceans*, 107:C11.

Deser, C., Phillips, A. S., and Hurrell, J. W. (2004). Pacific Interdecadal Climate Variability: Linkages between the Tropics and the North Pacific During Boreal Winter Since 1900. 17(16):3109–3124.

Desportes, C., Garric, G., Régnier, C., Drévillon, M., Parent, L., Garric, G., Drillet, Y., Masina, S., Storto, A., Mirouze, I., Cipollone, A., Zuo, H., Balmaseda, M., Peterson, D., Wood, R., Jackson, L., Mulet, S., Greiner, E., and Gounou, A. (2019). *Quality Information Document For Global Ocean Reanalysis Multi-model Ensemble Products GREP GLOBAL-REANALYSIS-PHY-001-03*. Copernicus Marine Environment Monitoring Service.

Dill, R. (2008). Hydrological Model LSDM for Operational Earth Rotation and Gravity Field Variations (Scientific Technical Report 08/09). Scientific report, GFZ Potsdam.

Dill, R. and Dobslaw, H. (2019). Seasonal Variations in Global Mean Sea Level and Consequences on the Excitation of Length-of-Day Changes. *Geophysical Journal International*, 218(2):801–816.

Dill, R., Dobslaw, H., Hellmers, H., Kehm, A., Bloßfeld, M., Thomas, M., Seitz, F., Thaller, D., Hugentobler, U., and Schönemann, E. (2020). Evaluating Processing Choices for the Geodetic Estimation of Earth Orientation Parameters with Numerical Models of Global Geophysical Fluids. *Journal of Geophysical Research: Solid Earth*, 125(9).

Ding, H., Pan, Y., Xu, X. Y., Shen, W., and Li, M. (2019). Application of the AR-z Spectrum to Polar Motion: A Possible First Detection of the Inner Core Wobble and Its Implications for the Density of Earth's Core. *Geophysical Research Letters*, 46(23):13765–13774.

Dobslaw, H., Bergmann-Wolf, I., Dill, R., Poropat, L., and Flechtner, F. (2017). *Product Description Document for AOD1B Release 06, Rev. 6.1*. GFZ Potsdam, Potsdam, Germany. Accessed 6 September 2023.

Dobslaw, H. and Dill, R. (2018). Predicting Earth Orientation Changes from Global Forecasts of Atmosphere-Hydrosphere Dynamics. *Advances in Space Research*, 61(4):1047–1054.

Dobslaw, H., Dill, R., Grötzsch, A., Brzeziński, A., and Thomas, M. (2010). Seasonal Polar Motion Excitation from Numerical Models of Atmosphere, Ocean, and Continental Hydrosphere. *Journal of Geophysical Research*, 115(B10):B10406.

Drożdżewski, M. and Sośnica, K. (2024). Troposphere Delay Modeling in SLR Based on PMF, VMF3o, and Meteorological Data. *Progress in Earth and Planetary Science*, 11(1):12.

Durand, F., Piecuch, C. G., Becker, M., Papa, F., Raju, S. V., Khan, J. U., and Ponte, R. M. (2019). Impact of Continental Freshwater Runoff on Coastal Sea Level. *Surveys in Geophysics*, 40(6):1437–1466.

Dussin, R., Barnier, B., Brodeau, L., and Molines, J.-M. (2016). Drakkar Forcing Set DFS5. Technical report, MyOcean Report.

EC-Earth Consortium (2019). EC-Earth-Consortium EC-Earth3 Model Output Prepared for CMIP6 CMIP Historical.

ECCO Consortium, Fukumori, I., Wang, O., Fenty, I., Forget, G., Heimbach, P., and Ponte, R. M. (2017). ECCO Version 4 Release 3. Last access: 19 August 2022.

Einšpigel, D. and Martinec, Z. (2017). Time-domain modeling of global ocean tides generated by the full lunisolar potential. *Ocean Dynamics*, 67(2):165–189.

Eubanks, T. M. (1993). Variations in the Orientation of the Earth. In Smith, D. E. and Turcotte, D. L., editors, *Geodynamics Series*, volume 24, pages 1–54. American Geophysical Union, Washington, D. C.

Eyring, V., Bony, S., Meehl, G. A., Senior, C. A., Stevens, B., Stouffer, R. J., and Taylor, K. E. (2016). Overview of the Coupled Model Intercomparison Project Phase 6 (CMIP6) Experimental Design and Organization. *Geoscientific Model Development*, 9(5):1937–1958.

Farrell, W. E. and Clark, J. A. (1976). On Postglacial Sea Level. *Geophysical Journal of the Royal Astronomical Society*, 46(3):647–667.

Fey, A. L., Gordon, D., Jacobs, C. S., Ma, C., Gaume, R. A., Arias, E. F., Bianco, G., Boboltz, D. A., Böckmann, S., Bolotin, S., Charlot, P., Collioud, A., Engelhardt, G., Gipson, J., Gontier, A.-M., Heinkelmann, R., Kurdubov, S., Lambert, S., Lytvyn, S., MacMillan, D. S., Malkin, Z., Nothnagel, A., Ojha, R., Skurikhina, E., Sokolova, J., Souchay, J., Sovers, O. J., Tesmer, V., Titov, O., Wang, G., and Zharov, V. (2015). The Second Realization of the International Celestial Reference Frame by Very Long Baseline Interferometry. *The Astronomical Journal*, 150(2):58.

Forget, G., Campin, J.-M., Heimbach, P., Hill, C. N., Ponte, R. M., and Wunsch, C. (2015). ECCO Version 4: An Integrated Framework for Non-Linear Inverse Modeling and Global Ocean State Estimation. *Geoscientific Model Development*, 8(10):3071–3104.

Fu, L.-L. (2002). Wind-Forced Intraseasonal Sea Level Variability of the Extratropical Oceans. *Journal of Physical Oceanography*, 33(2):436–449.

Fukumori, I., Raghunath, R., and Fu, L.-L. (1998). Nature of Global Large-scale Sea Level Variability in Relation to Atmospheric Forcing: A Modeling Study. *Journal of Geophysical Research*, 103(C3):5493–5512.

Garric, G. and Parent, L. (2017). *Quality Information Document For Global Ocean Reanalysis Products GLOBAL-REANALYSIS-PHY-001-025*. Copernicus Marine Environment Monitoring Service.

Göttl, F., Groh, A., Schmidt, M., Schröder, L., and Seitz, F. (2021). The Influence of Antarctic Ice Loss on Polar Motion: An Assessment Based on GRACE and Multi-Mission Satellite Altimetry. *Earth, Planets and Space*, 73(1):99.

Greatbatch, R. J. (1994). A Note on the Representation of Steric Sea Level in Models That Conserve Volume Rather than Mass. *Journal of Geophysical Research: Oceans*, 99(C6):12767–12771.

Greatbatch, R. J., Lu, Y., and Cai, Y. (2001). Relaxing the Boussinesq Approximation in Ocean Circulation Models. *Journal of Atmospheric and Oceanic Technology*, 18(11):1911–1923.

Gross, R. S. (1992). Correspondence Between Theory and Observations of Polar Motion. *Geophysical Journal International*, 109:162–170.

Gross, R. S. (2000). The excitation of the Chandler wobble. *Geophysical Research Letters*, 27(15):2329–2332.

Gross, R. S. (2007). Earth Rotation Variations – Long Period. In Herring, T., editor, *Treatise on Geophysics*, volume 3, pages 239–294. Elsevier, Amsterdam.

Gross, R. S., Fukumori, I., and Menemenlis, D. (2003). Atmospheric and Oceanic Excitation of the Earth's Wobbles During 1980–2000. *Journal of Geophysical Research: Solid Earth*, 108(B8):2370.

Gross, R. S., Fukumori, I., Menemenlis, D., and Gegout, P. (2004). Atmospheric and Oceanic Excitation of Length-of-Day Variations During 1980–2000. *Journal of Geophysical Research: Solid Earth*, 109(B1).

Harker, A. A., Schindelegger, M., Ponte, R. M., and Salstein, D. A. (2021). Modeling Ocean-Induced Rapid Earth Rotation Variations: An Update. *Journal of Geodesy*, 95(9):110.

Hellmers, H., Thaller, D., Bloßfeld, M., Kehm, A., and Girdiuk, A. (2019). Combination of VLBI Intensive Sessions with GNSS for Generating Low Latency Earth Rotation Parameters. *Advances in Geosciences*, 50:49–56.

Hofmann-Wellenhof, B., Lichtenegger, H., and Wasle, E. (2008). *GNSS — Global Navigation Satellite Systems: GPS, GLONASS, Galileo, and more*. SpringerLink Bücher. Springer-Verlag Wien, Vienna.

Hogg, A. M., Penduff, T., Close, S. E., Dewar, W. K., Constantinou, N. C., and Martínez-Moreno, J. (2022). Circumpolar Variations in the Chaotic Nature of Southern Ocean Eddy Dynamics. *Journal of Geophysical Research: Oceans*, 127(5):e2022JC018440.

Hu, R., Lian, T., Liu, T., Wang, J., Song, X., Chen, H., and Chen, D. (2024). Predicting the 2023/24 El Niño from a Multi-Scale and Global Perspective. *Communications Earth & Environment*, 5(1):675.

Hu, Z.-Z., Kumar, A., Huang, B., Zhu, J., L'Heureux, M., McPhaden, M. J., and Yu, J.-Y. (2020). The Interdecadal Shift of ENSO Properties in 1999/2000: A Review. *Journal of Climate*, 33(11):4441–4462.

Hughes, C. W., Williams, J., Blaker, A., Coward, A., and Stepanov, V. (2018). A Window on the Deep Ocean: The Special Value of Ocean Bottom Pressure for Monitoring the Large-Scale, Deep-Ocean Circulation. *Progress in Oceanography*, 161:19–46.

Jones, J., Guerova, G., Douša, J., Dick, G., De Haan, S., Pottiaux, E., Bock, O., Pacione, R., and Van Malderen, R., editors (2020). *Advanced GNSS Tropospheric Products for Monitoring Severe Weather Events and Climate: COST Action ES1206 Final Action Dissemination Report*. Springer International Publishing, Cham.

Jungclaus, J. H., Fischer, N., Haak, H., Lohmann, K., Marotzke, J., Matei, D., Mikolajewicz, U., Notz, D., and Von Storch, J. S. (2013). Characteristics of the Ocean Simulations in the Max Planck Institute Ocean Model (MPIOM) the Ocean Component of the MPI-Earth System Model. *Journal of Advances in Modeling Earth Systems*, 5(2):422–446.

Kiani Shahvandi, M., Schartner, M., and Soja, B. (2022). Neural ODE Differential Learning and its Application in Polar Motion Prediction. *Journal of Geophysical Research: Solid Earth*, 127(11):e2022JB024775.

Kiani Shahvandi, M., Schindelegger, M., Börger, L., Mishra, S., and Soja, B. (2024). Revisiting the Excitation of Free Core Nutation. *Journal of Geophysical Research: Solid Earth*, 129(9):e2024JB029583.

Klügel, T., Schlüter, W., Schreiber, U., and Schneider, M. (2005). Großringlaser zur kontinuierlichen Beobachtung der Erdrotation. *zfv - Zeitschrift für Geodäsie, Geoinformation und Landmanagement*, 130(2):99–108.

Knauss, J. A. and Garfield, N. (2017). *Introduction to Physical Oceanography*. Waveland Press, Inc, Long Grove, Illinois, third edition edition.

Koldunov, N. V., Aizinger, V., Rakowsky, N., Scholz, P., Sidorenko, D., Danilov, S., and Jung, T. (2019). Scalability and Some Optimization of the Finite-volumE Sea Ice–Ocean Model, Version 2.0 (FESOM2). *Geoscientific Model Development*, 12(9):3991–4012.

Koot, L., de. Viron, O., and Dehant, V. (2006). Atmospheric Angular Momentum Time-Series: Characterization of Their Internal Noise and Creation of a Combined Series. *Journal of Geodesy*, 79(12):663–674.

Kronfeld-Schor, N., Bloch, G., and Schwartz, W. J. (2013). Animal Clocks: When Science Meets Nature. *Proceedings of the Royal Society B: Biological Sciences*, 280(1765):20131354.

Kuang, W., Chao, B. F., and Chen, J. (2019). Reassessment of Electromagnetic Core-Mantle Coupling and Its Implications to the Earth's Decadal Polar Motion. *Geodesy and Geodynamics*, 10(5):356–362.

Kuhlmann, J., Dobslaw, H., and Thomas, M. (2011). Improved Modeling of Sea Level Patterns by Incorporating Self-Attraction and Loading. *Journal of Geophysical Research: Oceans*, 116(C11):2011JC007399.

Kur, T., Śliwińska-Bronowicz, J., Wińska, M., Dobslaw, H., Nastula, J., Partyka, A., Belda, S., Bizouard, C., Boggs, D., Bruni, S., Chen, L., Chin, M., Dhar, S., Dill, R., Duan, P., Ferrandiz, J. M., Gou, J., Gross, R., Guessoum, S., Han, S., Heinkelmann, R., Huang, C., Irrgang, C., Kudrys, J., Li, J., Ligas, M., Liu, L., Lu, W., Mayer, V., Miao, W., Michalczak, M., Modiri, S., Otten, M., Ratcliff, T., Raut, S., Saynisch-Wagner, J., Schartner, M., Schoenemann, E., Schuh, H., Shahvandi, M. K., Soja, B., Su, X., Thaller, D., Thomas, M., Wang, G., Wu, Y., Xu, C., Xu, X., Yang, X., Zhao, X., and Zhou, Z. (2024). Prospects of Predicting the Polar Motion Based on the Results of the Second Earth Orientation Parameters Prediction Comparison Campaign. *Earth and Space Science*, 11(11):e2023EA003278.

Kusche, J., Schmidt, R., Petrovic, S., and Rietbroek, R. (2009). Decorrelated GRACE Time-Variable Gravity Solutions by GFZ, and Their Validation Using a Hydrological Model. *Journal of Geodesy*, 83(10):903–913.

Lambert, S. (2019). Atmospheric Excitation of the Chandler Wobble along the 20th Century: Insights from ECMWF ERA-20c Reanalysis. In *Journées 2019*, pages 279–283, Observatoire de Paris, Paris, France.

Lambert, S. B., Marcus, S. L., and De Viron, O. (2017). Atmospheric Torques and Earth's Rotation: What Drove the Millisecond-Level Length-of-Day Response to the 2015–2016 El Niño? *Earth System Dynamics*, 8(4):1009–1017.

Larson, K. M., Gutmann, E. D., Zavorotny, V. U., Braun, J. J., Williams, M. W., and Nievinski, F. G. (2009). Can We Measure Snow Depth with GPS Receivers? *Geophysical Research Letters*, 36(17):2009GL039430.

Le Traon, P.-Y., Dibarboure, G., Lellouche, J.-M., Pujol, M.-I., Benkiran, M., Drevillon, M., Drillet, Y., Faugère, Y., and Remy, E. (2025). Satellite Altimetry and Operational Oceanography: From Jason-1 to SWOT. *Ocean Science*, 21(4):1329–1347.

Legeais, J.-F., Prandi, P., and Guinehut, S. (2016). Analyses of Altimetry Errors Using Argo and GRACE Data. *Ocean Science*, 12(3):647–662.

Lellouche, J.-M., Le Galloudec, O., Drévillon, M., Régnier, C., Greiner, E., Garric, G., Ferry, N., Desportes, C., Testut, C.-E., Bricaud, C., Bourdallé-Badie, R., Tranchant, B., Benkiran, M., Drillet, Y., Daudin, A., and De Nicola, C. (2013). Evaluation of Global Monitoring and Forecasting Systems at Mercator Océan. *Ocean Science*, 9(1):57–81.

Lentge, K. (2024). A Possible ENSO Imprint on Ocean Bottom Pressure. Master's thesis, University of Bonn, Bonn.

Leroux, S., Penduff, T., Bessières, L., Molines, J.-M., Brankart, J.-M., Sérazin, G., Barnier, B., and Terray, L. (2018). Intrinsic and Atmospherically Forced Variability of the AMOC: Insights from a Large-Ensemble Ocean Hindcast. *Journal of Climate*, 31(3):1183–1203.

Li, X., Barriot, J.-P., Lou, Y., Zhang, W., Li, P., and Shi, C. (2023). Towards Millimeter-Level Accuracy in GNSS-Based Space Geodesy: A Review of Error Budget for GNSS Precise Point Positioning. *Surveys in Geophysics*, 44(6):1691–1780.

Liu, K., Zhang, F. L., Li, Z. Y., Feng, X. H., Li, K., Lu, Z. H., Schreiber, K. U., Luo, J., and Zhang, J. (2019). Large-Scale Passive Laser Gyroscope for Earth Rotation Sensing. *Optics Letters*, 44(11):2732.

Liu, X., Feng, X., Ciais, P., and Fu, B. (2020). Widespread Decline in Terrestrial Water Storage and its Link to Teleconnections Across Asia and Eastern Europe. *Hydrology and Earth System Sciences*, 24(7):3663–3676.

Liu, Z. and Alexander, M. (2007). Atmospheric Bridge, Oceanic Tunnel, and Global Climatic Teleconnections. *Reviews of Geophysics*, 45(2):2005RG000172.

Llovel, W., Penduff, T., Meyssignac, B., Molines, J.-M., Terray, L., Bessières, L., and Barnier, B. (2018). Contributions of Atmospheric Forcing and Chaotic Ocean Variability to Regional Sea Level Trends Over 1993–2015. *Geophysical Research Letters*, 45(24):13,405–13,413.

Löcher, A. and Kusche, J. (2021). A Hybrid Approach for Recovering High-Resolution Temporal Gravity Fields from Satellite Laser Ranging. *Journal of Geodesy*, 95(1):6.

Loomis, B. D., Luthcke, S. B., and Sabaka, T. J. (2019). Regularization and Error Characterization of GRACE Mascons. *Journal of Geodesy*, 93(9):1381–1398.

Lösler, M., Eschelbach, C., Klügel, T., and Riepl, S. (2021). ILRS Reference Point Determination Using Close Range Photogrammetry. *Applied Sciences*, 11(6):2785.

Lovato, T., Peano, D., and Butenschön, M. (2021). CMCC CMCC-ESM2 Model Output Prepared for CMIP6 CMIP Historical.

Ma, Q., Wang, J., Wang, F., Lyu, Y., and Zhang, Z. (2022). Interdecadal Modulation of ENSO-Related Anomalous Equatorial Intermediate Currents in the Western Pacific by the PDO. *Geophysical Research Letters*, 49(6).

Madden, R. A. and Julian, P. R. (1972). Description of Global-Scale Circulation Cells in the Tropics with a 40–50 Day Period. 29(6):1109–1123.

Maher, N., Milinski, S., and Ludwig, R. (2021). Large Ensemble Climate Model Simulations: Introduction, Overview, and Future Prospects for Utilising Multiple Types of Large Ensemble. *Earth System Dynamics*, 12(2):401–418.

Mantua, N. J. and Hare, S. R. (2002). The Pacific Decadal Oscillation. *Journal of Oceanography*, 58(1):35–44.

Mantua, N. J., Hare, S. R., Zhang, Y., Wallace, J. M., and Francis, R. C. (1997). A Pacific Interdecadal Climate Oscillation with Impacts on Salmon Production. 78(6):1069–1080.

Marcus, S. L., Chao, Y., Dickey, J. O., and Gegout, P. (1998). Detection and Modeling of Nontidal Oceanic Effects on Earth's Rotation Rate. *Science*, 281(5383):1656–1659.

Marcus, S. L., De Viron, O., and Dickey, J. O. (2010). Interannual Atmospheric Torque and El Niño–Southern Oscillation: Where Is the Polar Motion Signal? *Journal of Geophysical Research: Solid Earth*, 115(B12):2010JB007524.

Marcus, S. L., Dickey, J. O., and De Viron, O. (2001). Links between Intraseasonal (Extended MJO) and ENSO Timescales: Insights via Geodetic and Atmospheric Analysis. *Geophysical Research Letters*, 28(18):3465–3468.

Marshall, J., Adcroft, A., Hill, C., Perelman, L., and Heisey, C. (1997). A Finite-Volume, Incompressible Navier Stokes Model for Studies of the Ocean on Parallel Computers. *Journal of Geophysical Research*, 102:5753–5766.

Mathews, P. M., Herring, T. A., and Buffett, B. A. (2002). Modeling of Nutation and Precession: New Nutation Series for Nonrigid Earth and Insights into the Earth's Interior. *Journal of Geophysical Research: Solid Earth*, 107(B4).

Mayer, M., Fasullo, J. T., Trenberth, K. E., and Haimberger, L. (2016). ENSO-Driven Energy Budget Perturbations in Observations and CMIP Models. *Climate Dynamics*, 47(12):4009–4029.

McDougall, T. J. and Barker, P. M. (2011). Getting Started with TEOS-10 and the Gibbs Seawater (GSW) Oceanographic Toolbox. *Scor/Iapso WG*, 127(532):1–28.

McPhaden, M. J. (2015). Playing Hide and Seek with El Niño. *Nature Climate Change*, 5(9):791–795.

McPhaden, M. J., Zebiak, S. E., and Glantz, M. H. (2006). ENSO as an Integrating Concept in Earth Science. *Science*, 314(5806):1740–1745.

Meyrath, T. and van Dam, T. (2016). A Comparison of Interannual Hydrological Polar Motion Excitation from GRACE and Geodetic Observations. *Journal of Geodynamics*, 99:1–9.

Moritz, H. and Mueller, I. I. (1987). *Earth Rotation: Theory and Observation*. Ungar, New York.

Mound, J. E. (2005). Electromagnetic Torques in the Core and Resonant Excitation of Decadal Polar Motion. *Geophysical Journal International*, 160(2):721–728.

Munk, W. H. and MacDonald, G. J. F. (1960). *The Rotation of the Earth: A Geophysical Discussion*. Cambridge University Press, New York.

Naghibi, S., Delizo-Salabit, C., and Karabasov, S. (2023). Excitations of the Earth's Chandler Wobble and Length of Day by the Southern Ocean. In *Journées 2019: Time and General Relativity*, pages 25–32. Observatoire de la Cote D'Azur, Nice, France.

Nakiboglu, S. M. and Lambeck, K. (1980). Deglaciation Effects on the Rotation of the Earth. *Geophysical Journal International*, 62(1):49–58.

Nastula, J. and Salstein, D. (1999). Regional Atmospheric Angular Momentum Contributions to Polar Motion Excitation. *Journal of Geophysical Research: Solid Earth*, 104(B4):7347–7358.

Nastula, J., Wińska, M., Śliwińska, J., and Salstein, D. (2019). Hydrological Signals in Polar Motion Excitation – Evidence after Fifteen Years of the GRACE Mission. *Journal of Geodynamics*, 124:119–132.

Nastula, J., Śliwińska, J., Kur, T., Wińska, M., and Partyka, A. (2022). Preliminary Study on Hydrological Angular Momentum Determined from CMIP6 Historical Simulations. *Earth, Planets and Space*, 74(1):84.

Neef, L. J. and Matthes, K. (2012). Comparison of Earth Rotation Excitation in Data-Constrained and Unconstrained Atmosphere Models. *Journal of Geophysical Research: Atmospheres*, 117(D2).

Niu, Y., Cheng, X., Qin, J., Ou, N., Yang, C., and Huang, D. (2022). Mechanisms of Interannual Variability of Ocean Bottom Pressure in the Southern Indian Ocean. *Frontiers in Marine Science*, 9:916592.

NOAA National Geophysical Data Center (2009). ETOPO1 1 Arc-Minute Global Relief Model. Accessed 6 January 2023.

Nothnagel, A. (2009). Conventions on Thermal Expansion Modelling of Radio Telescopes for Geodetic and Astrometric VLBI. *Journal of Geodesy*, 83(8):787–792.

Orfanidis, S. J. (1996). *Introduction to Signal Processing*. Prentice Hall Signal Processing Series. Prentice Hall, Englewood Cliffs, N.J.

O'Rourke, A. K., Arbic, B. K., and Griffies, S. M. (2018). Frequency-Domain Analysis of Atmospherically Forced Versus Intrinsic Ocean Surface Kinetic Energy Variability in GFDL's CM2-O Model Hierarchy. *Journal of Climate*, 31(5):1789–1810.

Pais, A. and Hulot, G. (2000). Length of Day Decade Variations, Torsional Oscillations and Inner Core Superrotation: Evidence from Recovered Core Surface Zonal Flows. *Physics of the Earth and Planetary Interiors*, 118(3-4):291–316.

Penduff, T., Bernier, B., Terray, L., Bessières, L., Sérazin, G., Gregorio, S., Brankart, J.-M., Moine, M.-P., Brankart, J.-M., and Brasseur, P. (2014). Ensembles of Eddying Ocean Simulations for Climate. *CLIVAR Exchanges, Special Issue on High Resolution Ocean Climate Modelling*, 19:26–29.

Peng, Y. and Scales, W. A. (2021). Ionospheric Remote Sensing with GNSS. *Encyclopedia*, 1(4):1246–1256.

Petit, G. and Luzum, B. (2010). *IERS Conventions 2010. IERS Technical Note No 36*. Verlag des Bundesamtes für Kartographie und Geodäsie, Frankfurt am Main.

Pfeffer, J., Cazenave, A., and Barnoud, A. (2022). Analysis of the Interannual Variability in Satellite Gravity Solutions: Detection of Climate Modes Fingerprints in Water Mass Displacements across Continents and Oceans. *Climate Dynamics*, 58(3-4):1065–1084.

Phillips, T., Nerem, R. S., Fox-Kemper, B., Famiglietti, J. S., and Rajagopalan, B. (2012). The Influence of ENSO on Global Terrestrial Water Storage Using GRACE. *Geophysical Research Letters*, 39(16):2012GL052495.

Piecuch, C. G., Fukumori, I., Ponte, R. M., Schindelegger, M., Wang, O., and Zhao, M. (2022). Low-Frequency Dynamic Ocean Response to Barometric-Pressure Loading. *Journal of Physical Oceanography*.

Pilo, G. S., Oke, P. R., Coleman, R., Rykova, T., and Ridgway, K. (2018). Impact of Data Assimilation on Vertical Velocities in an Eddy Resolving Ocean Model. *Ocean Modelling*, 131:71–85.

Ponte, R. M. (1994). Understanding the Relation Between Wind- and Pressure-Driven Sea Level Variability. *Journal of Geophysical Research: Oceans*, 99(C4):8033–8039.

Ponte, R. M. (1997). Oceanic Excitation of Daily to Seasonal Signals in Earth Rotation: Results from a Constant-Density Numerical Model. *Geophysical Journal International*, 130(2):469–474.

Ponte, R. M. (1999). A Preliminary Model Study of the Large-Scale Seasonal Cycle in Bottom Pressure Over the Global Ocean. *Journal of Geophysical Research: Oceans*, 104(C1):1289–1300.

Ponte, R. M. (2006). Oceanic Response to Surface Loading Effects Neglected in Volume-Conserving Models. *Journal of Physical Oceanography*, 36:426–434.

Ponte, R. M. and Ali, A. H. (2002). Rapid Ocean Signals in Polar Motion and Length of Day. *Geophysical Research Letters*, 29(15):6–1–6–4.

Ponte, R. M. and Piecuch, C. G. (2014). Interannual Bottom Pressure Signals in the Australian–Antarctic and Bellingshausen Basins. *Journal of Physical Oceanography*, 44(5):1456–1465.

Ponte, R. M. and Rosen, R. D. (1994). Oceanic Angular Momentum and Torques in a General Circulation Model. *Journal of Physical Oceanography*, 24(9):1966–1977.

Ponte, R. M. and Rosen, R. D. (1999). Torques Responsible for Evolution of Atmospheric Angular Momentum During the 1982–83 El Niño. 56(19):3457–3462.

Ponte, R. M., Stammer, D., and Marshall, J. (1998). Oceanic Signals in Observed Motions of the Earth's Pole of Rotation. *Nature*, 391(6666):476–479.

Ponte, R. M., Stammer, D., and Wunsch, C. (2001). Improving Ocean Angular Momentum Estimates Using a Model Constrained by Data. *Geophysical Research Letters*, 28(9):1775–1778.

Provost, C., Renault, A., Barré, N., Sennéchael, N., Garçon, V., Sudre, J., and Huhn, O. (2011). Two Repeat Crossings of Drake Passage in Austral Summer 2006: Short-Term Variations and

Evidence for Considerable Ventilation of Intermediate and Deep Waters. *Deep-Sea Research Part II*, 58(25-26):2555–2571.

Qin, J., Cheng, X., Yang, C., Ou, N., and Xiong, X. (2022). Mechanism of Interannual Variability of Ocean Bottom Pressure in the South Pacific. *Climate Dynamics*, 59(7-8):2103–2116.

Quinn, K. J., Ponte, R. M., Heimbach, P., Fukumori, I., and Campin, J.-M. (2019). Ocean Angular Momentum from a Recent Global State Estimate, with Assessment of Uncertainties. *Geophysical Journal International*, 216(1):584–597.

Quinn, K. J., Ponte, R. M., and Tamisiea, M. E. (2015). Impact of Self-Attraction and Loading on Earth Rotation. *Journal of Geophysical Research: Solid Earth*, 120:4510–4521.

Ramírez, I. J. and Briones, F. (2017). Understanding the El Niño Costero of 2017: The Definition Problem and Challenges of Climate Forecasting and Disaster Responses. *International Journal of Disaster Risk Science*, 8(4):489–492.

Ratcliff, T. and Gross, R. S. (2019). *Combinations of Earth Orientation Measurements: SPACE2018, COMB2018, and POLE2018*. Jet Propulsion Laboratory, California Institute of Technology, Publication 19-7.

Ray, R. D. and Egbert, G. D. (2012). Fortnightly Earth Rotation, Ocean Tides and Mantle Anelasticity: Mf Tides and Anelasticity. *Geophysical Journal International*, 189(1):400–413.

Ray, R. D. and Erofeeva, S. Y. (2014). Long-Period Tidal Variations in the Length of Day. *Journal of Geophysical Research: Solid Earth*, 119(2):1498–1509.

Rekier, J., Chao, B. F., Chen, J., Dehant, V., Rosat, S., and Zhu, P. (2022). Earth's Rotation: Observations and Relation to Deep Interior. *Surveys in Geophysics*, 43(1):149–175.

Rhines, P. B. (2019). Mesoscale Eddies. In Cochran, J. K., Bokuniewicz, H. J., and Yager, P. L., editors, *Encyclopedia of Ocean Sciences (Third Edition)*, pages 115–127. Academic Press, Oxford.

Rietbroek, R., Brunnabend, S.-E., Kusche, J., Schröter, J., and Dahle, C. (2016). Revisiting the Contemporary Sea-Level Budget on Global and Regional Scales. *Proceedings of the National Academy of Sciences*, 113(6):1504–1509.

Rochester, M. and Crossley, D. (2009). Earth's Long-Period Wobbles: A Lagrangean Description of the Liouville Equations. *Geophysical Journal International*, 176(1):40–62.

Rodell, M., Houser, P., Jambor, U., Gottschalck, J., Mitchell, K., et al. (2004). The Global Land Data Assimilation System. *B. Am. Meteorol. Soc.*, 85(3):381–394.

Rohith, B., Paul, A., Durand, F., Testut, L., Prerna, S., Afroosa, M., Ramakrishna, S. S. V. S., and Shenoi, S. S. C. (2019). Basin-Wide Sea Level Coherency in the Tropical Indian Ocean Driven by Madden–Julian Oscillation. *Nature Communications*, 10(1):1257.

Rosat, S., Gillet, N., Boy, J.-P., Couhert, A., and Dumberry, M. (2021). Interannual Variations of Degree 2 from Geodetic Observations and Surface Processes. *Geophysical Journal International*, 225(1):200–221.

Rosen, R. D. and Salstein, D. A. (1983). Variations in Atmospheric Angular Momentum on Global and Regional Scales and the Length of Day. *Journal of Geophysical Research: Oceans*, 88(C9):5451–5470.

Rosen, R. D., Salstein, D. A., Eubanks, T. M., Dickey, J. O., and Steppe, J. A. (1984). An El Niño signal in atmospheric angular momentum and Earth rotation. *Science*, 225(4660):411–414.

Rothacher, M., Beutler, G., Herring, T. A., and Weber, R. (1999). Estimation of Nutation Using the Global Positioning System. *Journal of Geophysical Research: Solid Earth*, 104(B3):4835–4859.

Salstein, D. A. and Rosen, R. D. (1986). Earth Rotation as a Proxy for Interannual Variability in Atmospheric Circulation, 1860–Present. *Journal of Climate and Applied Meteorology*, 25(12):1870–1877.

Sasgen, I., Dobslaw, H., Martinec, Z., and Thomas, M. (2010). Satellite Gravimetry Observation of Antarctic Snow Accumulation Related to ENSO. *Earth and Planetary Science Letters*, 299(3-4):352–358.

Scaife, A. A., Hermanson, L., Van Niekerk, A., Andrews, M., Baldwin, M. P., Belcher, S., Bett, P., Comer, R. E., Dunstone, N. J., Geen, R., Hardiman, S. C., Ineson, S., Knight, J., Nie, Y., Ren, H.-L., and Smith, D. (2022). Long-Range Predictability of Extratropical Climate and the Length of Day. *Nature Geoscience*, 15(10):789–793.

Schartner, M., Kern, L., Nothnagel, A., Böhm, J., and Soja, B. (2021). Optimal VLBI Baseline Geometry for UT1-UTC Intensive Observations. *Journal of Geodesy*, 95(7):75.

Schindelegger, M., Böhm, S., Böhm, J., and Schuh, H. (2013a). Atmospheric Effects on Earth Rotation. In Böhm, J. and Schuh, H., editors, *Atmospheric Effects in Space Geodesy*, pages 181–231. Springer Berlin Heidelberg, Berlin, Heidelberg.

Schindelegger, M., Green, J. A. M., Wilmes, S.-B., and Haigh, I. D. (2018). Can We Model the Effect of Observed Sea Level Rise on Tides? *Journal of Geophysical Research: Oceans*, 123(7):4593–4609.

Schindelegger, M., Salstein, D., and Böhm, J. (2013b). Recent Estimates of Earth-Atmosphere Interaction Torques and Their Use in Studying Polar Motion Variability. *Journal of Geophysical Research: Solid Earth*, 118(8):4586–4598.

Schreiber, K. U., Hugentobler, U., Kodet, J., Stellmer, S., Klügel, T., and Wells, J.-P. R. (2025). Gyroscope Measurements of the Precession and Nutation of Earth's Axis. *Science Advances*, 11(36):eadx6634.

Schreiber, K. U., Kodet, J., Hugentobler, U., Klügel, T., and Wells, J.-P. R. (2023). Variations in the Earth's Rotation Rate Measured with a Ring Laser Interferometer. *Nature Photonics*, 17(12):1054–1058.

Schreiber, K. U., Velikoseltsev, A., Rothacher, M., Klügel, T., Stedman, G. E., and Wiltshire, D. L. (2004). Direct Measurement of Diurnal Polar Motion by Ring Laser Gyroscopes. *Journal of Geophysical Research: Solid Earth*, 109(B6):2003JB002803.

Schreiber, K. U. and Wells, J.-P. R. (2013). Invited Review Article: Large Ring Lasers for Rotation Sensing. *Review of Scientific Instruments*, 84(4):041101.

Schuh, H. and Behrend, D. (2012). VLBI: A Fascinating Technique for Geodesy and Astrometry, shorttitle = VLBI. *Journal of Geodynamics*, 61:68–80.

Schuh, H. and Böhm, J. (2013). Very Long Baseline Interferometry for Geodesy and Astrometry. In Xu, G., editor, *Sciences of Geodesy - II*, pages 339–376. Springer Berlin Heidelberg, Berlin, Heidelberg.

Scott Yiu, Y. Y. and Maycock, A. C. (2019). On the Seasonality of the El Niño Teleconnection to the Amundsen Sea Region. *Journal of Climate*, 32(15):4829–4845.

Sérazin, G., Penduff, T., Barnier, B., Molines, J.-M., Arbic, B. K., Müller, M., and Terray, L. (2018). Inverse Cascades of Kinetic Energy as a Source of Intrinsic Variability: A Global OGCM Study. *Journal of Physical Oceanography*, 48(6):1385–1408.

Sérazin, G., Penduff, T., Grégorio, S., Barnier, B., Molines, J.-M., and Terray, L. (2015). Intrinsic Variability of Sea Level from Global Ocean Simulations: Spatiotemporal Scales. *Journal of Climate*, 28(10):4279–4292.

Soffel, M. and Frutos, F. (2016). On the Usefulness of Relativistic Space-Times for the Description of the Earth's Gravitational Field. *Journal of Geodesy*, 90(12):1345–1357.

Soffel, M. and Langhans, R. (2013). *Space-Time Reference Systems*. Astronomy and Astrophysics Library. Springer, Berlin Heidelberg.

Somerville, W. B. (1972). The Description of Foucault's Pendulum. *Quarterly Journal of the Royal Astronomical Society*, 13:40–62. ADS Bibcode: 1972QJRAS..13...40S.

Sommeria, J. (2017). Foucault and the Rotation of the Earth. *Comptes Rendus Physique*, 18(9-10):520–525.

Stammer, D., Balmaseda, M., Heimbach, P., Köhl, A., and Weaver, A. (2016). Ocean Data Assimilation in Support of Climate Applications: Status and Perspectives. *Annual Review of Marine Science*, 8(1):491–518.

Stepanov, V. N. and Hughes, C. W. (2006). Propagation of Signals in Basin-scale Ocean Bottom Pressure from a Barotropic Model. *Journal of Geophysical Research: Oceans*, 111(C12).

Stewart, R. H. (2008). *Introduction to Physical Oceanography*. Texas A & M University.

Stocker, T. (2016). Introduction to Climate Modeling. Lecture notes, FS 2016, University of Bern.

Storto, A., Alvera-Azcárate, A., Balmaseda, M. A., Barth, A., Chevallier, M., Counillon, F., Domingues, C. M., Drevillon, M., Drillet, Y., Forget, G., Garric, G., Haines, K., Hernandez, F., Iovino, D., Jackson, L. C., Lellouche, J.-M., Masina, S., Mayer, M., Oke, P. R., Penny, S. G., Peterson, K. A., Yang, C., and Zuo, H. (2019). Ocean Reanalyses: Recent Advances and Unsolved Challenges. *Frontiers in Marine Science*, 6.

Stuck, J., Güntner, A., and Merz, B. (2006). ENSO impact on simulated South American hydroclimatology. *Advances in Geosciences*, 6:227–236.

Swenson, S., Chambers, D., and Wahr, J. (2008). Estimating Geocenter Variations from a Combination of GRACE and Ocean Model Output. *Journal of Geophysical Research: Solid Earth*, 113:B8.

Tapley, B. D., Watkins, M. M., Flechtner, F., Reigber, C., Bettadpur, S., Rodell, M., Sasgen, I., Famiglietti, J. S., Landerer, F. W., Chambers, D. P., Reager, J. T., Gardner, A. S., Save, H., Ivins, E. R., Swenson, S. C., Boening, C., Dahle, C., Wiese, D. N., Dobslaw, H., Tamisiea, M. E., and Velicogna, I. (2019). Contributions of GRACE to Understanding Climate Change. *Nature Climate Change*, 9(5):358–369.

Tatebe, H. and Watanabe, M. (2018). MIROC MIROC6 Model Output Prepared for CMIP6 CMIP Historical.

Tavella, P. and Premoli, A. (1994). Estimating the Instabilities of N Clocks by Measuring Differences of Their Readings. *Metrologia*, 30(5):479–486.

Tavernier, G., Fagard, H., Feissel-Vernier, M., Lemoine, F., Noll, C., Ries, J., Soudarin, L., and Willis, P. (2005). The International DORIS Service. *Advances in Space Research*, 36(3):333–341.

Teke, K., Kayıkçı, E. T., Böhm, J., and Schuh, H. (2012). Modelling Very Long Baseline Interferometry (VLBI) Observations. *Journal of Geodesy and Geoinformation*, 1(1):17–26.

Teunissen, P. J. and Montenbruck, O., editors (2017). *Springer Handbook of Global Navigation Satellite Systems*. Springer International Publishing, Cham.

Torge, W. (2003). *Geodäsie*. de Gruyter Lehrbuch. de Gruyter, Berlin, 2., vollst. überarb. und erw. aufl edition.

Trenberth, K. E., Caron, J. M., Stepaniak, D. P., and Worley, S. (2002). Evolution of El Niño–Southern Oscillation and Global Atmospheric Surface Temperatures. *Journal of Geophysical Research: Atmospheres*, 107(D8).

Uebbing, B., Kusche, J., Rietbroek, R., and Landerer, F. W. (2019). Processing Choices Affect Ocean Mass Estimates From GRACE. *Journal of Geophysical Research: Oceans*, 124(2):1029–1044.

Venaille, A., Vallis, G. K., and Smith, K. S. (2011). Baroclinic Turbulence in the Ocean: Analysis with Primitive Equation and Quasigeostrophic Simulations. *Journal of Physical Oceanography*, 41(9):1605–1623.

Verdon, D. C. and Franks, S. W. (2006). Long-term Behaviour of ENSO: Interactions with the PDO over the Past 400 Years Inferred from Paleoclimate Records. *Geophysical Research Letters*, 33(6).

Vinogradova, N. T., Ponte, R. M., Quinn, K. J., Tamisiea, M. E., Campin, J.-M., and Davis, J. L. (2015). Dynamic adjustment of the ocean circulation to self-attraction and loading effects. *Journal of Physical Oceanography*, 45(3):678–689.

Wahr, J. M. (1982). The Effects of the Atmosphere and Oceans on the Earth's Wobble – I. Theory. *Geophysical Journal International*, 70(2):349–372.

Wahr, J. M. (1983). The Effects of the Atmosphere and Oceans on the Earth's Wobble and on the Seasonal Variations in the Length of Day — II. Results. *Geophysical Journal International*, 74(2):451–487.

Walker, G. T. and Bliss, E. W. (1932). World Weather V. Memories of the Royal Meteorological Society. 4:53–84.

Wang, C., Deser, C., Yu, J.-Y., DiNezio, P., and Clement, A. (2017). El Niño and Southern Oscillation (ENSO): A Review. In Glynn, P. W., Manzello, D. P., and Enochs, I. C., editors, *Coral Reefs of the World*, pages 85–106. Springer Netherlands, Dordrecht.

Wang, G. and Schimel, D. (2003). Climate Change, Climate Modes, and Climate Impacts. *Annual Review of Environment and Resources*, 28(1):1–28. Publisher: Annual Reviews.

Wang, J., Ge, M., Glaser, S., Balidakis, K., Heinkelmann, R., and Schuh, H. (2022). Improving VLBI Analysis by Tropospheric Ties in GNSS and VLBI Integrated Processing. *Journal of Geodesy*, 96(4):32.

Wang, X., Slawinska, J., and Giannakis, D. (2020). Extended-Range Statistical ENSO Prediction through Operator-Theoretic Techniques for Nonlinear Dynamics. *Scientific Reports*, 10(1).

Wang, Y.-C., Tseng, W.-L., Chen, Y.-L., Lee, S.-Y., Hsu, H.-H., and Liang, H.-C. (2023). ENSO Statistics, Teleconnections, and Atmosphere–Ocean Coupling in the Taiwan Earth System Model Version 1. *Geoscientific Model Development*, 16(15):4599–4616.

Watkins, M. M., Wiese, D. N., Yuan, D.-N., Boening, C., and Landerer, F. W. (2015). Improved Methods for Observing Earth's Time Variable Mass Distribution with GRACE Using Spherical Cap Mascons: Improved Gravity Observations from GRACE. *Journal of Geophysical Research: Solid Earth*, 120(4):2648–2671.

Weijer, W. (2010). An Almost-Free Barotropic Mode in the Australian-Antarctic Basin. *Geophysical Research Letters*, 37(10).

Weijer, W. (2015). Modal Variability in the Southeast Pacific Basin: Energetics of the 2009 Event. *Deep-Sea Research Part II: Topical Studies in Oceanography*, 114:3–11.

Welch, P. (1967). The Use of Fast Fourier Transform for the Estimation of Power Spectra: A Method Based on Time Averaging over Short, Modified Periodograms. *IEEE Transactions on Audio and Electroacoustics*, 15(2):70–73.

Willis, P., Jayles, C., and Bar-Sever, Y. (2006). DORIS: From Orbit Determination for Altimeter Missions to Geodesy. *Comptes Rendus. Géoscience*, 338(14-15):968–979.

Wińska, M. (2022). A Comparative Study of Interannual Oscillation Models for Determining Geophysical Polar Motion Excitations. *Remote Sensing*, 14(1):147.

Wolter, K. and Timlin, M. S. (1993). Monitoring ENSO in COADS with a Seasonally Adjusted Principal Component Index. In *Proceedings of the 17th Climate Diagnostics Workshop*, Norman, OK, NOAA/NMC/CAC, NSSL, Oklahoma Climate Survey, CIMMS and the School of Meteorology, University of Oklahoma.

Wolter, K. and Timlin, M. S. (1998). Measuring the Strength of ENSO Events: How Does 1997/98 Rank? *Weather*, 53(9):315–324.

Woodward, R. S. (1888). On the Form and Position of the Sea Level with Special References to its Dependence on Superficial Masses Symmetrically Disposed About a Normal to the Earth's Surface. Technical report, Govt. Print. Off.

World Meteorological Organization (2025). El Niño/La Niña Update. Technical Report 2025/02, Geneva.

Wunsch, C. and Heimbach, P. (2013). Dynamically and Kinematically Consistent Global Ocean Circulation and Ice State Estimates. In *Int. Geophys*, volume 103, pages 553–579. Elsevier.

Wunsch, C. and Stammer, D. (1997). Atmospheric Loading and the Oceanic "Inverted Barometer" Effect. *Reviews of Geophysics*, 35(1):79–107.

Yan, H. and Chao, B. F. (2012). Effect of Global Mass Conservation among Geophysical Fluids on the Seasonal Length of Day Variation. *Journal of Geophysical Research: Solid Earth*, 117(B2).

Yoder, C. F., Williams, J. G., and Parke, M. E. (1981). Tidal Variations of Earth Rotation. *Journal of Geophysical Research: Solid Earth*, 86(B2):881–891.

Yu, N., Liu, H., Chen, G., Chen, W., Ray, J., Wen, H., and Chao, N. (2021). Analysis of Relationships Between ENSO Events and Atmospheric Angular Momentum Variations. *Earth and Space Science*, 8(12):e2021EA002030.

Yukimoto, S., Koshiro, T., Kawai, H., Oshima, N., Yoshida, K., Urakawa, S., Tsujino, H., Deushi, M., Tanaka, T., Hosaka, M., Yoshimura, H., Shindo, E., Mizuta, R., Ishii, M., Obata, A., and Adachi, Y. (2019). MRI MRI-ESM2.0 Mdel Output Prepared for CMIP6 CMIP Historical.

Zhao, M., Ponte, R. M., and Penduff, T. (2023). Global-Scale Random Bottom Pressure Fluctuations from Oceanic Intrinsic Variability. *Science Advances*, 9(29):eadg0278.

Zhao, M., Ponte, R. M., Penduff, T., Close, S., Llovel, W., and Molines, J.-M. (2021). Imprints of Ocean Chaotic Intrinsic Variability on Bottom Pressure and Implications for Data and Model Analyses. *Geophysical Research Letters*, 48(24):e2021GL096341.

Zheng, D., Ding, X., Zhou, Y., and Chen, Y. (2003). Earth Rotation and ENSO Events: Combined Excitation of Interannual LOD Variations by Multiscale Atmospheric Oscillations. *Global and Planetary Change*, 36(1-2):89–97.

Zhou, Y. H., Chen, J. L., Liao, X. H., and Wilson, C. R. (2005). Oceanic Excitations on Polar Motion: A Cross Comparison among Models. *Geophysical Journal International*, 162(2):390–398.

Zuo, H., Balmaseda, M. A., and Mogensen, K. (2017). The New Eddy-Permitting ORAP5 Ocean Reanalysis: Description, Evaluation and Uncertainties in Climate Signals. *Climate Dynamics*, 49(3):791–811.

Zuo, H., Balmaseda, M. A., Tietsche, S., Mogensen, K., and Mayer, M. (2019). The ECMWF Operational Ensemble Reanalysis–Analysis System for Ocean and Sea Ice: A Description of the System and Assessment. *Ocean Science*, 15(3):779–808.

A. Supporting Information for “ENSO modulates the oceanic excitation of polar motion”

Contents of this file

1. Text S1 to S4
2. Figures S1 to S15
3. Tables S1 to S2

A.1. Introduction

This file provides additional information related to the calculation of the Oceanic Niño Index (ONI), the removal of co-seismic signals from the satellite gravimetry data (Section 2.2 in the main article), the design of the spatial weights used to derive the ENSO-related OAM series from the CMIP6 lagged regression fields (Section 3.2), and the polar motion excitation formalism. We further include all supplementary figures and tables mentioned in the main text.

A.2. Text S1. ONI Computation

A central metric for quantifying the intensity of ENSO is the ONI, which is defined as the three-month moving average of sea surface temperature (SST) anomalies in the Niño 3.4 region (5°N–5°S, 120°W–170°W). Our method of calculating these SST anomalies and ONI follows the strategy presently adopted by NOAA National Weather Service (Climate Prediction Center, 2017). Specifically, to prevent the long-term surface warming in the Niño 3.4 region from affecting the representation of ENSO variability, 30-year base periods are employed in the calculation of the SST anomalies for consecutive five-year periods. For instance, ONI values during 1950–1955 are formed with a 1936–1965 base period, while ONI values during 1956–1960 use a 1941–1970

base period, and so forth. However, calculation of the base periods for the first and last year on record is not feasible due to the unavailability of data. As a workaround, the first or last complete base period is extended (i.e., the base period from 1991 to 2020 is used when calculating the current NOAA ONI values). The index values themselves are computed as three-month moving average of the SST anomalies (SSTA), following

$$\mathrm{ONI}(\tau) = \frac{1}{3} \sum_{i=\tau-1}^{t+1} \mathrm{SSTA}(i), \tag{A.1}$$

where i represents the current month and τ is the centred month.

A.3. Text S2. Earthquake Correction

To correct the GRACE data for earthquake effects, we first create a circled mask with 15° radius around each epicenter. Then, the time series of each cell within the masked area are analyzed for potential co-seismic signals. To that end, we compute differences of consecutive values in the time series check if the largest difference matches in time within ± 1 month of real earthquakes. Subsequently, all p_b values that follow the discontinuity are adjusted to the magnitudes before the jump, the step itself is removed and replaced using autoregressive modeling based on the corrected p_b anomalies. Since several earthquakes can occur in vicinity to each other at different times, the previous steps are repeated until all jumps have been removed from the data set.

A.4. Text S3. Design of Spatial Weights

The spatial weights in the calculation of OAM changes from CMIP6 p_b anomalies and barotropic velocities are based on a significance test of the local correlation with ONI, using Pearson's correlation R and Student's t distribution. The test statistic $\mathcal{T}$ reads

$$\mathcal{T} = |R| \cdot \sqrt{\frac{N-2}{1-R^2}}, \tag{A.2}$$

where $N-2$ represents the (effective) degrees of freedom with the number of uncorrelated observations being N. The test statistic is evaluated for statistical significance by comparing it with the table value $t_{\alpha,N-2}$ of the Student distribution for significance level α. $\mathcal{T}$ is statistically significant if

$$\mathcal{T} > t_{\alpha,N-2}. \tag{A.3}$$

The spatial weights are then derived using different values of α corresponding to confidence levels in the range 68–100%, as listed in Table A.2. The computation of R and the related t test

are repeated for each lag at every grid point.

A.5. Text S4. Percentage of Variance Explained

The Percentage of Variance Explained (PVE) is a statistical quantity indicating the proportion to which a model or data set X accounts for the variance exhibited by a reference data set Y. It is given by

$$\text{PVE} = 100 \cdot \left(1 - \frac{\text{var}(Y - X)}{\text{var}(Y)}\right). \tag{A.4}$$

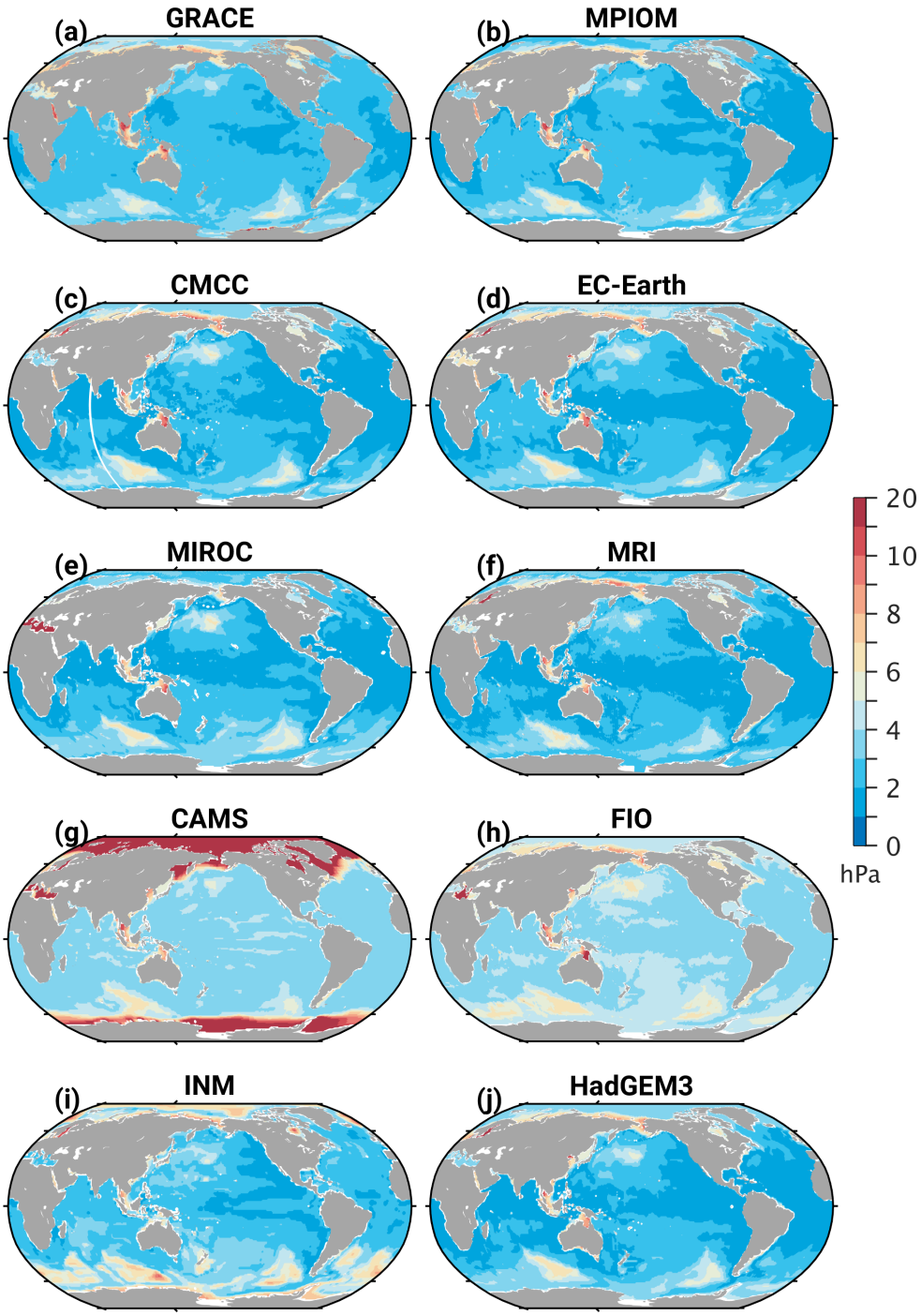

Figure A.1: Root-Mean Square (RMS) maps of the p_b fields in hPa for (a) GRACE, (b) MPIOM, and (c–j) different CMIP6 models.

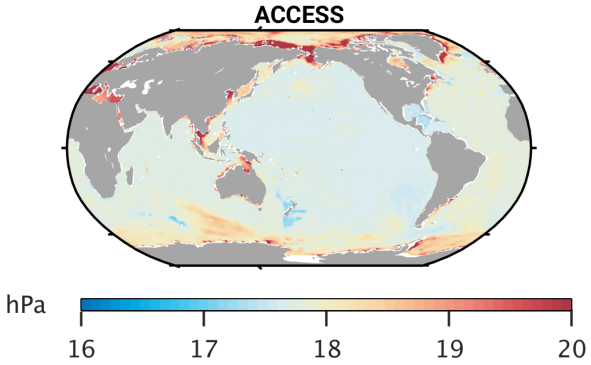

Figure A.2: As in Figure A.1 but for ACCESS with different limits.

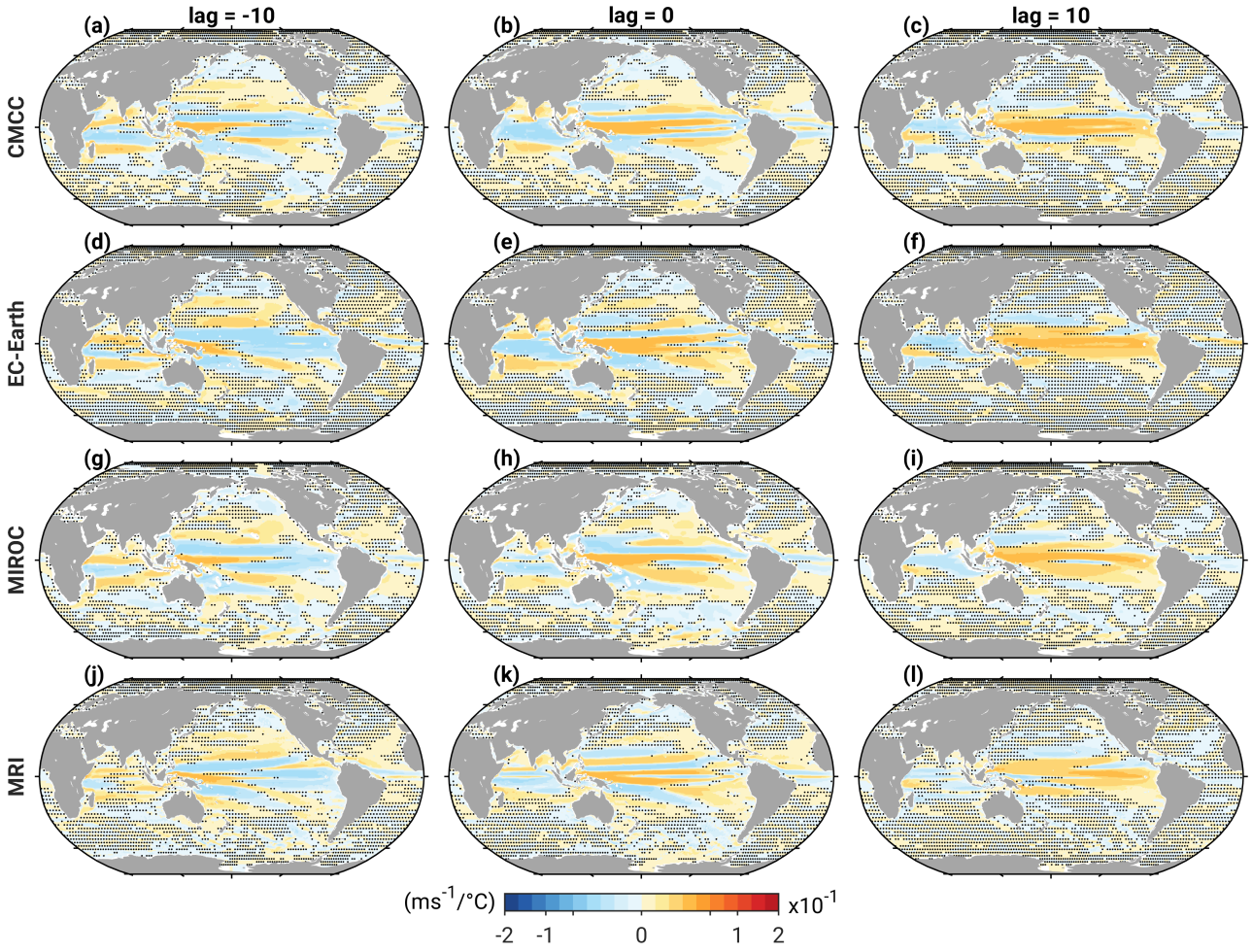

Figure A.3: Results of the lagged regression of the monthly zonal barotropic (u) velocities from (a–c) CMCC, (d–f) EC-Earth, (g–i) MRI, and (j–l) MIROC and for the three selected lags -10 (left column), 0 (middle column), and 10 (right column). The black points mark statistically insignificant values at 90% confidence.

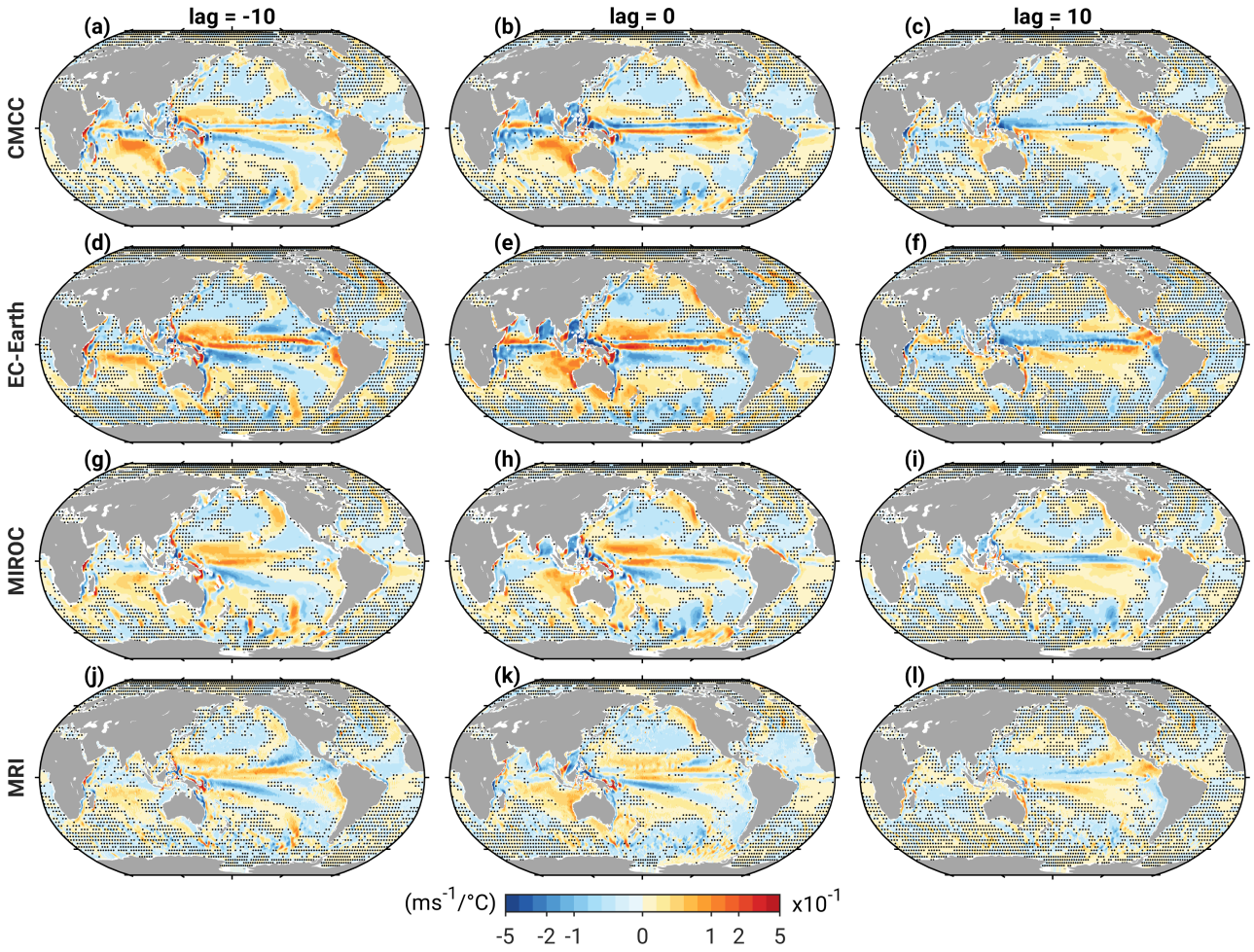

Figure A.4: As in Figure A.3 but for the meridional barotropic (v) velocities.

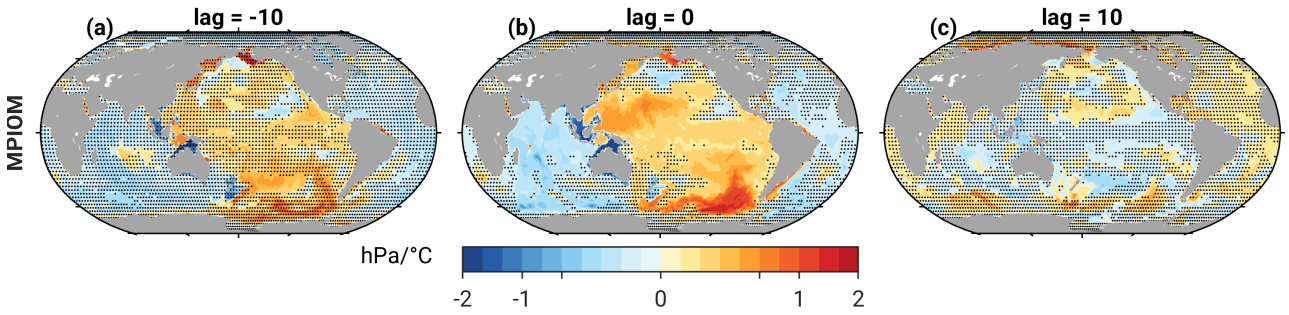

Figure A.5: As in Figure A.3 but for p_b fields of MPIOM.

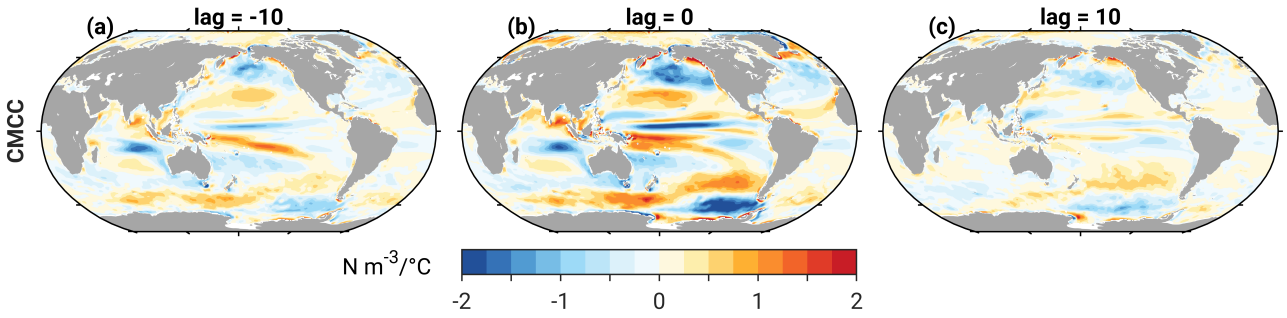

Figure A.6: As in Figure A.3 but for wind stress curls derived from wind stress τ_x, τ_y of CMCC.

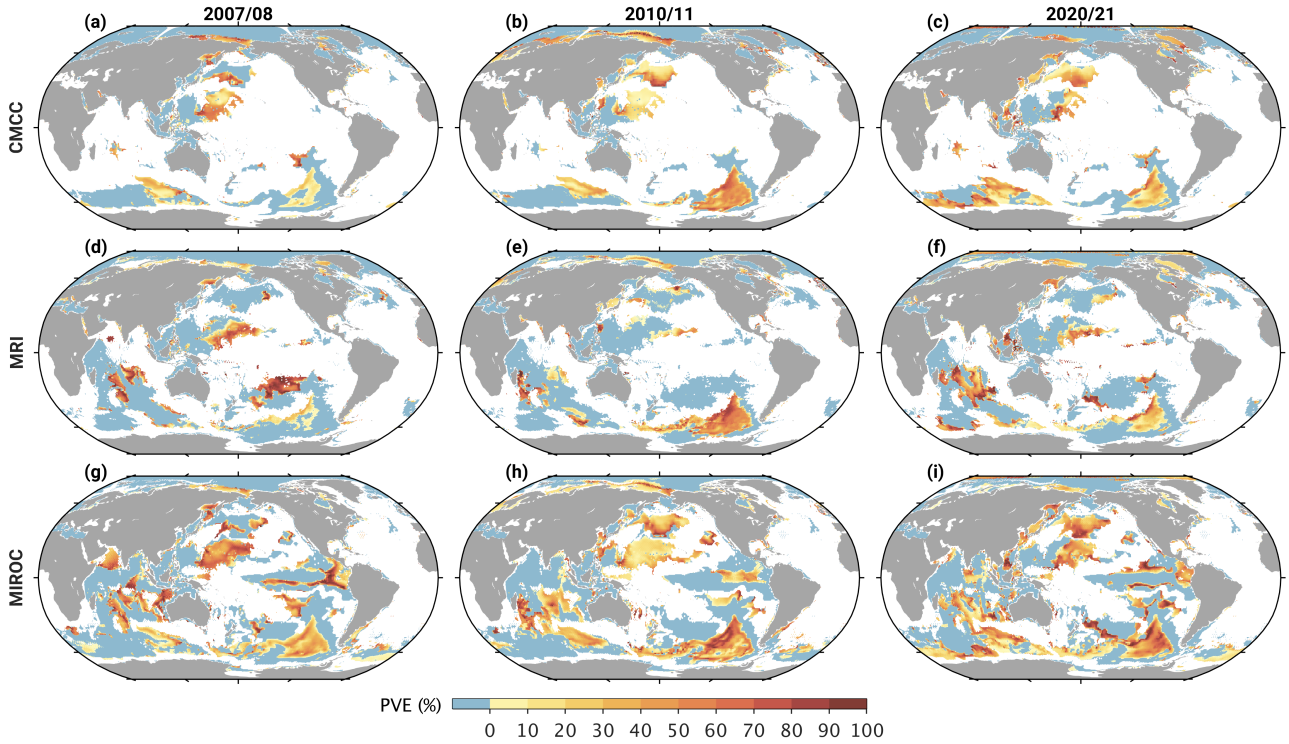

Figure A.7: Percentage of variance explained in the interannually filtered GRACE-based p_b fields by ENSO signals as deduced from three selected CMIP6 models (a–c) CMCC, (d–f) EC-Earth, (g–i) and MIROC. Results are shown for three La Niña events: 2007/08 (ONI $= -1.6$°C, left column), 2010/11 (ONI $= -1.6$°C, middle column), and 2020/21 (ONI $= -1.3$°C, right column). For each event, we use 21 lags ($\pm$10 months). White areas indicate grid points with regression coefficients smaller than 0.15 hPa/°C.

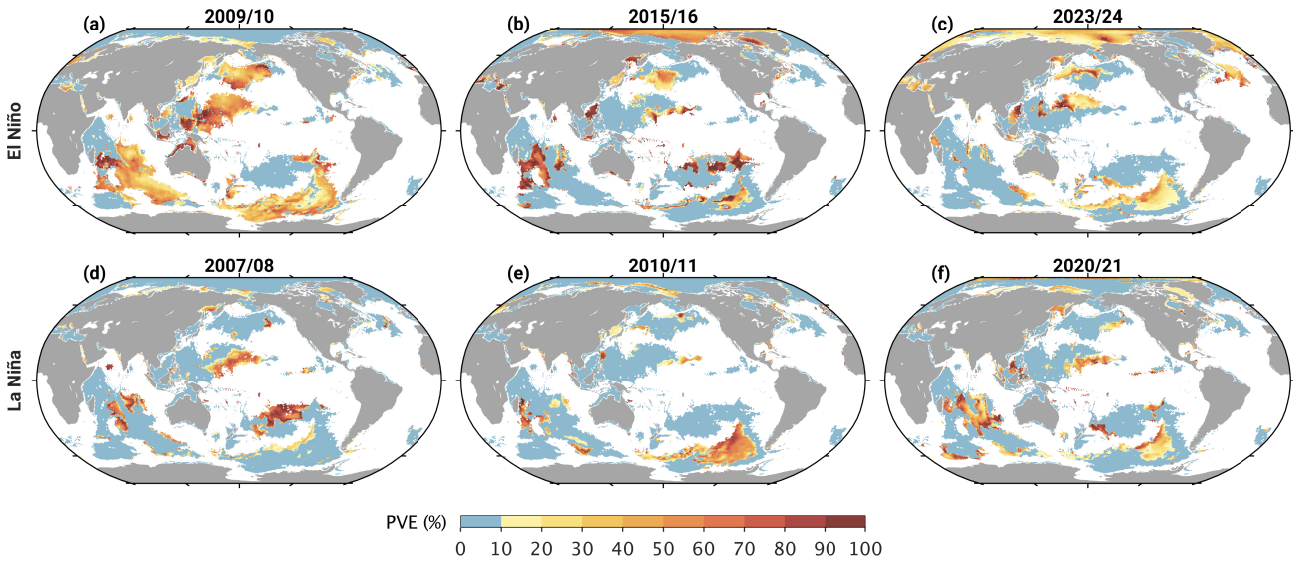

Figure A.8: Percentage of variance explained in the interannually filtered GRACE-based p_{b} fields by ENSO signals, derived from MRI, for three El Niño events (top row) and three La Niña events (bottom row). The respective ONI values are (a–c) 1.6°C, 2.6°C, 2.0°C, and (d–f) −1.6°C, −1.6°C, −1.3°C. Lags and masking are as in Figure A.7.

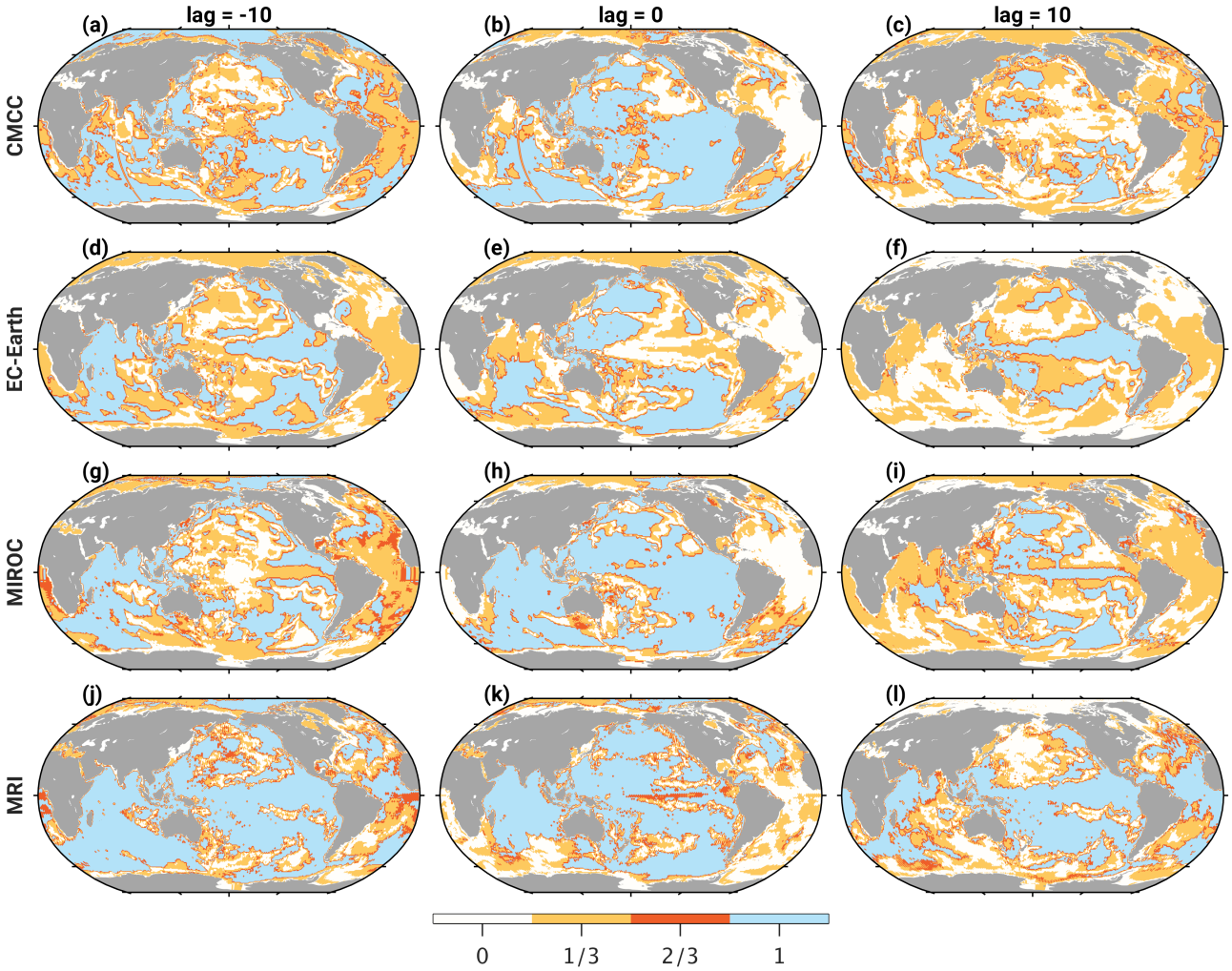

Figure A.9: Spatial weights applied to the p_{b} fields for the four different models (a–c) CMCC, (d–f) EC-Earth, (g–i) MRI, and (j–l) MIROC and for the four selected lags (a,d,g,j) -10, (b,e,h,k) 0, and (c,f,i,l) 10.

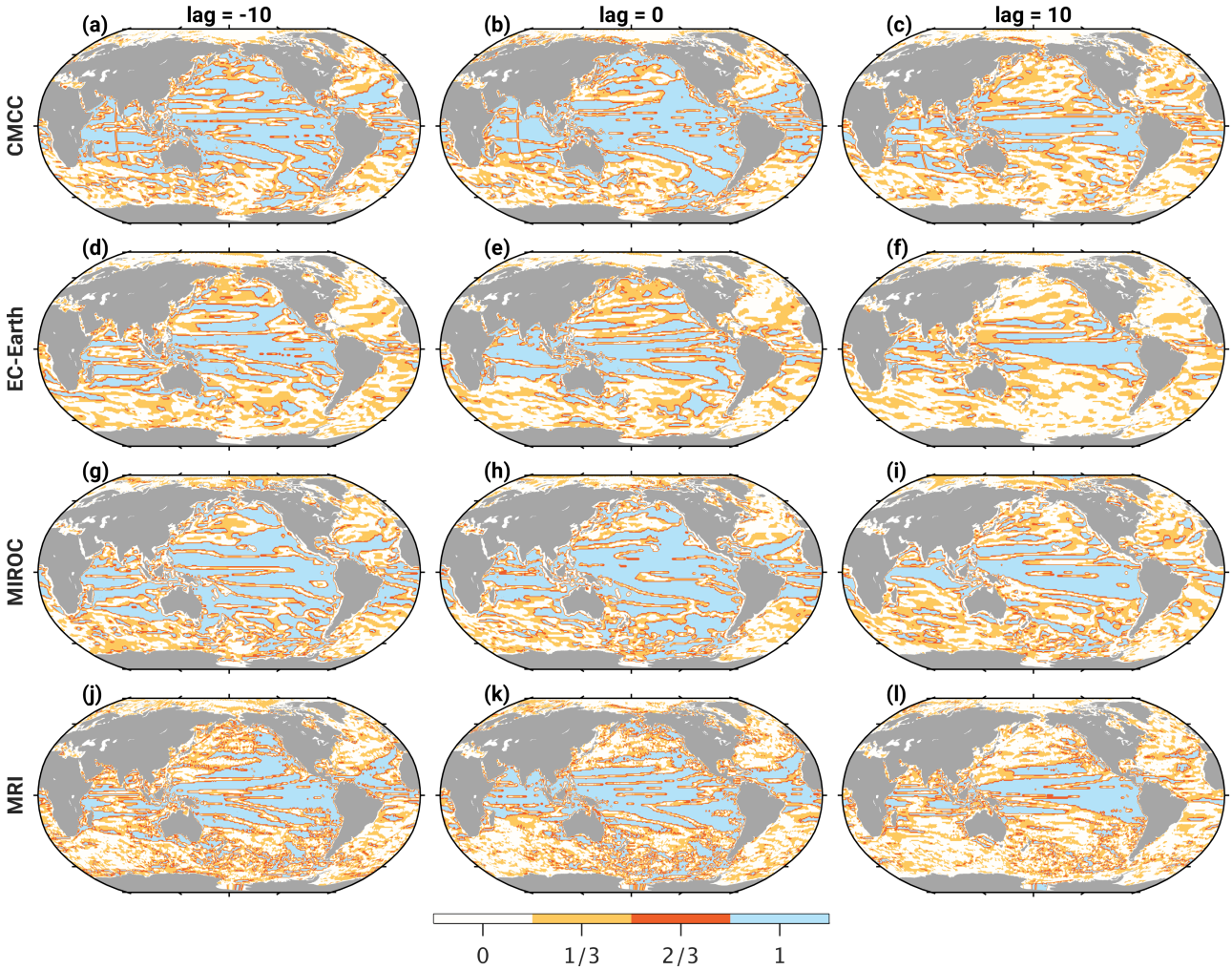

Figure A.10: As in Figure A.9 but for the zonal barotropic (u) velocities.

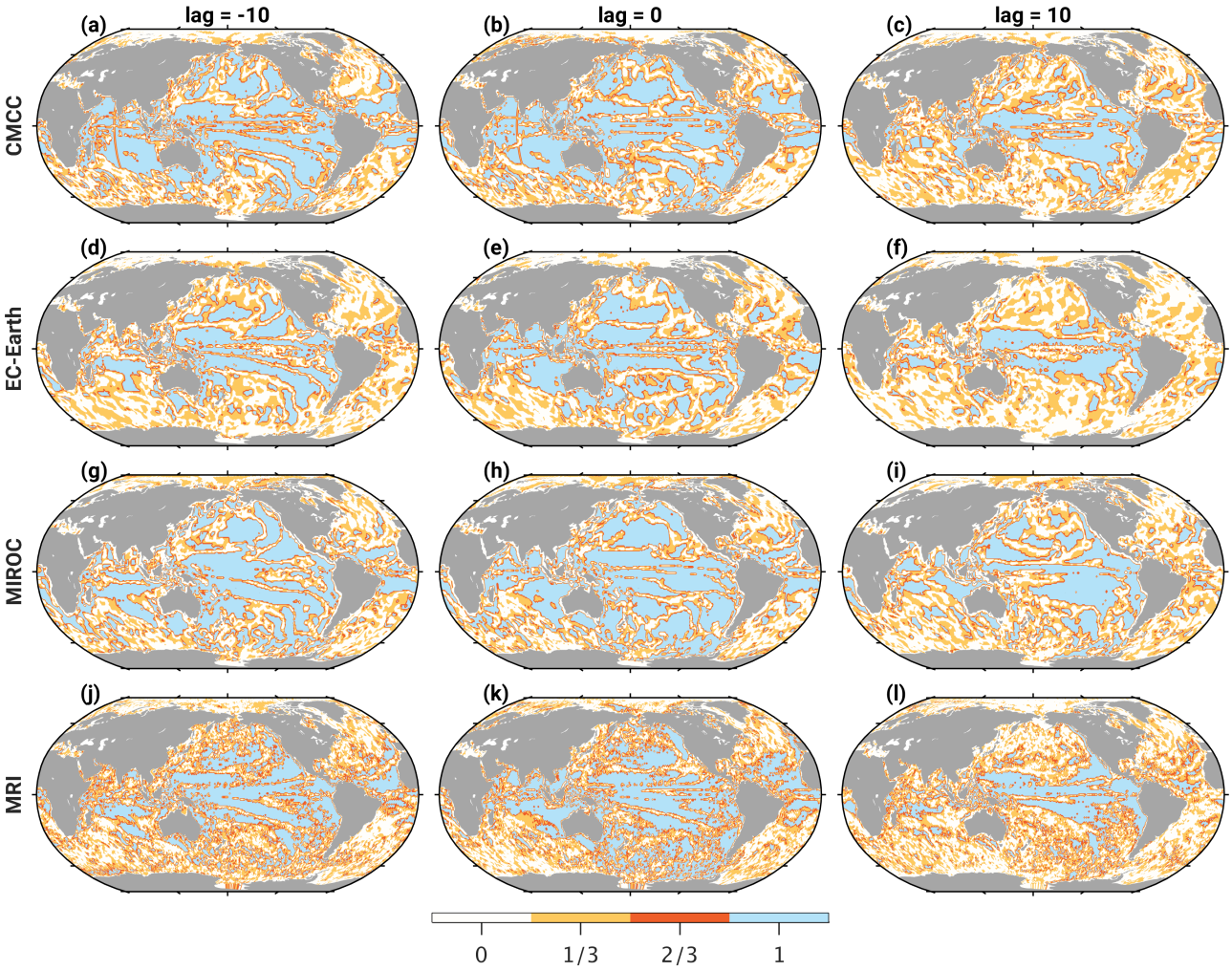

Figure A.11: As in Figure A.9 but for the meridional barotropic (v) velocities.

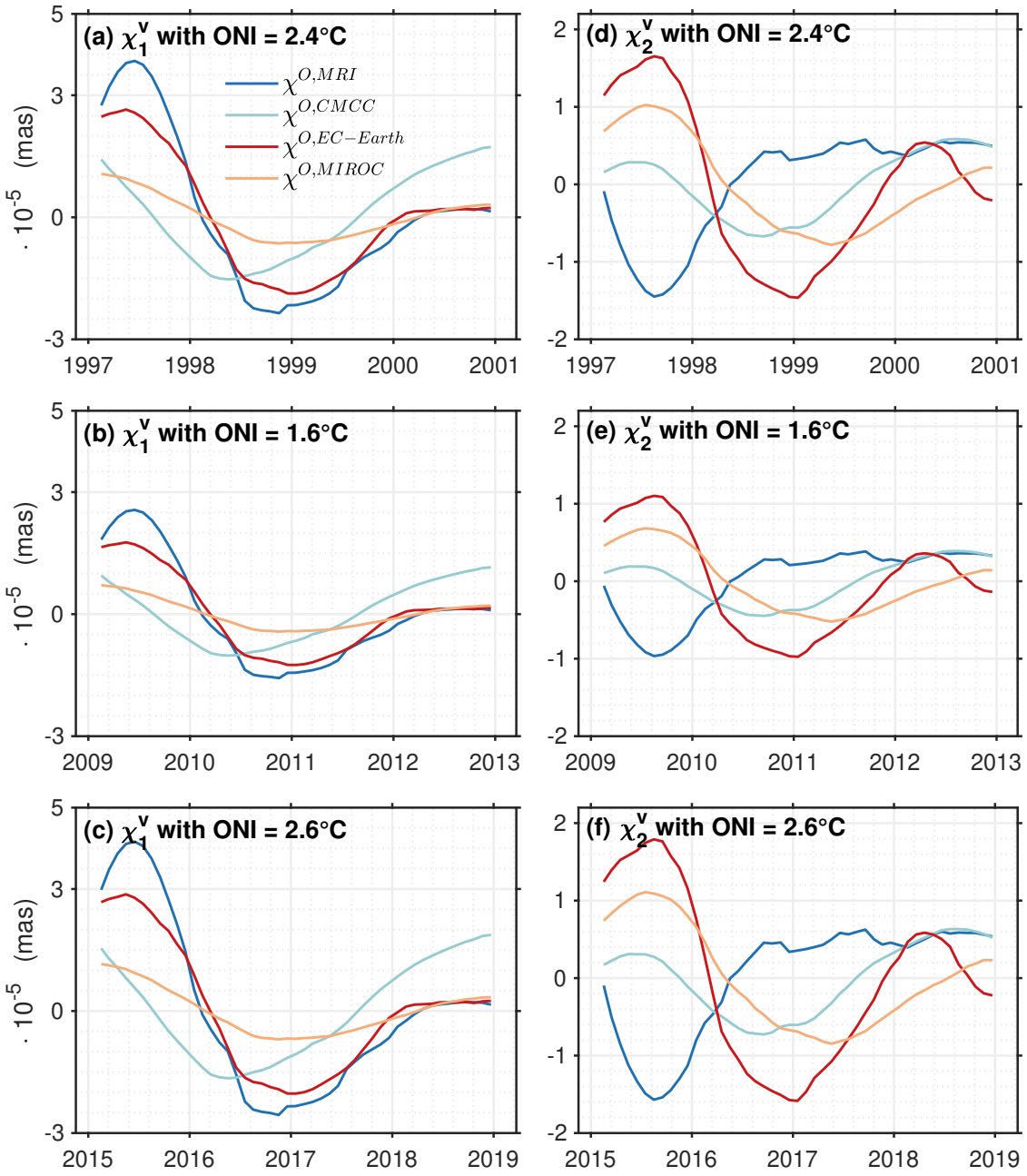

Figure A.12: ENSO-induced oceanic excitation signals in the motion term components χ_1^v (a–c) and χ_2^v (d–f) derived from CMCC ($\chi^{O,CMCC}$, light blue), EC-Earth ($\chi^{O,EC}$, red), MRI ($\chi^{O,MRI}$, blue) and MIROC ($\chi_2^{O,MIROC}$, orange) for the El Niño events in 1997/98 (left column), 2009/10 (middle column), and 2015/16 (right column). Note the difference in the y-axis limit compared to Figure 4 in the main text and Figure A.13.

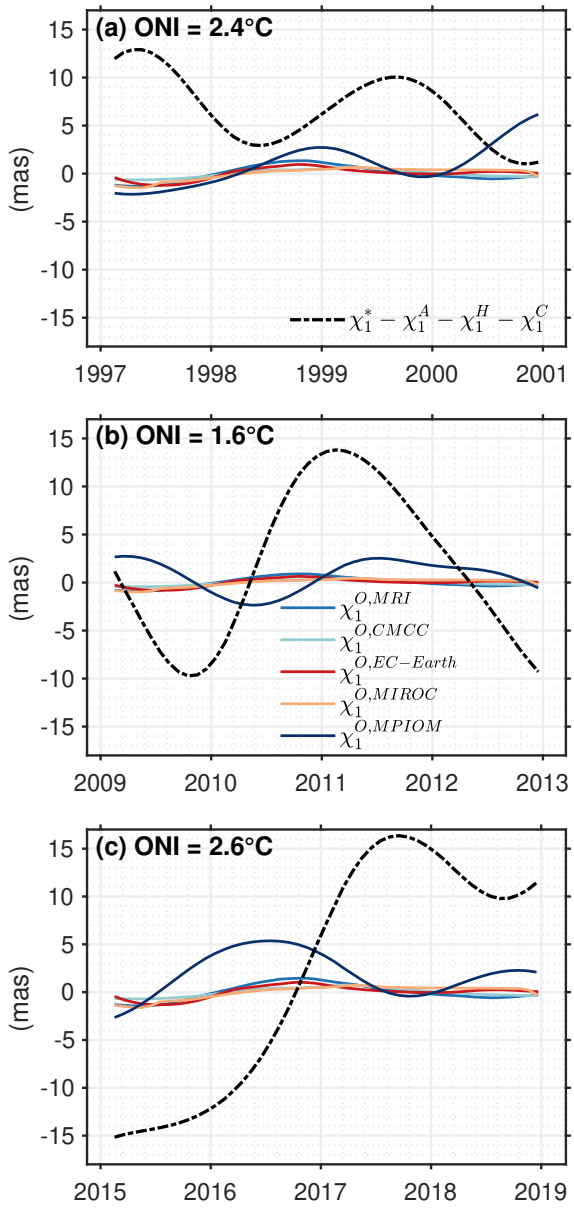

Figure A.13: As Figure 4 in the main text but for the χ_1^{O} mass term.

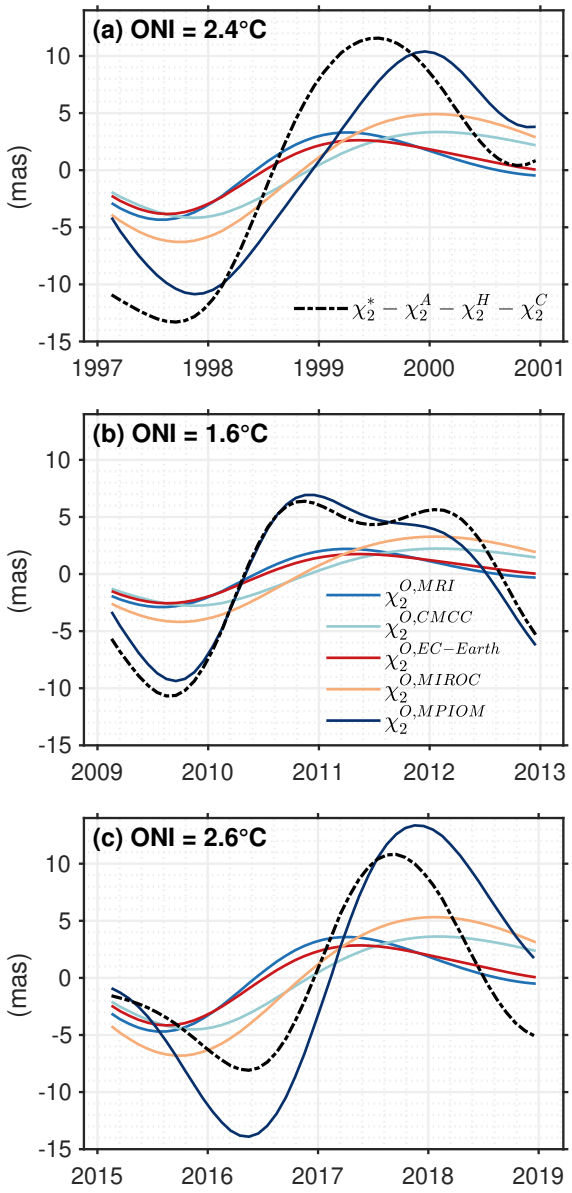

Figure A.14: As Figure 4 in the main text but without spatial weighting.

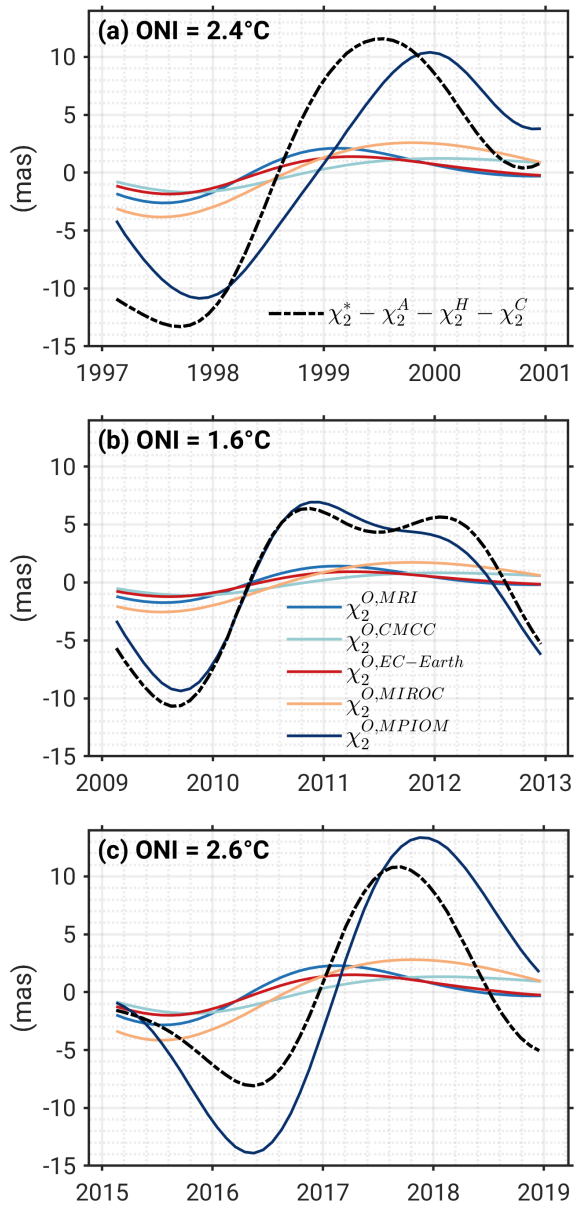

Figure A.15: As Figure 4 in the main text but with the Bellingshausen Basin masked out.

Table A.1: Selected specifications of the CMIP6 models used in this study

	CMCC-ESM2	EC-Earth3	MIROC6	MRI-ESM2
Short name	CMCC	EC-Earth	MIROC	MRI
Experiment	historical	historical	historical	historical
Variant label	r1i1p1f1	r1i1p1f1	r1i1p1f1	r1i1p1f1
Temporal resolution	monthly	monthly	monthly	monthly
Ocean/sea ice				
Ocean model[a]	NEMO 3.6	NEMO3.6	COCO4.9	MRI.COM4.4
Grid spacing (km)	100	100	100	100
Vertical levels	50	75	63	61
Atmosphere				
Atmospheric model[b]	CAM5.3	IFS cy36r4	CCSR AGCM	MRI.AGCM3.5
Vertical levels	30	91	81	80
Reference	Lovato et al. (2021)	EC-Earth Consortium (2019)	Tatebe and Watanabe (2018)	Yukimoto et al. (2019)

[a]Abbreviations: NEMO (Nucleus for European Modeling of the Ocean), COCO (CCSR Ocean Component Model of AORI/JAMSTEC), MRI.COM (Meteorological Research Institute Community Ocean Model)

[b]Abbreviations: CAM (Community Atmosphere Model of NCAR), IFS (Integrated Forecasting System of ECMWF), CCSR AGCM (Center of Climate System Research/National Institute for Environment Studies Atmospheric General Circulation Model), MRI.AGCM (Meteorological Research Institute Atmospheric General Circulation Model)

Table A.2: Spatial weights depending on the confidence level $100\% \cdot (1 - \alpha)$ for correlation with ONI

Confidence	$< 68\%$	68–90%	90–95%	$> 95\%$
Weight	0	1/3	2/3	1

B. Supporting Information for “Chaotic oceanic excitation of low-frequency polar motion variability”

B.1. Comparison of hydrological excitation series

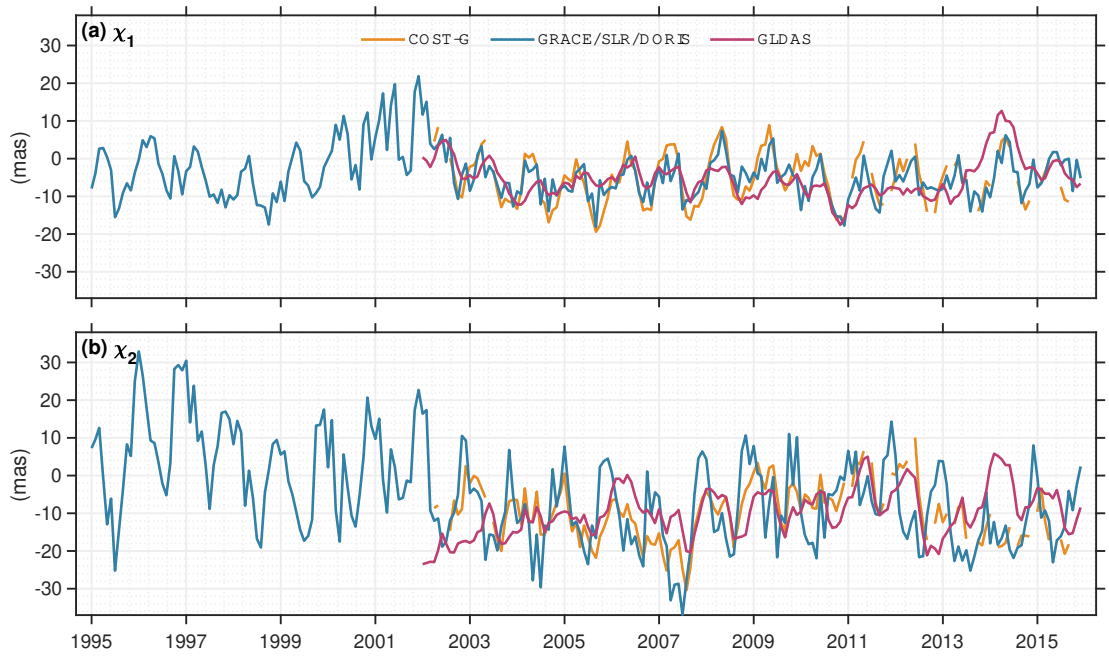

Figure B.1: Hydrological contribution $\hat{\chi}^{\mathrm{H}}$ to polar motion excitation $\hat{\chi} = \chi_1 + \mathrm{i}\chi_2$ (mas) deduced from the monthly GRACE/SLR/DORIS gravity field solution described in the main text (1995/01–2015/12, blue curves), the COST-G GravIS RL01 continental water storage anomalies (2002/04–2015/08 with gaps, yellow curves, Boergens et al., 2020), and the Global Land Data Assimilation System (GLDAS, 2002/01–2015/12, purple curves, Rodell et al., 2004). The COST-G and GLDAS time series have been adjusted such that their trends and mean values agree with those of GRACE/SLR/DORIS over the respective common time period, starting early 2002. Note that GRACE/SLR/DORIS was detrended over 1995–2015, as in the main text.

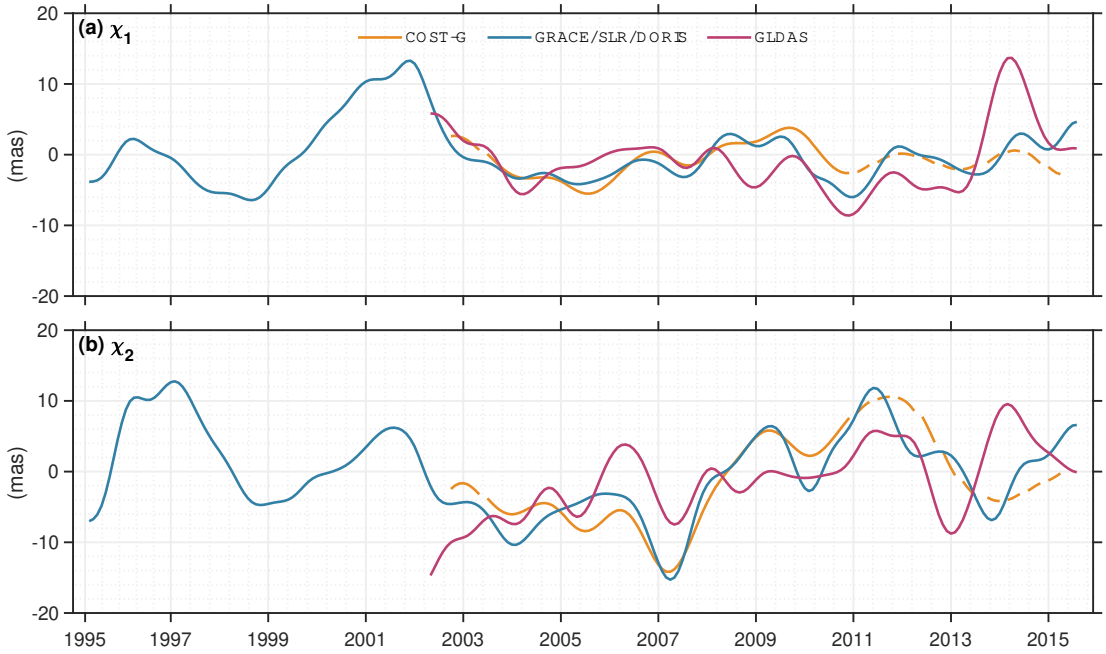

Figure B.2: As in Fig. B.1 but with each χ_1 and χ_2 time series filtered to periods longer than 14 months and cut back by 4 months at the respective end points.

List of abbreviations

AAM atmospheric angular momentum

BIH Bureau International de l'Heure

BTS84 BIH Terrestrial System 1984

CIO Celestial Intermediate Origin

CIP Celestial Intermediate Pole

cm centimetre

CMIP6 Coupled Model Intercomparison Project Phase 6

CRF Celestial Reference Frame

CW Chandler Wobble

DA data assimilation

DEBOT David Einšpigel's Barotropic Ocean Tide model

DECK Diagnostic, Evaluation and Characterization of Klima

$\triangle$LOD excess of Length-of-Day

DORIS Doppler Orbitography and Radiopositioning Integrated by Satellite

dUT1 difference to Universal Time 1

ECCO Estimating the Circulation and Climate of the Ocean

ECMWF European Centre for Medium-Range Weather Forecasts

EKE eddy kinetic energy

ENSO El Niño–Southern Oscillation

EOF empirical orthogonal function

EOP Earth Orientation Parameter

ERA Earth Rotation Angle

ERP Earth Rotation Parameter

EWDA equivalent water depth anomaly

EWH equivalent water height

FESOM2 Finite-Element/volumE Sea ice-Ocean Model version 2

GAL gravitational attraction and loading

GCM general circulation model

GCRS Geocentric Celestial Reference System

GIA Glacial Isostatic Adjustment

GLONASS Globalnaja nawigazionnaja sputnikowaja sistema

GNSS Global Navigation Satellite System

GRACE Gravity Recovery and Climate Experiment

GRACE/-FO Gravity Recovery and Climate Experiment - Follow On

GPS Global Positioning System

GSW Gibbs SeaWater

HAM hydrologic angular momentum

IAU International Astronomical Union

IB inverted barometer

ICRS International Celestial Reference System

ICRF International Celestial Reference Frame

IDS International DORIS Service

IERS International Earth Rotation and Reference Systems Service

ITRF International Terrestrial Reference Frame

ITRS International Terrestrial Reference System

JPL Jet Propulsion Laboratory

km kilometre

LOD Length-of-Day

m metre

mas milliarcseconds

MEI Multivariate ENSO Index

MEO Medium Earth Orbit

MIP Model Intercomparison Project

MITgcm Massachusetts Institute of Technology general circulation model

MJO Madden-Julian Oscillation

MPIOM Max Planck Institute Ocean Model

ms milliseconds

NASA National Aeronautics and Space Administration

N Newton

NEMO Nucleus for European Models of the Ocean

NOAA National Oceanic and Atmospheric Administration

NRO non-rotating origin

OAM oceanic angular momentum

OCCIPUT OceaniC Chaos—ImPacts, strUcture, predicTability

ONI Oceanic Niño Index

PDO Pacific Decadal Oscillation

Pa Pascal

PVE Percentage of Variance Explained

RMS Root-Mean-Square

s second

SAM Southern Annular Mode

SLA sea level anomalies

SLAM Sea Level Angular Momentum

SLR Satellite Laser Ranging

SOI Southern Oscillation Index

SST sea surface temperature

STF subtropical front

SWW Southern Westerly Winds

TCG Geocentric Coordinate Time

TIO Terrestrial Intermediate Origin

TIRS Terrestrial Intermediate Reference System

TRF Terrestrial Reference Frame

TWS terrestrial water storage

TWSA total water storage anomalies

UTC Coordinated Universal Time

UT1 Universal Time 1

VLBI Very Long Baseline Interferometry

WGS84 World Geodetic System 1984

yr year

List of figures

List of tables